TUM School of Natural Sciences
Technische Universität München

Structural Characterization of Gas Diffusion Layers for an Optimized Water Retention and Removal in Proton-Exchange-Membrane Fuel Cells

Anne Berger

Vollständiger Abdruck der von der TUM School of Natural Sciences der Technischen Universität München zur Erlangung des akademischen Grades einer

Doktorin der Ingenieurwissenschaften (Dr.-Ing.)

genehmigten Dissertation.

Vorsitz:

Prof. Dr.-Ing. Harald Klein

Prüfer der Dissertation:

1. Prof. Dr. Hubert A. Gasteiger
2. Prof. Dr.-Ing. Kai-Olaf M. Hinrichsen

Die Dissertation wurde am 19.05.2025 bei der Technischen Universität München eingereicht und durch die TUM School of Natural Sciences am 25.06.2025 angenommen.

Abstract

The urgent need to address climate change has propelled research and development in sustainable energy solutions, where hydrogen fuel cell technology emerges as a significant player. This thesis explores critical aspects of proton-exchange-membrane fuel cells (PEMFCs), specifically addressing mass transport challenges within gas diffusion layers (GDLs). The primary objective of this thesis is to study structural features of gas diffusion layer substrates (GDL-S) and microporous layers (MPLs), and their impact on the water management within single-cell fuel cells. The investigation covered in this thesis ranges from a detailed examination of the GDL-S and MPL under low relative humidity (RH) conditions to a thorough analysis during instances of flooding within the fuel cell. By elucidating these relationships, the research aims to provide crucial insights that can contribute to the improvement of fuel cell performance across a range of operating conditions.

The impact of the GDL structure on oxygen diffusivity under low-RH ("dry") conditions is characterized, introducing an approach to determine the tortuosity/porosity (τ/ε) ratio in operating fuel cells for GDL-S and MPLs. The analysis reveals the significance of small pores on the effective diffusivity, impacting both microporous layers (MPLs) and some GDL-S materials containing carbon black within the structure. The experimental finding are supported by simulations on the structure obtained by focused-ion-beam scanning-electron-microscopy (FIB-SEM). The study extends to liquid water management by studying how water filling of the MPL structure, steered by the binder's properties, impacts τ.

Understanding water removal becomes a focal point in the last part of this thesis, as it investigates the impact of interface properties between the MPL and GDL-S. By introducing an inhomogeneous intrusion of MPL material into the GDL-S material, this thesis provides a unique perspective on localized water removal. The performance differences, measured in a single-cell fuel cell, between the intruded-GDL and a reference GDL are correlated with structural data obtained through scanning electron microscopy (SEM) and mercury intrusion porosimetry (MIP). *Operando*-x-ray tomographic imaging (XTM) further enhances the understanding of liquid water distribution within the GDL-S.

In conclusion, this thesis provides crucial insights into GDL structure parameters that affect diffusivity and water management, offering design recommendations for an "ideal" GDL. The proposed ideal GDL

design, incorporating a highly porous MPL network with a low τ/ε-ratio, a hydrophobic MPL binder, and an inhomogeneous MPL intrusion, while large pores remain in the GDL-S, lays the foundation for future advancements for achieving efficient and reliable PEMFC systems.

Kurzfassung

Der dringende Bedarf, dem Klimawandel entgegenzuwirken, hat Forschung und Entwicklung im Bereich nachhaltiger Energielösungen vorangetrieben, wobei die Wasserstoff-Brennstoffzellentechnologie als bedeutender Akteur hervortritt. Diese Dissertation erforscht kritische Aspekte von Protonenaustauschmembran-Brennstoffzellen (PEMBZs) und befasst sich speziell mit den Herausforderungen des Massentransports innerhalb der Gasdiffusionsschichten (GDLs). Das Hauptziel dieser Arbeit besteht darin, die strukturellen Merkmale von Gasdiffusionsschichtsubstraten (GDL-S) und mikroporösen Schichten (MPLs) sowie deren Einfluss auf das Wassermanagement in Einzelzellen-Brennstoffzellen zu untersuchen. Die Untersuchung erstreckt sich von einer detaillierten Analyse der GDL-S und MPL unter trockenen Bedingungen (das heißt bei geringer relativer Feuchte) bis hin zu einer Untersuchung während Flutungssituationen durch die Bildung von flüssigem Wasser in der Brennstoffzelle. Durch die Aufklärung dieser Zusammenhänge zielt die Forschung darauf ab, entscheidende Erkenntnisse bereitzustellen, die zur Verbesserung der Leistung von Brennstoffzellen unter verschiedenen Betriebsbedingungen beitragen können.

Die Auswirkung der GDL-Struktur auf die Sauerstoffdiffusivität unter trockenen Bedingungen wird charakterisiert, wobei eine Methode zur Bestimmung des Verhältnisses von Tortuosität und Porosität (τ/ε) für GDL-S und MPLs vorgestellt wird. Die Analyse zeigt die Bedeutung kleiner Poren für die effektive Diffusivität auf, die sowohl mikroporöse Schichten (MPLs) als auch einige GDL-S mit im Strukturaufbau enthaltenem Ruß betrifft. Die experimentellen Ergebnisse werden durch Simulationen unterstützt. Die für die Simulation benötigte 3D Struktur wurde durch fokussierte Ionenstrahl-Rasterlelektronenmikroskopie (FIB-SEM) gewonnen. Die Studie wird um einen Aspekt des Wassermanagements erweitert, indem der Einfluss der Wasserauffüllung der MPL-Struktur auf τ durch die Eigenschaften des Binders untersucht wird.

Die Untersuchung des Wasserabtransports ist Schwerpunkt im letzten Teil dieser Arbeit, wo auf die Eigenschaften der Grenzfläche zwischen der MPL und der GDL-S eingegangen wird. Durch die Herstellung einer inhomogenen Intrusion von MPL-Material in das GDL-S-Material konnte ein lokalisierter Wasserabtransport aus der Zelle bestimmt werden. Die Leistungsunterschiede, die in einer Einzelzellen-Brennstoffzelle zwischen der intrudierten GDL und einer Referenz-GDL gemessen werden, korrelieren mit

strukturellen Daten, die durch Rasterelektronenmikroskopie (SEM) und Quecksilber-Intrusions-Porosimetrie (MIP) erhalten wurden. *Operando*-Röntgencomputertomographie (XTM) vertieft das Verständnis der Verteilung von Flüssigwasser in der GDL-S.

Zusammenfassend liefert diese Arbeit entscheidende Einblicke in die GDL-Strukturparameter für Diffusivität und Wassermanagement und bietet Gestaltungsempfehlungen für eine „ideale“ GDL. Das vorgeschlagene „ideale“ GDL-Design umfasst ein hochporöses MPL-Netzwerk mit einem niedrigen τ/ε-Verhältnis, ein hydrophobes MPL-Bindemittel und eine inhomogene MPL-Intrusion, bei der große Poren in der GDL-S erhalten bleiben. Die Erkenntnisse dieser Arbeit können zukünftige Fortschritte zur Erreichung effizienter und zuverlässiger PEMBZ-Systeme unterstützen.

Contents

List of Acronyms

Abbreviation	Description
CCM	Catalyst coated membrane
CL	Catalyst layer
ECSA	Electrochemically active surface area
EW	Equivalent weight
FIB	Focused-ion-beam
GDL	Gas diffusion layer
GDL-S	Gas diffusion layer substrate
HOR	Hydrogen oxidation reaction
MEA	Membrane electrode assembly
MPL	Microporous layer
OCV	Open circuit voltage
ORR	Oxygen reduction reaction
PEM	Proton-exchange-membrane
PEMFC	Proton-exchange-membrane fuel cell
PEN	Polyethylene naphthalate
PFSA	Perfluorosulfonic acid
PGM	Platinum group metal
PSD	Pore size distribution
PTFE	Polytetrafluoroethylene
RH	Relative humidity
SAXS	Small-angle x-ray scattering
SEM	Scanning electron microscopy
WAXS	Wide-angle x-ray scattering
XTM	X-ray tomographic imaging

List of Symbols

Latin Symbols

Symbol	Unit	Description
A	m^2	Area
b	V/dec	Tafel slope
c	mol/L	Concentration
d_{pore}	nm	Pore diameter
D	cm^2/s	Diffusion coefficient
E	V	Voltage/Potential
E^0	V	Standard electrode potential
F	C/mol	Faraday constant: 96485 C/mol
f	-	Form factor
G	kJ/mol	Gibb's free energy
H	kJ/mol	Enthalpy
i	A/cm^2	Current density
i_0	mA/cm^2	Exchange current density
M	g/mol	Molar mass
n	–	Number of electrons
$\dot{N}$	mol/s	Molar flux
p	Pa	Pressure
R	various	Resistance
R_Ω	Ωcm^2	Areal ohmic resistance
R_T	s/cm	Transport resistance
R	J/(mol K)	Ideal gas constant: 8.3145 J/(mol K)
rf	cm^2/cm^2	Roughness factor
S	J/(mol K)	Entropy
T	K	Temperature
x	-	Molar fraction

Greek Symbols

Symbol	Unit	Description
α	-	Transfer coefficient
γ	N/m	Surface tension
γ^*	-	Reaction order wrt. p_{O_2}
Δ	-	Difference
ε	-	Porosity
η	V	Overpotential
θ	°	Contact angle
ρ	kg/m³	Density

Indices

Symbol	Description
an	Anode
c	Capillary
cath	Cathode
ch	Channel
eff	Effective
geo	Geometric
lim	Limiting
rev	Reversible
theo	Theoretical
thermo-eq.	Thermo-equivalent
W	Water

1 Introduction

The climate change debate has been present in the daily news as new temperature records are continuously set, climate disasters such as wild fires and heavy rainfalls occur more and more often,[1,2] and as progressively legislation is passed to reduce greenhouse gas emissions. Yet, the legislative efforts still fall short of effectively reversing or slowing down the global warming to align with the 1.5℃ limit set by the Paris agreement.[3] The Intergovernmental Panel on Climate Change (IPCC) has published a study in 2023,[4] where they estimated the impact of the currently implemented policies on the global warming, and even in their best-case-scenario the projection of the temperature increase is not even close to meeting the 1.5℃ target. They postulate that CO_2-equivalent emissions need to be drastically reduced in the next years.

With this pending threat of the climate crisis and increasing political pressure, various sectors (energy supply, industry, transport, buildings, agriculture) that are largely responsible for greenhouse gas emissions are actively working on curtailing their climate impact. For example, heating of households can be realized with heat pumps,[5,6] the road transport is being electrified,[5,7] and the steel industry is developing processes to use hydrogen instead of coke,[5,8] just to name a few. All these processes rely on an increased energy production by renewable sources. However, the energy demand does not always align with the time or the place, when and where supply of renewable energy is available.

Therefore, the importance of energy storage and transport is steadily growing. Battery systems can buffer some energy and have the advantage of a high energy conversion efficiency. However, when needing to store large amounts of energy, their size and weight become the limiting factor. Also, transportation of large-scale batteries to distribute the energy is not a viable option. Therefore, other chemical energy carriers become increasingly important with one of the most promising being hydrogen. Hydrogen has a large gravimetric energy density and can be produced emission-free from water and energy by water electrolysis. The large advantage of hydrogen as an energy carrier is that the generation and the use of hydrogen is decoupled and that hydrogen can be transported by, e.g. pipeline, truck or ship.[9] One large criticism of the hydrogen use is the low power-to-power efficiency.[10] Yet, to convert hydrogen to

energy, the proton exchange membrane fuel cell (PEMFC) is known to be most efficient compared to more traditional combustion processes. Therefore, fuel cells would an essential element in a hydrogen economy.

One area, where fuel cells have widely attracted attention, is the transportation sector. Passenger cars, trucks, trains, ships, and even airplanes are implementing strategies to use hydrogen fuel cells. While battery electric vehicles (BEVs) have proven successful and are foreseen to take over much short-range heavy duty truck transport,[5] fuel cell electric vehicles (FCEVs) will met the demand for long-distance heavy duty truck transport,[5,11] ships,[12] trains,[13] and airplanes.[14]

To realize a hydrogen based transport scenario in all these sectors, the PEMFC system needs to be developed and optimized to be suitable in terms of performance and price. To achieve this goal on the small scale, the processes taking place inside a single cell fuel cell need to be better understood to reach the targets regarding activity, durability, and costs. While, there are many aspects to study, such as the activity of the oxygen reduction reaction (ORR) catalyst, the mass transport within the catalyst structure, and the degradation mechanisms of the catalyst layer (CL) or the membrane when exposed to accelerated stress tests (ASTs), this thesis deals with the mass transport within the gas diffusion layer (GDL). The water management within a fuel cell is subject to a delicate balance. The relative humidity needs to be high enough to ensure a good proton conductivity within the membrane and ionomer phase. Yet, the cell design and operating conditions must hinder the accumulation of liquid water within the GDL pores, which need to remain free for good oxygen diffusivity.

A GDL typically consist of a GDL substrate (GDL-S) and a microporous layer (MPL). The GDL-S is usually based on a fibrous substrate with porosities between 60-85%[15–17] and pore diameters between 10-50 µm.[16] The characteristic pore size of commonly used carbon-black based MPLs is < 1 µm.[18,19] The combination of both layers fulfill several important tasks. They target an even distribution of reactants (hydrogen and oxygen) towards the CL and remove the product water. Additionally, the GDL is responsible for a good electrical and thermal connection between the bipolar plate and the CL. The MPL in particular adds a protective layer from the carbon fibers of the GDL-S, which are known to puncture the membrane.[20] Additionally, the MPL serves as a percolation pathway for the water removal, which allows higher current densities at "wet" conditions (operating conditions where large amounts of liquid ware are formed in the cell).[21]

Fig. 1.1 summarizes the key research aspects, which are addressed in this thesis. The topics are covered in Chapter 4 and are separated into four different categories:

4.1 Determining the τ/ε-ratio for GDL-S and MPLs

4.2 Studying the impact on τ of the MPL as a function of the water filling, which can be steered by the hydrophobicity/hydrophilicity of the binder

4.3 The localization of water removal due to the interface properties between the MPL and GDL-S

In more detail, Fig. 1.1 shows a sketch of the cathode side of the cell, including the CL, the MPL, and the GDL-S. Different research questions on the structure of the individual layers are important, depending if the operating conditions are dry or wet. The dry structure of the GDL is often correlated with the performance behavior of the single cell. Therefore, this thesis deals with the determination of structural parameters of different GDL-S and MPLs. A method was developed to determine the τ/ε-ratio for both GDL substrates and MPLs in an operating fuel cell under realistic conditions, using limiting current measurements. To further analyze the porous structure of the MPL, a 3D model was obtained using focused-ion-beam scanning-electron-microscopy (FIB-SEM). The 3D model was used for simulation to support the fuel cell measurements.

Continuing with the topics of the thesis concerning liquid water management, the 3D MPL model was applied to study the influence of the binder properties on the liquid water filling of the MPL. Depending if the binder was hydrophobic or hydrophilic, large pores or small pores are filled first with condensing water, and the impact of the water filling on the porous network was studied. The theoretical considerations can be linked with fuel cell performance measurements with either PTFE (hydrophobic) or Nafion® (hydrophilic) as a binder.

In a last step, this thesis addresses the impact of the MPL/GDL-S interface by creating a GDL with an inhomogeneous MPL intrusion into the GDL-S. The performance of the intruded-GDL was compared to a reference GDL with an MPL that does not intrude into the GDL-S and the performance differences were linked with structural data from scanning-electron-microscopy (SEM) and mercury intrusion porosimetry (MIP). The structural analysis was supported by *ex-situ* x-ray tomographic imaging (XTM). Additionally, *operando*-XTM measurements could measure the liquid water distribution in the GDL-S.

This thesis will present the theoretical background for the different analyses, carried out throughout this work. Subsequently, a detailed description of the experimental procedures is provided, focusing on the cell assembly, limiting current measurements, and mercury intrusion porosimetry. The main results of the work are presented in form of journal publications covering the topics as summarized in Fig. 1.1, ranging

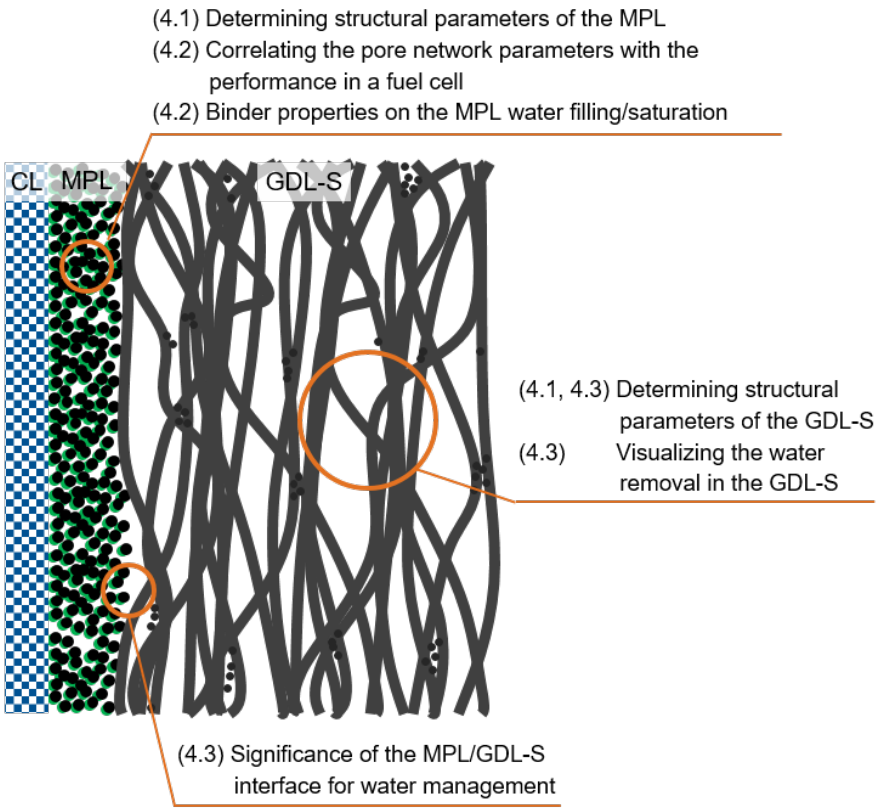

Figure 1.1 Summary of the research questions covered in this thesis, visualized and localized on a sketch of the components on the cathode side of the fuel cell (CL, MPL, GDL-S); the research aspects range from characterizing the structure at dry conditions to analyzing the water management at wet conditions; the numbers refer to the chapters of this thesis, where the corresponding topic is discussed

from dry diffusion resistance to liquid water removal. Lastly, final conclusions are drawn from the works of this thesis and combined in a proposal for an ideal GDL structure.

2 Theoretical Background

This chapter explores the theoretical foundation for the analyses conducted in this thesis. Initially, the fundamental principles of PEMFC are discussed, followed by a depiction of the essential components in a PEMFC. The theory behind diffusion is clarified, and the extraction process of transport resistances from limiting current measurements is explained. Finally, the water formation and removal are expanded on, and imaging techniques to determine structural parameters or image water droplets are considered.

2.1 Fundamental Principles of Proton-Exchange-Membrane Fuel Cell

This subsection covers the thermodynamic principles and discusses the individual voltage loss mechanisms such as kinetic, ohmic, and mass tranport losses.

2.1.1 Thermodynamics

A PEMFC can convert chemical energy from hydrogen together with the oxidizing agent oxygen to water and electricity. In the reaction, hydrogen is oxidized at the anode, while oxygen is reduced at the cathode. Water is formed as a product. The driving force for this reaction is the difference in electrochemical potential between the hydrogen oxidation reaction (HOR) and the oxygen reduction reaction (ORR). The reaction equations and the electrochemical half- and full-cell potentials (at standard conditions) are listed in Eq. 2.1-2.3.

$$\text{Anode}: \quad \mathrm{H_2} \rightarrow 2\mathrm{H^+} + 2\mathrm{e^-} \qquad E^0 = 0.00\ \mathrm{V} \tag{2.1}$$

$$\text{Cathode}: \quad \frac{1}{2}\mathrm{O_2} + 2\mathrm{H^+} + 2\mathrm{e^-} \rightarrow \mathrm{H_2O_{(l)}} \qquad E^0 = 1.23\ \mathrm{V} \tag{2.2}$$

$$\text{Total}: \quad \mathrm{H_2} + \frac{1}{2}\mathrm{O_2} \rightarrow \mathrm{H_2O}_{(l)} \qquad E^0 = 1.23\ \mathrm{V} \tag{2.3}$$

The thermodynamic voltage E is linked with the Gibb's energy or free energy of the reaction (ΔG) with the correlation given in 2.4 using the number of electrons n and the Faraday constant $\mathrm{F} = 96485\ \mathrm{C/mol}$.

$$E = -\frac{\Delta G}{n\mathrm{F}} \tag{2.4}$$

According to the definition of ΔG, the Gibb's energy is connected with the enthalpy (ΔH) and entropy (ΔS) of a process at the temperature T by:

$$\Delta G = \Delta H - T\Delta S. \tag{2.5}$$

The representation in Eq. 2.2 and 2.3 considers the formation of liquid water and thus uses the higher heating value (HHV). When the water is considered in gaseous form, the lower heating value (LHV) needs to be used. Table 2.1 summarized ΔG and ΔH for the reaction of hydrogen and oxygen to water depending on the state of the product water.

Table 2.1 Gibb's energy ΔG, enthalpy ΔH, entropy ΔS, and specific heat capacity Δc_P of the reaction $\mathrm{H_2} + \frac{1}{2}\mathrm{O_2} \rightarrow \mathrm{H_2O}$ depending of the state of the product water, taken from Atkins.[22]

	ΔG KJ/mol	ΔH kJ/mol	ΔS J/mol/K	Δc_P J/mol/K
HHV (liquid)	-237.13	-285.83	-163.34	32.09
LHV (gas)	-228.59	-241.83	-44.42	9.92

In a PEMFC, the chemical energy of the hydrogen is directly converted to electrical energy. The thermodynamic efficiency of a PEMFC is defined as:

$$\xi_\mathrm{PEMFC} = \frac{\Delta G}{\Delta H} \tag{2.6}$$

Usually, the efficiency is referenced to ΔH of the higher heating value,[23] which transfers (in a relationship analogous to that of Eq. 2.4) to the so-called thermo-neutral voltage of 1.48 ℃ at standard conditions. Fig. 2.1a shows the efficiency over temperature. For the calculation, ΔG is calculated for each temperature using the underlying equations as given in Eq. 2.7 and 2.8 under the assumption that the specific heat capacity Δc_p stays constant over the given temperature range.

$$\left(\frac{\partial \Delta G}{\partial T}\right)_\mathrm{p} = -\Delta S(T) \tag{2.7}$$

$$\left(\frac{\partial \Delta S}{\partial T}\right)_\mathrm{p} = -\frac{\Delta c_\mathrm{p}}{T} \tag{2.8}$$

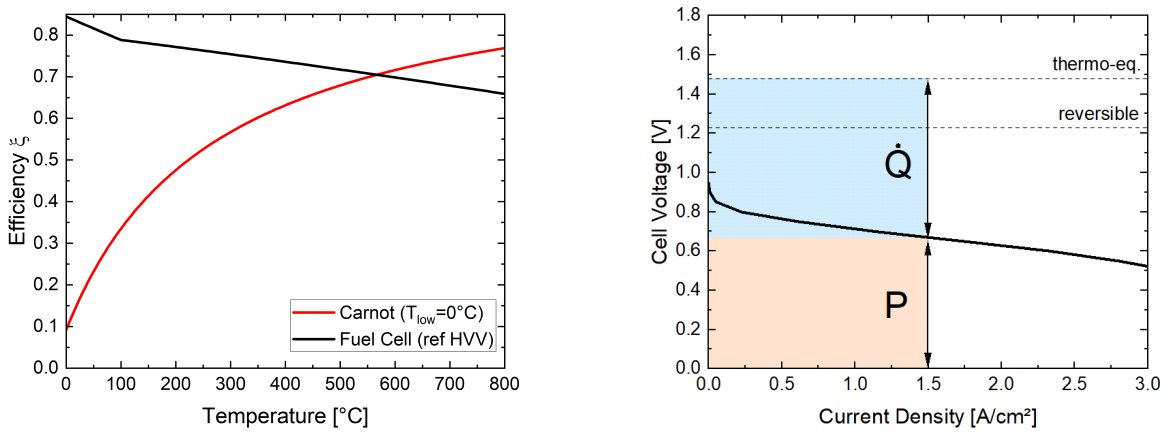

(a) **(b)**

Figure 2.1 a) Efficiency comparison from a thermodynamic perspective of traditional combustion process limited by the Carnot efficiency and a fuel cell referenced to the HHV at 25 °C and ambient pressure (change in ΔG was calculated using the assumption that c_P is constant for the given temperatures); b) Example of the polarization curve to demonstrate the proportion of power and heat released; the blue area represents $\dot{Q}$ and the orange area represents the electrical power P examplary at 1.5 A/cm².

The efficiency depicted in Fig.2.1a within the PEMFC is not a continuous function due to a shift in ΔG at 100 °C, transitioning from the higher heating value to the lower heating value. Generally, the thermodynamic efficiency of a PEMFC is highest at low temperatures and gradually decreases with rising temperatures. To give an example, the efficiency is 83% at 25 °C.

For reference, the thermodynamic efficiency of the PEMFC is compared with the efficiency of a traditional combustion process, where the chemical energy of the fuel is first converted into heat, then into mechanical energy, and finally into electrical energy. The thermodynamic efficiency is described by the Carnot efficiency, which considers the temperatures for the hot reservoir with the temperature T_{H} and the cold reservoir with the temperature T_{C}:

$$\xi_{\mathrm{Carnot}} = \frac{T_{\mathrm{H}} - T_{\mathrm{C}}}{T_{\mathrm{H}}} \tag{2.9}$$

For reference, the thermodynamic Carnot efficiency is plotted in Fig. 2.1a over the temperature of T_{H} with T_{C} being 25 °C. It can be observed that that a conventional combustion process can only be efficient at high temperatures. As the Carnot process efficiency rises with temperature, an ideal conventional combustion process surpasses the thermodynamic efficiency of a PEMFC beyond approximately 570 °C. Fig.2.1a distinctly illustrates that the advantage of PEMFCs lies in the low-temperature range, which illustrates the need to further develop PEMFC technology.

However, the PEMFC cannot be operated at the thermodynamic potential as there are different voltage losses taking place in the cell, which is further elaborated in section 2.1.2. Fig. 2.1b shows a so-called

polarization curve, which shows the achievable potential for current densities between 0-3 A/cm². Two horizontal lines mark the reversible (thermodynamic) and the thermo-equivalent voltage (voltage, where no heat flow occurs). The thermo-equivalent voltage at standard conditions is $E_{\mathrm{thermo-eq.}} = 1.48\ \mathrm{V}$. Fig. 2.1b marks additionally the potential difference exemplarily at 1.5 A/cm², which is proportional to the electrical power P and the heat $\dot{Q}$. Both variables are defined as:

$$P = -i \cdot E_{\mathrm{cell}} \tag{2.10}$$

$$\dot{Q} = -i \cdot (E_{\mathrm{thermo-eq.}} - E_{\mathrm{cell}}) \tag{2.11}$$

The electrical power P in Fig. 2.1b is represented by the orange square (Eq. 2.10), while the heat release $\dot{Q}$ is represented by the blue square (Eq. 2.11).

2.1.2 Voltage Losses

The voltage losses occurring in a PEMFC can be kinetic, ohmic, or mass transport related. In general, at low current densities, kinetic losses dominate, at intermediate current densities, ohmic losses are mostly responsible for the further potential drop, and at high current densities, mass transport losses determine the shape of the polarization curve.

In the following section, we would like to explain the following voltage losses:

- Kinetic losses due to the ORR: η_{ORR}
- Kinetic losses due to the HOR: η_{HOR}
- Ohmic losses due to the cell resistance R_{Ω}
- Losses due to the proton conduction resistance at the cathode $R^{\mathrm{eff}}_{\mathrm{H^+,cath}}$ and anode $R^{\mathrm{eff}}_{\mathrm{H^+,an}}$
- Mass transport losses η_{tx}

In summary, the cell voltage is described by Eq. 2.12,[24,25] and an example on the contribution of the individual voltage losses on a real polarization curve is demonstrated in Fig. 2.2.

$$E_{\mathrm{cell}} = E_{\mathrm{rev}} - \eta_{\mathrm{HOR}} - |\eta_{\mathrm{ORR}}| - i \cdot R_{\Omega} - i \cdot \left(R^{\mathrm{eff}}_{\mathrm{H^+,cath}} + R^{\mathrm{eff}}_{\mathrm{H^+,an}}\right) - \eta_{\mathrm{tx}} \tag{2.12}$$

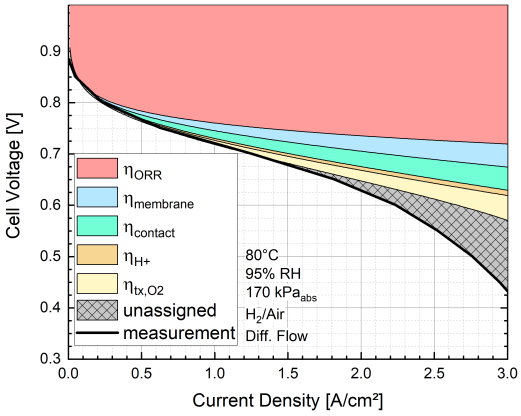

Figure 2.2 Breakdown of the voltage losses for a single-cell PEMFC polarization curve recorded on a 5 cm² active area at 80 °C, 170 $\mathrm{kPa_{abs}}$, and 95% RH at differential flow of H_2/air; each loss contribution given in Eq. 2.12 is subsequently subtracted from the Nernst potential. The kinetic losses due to the ORR (η_{ORR} marked in red, the ohmic losses are split into the losses due to membrane resistance (η_{membrane}, blue) and due to the contact resistance (η_{contact}, green); the losses for the proton conduction resistance (here from cathode only) are marked in orange, and the losses due to mass transport (η_{tx}) in yellow; the difference between the attributable voltage losses and the measurement is called unassigned voltage losses.

Kinetic Losses

Kinetic losses are caused by kinetic overpotentials from the HOR (η_{HOR}) or the ORR (η_{ORR}), as described by the Butler-Volmer equation. The Butler-Volmer equation, given in Eq. 2.13, connects the overpotential η with the corresponding current density, which is a function of several parameters. The exchange current density i_0 describes the kinetic reaction rate constant for a specific electrocatalyst. The electrode roughness factor rf connects the actual surface area of the catalyst particles to the geometric surface area of the electrode (e.g. if the total electrochemical surface area is 1200 cm² for a 5 cm² CL, the rf is $240\ \mathrm{cm^2_{Pt}/cm^2_{geo}}$). The transfer coefficient α describes the symmetry of the energy barrier of the rate-determining step. Additional parameters are the temperature T, the Faraday constant F, and the ideal gas constant and R.

$$i = i_0 \cdot rf \left(\exp\left(\frac{\alpha \cdot n \cdot \mathrm{F}}{\mathrm{R}T} \cdot \eta \right) - \exp\left(-\frac{(1-\alpha) \cdot n \cdot \mathrm{F}}{\mathrm{R}T} \cdot \eta \right) \right) \tag{2.13}$$

To simplify Eq. 2.13, the Tafel slope b is defined in Eq. 2.14 using a more general definition of the anodic or cathodic transfer coefficient $\alpha_{\mathrm{an,cath}}$ ($\alpha_{\mathrm{an}} \equiv \alpha \cdot n, \alpha_{\mathrm{cath}} \equiv (1-\alpha) \cdot n$). The Tafel slope describes the kinetic behavior of the voltage loss typically in units of mV/dec.

$$b = \frac{2.303 \cdot \mathrm{R}T}{\alpha_{\mathrm{an,cath}} \cdot \mathrm{F}} \tag{2.14}$$

Eq. 2.15 shows the Butler-Volmer reaction using the Tafel slope.

$$i = i_0 \cdot rf \left(10^{\frac{\eta}{b}} - 10^{\frac{\eta}{b}}\right) \tag{2.15}$$

It was determined in the literature that the HOR is very fast on a platinum catalyst[26–28] and that it causes very little voltage losses. In contrast, the ORR is often describes as sluggish and therefore, the kinetic losses of the ORR are responsible for a large fraction of the voltage losses in a PEMFC, as can be seen in Fig. 2.2.

Ohmic Losses

Another part of the voltage losses is caused by the ohmic resistance R_Ω of the cell. The higher the current density, the more relevant are ohmic losses, as R_Ω converts into a voltage drop by multiplication with the current density. Ohmic losses originate mostly from the contact resistance between the flow field and the GDL and from the membrane resistance. In Fig. 2.2, both contributions are separated and the ohmic losses from the membrane are shaded in blue and the ohmic losses from the contact resistance are shaded in green. The membrane resistance is a function of the conductivity and the thickness. The contact resistance can be minimized with a higher compression of the GDL. Fig. 2.2 reveals that below a voltage of ≈0.75 V, the ohmic losses become increasingly important and cause a linearly increasing voltage drop with current density.

$$\eta_\Omega = R_\Omega \cdot i \tag{2.16}$$

The voltage losses due to the proton conduction in the anode and the cathode are not simple ohmic losses, as the $R^{\text{eff}}_{\text{H}^+,\text{an}}$ and $R^{\text{eff}}_{\text{H}^+,\text{cath}}$ also depend on the current density. The effective proton conduction resistance can be calculated from the overall proton conduction resistance. This is exemplary shown for $R_{\text{H}^+,\text{cath}}$ by Eq.2.17, using ζ, which is a function $i, R_{\text{H}^+,\text{cath}}$, and the Tafel slope b (see Eq. 2.17). The initial $R_{\text{H}^+,\text{cath}}$ can be measured by electrochemical impedance spectroscopy in blocking conditions (with nitrogen at the cathode so that no faradaic reactions can take place).[29,30]

$$R^{\text{eff}}_{\text{H}^+,\text{cath}} = \frac{R_{\text{H}^+,\text{cath}}}{3 + \zeta} \tag{2.17}$$

In Fig. 2.2, the losses due to the proton conduction in the cathode are shown in orange. In this measurement at a high membrane hydration state, these losses amount to minimal voltage drops, especially at

high current densities. Proton conduction resistances at the anode are typically neglected because they are very small and only become significant at low RH.[24]

Mass Transport Losses

The influence of mass transport losses on the voltage losses can be described by Eq. 2.18. The equation considers additional losses to the kinetics (see Neyerlin et al. for more details[25]) and a change to the Nernst potential when the oxygen concentration is lower at the electrode than it is in the flow field channel. A detailed derivation was documented by Zihrul et al.[31]

$$\eta_{\mathrm{tx}} = \frac{\mathrm{R}T}{\mathrm{F}} \cdot \left(\frac{1}{4} \cdot \frac{\gamma}{\alpha}\right) \cdot \ln\left(\frac{p_{\mathrm{O_2,ch}} - \frac{\mathrm{R}T}{4\mathrm{F}} \cdot R_{\mathrm{T,O_2}} \cdot i}{p_{\mathrm{O_2,ch}}}\right) \tag{2.18}$$

In Eq. 2.18, α represents the transfer coefficient ($\alpha = 1$) and γ represents the ORR reaction order with respect to $p_{\mathrm{O_2,ch}}$ ($\gamma = 0.54$)

Unassigned Losses

It can be seen in Fig. 2.2 that there is a difference between the voltages losses accounted for by the known mechanism and the measurement data. The unassigned losses are marked in gray and represent a significant portion of the losses, especially at higher current densities (>2 A/cm²). This very simple model seems to not be able to realistically account for the mass transport losses. One possible reason is that the $R_{\mathrm{T,O_2}}$ is measured at very low cell voltages (0.05 V), where significantly more heat evolution occurs. Depending on the thermal conductivity of the materials, most importantly of the GDL, the CL can have a higher temperature than the temperature at which the cell is controlled at. As the Freudenberg GDLs have a lower thermal conductivity, the temperature effect is more pronounced than e.g. for a Toray material with a higher thermal conductivity.[32] Additionally, it was shown that the structure of the catalyst support can influence the unassigned losses. A support with accessible pores leads to less unassigned voltage losses compared to a Ketjenblack.[33]

2.2 Components of a Single-Cell

The working principle of a PEMFC is illustrated in Fig. 2.3. A PEMFC consists of several individual layers, each with a specific function. The electrochemical reaction occurs at the anode and the cathode of the cell. Both half-cells are separated by a proton-exchange membrane (PEM). The GDL (gas diffusion layer)

is comprised of a GDL-substrate (GDL-S; generally d≈ 150 µm thick) and a microporous layer (MPL; generally d≈ 30 µm thick). The GDL is supported by a flow field on each side, in this case, a flow field with a 0.5 mm land and a 0.5 mm channel.

The HOR takes place at the anode (see Eq. 2.1). The resulting protons can be transported through the proton-exchange membrane to the cathode side. The electrons are conducted through an external circuit towards the cathode. Before reaching the external circuit, the electrons need to be conducted from or to the anode and cathode CL, respectively, going through the GDL and the flow field. At the cathode, the ORR combines the protons and electrons with the oxygen to create water. The reactants ($\mathrm{H_2}$ and $\mathrm{O_2}$) are supplied at the individual flow fields and are transported through the pores of the GDL towards the CLs. The product water is removed mostly on the cathode side, as it is locally produced at the cathode CL. However, due to back-diffusion through the membrane to the anode, a fraction of the formed water can also be removed at the anode, as indicated by the smaller arrows in Fig. 2.3 at the lower right side. Heat can be removed from the catalyst layer towards the flow fields.

All individual components will be explained in further detail with a strong focus on the GDL material.

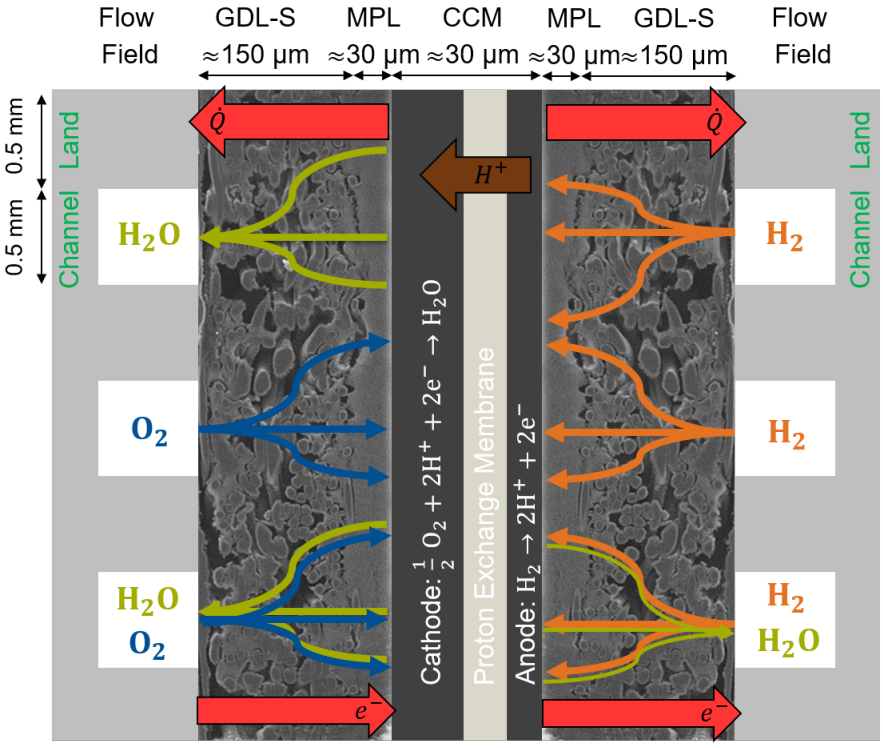

Figure 2.3 Working principle of a PEMFC, shown for the individual components (not to scale): the electrochemical reaction occurs at the anode and the cathode of the cell; both half-cells are separated by a PEM; the GDL (shown with an SEM picture of a self-made Li100 MPL on a Freudenberg H14 GDL-S) is comprised of a GDL-S (usually ≈150 µm thick) and an MPL (usually ≈30 µm thick); the GDL is supported by a flow field on each side (in this case a flow field with a 0.5 mm land and a 0.5 mm channel; heat ($\dot{Q}$) can be removed from the CL towards the flow fields; electrons are moved from the anode CL through an external circuit to the cathode CL; protons are transported through the membrane.

2.2.1 Catalyst Layer

The catalyst layer of a PEMFC usually consist of a platinum based catalyst on a conductive carbon support and an ionomer, which serves as a proton conductor and binder. The catalyst itself can be optimized to achieve a high activity. Recently, platinum-cobalt alloys have become a widely used to boost the ORR activity.[34–36] Additionally, the active catalyst needs to be dispersed on the support material to achieve a high electrochemically active surface area (ECSA). The platinum group metal (PGM) catalysts required for common PEMFCs are a major cost factor of a PEMFC system[37] and therefore, reducing the PGM loading in the electrode of a calatyst coated membrane (CCM) is essential. The requirements for the catalyst support are a good electrical conductivity and a (electro-)chemical stability at operating conditions. Usually, carbon is employed due to the low cost and the high electrical conductivity, sometimes in graphitized form to increase stability to carbon corrosion.[38] Carbon supports are distinguished by their internal porosity. A commonly used Vulcan carbon does not contain any internal pores and thus, all catalyst particles are located on the outside. Mass transport limitations are reduced as no intra-particle diffusion occurs. If a carbon type such as Ketjenblack contains internal pores, Pt particles are deposited on the outside and inside of the pores.[39] As an example for a mesoporous carbon, Toyota introduced mesoporous carbon nano dentrites, where around 80% of the catalyst particles are located inside the pores.[40] Even though, mass transport limitations are increased when Pt is located inside the mesoporous structure, ionomer poisoning is reduced[36] and the stability of the Pt due to voltage cycling in accelerated stress tests is increased.[41] The ionomer stretches over the surface of the catalyst structure, whereby its coverage depends on the ionomer to carbon ratio.[39]

2.2.2 Membrane

The proton-exchange-membrane (PEM, indicated in light grey in Fig. 2.3) separates anode and cathode compartment, while it serves as a proton conductor. Most commonly, it consists of a perfluorosulfonic acid (PFSA)-material. The structure of this polymer is composed of a backbone with attached side chains. The backbone is a copolymer of poly(tetrafluoroethylene) and poly(trifluoroethylene) and the side chains are made of perfluorosulfonic acid ether.[42,43] The proton conductivity is ensured through the acid groups and is highly dependent on the RH and moderately dependent on the temperature.[44] The membrane needs to be mechanically, chemically, and thermally stable during the operation of the fuel cell. Membrane failure is often related to a chemical attack on the backbone (main chain scission) or on the end group (end group unzipping)[45] and/or mechanical failure at specific locations that are being stressed because of RH cycling. To mitigate the degradation, membranes are usually mechanically reinforced (e.g. expanded PTFE)[46] and radical scavengers (e.g. cerium)[47] are added for chemical stability.

2.2.3 Bipolar Plates/ Flow fields

Bipolar plates/flow fields are made of graphite, graphite-composite, or metals such as stainless steel, titanium, and aluminum.[48,49] Bipolar plates in a PEMFC stack act as an anode for the one cell and a cathode for the adjacent cell. They need to be conductive, create a gas barrier between cells, transfer heat away from the cell, and they need to be corrosion resistant at the operating conditions.[50] Graphite or graphite-composite materials are known to be more stable, while metals can dissolve as cations, which can poison the membrane and therefore limit the lifetime. The bipolar plates/flow fields distribute the gases in sub-mm wide flow channels. Depending on their design, the flow fields can prompt a convective flow through the GDL. Convective transport can be realized with e.g. interdigitated flow fields[51,52] or with constrictions of the flow channels.[40]

2.2.4 Gas Diffusion Layers

In the following paragraphs, the structure of GDLs, GDL production, and the GDL functionality are covered.

Gas diffusion layers typically consist of a macroporous substrate (GDL-S) and a microporous layer (MPL).[53] The GDL-S can either be a carbon paper, a non-woven carbon felt, or a carbon cloth and is generally treated with a hydrophobing agent such a PTFE. The MPL consists of carbon or graphite particles and is equally treated by a hydrophobic binder (usually between 10 wt-% and 40 wt-%). The pore size domains between the two layers varies by at least an order of magnitude. The GDL-S commonly possesses pores between 10-50 µm in diameter.[16,54] The pores of the MPL are far smaller than these of a fibrous GDL-S, with characteristic pore sizes of less than 1 µm.[18,19,54,55]

The GDL is commonly fabricated using a large-scale high-volume reel-to-reel process.[56] Firstly, for the GDL-S, the base material is acrylonitrile, which is polymerized and consecutively spun to a polyacrylonitrile (PAN) fiber material.[56] The resulting polymer fiber is then either stabilized directly by a temperature treatment, chopped, and carbonized before the papermaking (e.g. Toray/SGL) or dry-laid with a subsequent hydroentangling step and a carbonization as one of the last steps (e.g. Freudenberg).[53,56] The difference from both methods can be observed in the fiber shape: the stabilization and carbonization before the papermaking leads to straight fibers, while the dry-laid fibers exhibit a more “wavy“ structure. A different approach is a woven carbon cloth. The hydrophobization is realized as one of the final steps usually through a dipping step.[56]

Conventionally, the MPL is coated onto the GDL substrate in slurry form, using a solvent, a dispersing agent, and thickening agents.[18] However, as dry coating processes gain increasing attention mostly in

Li-ion battery research, dry coating approaches are also explored with MPL coatings, e.g. as done by Toyota.[19,57]

Despite adding an additional diffusion length and thus an additional transport resistance,[18,58] including the MPL has various advantages, among them a reduced contact resistance between the GDL-S and the CL[59] and a protection against puncturing of the membrane.[44] However, most importantly, the addition of the MPL has a tremendous effect on the water removal capabilities of the GDL. This improvement is often rationalized by the water saturation jump at the interface between the small pores of the MPL and the large pores of the GDL-S.[60,61] The MPL serves as a percolation pathway and allows a more directed water flow towards the GDL.[21] Owejan et al. explain that the MPL prevents the formation of a liquid water film in the large pores at the CL/MPL interface.[62] The MPL usually remains liquid water free[63] and promotes gas phase transport of water vapor. Therefore, it was also shown that the water content in the GDL-S is reduced. Not only does the MPL facilitate gas phase transport through the MPL by its smaller pores but it also affects the thermal management.[64–66] Zhou et al. have shown this effect using simulations, where they showed that the MPL causes to preserve heat within the CL.[64] There is a pareto-optimum for the PTFE content in the MPL. In principle, adding more PTFE makes the structure more hydrophobic and thus increases the performance, especially at wet conditions. However, a high amount of PTFE (such as 40 wt-%) leads to a lower porosity and thus, a worse water removal capability.[67]

In an attempt to separate the oxygen and the liquid water pathways, MPLs with a bi-modal pore size distribution have been proposed.[19,55,68,69] Large features in the MPL such as cracks or large pores (>10 µm) have shown to improve the cell performance under wet conditions, because liquid water can be transported more readily through the large open features, while the bulk MPL remains dry for oxygen transport.[18,70–72] While these large features in the MPL increase the water removal capabilities of the GDL, it was also shown in the literature that cracks and large pores unfortunately enhance membrane degradation from relative humidity cycling as the membrane can creep into the large opening.[20,73]

In contrast to the management of liquid water, the GDL can also help maintaining water in the CL at dry conditions, which is increasingly important at higher temperatures.[74] The GDL is commonly tailored to the envisaged operating conditions.

2.3 Diffusion

Stationary diffusion processes can be described using Fick's first law, where the 1-dimensional diffusive molar flux $\dot{N}$ is a function of the diffusion coefficient D and the gradient of the concentration c over the position x (see Eq. 2.19). The concentration gradient is the driving force for diffusive processes.

$$\dot{N} = -D\frac{\partial c}{\partial x} \tag{2.19}$$

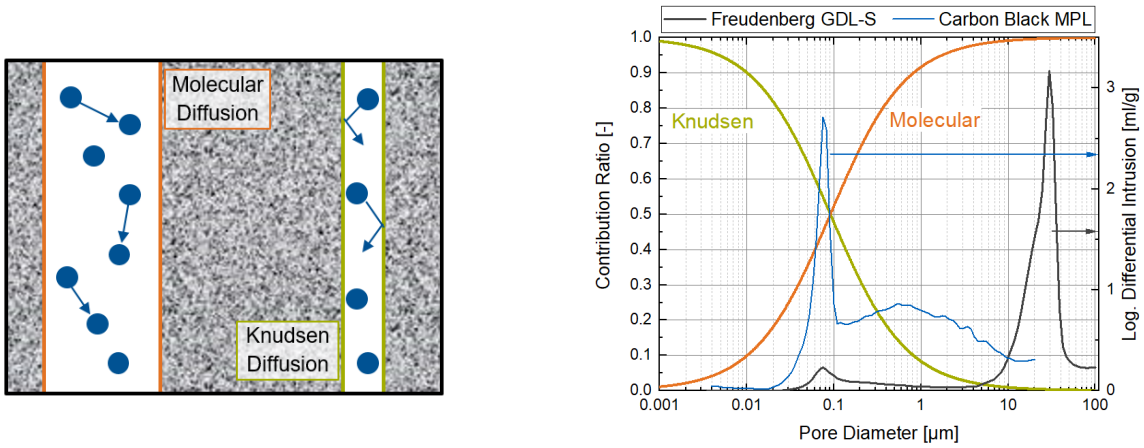

(a) **(b)**

Figure 2.4 a) Scheme of the two different diffusion mechanisms: left/orange: molecular diffusion occurring in larger pores, where the interactions between gas molecules dominate; right/green: Knudsen diffusion occurring in small pores, where interactions between gas molecule and the pore wall dominate. b) Contribution ratio of molecular (orange line) and Knudsen diffusion (green line; both plotted along the left y-axis) over the pore size diameter at 80 °C and 200 kPa_{abs}. Pore size distribution as measured through MIP (log differential intrusion) exemplary for the Freudenberg GDL-S and a home-made Li100 carbon black MPL (plotted along the right y-axis). While molecular diffusion dominates for the GDL-S, there is roughly equal contribution of Knudsen and molecular diffusion occurring in the carbon black MPL at the peak pore size. Note that panel b) uses a similar representation as used by Nonoyama et al.[75] and is adapted from Berger et al.[76] and Bozzetti et al.[77]

Two different diffusion mechanisms can be distinguished: molecular and Knudsen diffusion. Molecular diffusion describes the diffusion in the bulk gas phase. The diffusion coefficient D_{AB} for a binary gas system can be described by Eq. 2.20[78] with the critical pressure p_{ci}, the critical temperature T_{ci}, and the molecular mass M_i of each component A and B. The constants a and b differ depending on whether it is a polar or non-polar gas mixture. The diffusion coefficient is dependent on the diffusing material and the matrix in which it diffuses. Additionally, it is inversely proportional to the pressure and it increases with increasing temperature.

$$\frac{pD_{\mathrm{AB}}}{\left(p_{\mathrm{cA}}p_{\mathrm{cB}}\right)^{\frac{1}{3}}\left(T_{\mathrm{cA}}T_{\mathrm{cB}}\right)^{\frac{5}{12}}\left(1/M_{\mathrm{A}}+1/M_{\mathrm{B}}\right)^{\frac{1}{2}}}=a\left(\frac{T}{\sqrt{T_{\mathrm{cA}}T_{\mathrm{cB}}}}\right)^{b} \tag{2.20}$$

For a three-component mixture, such as oxygen in nitrogen and water, the ternary diffusion coefficient of oxygen in nitrogen and oxygen in water vapor, D_{OM}, can be determined as a function of the molar water fraction x_{W} and of the binary diffusion coefficients of oxygen in nitrogen D_{ON} and of oxygen in water D_{OW} (both calculated via Eq. 2.20):[79]

$$\frac{1}{D_{\mathrm{OM}}}=\frac{1-x_{\mathrm{W}}}{D_{\mathrm{ON}}}+\frac{x_{\mathrm{W}}}{D_{\mathrm{OW}}} \tag{2.21}$$

A second diffusion mechanism occurs in smaller pores, which is known as Knudsen diffusion. Knudsen diffusion occurs when the characteristic pore size is smaller than the mean free path between the molecules. The mean free path depends on the specific molecule (the molecule's diameter) and it changes with pressure and temperature. The Knudsen diffusion coefficient is given by Eq. 2.22:

$$D_{\mathrm{Knudsen}}=\frac{4}{3}d\sqrt{\frac{RT}{2\pi M}} \tag{2.22}$$

The diffusion mechanism in a porous structure can be determined by comparing the pore sizes in the structure with the mean free path of the diffusing molecule. Fig. 2.4a visualizes the two different diffusion mechanisms by demonstrating the diffusion of the same molecule in pores with two different pore diameters. In the larger pore (orange), the pore diameter is large enough and the gas molecules interact more strongly with each other than they interact with the wall, which is referred to as molecular diffusion. In the smaller pore (green), the diameter is smaller than the mean free path and therefore, the molecules interact more strongly with the walls than with one another, which is referred to as Knudsen diffusion. In a porous network with a variety of pore sizes, molecular and Knudsen diffusion can occur simultaneously in the structure, depending on the local pore diameter. This phenomenon of molecular and Knudsen diffusion in a porous structure is visualized in Fig. 2.4b, which shows the contribution ratio of molecular (orange) and Knudsen diffusion (green) to the overall diffusion at 80 °C and 200 kPa_{abs}. It can be seen that Knudsen diffusion dominates at small pore diameters (<10 nm), while molecular diffusion takes precedence at large pore diameters (>800 nm). If a mixture of both diffusion mechanisms occurs, the Bosanquet equation can be used to describe the diffusivity of the mixed diffusion process as shown in Eq. 2.23:

$$D_{\text{mixed}} = \left(\frac{1}{D_{\text{Knudsen}}\,(d)} + \frac{1}{D_{\text{molecular}}\,(p)} \right) \tag{2.23}$$

Fig. 2.4b additionally contains the pore size distributions (PSDs) from mercury intrusion porosimetry (MIP), exemplarily for a Freudenberg GDL-S (gray) and a carbon black MPL (blue), delineating which diffusion regimes are important in which structure. The majority of the pores in the GDL-S are above 10 µm and are therefore dominated by molecular diffusion. However, during the fabrication of the GDL-S, carbon black is added by the manufacturer, which can be seen by a PSD peak at approximately 80 nm. At this pore diameter, Knudsen diffusion contributes to a high percentage to the diffusion mechanism and thus, Knudsen diffusion effects can be observed even for this GDL-S (see Chapter 4.1 for more detail). The carbon black MPL has significantly smaller pores and Knudsen diffusion is predominant in the MPL structure (see Chapter 4.2 for more detail).

The effective diffusivity D_{theo} in a porous structure is related to the theoretical diffusivity D_{theo} by the porosity ε and the tortuosity τ, as can be seen in Eq. 2.24

$$D_{\text{eff}} = D_{\text{theo}} \frac{\varepsilon}{\tau} \tag{2.24}$$

The effective diffusivity is closer to the theoretical diffusivity when the porosity is higher and when the tortuous pathway is close to the actual thickness of the porous medium.

2.4 Limiting Current Analysis

Oxygen mass transport limitations can be determined by measuring the limiting current density at large overpotential. As already discussed in section 2.1.2, oxygen mass transport resistances become dominating at high current densities. The limiting current density is the maximum current density that can be achieved. At this current density, every oxygen molecule that is transported to the cathode CL is immediately consumed by the reaction. The oxygen transport resistance $R_{\text{T,O}_2}$ is defined by Baker et al. as the ratio of the change in oxygen concentration Δc_{O_2} over the molar flux of oxygen at the CL $\dot{N_{\text{O}_2}}$:[79]

$$R_{\text{T,O}_2} = \frac{\Delta c_{\text{O}_2}}{\dot{N}_{\text{O}_2}} \tag{2.25}$$

The molar flux $\dot{N}_{\mathrm{O}_2}$ can be expressed using Faraday's law for the 4-electron process, with i_{lim} being the limiting current density:

$$\dot{N}_{\mathrm{O}_2} = \frac{i_{\mathrm{lim}}}{4F} \tag{2.26}$$

The change in oxygen concentration Δc_{O_2} from the flow field channel to the CL in through-plane direction is clearly defined at limiting current conditions, where the concentration in the catalyst layer is 0. Under this condition, $\Delta c_{\mathrm{O}_2} = c_{\mathrm{O}_2}$, which can be rewritten using the ideal gas law with the dry molar fraction of oxygen x_{O_2}, the cell pressure p, the water vapor pressure p_{w}, the ideal gas constant R, and the temperature T:

$$c_{\mathrm{O}_2} = x_{\mathrm{O}_2} \frac{p - p_{\mathrm{w}}}{\mathrm{R}T} \tag{2.27}$$

Combining Eq.2.25-2.27, the definition for $R_{\mathrm{T},\mathrm{O}_2}$ is:

$$R_{\mathrm{T},\mathrm{O}_2} = \frac{4\mathrm{F}x_{\mathrm{O}_2}}{i_{\mathrm{lim}}} \frac{p - p_{\mathrm{w}}}{\mathrm{R}T} \tag{2.28}$$

Baker et al. proposed to separate $R_{\mathrm{T},\mathrm{O}_2}$ into a series of individual resistors: the channel resistance R_{ch}, the transport resistance in the GDL-S $R_{\mathrm{GDL-S}}$, the transport resistance in the MPL R_{MPL}, and the transport resistance of other components R_{other} (see Eq. 2.29).[79] They found that for a Toray 060 GDL substrate coated with a 25 µm MPL and operated a 80 °C and 150 $\mathrm{kPa}_{\mathrm{abs}}$, the GDL-S would contribute to roughly half of the transport resistance (53%). The channel resistance was the second highest contributor, with a 24% share. The MPL only added 8% to the total transport resistance and the remaining 15% were unassigned.

$$R_T = R_{\mathrm{ch}} + R_{\mathrm{GDL-S}} + R_{\mathrm{MPL}} + R_{\mathrm{other}} \tag{2.29}$$

Baker et al. also offer a way to deconvolute the pressure-independent and the pressure-dependent contributions, which is often applied in research on the $R_{\mathrm{T},\mathrm{O}_2}$ of the CL. The pressure-independent part of $R_{\mathrm{T},\mathrm{O}_2}$, which mostly describes Knudsen diffusion in the CL, can be separated from the pressure-dependent part

of $R_{\mathrm{T,O_2}}$, which mostly describes molecular diffusion in the GDL.[1] In this thesis however, as the CL was a commercial product, which was kept constant throughout each study, the CL adds a constant transport resistance and all observed changes in $R_{\mathrm{T,O_2}}$ were caused by the change in the cathode GDL. Therefore, no separation between the pressure-dependent and pressure-independent contributions was performed.

2.5 Water Formation and Removal

Water management is a very important topic in fuel cell research. Water can enter the system by the humidification of the inlet gas streams and is also formed through the reaction, both of which control the humidify of the fuel cell stack. A sufficient hydration state of the membrane and the ionomer is important to ensure good proton conduction. Yet, a flooding of the GDL will hinder oxygen mass transfer to the CL.

The inlet RH can be set by steering the dew point, which is correlated with the saturation pressure of water through the Antoine equation, as given in Eq. 2.30. The RH is defined as the ratio of the water vapor pressure over the saturation vapor pressure (Eq. 2.31). The parameters for the Antoine equation A, B, and C for water are 8.07131, 1730.63, and 233.426, respectively, when the pressure p is given in mmHg and the temperature is given in °C.

$$\log_{10}\left(p_{\mathrm{sat}}\right) = A - \frac{B}{C + T_{\mathrm{DP}}} \tag{2.30}$$

$$\mathrm{RH} = \frac{p_{\mathrm{W}}}{p_{\mathrm{sat}}} \tag{2.31}$$

Fig. 2.5 shows the water vapor pressure over the temperature. It can be seen that there is an exponential increase of the water vapor pressure with temperature. For the temperatures relevant in this thesis, the water vapor pressure at 50 °C is 12.3 $\mathrm{kPa_{abs}}$ and at 80 °C 47.3 $\mathrm{kPa_{abs}}$. Consequently, less water can be transported in the gas phase at lower temperatures, and flooding occurs more readily compared to higher temperatures. At high temperatures, it is increasingly complicated to keep the membrane humidified, as the saturation vapor pressure is so high.

[1] When distinguishing between the pressure-dependent and pressure-independent part of the transport resistance, it is important to understand the influence of the water vapor pressure on the transport resistance. The basic principle for the separation is measuring the $R_{\mathrm{T,O_2}}$ at different pressures. The resulting dataset of $R_{\mathrm{T,O_2}}$ over the pressure can be fitted linearly. The y-intercept (at 0 kPa pressure) and the slope (in s/cm/kPa) are used to determine the pressure-independent and -dependent contribution to $R_{\mathrm{T,O_2}}$. When doing the analysis, it is important to understand that when experimentally varying the pressure at a constant RH, the $R_{\mathrm{T,O_2}}$ coming from the water vapor pressure stays constant, meaning that it is part of the y-intercept. Some groups report the pressure-independent $R_{\mathrm{T,O_2}}$ as the y-intercept, which represent all pressure-independent parts of this measurement (including the water vapor pressure related effects).[80] Other groups try to separate the pressure-independent processes (such as Knudsen diffusion or diffusion through the ionomer or water phase) from the y-intercept of this measurement. Baker et al. calculate the real pressure-independent processes by subtracting pressure-dependent effects from the water vapor phase from the y-intercept using an elaborate set of equations, which is specific for the conditions and flow field geometries that they use.[79] Lu et al. have adapted this approach with some simplifications.[81]

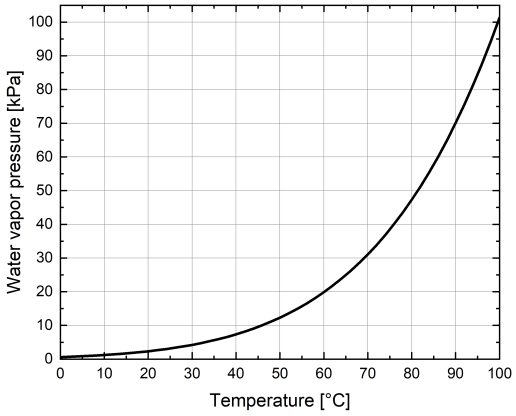

Figure 2.5 Water vapor pressure over the temperature as calculated via the Antoine equation; the vapor pressure increases exponentially with temperature

When liquid water is formed in the MPL or GDL-S, it has to be transported away through the structure. The capillary pressure, which is the difference between the pressure of the liquid p_{l} and the vapor phase p_{v} of water inside a pore is defined by the Young-Laplace equation (Eq. 2.32). The Young-Laplace equation connects the capillary pressure with the surface tension of water γ_{W}, the contact angle θ, and the pore diameter d_{pore}.

$$p_{\mathrm{c}} = p_{\mathrm{l}} - p_{\mathrm{v}} = \frac{4 \cdot \gamma_{\mathrm{W}} \cdot \cos\theta}{d_{\mathrm{pore}}} \tag{2.32}$$

The term capillary fingering is often used for describing liquid water transport by capillary forces.[82,83] Unfortunately, the water is being transported along the path of least resistance, which is not directed towards the outlet of the cell. Much research has focused on developing materials to direct water removal e.g., via the physical design of the GDL structure in order to steer the water management to a certain extent.

2.6 Imaging Techniques to Study the Dry Structure and Water Formation

To study the effect of GDLs on the fuel cell performance, imaging techniques have been applied to either study the dry structure of the GDL or to investigate the water distribution within the GDL. Imaging concepts range from electron over neutron to x-ray beams, and different techniques can resolve a different pore size domain. Most imaging techniques are non-destructive and can be applied *operando*.

To analyze the dry structure of the GDL-S, XTM can be used. XTM can resolve pores as small as 0.3-2.5 µm,[16,84,85] which is sufficient to resolve the ≈7 µm fibers of GDL-substrates. XTM on the dry GDL-S structure is often used to compare different materials and characterize the porosity, pore size distribution,

and behavior under compression.[16,86,87] As an example, Zenyuk et al. have analyzed the change in pore size and porosity under compression.[16] They determined that the τ/ε-ratio increases with compression for all tested GDLs, which has been confirmed by simulation[88] or ex-situ techniques.[89]

The general resolution of XTM is too low to resolve the MPL pores, however several bulk properties of an MPL such as its thickness and its homogeneity, as well as MPL porosity and MPL crack density can be determined.[90] FIB-SEM has been used to reconstruct a 3D representation of the MPL.[91–93] To correctly image the MPL structure composed of carbon and PTFE correctly, FIB-SEM requires a careful sample preparation. E.g., Bozzetti et al. have used a ZnO deposited layer on the surface.[91]

XTM cannot only be applied to study the dry GDL-S structure, but it can also be utilized to reconstruct water droplets on a pore scale range of the GDL-S. X-ray radiography and XTM are powerful techniques to achieve a 2D or 3D resolution, respectively, of the water accumulation inside the GDL-S. XTM requires the acquisition of a large number of images at different angles, while 2D radiography images have a better time resolution. However, due to the development of fast XTM, a resolution of 1s is nowadays possible.[85,94,95] Water typically accumulates under the land of the flow field rather than in the channel,[96,97] which is predicted by simulations as a temperature effect.[98]

As already stated above, the resolution of XTM is too low to resolve the MPL pores and, consequently, it is impossible to resolve water clusters in the MPL pores. However, it is possible to connect the gray scale value of the MPL with a saturation value as liquid water accumulation within the pores changes the gray scale value compared to a dry MPL.[70,84,99,100] Sasabe et al. used soft X-ray radiography to image the MPL, where large features of the MPL such as cracks are resolvable, while only the gray scale value of the isotropic MPL structure can be evaluated.[70] They found that liquid water is indeed transported in these large openings, while the rest of the MPL structure remained free of liquid water. Catalyst "shining" is an unavoidable drawback when trying to image the water transport in the MPL during *operando* measurements, which often hinders or limits *operando* water imaging in the MPL.[96,99]

An *ex-situ* technique to image water formation in an MPLs is using environmental-SEM (ESEM).[61,101] Water condensation can be recorded in low-pressure atmosphere when cooling the sample holder. Comparing the droplet size and shape can give information on the interaction of the material with liquid water.

Another technique to image water is via neutron radiography. The advantage of neutron radiography compared to X-ray techniques is its good penetration through common fuel cell component materials (stainless steel, graphite) and thus, the capability to use larger and more realistic PEMFC active areas.[102–104] Because of the large spatial capabilities, an analysis of water back-diffusion from the cathode to the anode side has been studied by several groups as a function of the GDL.[105,106]

Another technique that has recently been explored for CL research is small-angle x-ray or small-angle neutron scattering.[107–109] The method can only be used to image some types of MPL, as the resolution is at most ≈400 nm.[107]

3 Experimental Methods

This chapter gives a detailed overview over the experimental methods used in this work. First, the cell geometry with all its components is displayed and their function explained. A special focus is laid on the local compressibility of the cell components When a CCM with a subgasket is being used. Subsequently, the fuel cell testing is explained. In the last part, material fabrication and characterization is described with a focus on mercury intrusion porosimetry.

3.1 Cell Design

After having discussed the purpose of the individual fuel cell components in Chapter 2.2, the incorporation of all parts in a realistic single-cell is presented in the following. Two different cell designs were used in this work, both having a 5 cm² active area. The cell configurations are shown in Fig. 3.1. The square configuration (left side of Fig. 3.1) relies on a square-shaped catalyst coated membrane (CCM). The flow field consists of seven channels arranged in one serpentine,[32,110] which causes a pressure drop along the active area. The second cell configuration (right side of Fig. 3.1) is based on the design that was initially proposed by Baker et al.[79] and adjusted by Du et al.[111] The active area of 5 cm² is placed on the straight-channel segment of a 50 cm² flow field, resulting in a quasi constant pressure along the active area.

For both cell geometries, the custom-made aluminum anode (A) and cathode (C) end plates compress the cell evenly and serve as a heat reservoir to keep the temperature constant. The end plates are tightened around the cell setup using 8 screws. For heat regulation, a heater rod is inserted into the aluminum material. The end plates are sandwiched around the copper current collectors. End plates and current collectors are electrically insulated against each other by using an insulating material (in this case Fiberflon® from Fiberflon GmbH & Co. KG). For a more homogeneous compression, a carbon paper material is inserted between two Fiberflon® sheets at this insulation stage. The current collectors are gold coated on the flow field side to reduce the contact resistance at the interface. The components of the fuel cell as depicted in Fig. 2.3 are situated between the anode and cathode flow field. In the center, a catalyst coated membrane (CCM) with a subgasket is enclosed on either side by the GDL. The cell is sealed

towards the outside using a hard-stop sealing approach by means of a nearly incompressible Fiberflon® gasket.

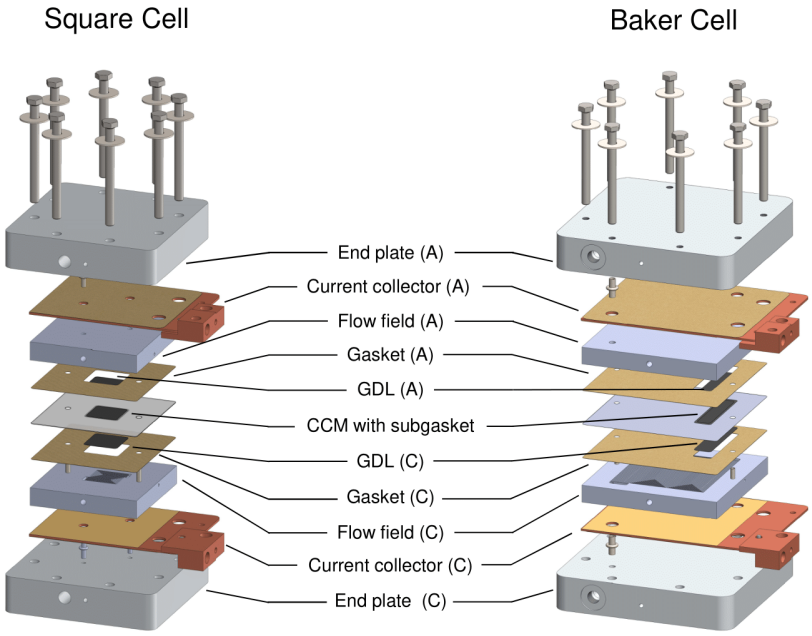

Figure 3.1 Explosion view of the two different cell geometries with an active area of 5 cm² used in this work; left: square cell; right: Baker cell. In both cases, the cell consists of end plates, current collectors (electrically insulated against the end plate and gold coated towards the flow field), flow fields, gaskets, and GDLs for each the anode (A) and the cathode (C) side, which are sandwiched around the subgasketed CCM.

The application of two distinct cell configurations stems from the presence or absence of a pressure drop along the active area. While the pressure drop along the active area is helpful when removing liquid water from the cell, the homogeneous pressure distribution under the active area creates controlled conditions for theoretical considerations (e.g. extracting the τ/ε-ratio of GDLs). Additionally, cross flow through the GDL might occur in the serpentine flow field between two adjacent channels having a different pressure due to the pressure drop caused by the serpentine turn. It is common practice to focus a detailed limiting current measurements in a straight channel design, while performance measurements are preferably conducted on a more optimized flow field setup.[79,112,113] Thus, fundamental studies (Chapter 4.1 and 4.2) were conducted in the Baker cell setup, while the performance study (Chapter 4.3) was done using the square cell.

The cell designs for the *operando* measurements are optimized to X-ray beam accessibility. The design for the SAXS setup is described in detail by Aliyah et al.[114] The cell design for XTM measurements was described by Nagai et al. and Hong et al.[85,115]

3.1.1 Subgasketing a CCM and Its Impact on Cell Compression

The subgasketing procedure is used as was described by Du et al.[111] The CCM dimensions were chosen to have the same size of the GDL as it resulted in the most even and reproducible pressure distribution with the subgasketing approach. A cross section of the stack of components is shown in Fig. 3.2. The hard-stop sealing works by applying most of the compressive force from the end plates onto the gasket material. The gasket material then determines the space available for compressing the GDL. Only a fraction of the applied force is transferred directly onto the GDL. The left side of Fig. 3.2 displays an uncompressed representation of all components to demonstrate their thickness prior to compression. In the compressed representation on the right side of Fig. 3.2, the Fiberflon® glass fiber material compresses to a low extent (≈7%), while the PEN foil subgasket and the CCM are considered incompressible. The GDL-S and the MPL can compress to fill the gap determined by the gasket thickness. The PEN foil subgasket extends over the edge of the Fiberflon® gasket, restricting the active area to the correct size. The GDL is thus more compressed in the overlapping area. In the current hard-stop sealing approach, the stronger compression in the overlapping area is not detrimental, as it does not affect the diffusive flux through the GDL over the active area. However, when using a soft sealing approach, the overlapping area might adversely impact the pressure distribution at the active area, as it will form a ring around the active area with a high local pressure.

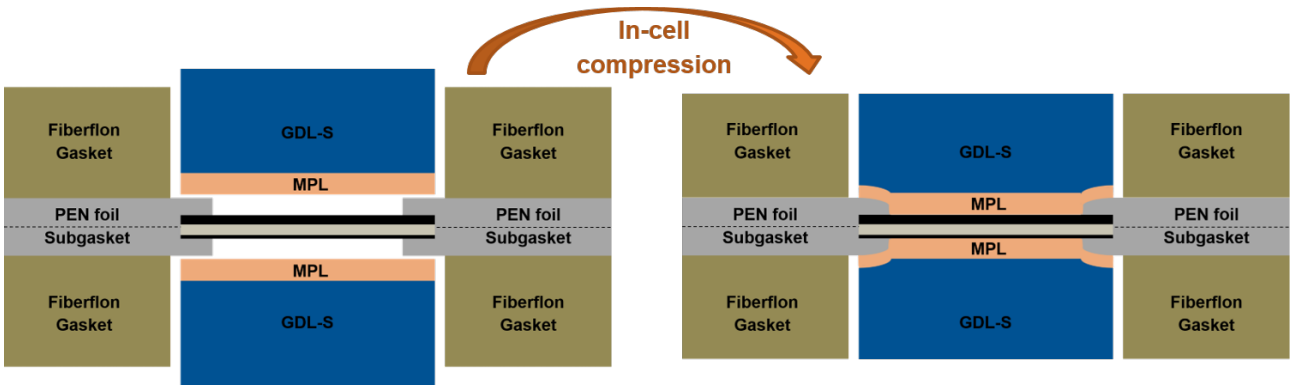

Figure 3.2 Cell configuration for single-cell testing with a PEN-foil sealed CCM. Left: uncompressed depiction of the sealed CCM, demonstrating the size ratio of all components: the GDL with the MPL is cut to the same dimension as the CCM with a gap between the GDL and the Fiberflon® gasket. Right: compressed depiction showing that the GDL/MPL combination is severely compressed in the range of the overlap of GDL and PEN-foil subgasket.

3.1.2 Cell Compression

Setting the correct cell compression (this relates to the compression of the GDL) can be essential for a good cell performance. A good cell compression is found at the pareto-optimum between two effects.[116–118] The more the GDL is compressed, the lower its porosity and pore size[16] and, consequently,

the lower is the oxygen diffusivity at dry conditions.[88,116,119] If the compression is too little, significant contact resistances at the flow field/GDL and at the GDL/catalyst layer interface start to occur.[120,121]

The compression is determined by measuring the thickness of the GDL at 5 points and of the gasket at 8 points, as illustrated by Simon et al.[110] However, different GDLs require a different optimum compression.[117,118,120] Therefore, the cell compression was not determined by the compression value, but by the contact pressure between the flow field and the GDL, which was determined by placing a pressure sensitive film (Fujifilm) between the flow field and the cathode GDL.[116] The compression was adjusted until a pressure of 1.3-1.5 MPa was obtained.

3.2 Fuel Cell Characterization

Single-cell fuel cell test were conducted using a custom-designed and fully automated G60 test station from Greenlight Innovation (Canada), which is equipped with a load bank (N3306A, Agilent Technologies) and an additional potentiostat (Reference3000, Gamry Instruments). Gas flows are controlled using mass flow controllers (Alicat), calibrated for the specific gases (hydrogen, nitrogen, or oxygen/air). Several mass flow controllers with different maximum flows were installed to achieve a high accuracy over a wide range of gas flows. Type T thermocouples were used to measure the temperature at different points, whereby the measured temperature serves as input for the regulation of the heating tapes. The gas flows were humidified with dew point control. The gas connections from the humidifier to the fuel cell were always heated to a temperature that is 20℃ higher than the dew point temperature to avoid condensation. The cell pressure was regulated using back-pressure regulators (Equilibar).

3.2.1 Limiting Current Measurements

Limiting current measurements are conducted to obtain the oxygen transport resistance, as explained in section 2.4. To scan a wide range of current densities, the oxygen concentration in nitrogen in the dry gas feed is varied between 0.5-28%. To reach limiting current densities, low voltages of 0.3 V, 0.15 V, 0.1 V, and 0.05 V are set. Fig. 3.3a shows the results for a typical limiting current measurement procedure at 80°C, 62% RH, and 150 kPa_{abs} in the Baker cell setup, using a Toray GDL-S as a cathode GDL.

The limiting current density was extracted at 0.15 V for concentrations 0.5-2%, at 0.1 V for concentrations 4-12% and at 0.05 V for the remaining higher concentration. The reason for the step-wise decrease of voltages is the onset potential of the hydrogen evolution, which can be seen at low concentrations and thus low current densities. At higher current densities, ohmic losses become increasingly important and, consequently, shift the hydrogen evolution reaction onset potential.[79] The polarization curves at the low

voltages are vertical, which shows that a mass transport limiting current has been reached. The extracted limiting current can be converted to a transport resistance using Eq. 2.28.

Fig. 3.3b shows the oxygen transport resistance calculated from the dataset from Fig. 3.3a, which depicts the limiting current density for the 150 kPa_{abs} conditions and additionally for the three different pressures of 115 kPa_{abs}, 200 kPa_{abs}, and 300 kPa_{abs}. The oxygen transport resistance at the lowest pressure of 115 kPa_{abs} shows a constant $R_{\mathrm{T,O_2}}$. With increasing pressure, an increase of $R_{\mathrm{T,O_2}}$ can be observed at higher current densities, which is an indication for the flooding of the GDL and/or the catalyst layers. With higher pressure, more water is formed in the liquid state, which causes an increase in the liquid water content in the porous media, concomitant with a blockage of pores. The onset limiting current density for the flooding shifts to lower limiting current densities with higher pressure, as liquid water is formed already at lower current densities. The Toray material floods more readily than other GDL-S materials (e.g. a Freudenberg material), because its thermal conductivity is higher. Thus, the temperature increase from the CL to the flow field is lower, which causes a faster flooding compared to a material with a low thermal conductivity.

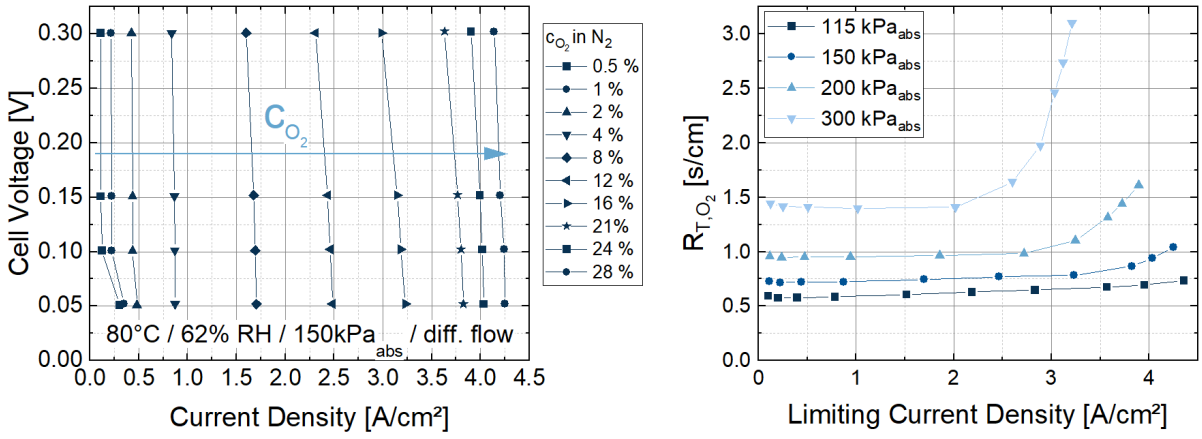

Figure 3.3 a) Demonstration of the limiting current measurement sequence: polarization curves recorded only at low voltages for different oxygen concentrations between 0.5%-28% of oxygen in nitrogen of the dry gas feed; the data were recorded at 80°C, 62% RH, 150 kPa_{abs} at differential flow conditions in the Baker cell. The higher the oxygen concentration, the higher the mass transport limiting current densities that can be reached. b) Oxygen transport resistance over the limiting current density for four different pressures (115 kPa_{abs}, 150 kPa_{abs}, 200 kPa_{abs}, 300 kPa_{abs}); the 150 kPa_{abs} curve represents the raw data from panel a); at higher pressures, the onset of flooding can be observed as a sudden increase in $R_{\mathrm{T,O_2}}$.

Fig. 3.4a demonstrates in more detail the impact of the oxygen transport resistance on either the dry or the wet state of the GDL structure. The limiting current measurements were conducted at conditions, where the GDL structure is dry at low current densities and transitions into a wet state with higher current densities. The dataset is recorded at 50°C, 77% RH, 400 kPa_{abs} in differential-flow conditions, using the square cell setup for an home-made MPL (made with Li100 carbon from Denka) on a Freudenberg

H14 GDL-S. While the gas stream enters relatively dry at 77% RH, the low temperature of 50°C and the high pressure of 400 kPa_{abs} cause that the water formed by the reaction is mostly in its liquid state. When regarding Fig. 3.4a at low current densities, the dry $R_{\mathrm{T,O_2}}$ of the GDL structure at this pressure is ≈1.6 s/cm. When increasing the current density by increasing the oxygen concentration, the $R_{\mathrm{T,O_2}}$ increases drastically, until $R_{\mathrm{T,O_2}}$ reaches the plateau of the wet structure between 2.8-3.1 s/cm.

Fig.3.4b shows the impact of a low RH on the oxygen transport resistance. It contains the results of limiting current measurements at 40% RH, 60% RH, and 80% RH at 80°C and 115 kPa_{abs} at differential-flow conditions in the Baker cell. The cathode GDL was a 60 µm thick custom-made MPL based on Li100 carbon black from Denka on a Freudenberg H14 substrate (hydrophobically treated by the manufacturer). For all RHs, the oxygen transport resistance increases with increasing current density. However, the trend is stronger for the lower RH curves. While the 80% RH dataset increases from 0.6 s/cm to 0.8 s/cm, the 40% RH dataset increases from 0.6 s/cm to 1.2 s/cm. As discussed for Fig. 3.4a, one possible reason for an increased transport resistance could be flooding. However at this low RH, flooding can be excluded. A second explanation could be the difference in HFR. It is known in the literature for undercompressed GDL samples that the high HFR prevents reaching the limiting current density, which causes an overestimation of $R_{\mathrm{T,O_2}}$.[113,116] The HFR for a 40% RH measurement is roughly between 100-120 mΩ cm², which translates at 3 A/cm² to 300-360 mV. This voltage suggests that the measurement at 40% RH has not yet entirely reached the limiting current. From a polarization curve in the same configuration at 70% RH (data not shown), one can estimate the difference in limiting current density, which translates into an overestimation of $R_{\mathrm{T,O_2}}$ of at most ≈0.15 s/cm. Thus, it cannot solely explain the drastic increase for the 40% RH dataset. A third rationale is that the limiting current is not solely attributed to oxygen transport limitations but also to limitations in proton transport. Similar to the HFR, which serves as a measure of the membrane hydration state, the proton sheet resistance R_{sheet} represents how well protons can be conducted in the ionomer phase in the CL. Gerling et al. show that the difference in proton sheet resistance is an order of magnitude higher between 40% RH and 80% RH.[29] Neyerlin et al. have shown that if the product of the current density and the proton sheet resistance become high, the CL utilization is lowered.[122] Both conclusions combined explain why $R_{\mathrm{T,O_2}}$ increases with current density as the CL utilization degree is decreased with current densities at high R_{sheet}.

3.2.2 Polarization Curves

Polarization curves can be measured galvanostatically or potentiostatically, meaning that either the current is set and the voltage response is recorded or the voltage is set and the current response is recorded. In this work, polarization curves were recorded in potentiostatic mode to ensure that polarization curves are screened to low potentials, i.e. close to mass transport limiting conditions. At each voltage step,

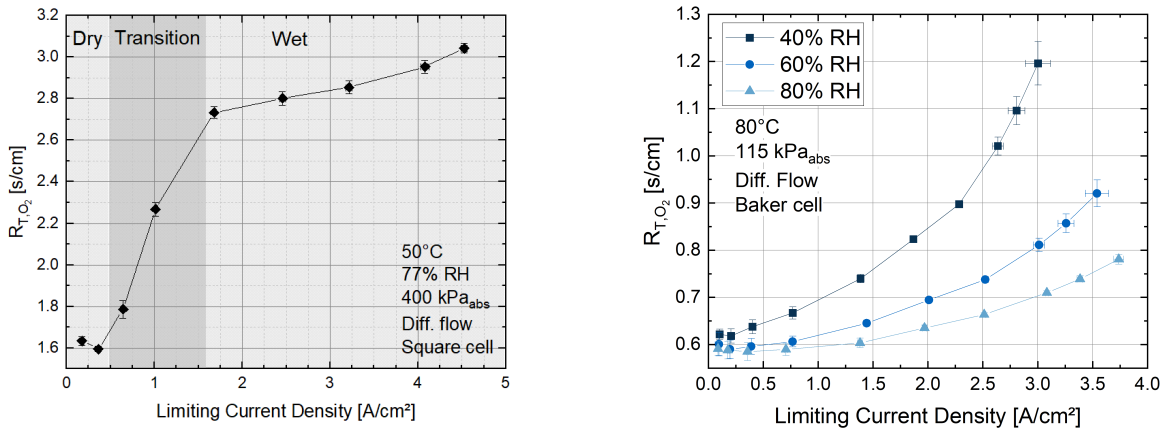

(a) **(b)**

Figure 3.4 a) Oxygen transport resistance over the limiting current density measured at 50 °C, 77% RH, and 400 kPa$_{\mathrm{abs}}$ at differential flow conditions in the square cell setup. The oxygen transport resistance at low current densities (<0.5 A/cm²) represents the $R_{\mathrm{T,O_2}}$ for the dry GDL structure, at intermediate current density (0.5 A/cm²<i_{lim}<1.5 A/cn²) $R_{\mathrm{T,O_2}}$ represents the transition regime between dry and wet, and at high current densities (>1.5 A/cm²) $R_{\mathrm{T,O_2}}$ represents the resistance of a wet GDL structure. b) Oxygen transport resistance over the limiting current density measured at 80 °C, 115 kPa$_{\mathrm{abs}}$ in differential-flow conditions in the Baker cell for three different RH values of 40%, 60%, and 80%; the increase in apparent $R_{\mathrm{T,O_2}}$ is caused by proton conduction limitations.

electrochemical impedance spectroscopy was measured in hybrid mode from 100 kHz to 10 Hz with a perturbation voltage of 10 mV.

3.3 MPL Fabrication

MPLs were fabricated by the method developed by Simon et al.[18,55] In short, the carbon was mixed with water, Trition X-100 (emulsifier), and methyl cellulose (thickener). In a second step, a PTFE dispersion (with PTFE particles ≈200 nm) is added. After further mixing, the last mixing step is a degassing step at 30 kPa. The MPLs are coated using a stainless steel stencil and a doctor blade.

3.4 Mercury Intrusion Porosimetry

MIP is a powerful method in GDL research, as it allows to scan a wide range of pore size diameters ranging from 4 nm to 500 µm. The basic principle behind MIP is that mercury is forced into the pores of a material under a controlled pressure. The pressure is step-wise increased and the volume of intruding mercury is measured at each pressure step. The pressure relates to the pore diameter using Washburn's equation (see Eq. 3.1), which requires the surface tension of mercury and the contact angle of the material to be known. The advantage of mercury is its non-wetting behavior on most surfaces, which means that pores are not filled by surface interaction but only because of the pressure impact. Additionally, the contact

angle is assumed constant on most surfaces, which makes the complicated and in most cases impossible determination of the contact angle on porous substances redundant. Furthermore, many of the properties of mercury such as its density and surface tension stay relatively constant over a range of temperatures, meaning that minor temperature variations during the measurement will not cause a large error. A MIP measurement becomes problematic if the material reacts with mercury, as for example in the case of gold.

Washburn's equation given in Eq. 3.1 converts the applied pressure p to the intrusion of a certain pore diameter d_{pore} given that the surface tension γ_{Hg} and the contact angle θ are known. This thesis uses a contact angle of 140° and a surface tension of 0.480 N/m.

$$d_{\mathrm{pore}} = -\frac{4\gamma_{\mathrm{Hg}}\cos\theta}{p} \tag{3.1}$$

MIP results are usually displayed in two representations, namely the cumulative intrusion volume and log differential intrusion volume, both over a logarithmic scale of the pore diameter. The former shows the intruding volume of mercury over the respective pore sizes in an additive way. The latter shows the derivative of the cumulative intrusion over a logarithmic pore diameter, which offers the advantage that the area under the curve is proportional to the pore volume.

There are several ways to determine the porosity. In principle, the MIP instrument can determine the porosity by comparing the bulk with the skeletal density. This method requires a careful calibration of the volume of the penetrometer (sample holder).

Alternatively, when knowing the skeletal density of the individual components (ρ_{i}) and their composition (mass fractions x_{i}), Eq. 3.2, formulated for an MPL consisting of carbon and PTFE, can be applied using the reliable output of the pore volume per sample mass from the MIP instrument.

$$\varepsilon = \frac{v_{\mathrm{pore}}}{v_{\mathrm{MPL}}} = \frac{v_{\mathrm{pore}}}{v_{\mathrm{pore}} + \frac{x_{\mathrm{carbon}}}{\rho_{\mathrm{carbon}}} + \frac{x_{\mathrm{PTFE}}}{\rho_{\mathrm{PTFE}}}} \tag{3.2}$$

When measuring GDL samples, it is important to not stack several layers of GDLs to avoid artifacts. The effect of GDL stacking can be observed in Fig. 3.5. Fig. 3.5 shows the cumulative intrusion (upper panel) and the log differential intrusion (lower panel) over the pore size diameter. The red curve shows a stacking of 2 GDL-S layers (Freudenberg) and the green curve shows the result for the same GDL-S, but measured without stacking. The results for both measurements mostly differ in the pore size domain between 10-50 µm. The log differential intrusion volume shows a different peak position and size of the GDL-S network. Thus, when stacking two layers, the peak pore size is shifted to larger pore diameters. While the results for only 1 GDL-S show a peak at 24 µm, the stacked layers show a peak at 27 µm.

Additionally, it can be observed that there is significantly more pore volume detected for the stacking case, as the area under the curve (proportional to the pore volume) is larger for the measurement with two GDL-S pieces than for that with one GDL-S. The same observation can be seen in the cumulative intrusion curve, where the measurement with two GDL-S pieces exhibits a higher mercury volume than that with one GDL-S. The difference in porosity from these measurements equates to 3%. The observation of the higher pore volume at larger pore diameters when GDL-S pieces are stacked can be rationalized by the extra pore space between the pieces. The surface roughness of both adjacent GDLs create larger pores with additional volume. While artifacts can be avoided when not stacking GDL samples, the measurement accuracy suffers when adding less material to the penetrometer. A careful penetrometer choice is therefore necessary. In our case (Fig. 3.5), the stem usage was 17% for the 1 GDL-S case and 36% for the 2 GDL-S case. The drawback of artifacts when stacking must be weighed against the loss in measurement accuracy. A detailed analysis of how to use MIP with GDLs and MPLs is given by Berger et al.[123]

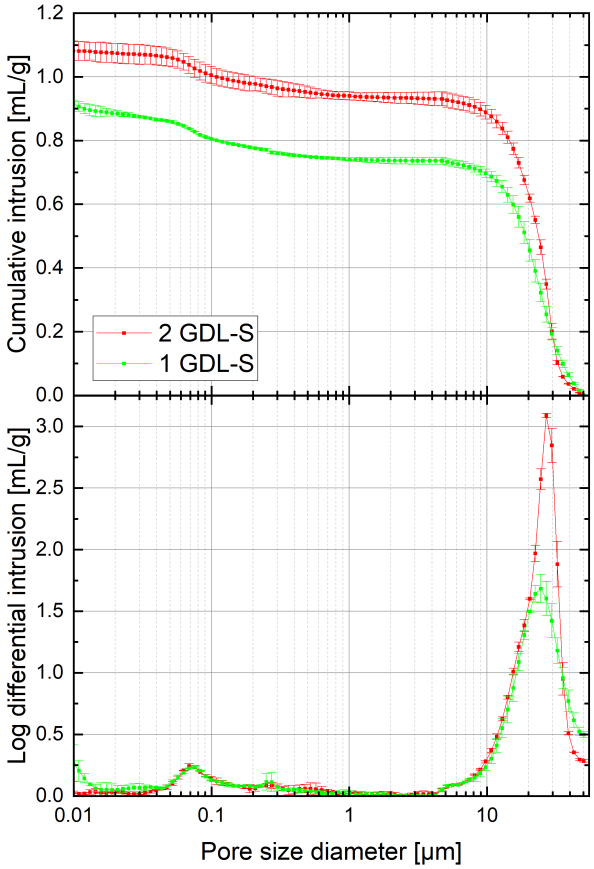

Figure 3.5 Cumulative (upper panel) and log differential intrusion (lower panel) over the pore size for MIP measurements on a Freudenberg GDL-S showing the impact of stacking GDL layers in the sample holder; stacking GDL layers leads to an artifact in form of additional pore volume being detected in between the layers, which falsifies the porosity and the pore size distribution.

3.5 Cross Section Polishing and Scanning Electron Microscopy

The sample preparation for Scanning Electron Microscopy (SEM) was conducted using an IB-19520CCP cross-section polisher manufactured by JEOL in Japan. The samples were ion-milled at an accelerating voltage of 6 kV for 5.5 hours at a temperature of -40℃ with an argon source. The SEM images were captured using a JSM-IT200 InTouchScope™, also manufactured by JEOL in Japan, with an acceleration voltage of 10 kV.

4 Results

This chapter provides a summary of the journal articles presenting the outcomes of this thesis. First, diffusive transport in a dry GDL is analyzed and structural parameters (τ/ε-ratio) are extracted for GDL-Ss and MPLs. After characterizing the dry structure, the liquid water filling in the MPL and a saturation analysis of the MPL and the CL is presented. Lastly, MPL intrusion into the GDL is analyzed. A summary of all the topics covered in this chapter are visualized in Fig. 1.1.

4.1 Determination of the τ/ε-Ratio for Gas Diffusion Substrates and Microporous Layers in an Operating Proton Exchange Membrane Fuel Cell

The article "Determination of the τ/ε-ratio for Gas Diffusion Substrates and Microporous Layers in an Operating Proton Exchange Membrane Fuel Cell" was submitted in 15.9.2024 and accepted for publication in the Journal of the Electrochemical Society on 22.1.2025 distributed under the terms of the Creative Commons Attribution 4.0 License (CC BY). The paper was presented by Anne Berger at the 244th ECS meeting (May 2022) in Vancouver, Canada (abstract number: 1456). The permanent web link to the article is https://doi.org/10.1149/1945-7111/ada63e.

Oxygen is transported through the GDL towards the CL. While there are concepts to add a convective distribution to the oxygen mass transport, the most important mechanism for the oxygen supply is diffusion. The diffusivity across the GDL is largely dependent on its structural parameters, most importantly the porosity (ε) and the tortuosity (τ). In this work, the porosity and the tortuosity for two types of GDL-S and one type of MPL are determined in an operating fuel cell using the work of Baker et al. as the underlying concept.[79] Baker et al. have established the theoretical concept to deconvolute the mass transport resistances into the individual contributions. They were able to extract the effective diffusivity of a Toray GDL-S by stacking several layers and conducting limiting current measurements. However, their study was based on a material that was largely macroporous i.e. falling within a pore size regime, where mostly molecular diffusion takes place for the examined operating conditions.

However, our work revealed that a careful consideration of Knudsen and molecular diffusion is necessary when analyzing a GDL-S containing carbon black in their structure or when analyzing MPLs, which typically have smaller pores. It was found that the extraction of a constant τ/ε-ratio from measurements with varying pressure was not possible when considering only molecular diffusion (as done by Baker et al.[79]). A decreasing trend of the τ/ε with increasing pressure could be observed. Only the addition of Knudsen diffusion to the model allowed a reliable τ/ε-ratio determination, as the contribution ratio of both diffusion processes varies with pressure. The inclusion of Knudsen diffusion is based on the pore size distribution within either the GDL-S or the MPL. The theoretically expected diffusivity can be determined by determining the diffusivity of each individual pore size diameter present in the structure using the Bosanquet equation and weighing each diffusivity according to their relative presence in the pore size distribution based on concepts found in heterogeneous catalysis.

The analysis revealed that even with the inclusion of Knudsen diffusion with the weighted pore size diameters according to the pore size distribution, a small decrease of τ/ε with increasing pressure is visible. We concluded that the diffusion through small pores occurs more often than statistically expected by the pore size distribution. It is known in the literature that the small pores largely interconnect the network.[91]

Author Contributions

A.B. conducted the experimental work, analyzed the data and developed the method to include Knudsen diffusion. M.S. and C.S. developed the idea and method to extract the τ/ε-ratio by varying the MPL thickness, and conducted preliminary experiments. A.B. and H.G. discussed the data and their interpretation. A.B. wrote and M.S., C.S., and H.G. revised the manuscript. All authors commented on the results and reviewed the manuscript. H.G. supervised and secured funding for the project.

Journal of The Electrochemical Society, 2025 **172** 014508

Determination of the τ/ε-Ratio for Gas Diffusion Substrates and Microporous Layers in a Proton Exchange Membrane Fuel Cell

Anne Berger,[z] Michael Striednig, Christoph Simon, and Hubert A. Gasteiger[*]

Technical University of Munich, Germany; TUM School of Natural Sciences, Department of Chemistry and Catalysis Research Center, Chair of Technical Electrochemistry, D-85748 Garching, Germany

An understanding of the GDL properties is crucial for high-current-density operation of proton exchange membrane fuel cells (PEMFCs). The parameters porosity (ε) and tortuosity (τ) directly link the theoretical diffusivity in free space and the effective diffusivity in the structure. The τ/ε-ratio is therefore an important descriptor for the gas diffusion in a porous network. This study characterizes the τ/ε-ratio for gas diffusion layer substrate (GDL-S) materials from two suppliers (Toray, Freudenberg) and for one microporous layer (MPL) using limiting current measurements in an operating fuel cell. However, only the application of a new analysis method that considers the contribution from Knudsen diffusion allows for the τ/ε-determination of GDL-S materials which have carbon black added to the structure (e.g., Freudenberg GDL-S); this method can then also be used for the determination of the τ/ε-ratio of porous networks containing small pores like MPLs. Here, we assess the contribution of pressure-independent Knudsen diffusion to the overall diffusion and introduce a mixed diffusion coefficient, which includes both Knudsen and molecular diffusion. This analysis serves as a guideline to estimate the contribution of the respective diffusive processes for gas diffusion materials utilized in PEMFCs, where pore sizes resulting in different diffusion regimes are present.
 [DOI: 10.1149/1945-7111/ada63e]

Manuscript submitted September 15, 2024; revised manuscript received November 12, 2024. Published January 22, 2025.

List of Symbols

a	constant from Eq. 7 [-]
b	constant from Eq. 7 [-]
A_{ch}	Coefficient used in the appendix representing the flow-rate-independent part of the channel transport resistance
A_{other}	coefficient in Eq. 4 representing the pressure-dependent part of the other transport resistance [m]
B_{ch}	Coefficient used in the appendix representing the flow-rate-dependent part of the channel transport resistance
$d_{peak,macro}$	pore size distribution peak for the largest macropores [m]
d_p	pore diameter [m]
$D^i_{theo,AB}$	theoretical diffusion coefficient of components A in a binary gas mixture of A and B in direction i (x= in-plane, y= through-plane) [m^2/s]
$D^i_{theo,ABC}$	theoretical diffusion coefficient of components A in a ternary gas mixture of A and B and C in direction i (x=in-plane, y=through-plane) [m^2/s]
$D^i_{theo,Knudsen}$	theoretical diffusion coefficient of Knudsen diffusion in direction i (x=in-plane, y=through-plane) [m^2/s]
$D^i_{theo,mixed}$	theoretical diffusion coefficient of mixed diffusion (Knudsen+molecular) in direction i (x=in-plane, y=through-plane) [m^2/s]
$D^i_{eff,j}$	effective diffusion coefficient in component j (e.g., GDL-S, MPL, channel, etc) in direction i (x=in-plane, y=through-plane) [m^2/s]
$D^i_{theo,j}$	theoretical diffusion coefficient in component j (e.g., GDL-S, MPL, channel, etc) in direction i (x=in-plane, y=through-plane) [m^2/s]
$D^i_{theo,PSD}$	theoretical diffusion coefficient using the pore-size-distribution approach in direction i (x=in-plane, y=through-plane) [m^2/s]
e	half-width of the flow channel [m]
f	form factor [-]
F	Faraday constant: 96485 A s/mol
h	thickness of GDL-S [m]
L	channel length [m]
M	molar mass [g/mol]
N	molar flux [mol/s/m^2]
p	pressure [kPa_{abs}]
p_{ci}	critical pressure of i [atm]
p_0	saturation pressure used for BET measurements [kPa]
p_{ref}	atmospheric pressure [kPa_{abs}]
Q	total inlet gas flow rate [m^3/s]
R	universal gas constant: 8.314 J/(K mol)
R_T	oxygen transport resistance [s/cm]
R_i	R for component i [s/cm]
$R_{ch,real}$	real channel resistance: part of thought-experiment, where R_{ch} as determined by measurements, contains $R_{ch,real}$ and $R_{other,PD}$ [s/cm]
$R_{other,PD}$	pressure dependent part of R_{other} [s/cm]
s	Flow channel depth [m]
T	temperature [°C]
T_{ci}	critical temperature of i [K]
t_{MPL}	thickness of MPL [m]
v_{pore}	pore volume [mL]
x_i	molar fraction of component i [-]

Greek Symbols

ε	porosity [-]
λ	dimensionless GDL-S thickness as given in Eq. 6 [-]
ρ_i	density of component i [kg/m^3]
τ	tortuosity [-]

Sub- and Superscripts

ch	channel
dry	dry gas stream RH=0
eff	effective
lim	value at limiting current
O, N, W	corresponding to oxygen, nitrogen, water, respectively
NP	pressure-independent
PD	pressure-dependent

*Electrochemical Society Fellow.
[z]E-mail: anne.berger@tum.de

T	transport
theo	theoretical
x	in-plane direction
y	through-plane direction

Hydrogen is believed to be an essential contributor to the decarbonization of the transportation sector. Industry and policy programs worldwide increasingly support the shift to a hydrogen economy, while fossil fuels are progressively being banned. The EU has announced a 55% reduction of CO_2 emissions for passenger vehicles and a 50% reduction of CO_2 emissions for heavy-duty vehicles by 2030 compared to the level of 1990.[1,2] Similarly, California requires 100% of in-state sales for heavy-duty vehicles to be emission-free in 2035 and that all heavy-duty vehicles in the state be emission-free by 2045.[3,4] Especially in the heavy-duty transportation sector, battery electric vehicles alone cannot satisfy these requirements, as their payload capabilities are limited and as charging-time and charging-power requirements become excessively difficult to meet.

To boost power density of the fuel cell system, an enhancement of the high-current density performance is crucial. One major issue at high current densities are mass transport limitations, as a high oxygen flux needs to be supplied to the electrode. Thus, a gas diffusion layer (GDL) consisting of a macroporous substrate (GDL-S) and a microporous layer (MPL) is applied to ensure, among other advantages (e.g., pressure and current distribution, mechanical strength, etc), a fast and well-distributed oxygen diffusion from the bipolar plate to the electrode. Even though there are concepts of invoking convective transport processes to the mass transport in the GDL,[5] oxygen is mostly transported through the GDL via diffusion. The through-plane diffusion across a porous structure can be described with the following equation:

$$D_{\mathrm{eff}}^{\mathrm{y}} = D_{\mathrm{theo}} \cdot \frac{\varepsilon}{\tau} \qquad [1]$$

The effective diffusion coefficient in through-plane (y) direction ($D_{\mathrm{eff}}^{\mathrm{y}}$) is described by the theoretical diffusion coefficient (D_{theo}) and the structural properties of the porous medium, which can be characterized by its porosity (ε) and its tortuosity (τ). Therefore, an understanding of the structural properties of porous media is necessary when describing diffusivity. Note that in the following, it will be necessary in some cases to specify the porous medium for which the diffusion coefficient is evaluated (i.e., for the GDL-S or the MPL), which will be indicated by the notation $D_{\mathrm{eff(porous\ medium)}}^{\mathrm{y}}$ and $D_{\mathrm{theo(porous\ medium)}}$.

In the literature, different ex situ and in situ methods are used to estimate the effective diffusivity. For example, Yoshimune et al. have determined the τ/ε-ratio of a Toray GDL-substrate by ex situ CO_2 diffusivity measurements with CO_2 sensitive sensors.[6] By tracking the CO_2 concentration as a function of time, the data could be fitted according to Fick's second law. Another ex situ technique to investigate the transport properties of the GDL is electrochemical impedance spectroscopy (EIS) on a GDL material saturated with liquid electrolyte. By this method, the in-plane and through-plane diffusion resistance of the GDL-substrate could be determined for different GDL substrates.[7,8] Zenyuk et al. have used X-ray tomographic microscopy (XTM) and subsequent computational fluid dynamics (CFD) simulations for an ex situ determination of the τ/ε-ratio, which allowed a careful analysis of the change of the structure of different materials upon compression.[9]

Simple analytical expressions linking the tortuosity and the easily determinable porosity have been proposed, such as the Bruggeman correlation for an isotropic structure of spherical particles[10,11] or the model suggested by Tomadakis and Sotirchos, which included anisotropy.[12] However, it was found that both models overestimate the diffusivity for GDL-substrate materials.[13] More computationally advanced models were introduced, such as the lattice Boltzmann method,[14] the Monte Carlo method,[15] or the random walk method.[16] However, they require knowledge or an estimation of the porous structure, which can be determined by ex situ and in situ imaging methods, such as X-ray tomographic microscopy (XTM) or focused-ion-beam-scanning electron-microscopy (FIB-SEM).

For the in situ determination, considering a flow field design that is based on channel and land geometries, the diffusion problem is not one-dimensional, since the reactant gas needs to be transported in-plane underneath the land areas. Flückinger et al. have shown that for Toray GDL-substrate materials, the resin binder is responsible for a lower through- than in-plane diffusivity.[8] Kramer et al. determined the ratio of in-plane to through-plane conductivity via EIS measurements to be 1.8 for a Toray GDL-substrate material (TGPH-060 paper).[7] The same value of ∼1.8 was determined by Xu et al. using XTM in a special tomographic cell design combined with a simulation in GeoDict©, when considering the area under the land.[17] For the channel region, where the GDL-substrate is under a lower compression, the ratio of in-plane to through-plane diffusivity is lowered to ∼1.3. In contrast to the Toray GDL-substrate material, the Freudenberg GDL-S exhibits no difference between in-plane and through-plane diffusivity, independent of channel or land location.

To approximate this 2D-problem with an equivalent 1D-approach, Baker et al. suggested to multiply the GDL thickness with a form factor.[18] The form factor is a function of the land-channel-geometry and the ratio of the in-plane to through-plane diffusivity. They have introduced a method to determine the τ/ε-ratio in situ from single-cell fuel cell measurement through the determination of the diffusion-limited current density. Based on their work, the present study explores the applicability of this theory to different GDL-S materials and also transfers this approach to the description of an MPL.

The oxygen transport resistance (R_{T}) under differential-flow condition is defined in Eq. 2 as a function of the dry oxygen molar fraction ($x_{\mathrm{O}}^{\mathrm{dry}}$), the cell pressure ($p$), the water vapor pressure (p_{W}), the cell temperature (T), the limiting current density (i_{lim}), the Faraday constant (F), and the universal gas constant (R). The expression is derived from combining Fick's first law with Faraday's law.

$$R_{\mathrm{T}} = 4F \cdot \frac{x_{\mathrm{O}}^{\mathrm{dry}}}{i_{\mathrm{lim}}} \cdot \frac{p - p_{\mathrm{W}}}{RT} \qquad [2]$$

Baker et al. describe the transport resistances as resistances in series, which is summarized in Eq. 3: transport resistances arise from the channel of the flow field (R_{ch}), from the GDL-S ($R_{\mathrm{GDL-S}}$), from the MPL (R_{MPL}), and from other influencing factors ($\mathrm{R_{other}}$).[18]

$$R_{\mathrm{T}} = R_{\mathrm{ch}} + R_{\mathrm{GDL-S}} + R_{\mathrm{MPL}} + \mathrm{R_{other}} \qquad [3]$$

In a detailed analysis, Baker et al. have evaluated the individual components, which resulted in Eq. 4.[18] We assume that R_{other} mostly comprises the transport resistance of the electrode, which contains smaller pores where mostly Knudsen diffusion dominates. Therefore, R_{other} is mostly a pressure-independent contribution to the overall transport resistance. The GDL-S and MPL contributions were described as a function of the molecular diffusion coefficient of oxygen in a water-nitrogen mixture ($D_{\mathrm{theo,ONW}}$), the form factor accounting for the anisotropy of the diffusivity and of the flow field geometry (f), the thicknesses of the GDL-S (h) and of the MPL (t_{MPL}), the effective diffusion coefficients of the GDL-S ($D_{\mathrm{eff(GDL-S)}}^{\mathrm{y}}$, in through-plane direction) and of the MPL ($D_{\mathrm{eff(MPL)}}$, assumed to be isotropic). A_{other} describes other pressure-dependent factors, while R_{NP} accounts for non-pressure dependent contributions. More information about the individual components can be found in Ref. 18

$$R_T = R_{ch} + \frac{1}{D_{theo,ONW}}\left(f \cdot h \cdot \frac{D_{theo,ONW}}{D^{y}_{eff(GDL-S)}} + t_{MPL} \cdot \frac{D_{theo,ONW}}{D_{eff(MPL)}} + A_{other} \right) + R_{NP} \quad [4]$$

The form factor f can be calculated using the fit given by Baker et al. for $0.5 < \lambda < 10$:

$$f(\lambda) = 1 + 0.803 \cdot \exp(-1.17\lambda) + 0.197 \cdot \exp(-0.164\lambda) \quad [5]$$

Here, λ is a function of the ratio of the diffusion coefficient in x-direction (in-plane) and y-direction (through-plane) (D^x/D^y), the thickness of the GDL-S (h), and the half-width of the channel (e):

$$\lambda = \sqrt{\frac{D^x}{D^y} \cdot \frac{h}{e}} \quad [6]$$

Refer to reference[18] for more details.

Baker et al. have estimated diffusive transport by bulk molecular diffusion. Molecular diffusion occurs in larger pores and is pressure-dependent. The diffusion coefficient for a binary system can be described by the following formula, taken from Bird, Steward, and Lightfoot:[19]

$$D_{theo,AB} = \frac{1}{p} \cdot a \left(\frac{T}{\sqrt{T_{cA} \cdot T_{cB}}} \right)^{b} \cdot (p_{cA} \cdot p_{cB})^{1/3} \cdot (T_{cA} \cdot T_{cB})^{5/12} \cdot (1/M_A + 1/M_B)^{1/2} \quad [7]$$

This formula yields the theoretical binary diffusion coefficient of component A in B ($D_{theo,AB}$) in units of $cm^2\ s^{-1}$, for a given pressure (p, in units of atm) and temperature (T, in units of K), using the molar mass of components A (M_A) and B (M_B) in units of g/mol. The constants a and b are $a = 2.745 \cdot 10^{-4}$ and $b = 1.823$ for nonpolar gas pairs (i.e., for O_2 and N_2) and are $a = 3.640 \cdot 10^{-4}$ and $b = 2.334$ for pairs consisting of H_2O vapor and a nonpolar gas (i.e., for O_2 and H_2O and for N_2 and H_2O). The parameters p_{cA}, p_{cB}, T_{cA}, and T_{cB} are the critical pressures (in units of atm) and temperatures (in units of K) of the respective gas component (the p_c values for O_2, N_2, and H_2O are 49.8 atm, 33.5 atm, and 217.7 atm, respectively; the T_c values for O_2, N_2, and H_2O are 154.58 K, 126.2 K, and 647.0 K, respectively).[20] As shown by Eq. 7, the binary diffusion coefficients are inversely proportional to the pressure, and thus molecular diffusion is highly pressure-dependent; however, the product of $D_{theo,AB}$ and p is pressure-independent. The ternary diffusion coefficient of O_2 in a given mixture of O_2, N_2, and H_2O, further on referred to as $D_{theo,ONW}$, is calculated by:[18]

$$D_{theo,ONW} = \left(\frac{1 - x_W}{D_{theo,ON}} + \frac{x_W}{D_{theo,OW}} \right)^{-1} \quad [8]$$

In this study, additionally Knudsen diffusion is considered, which occurs when the dimensions of the porous medium (e.g., the pore diameters) are comparable or smaller than the mean free path. Knudsen diffusion can be described by the Knudsen diffusion coefficient defined as:[19]

$$D_{theo,Knudsen} = \frac{4}{3} \cdot d_p \cdot \sqrt{\frac{RT}{2\pi M}} \quad [9]$$

with the pore diameter d_p, the gas constant R, the temperature T, and the molar mass M. The equation underlines that $D_{theo,Knudsen}$ is independent of the pressure. However, the mean free path is pressure-dependent, so that the contribution of Knudsen diffusion might change with the pressure. By considering the effect of Knudsen diffusion, we will analyze the τ/ε-ratio for two different GDL-S materials in an operating fuel cell using the theory developed by Baker et al.,[18] examining the effects of a variation of the GDL-S thickness and of the operational pressure. By this analysis we will show that the determination of the τ/ε-ratio is only possible for the Freudenberg GDL-S when including Knudsen diffusion into the model. This addition of Knudsen diffusion in the calculation also allows to apply the here outlined methodology to the determination of the τ/ε-ratio of an MPL, the validity of which will be demonstrated for an MPL based on vapor grown carbon fibers (VGCF).

Experimental

Mercury intrusion porosimetry.—Mercury intrusion porosimetry (MIP) measurements were carried out on an Autopore Instrument (9600, Micromeritics Instrument Corporation, USA). A penetrometer (sample holder) with a 5 mL bulb volume and 0.392 mL stem volume was used. A mass of ∼110 mg for the Toray and ∼220 mg for the Freudenberg GDL-substrate was used, resulting in a stem usage of ∼58% and ∼80%, respectively. To reduce the influence of the hydrostatic pressure of Mercury in the low-pressure region, the pressure range of 0.5–45 psi was measured in a horizontal penetrometer position, while the pressure range from 45–61,000 psi was measured in a vertical penetrometer position. The pressure steps were chosen to achieve an even spacing on the logarithmic scale, with 25 points per decade on the pressure scale. The pressure at each pressure step was held constant until the intrusion rate was below 0.001 $\mu l(g \cdot s)^{-1}$. To convert the pressure p to a pore diameter d_p, the Washburn equation was applied:

$$d_p = -\frac{4 \cdot \gamma_{Hg} \cdot \cos\theta}{p} \quad [10]$$

with the surface tension of Mercury γ_{Hg} (0.480 N m^{-1}) and the contact angle θ (140°). The porosity was converted using skeletal densities (ρ_{GDL}) taken from the literature via the following formula:

$$\varepsilon = \frac{\nu_{pore}}{\nu_{GDL}} = \frac{\nu_{pore}}{\nu_{pore} + \frac{1}{\rho_{GDL}}} \quad [11]$$

with the pore volume ν_{pore} and the total GDL volume ν_{GDL}. The skeletal densities were taken from Rashapov et al.,[21] namely 1.931 g/cm^3 for the untreated Toray GDL-S and 1.772 g/cm^3 for a Freudenberg GDL-S with a similar PTFE content (H2315T10A).

Physisorption.—To determine the Brunauer-Emmet-Teller (BET) surface area of the GDL-substrates, krypton physisorption measurements were carried out on an Autosorb iQ gas sorption analyzer (Quantachrome Instruments, USA). The samples were prepared by cutting the sheets by hand to smaller stripes (approximately 4 cm x 0.5 cm) to fit the sample tube. Roughly 1.2 g for the Toray GDL-S and roughly 0.8 g for the Freudenberg GDL-S were added to the sample tube. Prior to the measurements, the samples were heated under vacuum to 120 °C for at least 8 h. Adsorption and desorption isotherms were recorded in a relative pressure range of $0.05 < p/p_0 < 0.29$ at a temperature of 77 K. The specific surface area was evaluated from the adsorption isotherms in the relative pressure range of $\approx 0.12 < p/p_0 < 0.29$ with seven data points.

Scanning electron microscopy.—Scanning Electron Microscopy (SEM) images were recorded on a JSM-IT200 InTouchScope™ (JEOL, Japan) using an accelerating voltage of 10 kV. Sample preparation for cross-sections was performed using an IB-19520CCP cross-section polisher (JEOL, Japan). The samples were ion-milled without any prior embedding at an accelerating voltage of 6 kV for 5.5 h at a temperature of −40 °C using an argon source.

5 cm² single-cell PEMFC measurement setup and analysis procedures.—Differential-flow single-cell fuel cell test were conducted on an active area of 5 cm^2 in a special cell design, which was developed by Baker et al.[18] and adapted with the suggestions by Du et al. of using the cell geometry of a width of 1 cm meaning not all of the flow field channels were under the active area.[22] A flow field (Poco Graphite, USA) originally designed to accommodate an active area of 50 cm^2 with 14 channels arranged in three serpentines (0.5/0.8 mm channel width/depth and 0.5 mm land width) was used. The active area of 5 cm^2 was located at the cathode outlet containing the straight section of the last serpentine to avoid a large pressure gradient along the active area and reduce the chance of convective in-plane transport between adjacent channels with a different local pressure. Since the operation was in counter-flow mode, the active area at the cathode outlet represents the position of the anode inlet. The special cell geometry required three important experimental considerations: i) the temperature sensor needs to be positioned inside the graphite block in the center of the 5 cm^2 active area in order to achieve an accurate temperature measurement and control; ii) the pressure of the cell needs to be regulated to the cathode outlet cell pressure in order to account for the pressure drop along the flow channels of the entire 50 cm^2 flow field (there is only a small pressure drop along the active area under the straight flow channels); and, iii) the dew point of the humidifier (under a pressure that is close to the cell inlet pressure) needs to be adjusted to achieve the correct RH at the cathode outlet pressure. The flow fields were sandwiched between two gold-coated copper current collectors, which were electrically isolated from the adjacent in-house made aluminum end plates.

A Primea Mesga catalyst coated membrane (CCM, W. L. Gore & Associates A510.1/M715.18/C580.4, USA) was cut to an area of 8.25 cm^2 (5.5 cm x 1.5 cm). The CCM was laminated using the procedure by Du et al. with a PEN-foil subgasket (CMC 61325, CMC Klebetechnik, Germany), exposing an active area of 5 cm x 1 cm. GDLs (with or without MPLs) were cut to the same dimensions as the CCM (8.25 cm^2, 5.5 cm x 1.5 cm).[22]

A commercial Freudenberg H14C10 was used as the anode GDL, while the cathode GDL (with or without MPL) was added as indicated for each figure. Two GDL-substrates (GDL-S) were investigated in this work: Toray (TP-060, without hydrophobic treatment) and Freudenberg H14 (hydrophobically treated by the manufacturer). An MPL based on vapor grown carbon fibers (VGCF-H, Showa Denko) was applied to the Freudenberg H14 GDL-S. The protocol for the MPL preparation was described previously,[23,24] using a PTFE dispersion (TF 5035GZ, 58 wt% PTFE from 3 M Dyneon, Germany) for binding and hydrophobization, and targeting a final PTFE content of 20 wt% in the MPL. Briefly, the slurry was prepared by first mixing the carbon fibers with deionized water (Milli-Q, 18 MΩ cm), Triton X-100 (Sigma Aldrich), and methyl cellulose (Sigma Aldrich, USA) in an ARV-310 planetary mixer (Thinky, Japan), to which the PTFE dispersion was added in a subsequent mixing step. The thus prepared slurry was coated onto the Freudenberg H14 GDL-S using a stencil; in addition, a free-standing MPL was prepared by coating the slurry onto a glass plate. Subsequently, the MPLs were subjected to a heat treatment procedure with a final temperature of 380 °C. For further details about the slurry preparation and MPL coating see Simon et al.[24]

The compression of the single-cell could be varied by different sealing material thicknesses (Fiberflon GmbH & Co. KG, Germany) and was individually chosen to result in a contact pressure of 1.4–1.6 MPa, which was verified by a pressure-sensitive film (FUJIFILM Prescale film, super low pressure range, LLW, Japan). The pressure-sensitive film was placed between the cathode flow field and the cathode GDL. The pressure was held for 2 min. The films were scanned (Epson Perfection V33) and evaluated using the provided software (Fujifilm FPD-8010E). The evaluation of cells with different compression resulted in an optimal compression pressure of 1.4–1.6 MPa of 14% for the Toray TP-060 and 15% for the hydrophobically treated Freudenberg H14. The Freudenberg H14 + MPL was compressed to an overall compression of 15%-20% depending on the MPL thickness. Different thicknesses of GDL-S were realized by stacking 1, 2, or 3 GDL-S on top of each other, and different MPL thicknesses were achieved by coating with stencils of different thicknesses.

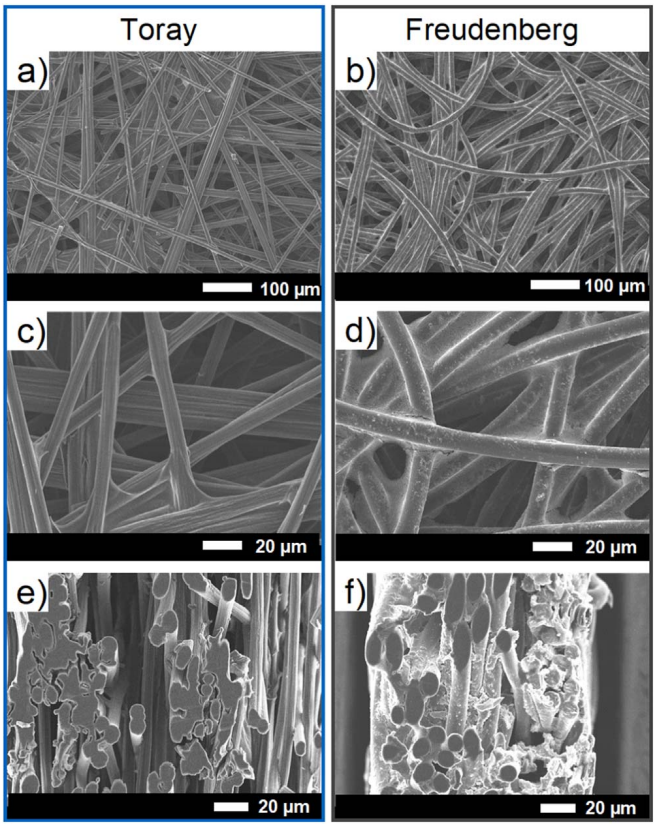

Figure 1. SEM images of the Toray TP-060 (a, c, e) and the Freudenberg H14 (b, d, f) GDL-substrates; panels a-d are taken in top-view and panels e-f in cross-sectional view. While both materials rely on a similar carbon fiber diameter, the production steps lead to the following differences: i) straight fibers for the Toray and entangled fibers for the Freudenberg GDL-S, ii) connecting resin material at the junction points of the Toray and additional carbon black for the Freudenberg GDL-S.

The electrochemical characterization was conducted on a fully automated fuel cell test station (G60, Greenlight Innovation, Canada). To condition the CCM, H2/air flows of 1390/3320 nccm at 80 °C, 100% relative humidity (RH), and 150 kPaabs were applied and the cell was subjected to 10 cycles of the following three voltage-hold steps: 45 min at 0.6 V, 5 min at open circuit voltage (OCV), and 10 min at 0.85 V. After the conditioning, a recovery step was applied, where a voltage of 0.3 V was held at 40 °C, 100% RH, and 170 kPa_{abs} (controlled at the cell outlet) under H2/air flows of 2000/5000 nccm.

Limiting current measurements were implemented by diluting oxygen with nitrogen at the cathode side to achieve O2 dry mole fractions of 0.5%, 1%, 2%, 4%, 8%, 12%, 16%, 21%, 24%, and 28%, similarly to what was done by Baker et al.[18] and Simon et al.,[23] using a total flow rate of 5000 nccm. Pure H_2 (2000 nccm) was used at the anode side. To scan the mass transport limited current regime, the voltage was set to 0.3, 0.15, 0.1, and 0.05 V and held for 2 min at each voltage step, whereby the last 15 s for each data point were averaged.

Results

GDL-substrate characterization.—Fig. 1 shows SEM images of the Toray (a, c, e) and the Freudenberg GDL-S (b, d, f). While panels a-d demonstrate top-view images, panels e and f contain cross-sectional images. Especially in Figs. 1a and 1b, it can be observed

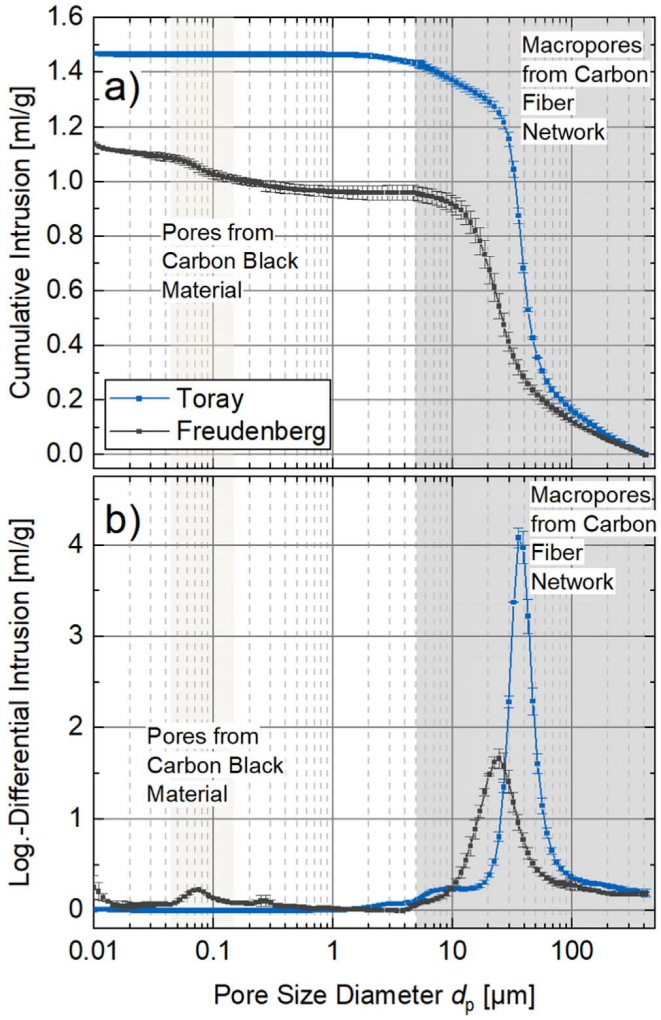

Figure 2. Mercury intrusion porosimetry data for the Toray TP-060 GDL-S (blue symbols/lines) and the Freudenberg H14 GDL-S (black symbols/lines): (a) cumulative Mercury intrusion; (b) log.-differential Mercury intrusion. These data demonstrate the presence of carbon black material in the Freudenberg H14 GDL-S, indicated by the significant pore volume between 0.045–0.15 µm, a pore size region where no pore volume is observed for the Toray TP-060 GDL-S.

that both materials rely on a similar base material, which is a polyacrylonitrile(PAN)-precursed 7 µm carbon fiber.[25] However, different manufacturing steps lead to alterations in the form and orientation of the fibers and also different additional components are used. The prior carbonization and chopping of the fibers leads to straight fibers with random in-plane orientation for the Toray paper, while the fibers for the Freudenberg materials are dry-laid and hydroentangled before the carbonization step. The Toray paper is stabilized with a carbonizable thermoset resin, while the Freudenberg paper is treated with carbon powder to increase its electrical conductivity.[25,26] These components can be observed in the zoomed-in views in panels c and d. For the Toray paper (Fig. 1c), the fibers are reinforced with the resin at the connection points. For the Freudenberg GDL-S (Fig. 1d), it can be seen that the carbon powder is spread in between the fibers. While the resin is primarily deposited at the connection points of straight fibers for the Toray paper, the carbon powder is distributed more evenly along the fibers for the Freudenberg material. The position of the carbon black powder and its importance will be discussed in more detail throughout the manuscript. The cross-sections in panels e and f display a similar through-plane fiber arrangement for both GDL-S, with similar spacings between the fibers.

To analyze the porosity and pore size distribution (PSD) of both GDL-substrates, MIP measurements were performed. Figure 2a shows the cumulative Mercury intrusion and Fig. 2b the log.-differential intrusion. The Toray GDL-S (blue symbols/lines) displays a very narrow pore size distribution of macropores between 30–50 µm, which can be seen by the steep gradient in Fig. 2a and the narrow peak in Fig. 2b. The pore size distribution of macropores in the Freudenberg GDL-S (black symbols/lines) exhibits smaller pore diameters between 10–40 µm. In contrast to the Toray GDL-S, the Freudenberg GDL-S additionally exhibits a significant volume contained in smaller pores around 80 nm, which are characteristic of the carbon black that is part of the Freudenberg GDL-S (see Fig. 1d). The MIP-derived porosities (see Eq. 11) of the Toray and the Freudenberg GDL-S are 74% and 67%, respectively. These values are consistent with the literature: for the Toray GDL-S, the reported porosity values are 74%-77%,[6,8,21,27–29] while for the Freudenberg GDL-S a much wider range of porosity values of 68%-80%[21,30] have been reported. The fraction of the pore volume ascribed to the carbon black material in the Freudenberg GDL-S, ranging from 0.045–0.15 µm (see Fig. 2b) was found to be 13%. These results are summarized in Table I.

The presence of high-surface area carbon black material in the Freudenberg H14 GDL-S is also reflected by its more than one order of magnitude higher specific surface area compared to a Toray GDL-substrate, as determined by Kr-physisorption measurements and yielding ∼4.68 m^2/g for the Freudenberg H14 GDL-S compared to ∼0.33 m^2/g for a Toray GDL-S. Note that the BET surface area for the latter was evaluated for the thicker Toray TP-H-120 GDL-S, as BET measurements event with krypton, which requires ∼100 times less sample surface area compared to N_2,[31] would require too much material to obtain reliable BET values for the thinner TP-060 GDL-S. Even though the Toray TP-060 GDL-S is not hydrophobized (i.e., contains no PTFE) while the Toray TP-H-120 GDL-S is hydrophobized with 5 wt% PTFE, we do not expect that this small amount of PTFE would substantially change the BET surface area of the Toray GDL-S materials. The larger error for the BET measurements of the Toray TP-H-120 GDL-S can be explained by the sample preparation: as the material was cut to smaller stripes to fit the sample tube by hand, the number and size of the samples was not controlled. Nevertheless, the difference in the BET surface area

Table I. MIP-based values (derived from Fig. 2) of the overall porosity (ε, via Eq. 11), the pore size distribution peak for the largest macropores ($d_{peak,macro}$), and the volume fraction of pores from carbon black additive ($\varepsilon_{Carbon\ black}$, defined as the pore volume between 0.045–0.15 µm) for the non-hydrophobized, untreated Toray TP-060 GDL-S, Toray TP-H-120 (5% hydrophobical agent) and Freudenberg H14 GDL-S (hydrophobically treated). Also listed are the Kr-based BET values determined for the Freudenberg H14 GDL-S and for a Toray TP-H-120 GDL-S (with 5 wt% PTFE), whose BET surface area is expected to be essentially identical with that of the Toray TP-060 GDL-S (note: the BET could not be determined for the latter due to its very low overall surface area); the given errors represents the standard deviation of three independent measurements.

	GDL-S ε-value	GDL-S $d_{peak,macro}$	$\varepsilon_{Carbon\ black}$	BET Area
Toray TP-060 (untreated)	74%[a)]	43 µm	0%	—
Toray TP-H-120 (with 5 wt% PTFE)	—	—	—	0.33 ± 0.07 m^2/g
Freudenberg H14 (hydrophobically treated)	67%[b)]	30 µm	13%	4.68 ± 1.01 m^2/g

a) based on a skeletal density of 1.931 g/cm^3 [21] b) based on a skeletal density of 1.772 g/cm^3 [21]

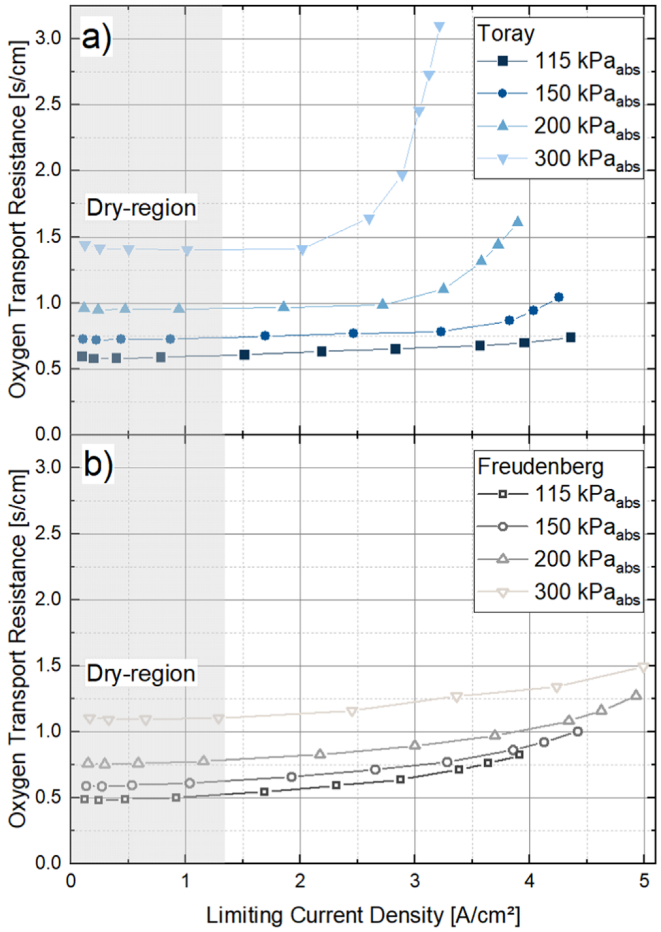

Figure 3. Oxygen transport resistance (R_T) versus limiting current density acquired at 80 °C/62% RH under differential-flow conditions at cell pressures of 115 (■), 150 (●), 200 (▲), and 300 kPa$_{abs}$ (▼) for: (a) the Toray TP-060 GDL-S; (b) the Freudenberg H14 GDL-S. The i_{lim}-independent R_T values in the dry-region at low current densities is shaded in gray; at high current densities and with increasing pressure, flooding can be observed for the Toray GDL-S.

between the Toray and the Freudenberg GDL-S by one order of magnitude is significant.

Limiting current-derived oxygen transport resistances of the GDL-S materials.—After having established the similarities and differences of the two materials, limiting current measurements were conducted with the aim of determining the τ/ε-ratio as suggested by Baker et al.[18] The measurements were carried out at 80 °C, at an RH of 62%, and at differential-flows of 2000 nccm and 5000 nccm at the anode and cathode side, respectively; measurements were conducted at four different cell pressures, namely 115, 150, 200, and 300 kPa$_{abs}$. The oxygen transport resistances (R_T), determined from the measured limiting current densities (i_{lim}) via Eq. 2 are plotted versus the limiting current density for the Toray GDL-S in Fig. 3a and for the Freudenberg GDL-S in Fig. 3b. For both GDL-substrates, the R_T values generally increase with pressure, as is typically observed.[32,33] At low limiting current densities (<1.3 A cm^{-2}), the R_T values thus increase with pressure from ∼0.5 to ∼1.1 s/cm for the Toray GDL-S and from ∼0.6 to ∼1.5 s/cm for the Freudenberg GDL-S, but for each pressure remain essentially constant. On the other hand, at higher limiting current densities, the R_T values increase with i_{lim}, showing different characteristics for the two materials: For the Freudenberg GDL-S (Fig. 3b), the R_T values gradually increase with i_{lim} at each of the four different measurement pressures. A similar behavior is observed for the Toray GDL-S (Fig. 3a) at the lower pressures of 115 kPa$_{abs}$ and 150 kPa$_{abs}$, but at the higher pressures of 200 and 300 kPa$_{abs}$, the R_T values of the Toray GDL-S sharply increase at i_{lim} >3 A/cm^2 and >2 A cm^{-2}, respectively.

In summary, two different trends of R_T versus i_{lim} are observed for the two GDL-substrates at higher limiting current densities: a sudden increase of the R_T values as a threshold i_{lim} value is exceeded for the Toray GDL-S (the threshold i_{lim} value decreasing with increasing pressure), contrasting the only rather gradual increase of the R_T values for the Freudenberg GDL-S. Both observations can be explained by the difference in thermal conductivity of the two GDL-substrates. It was previously shown that the Toray material has a ∼2-fold higher thermal conductivity than the Freudenberg material, which influences the transport resistance especially under wet conditions.[34] At high current densities, the heat produced by the electrochemical reaction leads to a temperature gradient between the cathode electrode and the flow field, which increases with increasing current density (i.e., with increasing heat generation rate), whereby the temperature gradient is the higher the lower the thermal conductivity of the GDL-S. The resulting higher temperature in the cathode electrode when using the Freudenberg GDL-S facilitates water removal by gas-phase water vapor transport. Owejan et al. have previously confirmed in ex situ measurements that the water transport in the presence of a temperature gradient is improved due to the higher water saturation pressure at the cathode electrode compared to that at the flow field, enabling efficient gas-phase water transport via a water vapor partial pressure gradient.[35] Thus, the steep R_T increase at higher pressures and higher current densities for the Toray GDL-S can be explained as an accumulation of liquid water on account of the high thermal conductivity of the Toray material, which does not allow for the build-up of a sufficiently large temperature gradient to remove the product water by water vapor diffusion.[36] In contrast, the gradual R_T increase at higher current densities at all pressure levels for the Freudenberg material can be explained with a lowering of the membrane RH due to the increased water removal rate at the higher temperature gradient that also leads to a higher electrode and membrane temperature. On the one hand, this results in the commonly observed increase of the HFR with increasing current density for the Freudenberg GDL-S (see, e.g., Ref. 23). On the other hand, this dry-out leads to a lower cathode catalyst utilization[37] and thus a lower effective electrode roughness factor, which in turn results in an R_T increase due to the increasing importance of the local oxygen transport resistance at low roughness factors. The limiting current is not only limited by the oxygen transport to the electrode but here also by the proton transport. The observed effect of an increased transport resistance at higher currents densities was enlarged at even lower relative humidities, supporting the general trend (data not shown). An alternative explanation was given by Nonoyama et al., who explained that a higher oxygen transport resistance at lower RH (in our case: lowering of RH with current density through the temperature gradient between electrode and flow field at high current densities) can be correlated with a lower oxygen permeability of the ionomer film at lower RHs.[38]

To avoid the effects of either GDL-S flooding or electrode/membrane dry-out at high current densities, only the essentially i_{lim}-independent oxygen transport resistance at low limiting current densities (<1.3 A cm^{-2}), i.e., in the so-called dry-region where RH and temperature gradients are insignificant (gray-shaded region in Fig. 3), was evaluated for the following analysis.

Determination of the τ/ε-ratio of GDL-substrates.—Baker et al. have explained two different methods to extract the τ/ε-ratio of a GDL-S from limiting current data, which in the following are labeled as Method A and Method B. Method A relies on the change of the oxygen transport resistance with pressure. It is based on the derivative of Eq. 4 with respect to pressure, which after some simplification results in Eq. 12.[18]

$$\frac{\partial R_T}{\partial p} = \frac{\partial R_{ch}}{\partial p} + \frac{1}{p \cdot D_{theo,ON}}\left(fh \cdot \frac{D_{theo,ONW}}{D^y_{eff(GDL-S)}}\right) = \frac{\partial R_{ch}}{\partial p} + \frac{1}{p \cdot D_{theo,ON}}\left(fh \cdot \left(\frac{\tau}{\varepsilon}\right)_{GDL-S}\right) \quad [12]$$

While $\frac{\partial R_T}{\partial p}$ is determined from limiting current density measurements at different pressures as shown in Fig. 3, $\frac{\partial R_{ch}}{\partial p}$ needs to be known. Baker et al. have solved for the term computationally for a given flow field geometry, temperature, pressure, and gas flow.[18] They were able to verify their computational results experimentally, and we will discuss later in more detail why the experimental determination is preferable. Another term in Eq. 12 is the product of the pressure p and the diffusion coefficient of oxygen in nitrogen $D_{theo,ON}$ ($p \cdot D_{theo,ON}$), which is pressure-independent (see Eq. 7). Finally, f is the shape factor (see Eqs. 5 and 6), which transforms the 2D diffusion problem due to the channel/land-geometry into a 1D diffusion problem; a more detailed derivation and explanation of Eqs. 5 and 6 is given by Baker et al.[18] In this work, f is determined using the half-width of our flow field channel ($e = 250\,\mu m$) the GDL-S thickness h, and the D^x/D^y ratio of the GDL-S, which was assumed to be 1[17] for the Freudenberg and 1.8[7,18] for the Toray GDL-S (taken from the literature). The product fh represents the shape factor-corrected GDL-S thickness.

Method B relies on the second derivative of the transport resistance with respect to pressure and to the shape factor-corrected thickness ($\frac{\partial^2 R_T}{\partial(fh)\partial p}$) in order to determine the τ/ε-ratio. The experimental procedure consists of two steps: i) first, a determination of $\frac{\partial R_T}{\partial p}$ as done in Method A, but this time conducted with nominally identical porous media that differ in thickness, which in the case of GDL-substrates can be achieved by stacking different numbers of a given GDL-S; (ii) second, determination of $\frac{\partial^2 R_T}{\partial(fh)\partial p}$ from the slope of a plot of the $\frac{\partial R_T}{\partial p}$ values versus fh. The underlying equation relating the thus determined $\frac{\partial^2 R_T}{\partial(fh)\partial p}$ value to the τ/ε-ratio is given in Eq. 13,[18] whereby in contrast to Method A, the value of $\frac{\partial R_{ch}}{\partial p}$ does not need to be known beforehand:

$$\frac{\partial^2 R_T}{\partial(fh)\partial p} = \frac{1}{p \cdot D_{theo,ON}} \cdot \frac{D_{theo,ONW}}{D^y_{eff(GDL-S)}} = \frac{1}{p \cdot D_{theo,ON}} \cdot \left(\frac{\tau}{\varepsilon}\right)_{GDL-S} \quad [13]$$

In addition to these two methods, a third method is proposed here and referred to as Method C, where the underlying principle relies on the derivation of R_T with respect to the shape factor-corrected thickness fh. It is based on taking the derivative of Eq. 3 with respect to fh, where only R_{GDL-S} is a function of fh. Including Eq. 14 (taken from Baker et al.[18]) in Eq. 3, the derivative with respect to fh results in Eq. 15, which shows that this derivative is the inverse of the effective diffusion coefficient in through-plane direction D^y_{eff} of the GDL-S. Dividing the theoretical diffusion coefficient D_{theo} in the GDL-S (as described in Eq. 1) by the thus obtained $D^y_{eff(GDL-S)}$ value yields the τ/ε-ratio of the GDL-S, as shown in Eq. 16. Here it is important to note that in this first part of the present study, D_{theo} is considered to be the diffusion coefficient for molecular diffusion $D_{theo,ONW}$, as was done by Baker et al.,[18] and which can be derived from Eqs. 7 and 8.

$$R_{GDL-S} = \frac{fh}{D^y_{eff(GDL-S)}} \quad [14]$$

$$\frac{\partial R_T}{\partial(fh)} = \frac{1}{D^y_{eff(GDL-S)}} \quad [15]$$

$$\left(\frac{\tau}{\varepsilon}\right)_{GDL-S} = \frac{D_{theo}}{D^y_{eff(GDL-S)}} = D_{theo} \cdot \frac{\partial R_T}{\partial(fh)} \quad [16]$$

The different methods to evaluate the τ/ε-ratio, including all the underlying equations, are summarized in Table II.

To test and compare all three methods, limiting current experiments were conducted at four different pressures and three different GDL-S thicknesses. The GDL-S layers were stacked on top of each other, as it was shown that the interface between the layers does not add any additional dry-region transport resistance.[18] The results are displayed in Fig. 4. Figure 4a shows exemplarily the dry-region oxygen transport resistances of the Toray GDL-S versus pressure for 1, 2, or 3 GDL-S layers. From the slope $\frac{\partial R_T}{\partial p}$ for each configuration,

Table II. Summary of the underlying equations to determine the τ/ε-ratio using Method A, B, or C, describing the measurement procedure (left column) and the relationship to determine the τ/ε-ratio (right column). The term $p \cdot D_{theo,ON} = 2.84 \cdot 10^{-3}$ kPa m²/s is pressure independent and can be calculated from Eq. 7. The value of $\frac{\partial R_{ch}}{\partial p}$ can either be calculated through the approach from Baker et al.[18] or determined experimentally, which then also includes the intrusion of the GDL-S into the flow field (see appendix); the here experimentally determined values tor the two different GDL-substrates are $\left(\frac{\partial R_{ch}}{\partial p}\right)_{Freudenberg}$ = 0.00184 s/cm/kPa and $\left(\frac{\partial R_{ch}}{\partial p}\right)_{Toray}$ = 0.0022 s/cm/kPa. The form factor f depends on the flow field geometry (e = 250 µm), the used GDL-S, and the GDL-S thickness h and can be calculated from Eqs. 5 and 6; furthermore required is the D^x/D^y value, which was assumed to be 1[17] for the Freudenberg and 1.8[7,18] for the Toray GDL-S. In this study, the resulting value of f varied between 1.62 and 1.15, with the higher values representing the thinner layers. Finally, D_{theo} is traditionally taken to be the oxygen diffusion coefficient for molecular diffusion $D_{theo,ONW}$ (Eq. 8), but for porous media with small pores where Knudsen diffusion plays a role, D_{theo} would correspond to $D_{theo,PSD}$ (see Eq. 23), which is the pore size distribution-weighted mixed diffusion coefficient $D_{theo,mixed}$ that considers both Knudsen and molecular diffusion contributions (see Eq. 20).

Method A (see Fig. 4a): measure R_T vs p for a GDL-S	
plot R_T vs p to get $\frac{\partial R_T}{\partial p}$	$\rightarrow \left(\frac{\tau}{\varepsilon}\right)_{GDL-S} = \left(\frac{\partial R_T}{\partial p} - \frac{\partial R_{ch}}{\partial p}\right) \cdot \frac{p \cdot D_{theo,ON}}{fh}$
Method B (see Fig. 4b): measure R_T vs p for 1, 2, 3, etc stacked GDL-S with total thickness of h, 2 h, 3 h, etc.	
(1) plot R_T vs p to get $\frac{\partial R_T}{\partial p}$ for each (2) plot $\frac{\partial R_T}{\partial p}$ versus fh to get $\frac{\partial^2 R_T}{\partial(fh)\partial p}$	$\rightarrow \left(\frac{\tau}{\varepsilon}\right)_{GDL-S} = p \cdot D_{theo,ON} \cdot \frac{\partial^2 R_T}{\partial(fh)\partial p}$
Method C (see Fig. 4c): measure R_T vs fh for 1, 2, 3, etc stacked GDL-S with total thickness of h, 2 h, 3 h, etc.	
plot R_T vs fh at a given p = const. to get $\frac{\partial R_T}{\partial(fh)}$	$\rightarrow \left(\frac{\tau}{\varepsilon}\right)_{GDL-S} = D_{theo} \cdot \frac{\partial R_T}{\partial(fh)}$

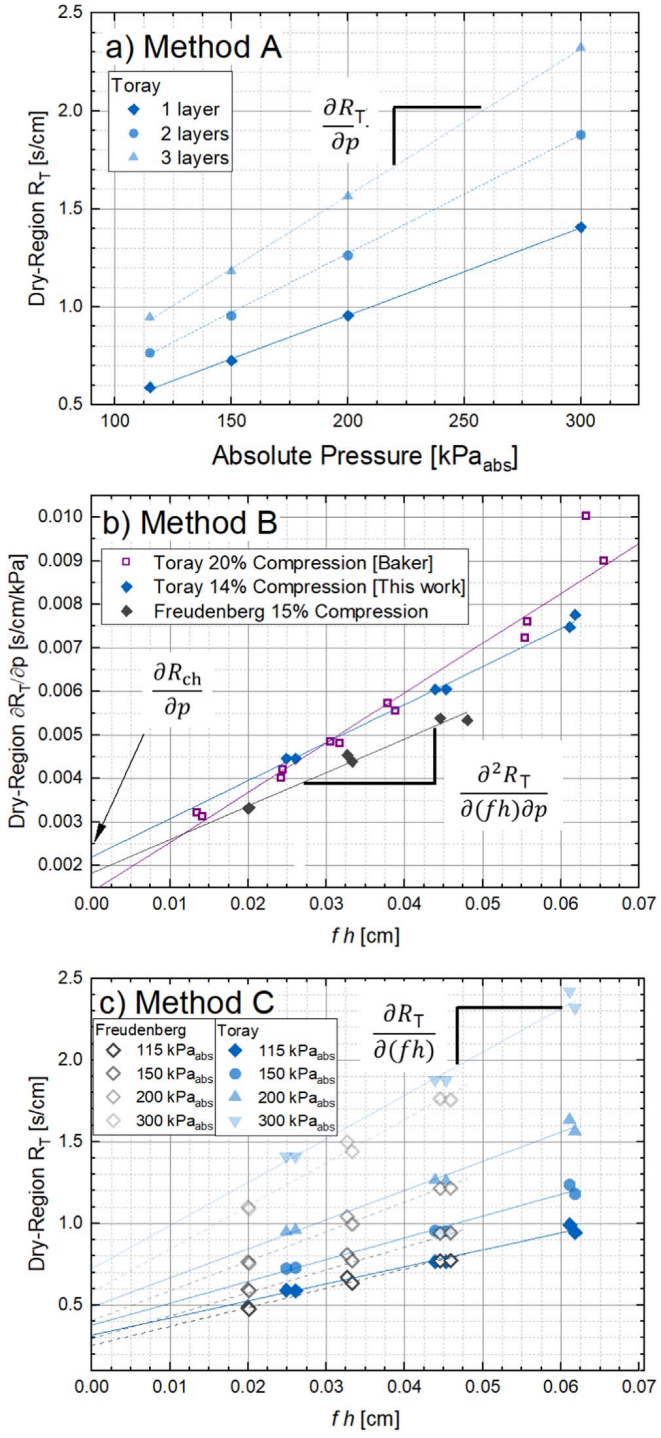

Figure 4. (a) Dry-region oxygen transport resistance over the absolute pressure for 1 (●), 2 (▲), or 3 (▼) GDL-S layers, shown exemplarily for a Toray TP-060 GDL-S (the same analysis was equally conducted for the Freudenberg H14 GDL-S; data not shown). (b) Plot of $\partial R_T/\partial p$ over fh for the Toray (blue symbols) and Freudenberg (gray symbols) GDL-substrates, with the solid lines representing a linear regression fit of the data; the dataset from Baker et al.[18] for an untreated Toray GDL-S is shown for comparison (□), whereby it should be noted that it was compressed by 20% compared to 14% for the data measured in this study. (c) Dry-region oxygen transport resistance over fh for the Toray (blue symbols) and the Freudenberg (gray symbols) GDL-S for different pressures, with the lines representing a linear regression fit of the data.

the τ/ε-ratio can be calculated according to Method A. The same data were acquired for the Freudenberg GDL-S (data not shown), and the τ/ε-ratios obtained for the two GDL-substrates at the four different pressures are listed in Table III (first row), yielding average τ/ε-ratios of 2.49±0.03 and 2.18±0.07 for the Toray and the Freudenberg GDL-S, respectively.

In Fig. 4b, the $\frac{\partial R_T}{\partial p}$ values obtained from the three lines in panel a for the Toray GDL-S are plotted on the *y*-axis versus the shape factor-corrected thickness, yielding a straight line (blue symbols/line), the slope of which is the second derivative $\frac{\partial^2 R_T}{\partial (fh) \partial p}$ that is needed for the evaluation of the τ/ε-ratio based on Method B. The resulting τ/ε-ratio for the Toray GDL-S of 2.51 (see second row in Table III) is in reasonably good agreement with the average value obtained by Method A (first row). Figure 4b also shows a comparison with literature data from Baker et al.[18] for the same type of untreated Toray GDL-substrates (open black symbols), which yield a ∼30% higher slope in Fig. 4b and thus a ∼27% higher τ/ε-ratio (see Eq. 13). This can be explained by the higher GDL-S compression in the study by Baker et al. (20%) compared to our study (14%), since it is well-known that a higher compression results in a higher tortuosity and a lower porosity, i.e., in a higher τ/ε-ratio.[7,9,18,29] Finally, the analysis of the Freudenberg GDL-S with Method B (blue symbols/line in Fig. 4b) yields a τ/ε-ratio of 2.29, which is ∼5% higher than what was obtained by Method A.

The *y*-axis intercepts of the regression lines through the various data sets in Fig. 4b represent the transport resistance without the contribution originating from the GDL-S ($R_{GDL-S} = 0$). It can be used to determine the value for $\frac{\partial R_{ch}}{\partial p}$, which is explained in the following. For $R_{GDL-S} = 0$ and $R_{MPL} = 0$ (no MPL in this set of experiment), these terms can be omitted from Eq. 3, which then can be differentiated with respect to the pressure, leading to:

$$\left.\frac{\partial R_T}{\partial p}\right|_{fh=0} = \frac{\partial R_{ch}}{\partial p} + \frac{\partial R_{other}}{\partial p} \qquad [17]$$

Given that we assume that the ∂R_{other} terms are mostly pressure-independent due to their predominantly Knudsen diffusion dependence in the catalyst layer, their derivative with respect to pressure in Eq. 17 is roughly zero:

$$\frac{\partial R_{other}}{\partial p} \approx 0 \qquad [18]$$

Thus, Eq. 17 can be simplified to:

$$\left.\frac{\partial R_T}{\partial p}\right|_{fh=0} \approx \frac{\partial R_{ch}}{\partial p} \qquad [19]$$

Even if the assumption leading to Eq. 18 were not exactly true, i.e., even if there were indeed other pressure-dependent transport losses ($R_{other,PD}$) present in our cell, we would include them in the experimental determination of what claim as R_{ch}. Yet, in this thought experiment $R_{ch} = R_{ch,real} + R_{other,PD}$. When correcting for R_{ch}, we would equally correct for both $R_{ch,real}$ and $R_{other,PD}$. Thus, the experimental determination of R_{ch} is advantageous compared to the computational determination suggested by Baker et al.,[18] as it can be applied more universally. The thus determined $\frac{\partial R_{ch}}{\partial p}$ values from the data in Fig. 4b are $\left(\frac{\partial R_{ch}}{\partial p}\right)_{Freudenberg} = 0.00184$ s/cm/kPa and $\left(\frac{\partial R_{ch}}{\partial p}\right)_{Toray} = 0.0022$ s/cm/kPa. The difference between these two values can be explained with the difference in penetration of the two GDL-substrates into the channel region, since it was shown that the Freudenberg GDL-S intrudes further into the channel upon compression than the Toray GDL-S.[39] A further discussion and an additional analysis of the dataset from Fig. 4, which explains the correlation between GDL intrusion and R_{ch}, can be found in the appendix.

Finally, Fig. 4c illustrates the determination of the τ/ε-ratio via Method C. Here, the dry-region R_T value at a given pressure is

Table III. Summary of the τ/ε-ratios determined for the Toray TP-060 and the Freudenberg H14 GDL-substrates with Methods A, B, and C (see Table II), based on the data from Fig. 4. The procedure for the three methods are given in Table II and the values for the various required parameters are listed in the description of Table II; for Method C, D_{theo} was taken to be $D_{theo,ONW}$ (see Eq. 8). Pressure-independent effects are related to Knudsen diffusion.

Method	Pressure dependence		τ/ε-ratio	
			Toray	Freudenberg
A	Pressure-independent effects excluded	1 layer	2.51	2.10
		2 layer	2.46	2.24
		3 layer	2.51	2.21
B	Pressure-independent effects excluded		2.51	2.29
C	Pressure-independent effects included	115 kPa_{abs}	2.75	3.04
		150 kPa_{abs}	2.65	2.74
		200 kPa_{abs}	2.62	2.65
		300 kPa_{abs}	2.57	2.54

plotted versus the shape factor-corrected thickness for each GDL-S. Based on Eq. 15, the slope of the resulting straight line equals the inverse of the effective diffusion coefficient D_{eff}^{y}, from which the τ/ε-ratio can be calculated based on Eq. 16.

The τ/ε-ratios determined with Method A, B, and C are summarized in Table III. For Method A, we have analyzed separately the datasets for 1, 2, and 3 GDL-S layers by taking the derivative of each set of transport resistances with respect to pressure (see first row of Table II). Within the measurement accuracy, the values for the different number of layers are similar for each material, with average τ/ε-ratios of 2.49±0.03 for the Toray TP-060 GDL-S and slightly lower values of 2.18±0.07 for the Freudenberg H14 GDL-S. Method B utilizes the values for all pressures and all thicknesses, as the method is based on the determination of the second derivative of R_T with respect to pressure and the shape factor-corrected thickness (see second row of Table II). For the Toray GDL-S, Method B yields a τ/ε-ratio of 2.51, which is in excellent agreement with the value obtained by Method A (2.49±0.03). Nevertheless, it must be noted that the here determined τ/ε-ratio of ∼2.5 is ∼17% lower than the value of ∼3.0 from the interpolation of data reported by Baker et al. for the same type of Toray materials at the same GDL-S compression of 14% (see figure 16 in Ref. 18), which we attribute to uncertainties in cell setup and in compression. For the Freudenberg GDL-S, the τ/ε-ratio of 2.29 obtained by Method B is slightly higher compared to that obtained by Method A (2.18±0.07), but still within the expected accuracy of the method, considering the accuracy with which $\frac{\partial R_{ch}}{\partial p}$ (as required for Method A) can be determined.

In summary, within the accuracy of the measurements, methods A and B yield essentially identical τ/ε-ratios for each of the two GDL-S materials, with roughly 9%-15% higher τ/ε-ratios for the Toray GDL-S. On the other hand, the τ/ε-ratios obtained by Method C differ from those obtained by Methods A and B, and apparently decrease with increasing pressure (see last rows in Table III). Method C is based on the derivative of R_T with the shape factor-corrected GDL-S thickness at a given pressure (see last row in Table II), so that one obtains a τ/ε-ratio for each pressure (115, 150, 200, and 300 kPa_{abs}). For the Toray GDL-S, the τ/ε-ratio decreases from 2.75 at 115 kPa_{abs} to 2.57 at 300 kPa_{abs} (i.e., by ∼6.5%), while this trend is even more pronounced for the Freudenberg material, where the τ/ε-ratio decreases from 3.04 at 115 kPa_{abs} to 2.54 at 300 kPa_{abs} (i.e., by ∼16.4%). It is noticeable that for the Toray GDL-S, the τ/ε-ratio at 300 kPa_{abs} matches the results from Methods A and B; in contrast, the τ/ε-ratio for the Freudenberg GDL-S at 300 kPa_{abs} obtained from Method C (2.49) is still higher than that from Methods A and B (2.18 and 2.29, respectively).

To explain the discrepancy in the τ/ε-ratios obtained from Methods A and B versus Method C, all originating from the same dataset, we will next focus on the transport mechanisms which are included or excluded in Methods A-C: i) Methods A and B contain the derivative of R_T with respect to the pressure, so that the pressure-independent contributions of the oxygen mass transport resistance are not being considered in the evaluation of the τ/ε-ratio; ii) Method C, instead, is based only on the derivative of R_T with respect to the shape factor-corrected GDL-S thickness, only using data at a given constant pressure to determine the τ/ε-ratio, so that pressure-independent effects are included in the analysis according to Method C.

Including Knudsen diffusion in the determination of the τ/ε-ratio.—The total diffusion coefficient of a mixed diffusion problem, where molecular and Knudsen diffusion occur simultaneously can be determined by the Bosanquet equation:

$$D_{theo,mixed} = \left(\frac{1}{D_{theo,Knudsen}(d_p)} + \frac{1}{D_{theo,ONW}(p)} \right)^{-1} \quad [20]$$

Here, the first term on the right-hand side is the theoretical Knudsen coefficient acc. to Eq. 9, which depends on the pore size d_p and is independent of pressure p, while the second term is the pressure-dependent, theoretical molecular diffusion coefficient of the ternary gas mixture acc. to Eqs. 7–8. The contribution ratio $\eta_{Knudsen}$ of the Knudsen diffusion mechanism can then be determined by:

$$\eta_{Knudsen} = \frac{\frac{1}{D_{theo,Knudsen}}}{\frac{1}{D_{theo,mixed}}} \quad [21]$$

Consequently, the contribution ratio $\eta_{molecular}$ of the molecular diffusion is defined as:

$$\eta_{molecular} = \frac{\frac{1}{D_{theo,ONW}}}{\frac{1}{D_{theo,mixed}}} = 1 - \eta_{Knudsen} \quad [22]$$

Figure 5 shows the results for the contribution ratio of Knudsen diffusion (green lines) and molecular diffusion (orange lines; both plotted vs the left y-axis) as a function of pore size at the experimental conditions for the limiting current density measurements conducted at 80 °C/62% RH and 115 kPa_{abs} (solid), 150 kPa_{abs} (dashed), 200 kPa_{abs} (dotted), or 300 kPa_{abs} (dash-dotted). A similar analysis was previously done by Nonoyama et al.[38] Two trends become visible in Fig. 5: (i) the increasing importance of the Knudsen diffusion at small pore diameters, and, (ii) the increasing importance of Knudsen diffusion with decreasing pressures. Figure 5 also shows the MIP results for the Toray TP-060 (blue) and the Freudenberg H14 (gray) GDL-substrates in terms of the log.-differential intrusion as presented in figure 2b (plotted vs the right y-axis). As expected, within the largest pores of the macroporous GDL-substrates, diffusion is mostly governed

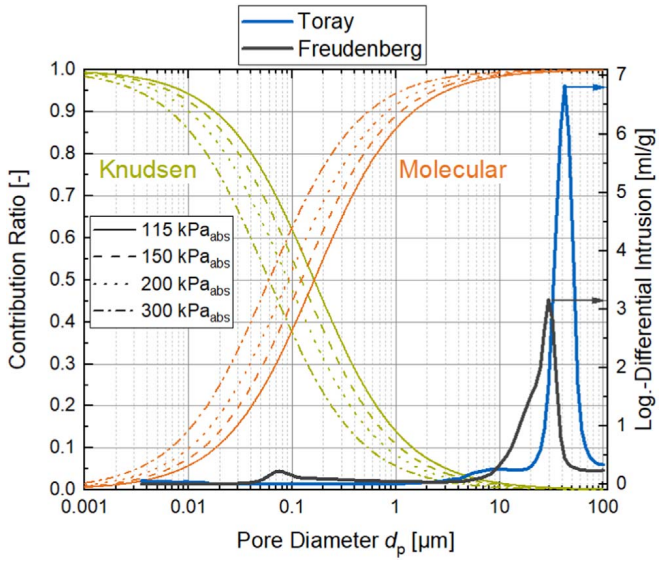

Figure 5. Left *y*-axis: contribution ratio of Knudsen (green) and molecular diffusion (orange) as a function of the pore diameter at the conditions of the limiting current density measurements conducted at 80 °C/62% RH and 115 kPa$_{abs}$ (solid), 150 kPa$_{abs}$ (dashed), 200 kPa$_{abs}$ (dotted), or 300 kPa$_{abs}$ (dash-dotted). The calculation of the contribution ratios was done similarly as by Nonoyama et al.;[38] it is based on Eqs. 20–22, with $D_{theo,Knudsen}$ determined acc. to Eq. 9 and $D_{theo,ONW}$ determined acc. to Eqs. 7–8. Right *y*-axis: MIP pore size distribution of the Toray TP-060 (blue) and the Freudenberg H14 (gray) GDL-S given as log.-differential intrusion (same data as in Fig. 2b).

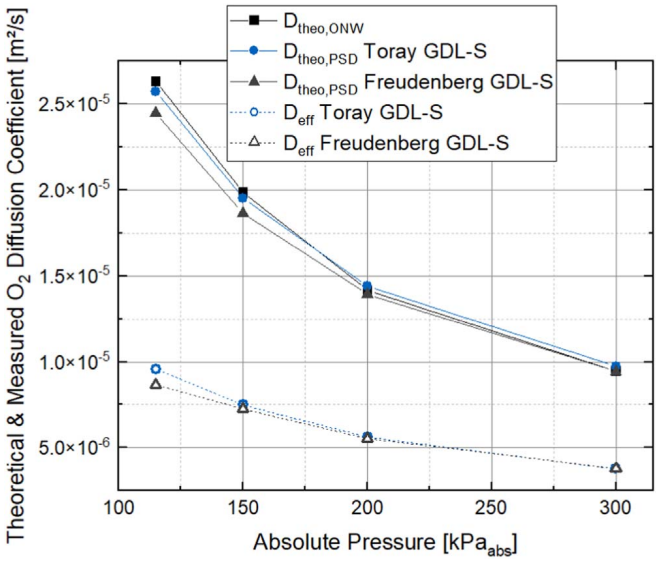

Figure 6. Pressure dependence of the various oxygen diffusion coefficients, determined under the limiting current density measurement conditions of 80 °C/62% RH at four different pressures: i) the theoretical molecular diffusion coefficient $D_{theo,ONW}$ (black solid squares, acc. to Eq. 8); ii) the theoretical mixed diffusion coefficients $D_{theo,PSD}$ (acc. to Eq. 23) derived from the MIP-based pore size distribution (see Fig. 5) for the Toray TP-060 (blue solid circles) and for the Freudenberg H14 (gray solid triangles) GDL-S; iii) the effective diffusion coefficients D_{eff}^{y} obtained from the limiting current density measurements shown in Fig. 4c for the Toray (blue open circles) and the Freudenberg (gray open triangles) GDL-S.

by molecular diffusion. However, at the pore size distribution peak related to carbon black (at ~80 nm) for the Freudenberg GDL-S, there is a roughly equal contribution by Knudsen and molecular diffusion.

In the following part, we will perform a detailed analysis on how to estimate the impact of Knudsen diffusion for the oxygen transport through the GDL-substrates, which mostly contributes in the pores formed by the carbon black in the Freudenberg H14 GDL-S, and we will show how one can include Knudsen diffusion in the determination of the τ/ε-ratio. According to Eq. 1, the τ/ε-ratio describes the ratio of the theoretical diffusivity (D_{theo}) to the effective diffusivity (D_{eff}^{y}). However, the theoretical diffusivity needs to be adapted to the governing diffusion regimes in the various pores available for diffusion, and, depending on the pore size, the diffusional transport can be affected by the pressure. The green-colored lines in Fig. 5 illustrates the significant impact of pressure (115 kPa$_{abs}$ to 300 kPa$_{abs}$) on the contribution ratio of the Knudsen diffusion mechanism ($\eta_{Knudsen}$) in the region of the pore sizes of the carbon black additive in the Freudenberg GDL-S (i.e., at ~80 nm): when increasing the pressure from 115 kPa$_{abs}$ to 300 kPa$_{abs}$, $\eta_{Knudsen}$ at ~80 nm decreases from 66% to 42%.

In the field of heterogeneous catalysis, bimodal pore size distributions are commonly used to describe the diffusion coefficient resulting from Knudsen and molecular diffusion contributions. Wakao et al. developed a model to account for the molecular diffusivity in the larger pores between catalyst pellets and for the Knudsen diffusion within catalyst pellets, which they also validated experimentally.[40] Later, Reyes et al.[41] generalized this theory for any given pore size distribution (PSD), resulting in the following expression:

$$D_{theo,PSD} = \int D_{theo,mixed}(d_p) \cdot f(d_p) \cdot \mathrm{d}d_p \qquad [23]$$

The mixed diffusion coefficient $D_{theo,mixed}(d_p)$ at the pore diameter d_p can be determined according to Eq. 20, combining molecular and Knudsen diffusion. The term $f(d_p)$ weighs the fraction of the total pore volume contained in pores with diameters between d_p and $d_p + \mathrm{d}d_p$. The product of $D_{theo,mixed}(d_p)$ and $f(d_p)$ is then integrated over all pore diameters d_p. In other words, Eq. 23 evaluates the respective diffusivity for each pore size (governed mostly by Knudsen diffusion in smaller pores and mostly by molecular diffusion in larger pores), and weighs the contribution to the overall diffusivity for a given pore diameter with the respective pore volume fraction. The formula considers all pores based on their volume fraction and excludes preferred diffusion pathways. If the pore size distribution was determined from MIP measurements, the possible effect of pore constriction is partially already included, since MIP determines the pore diameter at which the Mercury fills the pore, so that the pore diameter for a bottleneck pore would be the size of the bottleneck. However, there is no directed Mercury intrusion, i.e., Mercury intrudes from all three spatial directions, which is different from the diffusive transport in a fuel cell configuration, where oxygen diffuses from the channel to the electrode.

Figure 6 shows the pressure-dependence of the various calculated theoretical oxygen diffusion coefficients (solid lines) as well as the measured effective oxygen diffusion coefficients for the Toray and the Freudenberg GDL-substrates (dashed lines), which were determined from limiting current density measurements by Method C (see Fig. 4c). The ternary molecular oxygen diffusion coefficient $D_{theo,ONW}$ (O_2 in N_2 and H_2O, black solid squares) calculated from Eqs. 7 and 8 shows an approximately inverse relationship with pressure. A similar trend is observed for the measured effective oxygen diffusion coefficients $D_{eff,}^{y}$ for the Toray (blue open circles) and the Freudenberg (gray open circles) GDL-substrates, with a slightly less pronounced drop of D_{eff}^{y} with increasing pressure for the latter. The origin of this difference may be understood by evaluating the theoretical oxygen diffusion coefficient that is obtained when including Knudsen diffusion effects, namely by examining the pressure dependence of the theoretical mixed diffusion coefficient $D_{theo,PSD}$ that is calculated on the basis of the MIP-derived pore size distribution acc. to Eq. 23; these values are shown in Fig. 6 for the Toray (blue solid circles) and the Freudenberg (gray solid circles)

Table IV. Comparison of the τ/ε-ratios calculated from the data shown in Fig. 4c via Method C (see last row in Table II for the Toray TP-060 and the Freudenberg H14 GDL-S, with D_{theo} being either $D_{theo,ONW}$ (Eqs. 7–8) or $D_{theo,PSD}$ (Eq. 23, based on the PSDs in Fig. 2b). Note that the τ/ε-ratios calculated via $D_{theo,ONW}$ are the same as those listed for Method C in Table III.

	τ/ε-ratio			
	Toray		Freudenberg	
Pressure	via $D_{theo,ONW}$	via $D_{theo,PSD}$	via $D_{theo,ONW}$	via $D_{theo,PSD}$
115 kPa_{abs}	2.75	2.70	3.04	2.83
150 kPa_{abs}	2.65	2.61	2.74	2.58
200 kPa_{abs}	2.62	2.59	2.65	2.52
300 kPa_{abs}	2.57	2.53	2.54	2.45

GDL-substrates. For the Toray GDL-S, $D_{theo,PSD}$ and $D_{theo,ONW}$ are essentially identical, with the former only being slightly smaller at the lowest pressure of 115 kPa_{abs}. On the other hand, for the Freudenberg GDL-S, $D_{theo,PSD}$ is smaller than $D_{theo,ONW}$ at all pressures, whereby this difference increases with decreasing pressure, particularly apparent at the two lowest pressures of 115 kPa_{abs} and 150 kPa_{abs}. This can be ascribed to the increasing contribution from Knudsen diffusion in the small pores of the Freudenberg GDL-S, which are caused by the carbon black additive in this material (see Fig. 2b).

The differences between $D_{theo,ONW}$ and $D_{theo,PSD}$ shown in Fig. 6 result in differences in the τ/ε-ratios determined via Method C, depending on whether D_{theo} in Eq. 16 is taken to be either $D_{theo,ONW}$ (as done for the Method C values in Table III) or $D_{theo,PSD}$. The resulting τ/ε-ratios are shown in Table IV. As one would expect on the basis of Fig. 6, the τ/ε-ratios evaluated via the two different theoretical diffusion coefficients differ most strongly at the lowest pressure of 115 kPa_{abs}, being ~1.8% lower for the $D_{theo,PSD}$-derived values for the Toray GDL-S and ~6.9% lower for the Freudenberg GDL-S (see first row in Table IV). At the highest pressure of 300 kPa_{abs}, this difference is reduced slightly to ~1.6% for the Toray GDL-S and more pronouncedly to ~3.5% for the Freudenberg GDL-S. For the $D_{theo,PSD}$-derived τ/ε-ratios, the resulting values for the Toray GDL-S decrease from 2.70 at 115 kPa_{abs} to 2.53 at 300 kPa_{abs} (i.e., by ~6.3%) and for the Freudenberg GDL-S from 2.83 at 115 kPa_{abs} to 2.45 at 300 kPa_{abs} (i.e., by ~13.4%). When the τ/ε-ratios instead are calculated from the $D_{theo,ONW}$ values, the pressure dependence of the resulting τ/ε-ratios is essentially identical for the Toray GDL-S (~6.5% from 115 to 300 kPa_{abs}) but is significantly higher for the Freudenberg GDL-S (~16.4%). In summary, one can conclude that considering Knudsen diffusion is important when determining τ/ε-ratios, as it reduces the pressure dependence of the resulting τ/ε-ratios, which of course should be pressure-independent. However, even when using $D_{theo,PSD}$ rather than $D_{theo,ONW}$, there still remains a significant pressure dependence of the experimentally determined τ/ε-ratios, which implies that the contribution by Knudsen diffusion may be underestimated when calculated on the basis of the MIP-based pore size and pore volume distribution. This could be explained by assuming that the through-plane oxygen diffusion occurs more through smaller pores (thus increasing Knudsen diffusion effects) due to, e.g., constriction effects. It was shown previously, that the percolation of a porous MPL network is maintained through smaller pores.[42]

From Table IV, it also becomes apparent that the $D_{theo,PSD}$-derived τ/ε-ratios according to Method C are quite similar for the Toray and the Freudenberg GDL-substrates, particularly when comparing the values obtained at 150–300 kP_{aabs}; averaging over all pressures, the τ/ε-ratios are 2.61±0.07 and 2.60±0.17 for the Toray and the Freudenberg GDL-S, respectively. When evaluated by Method A and B, the τ/ε-ratios of the Toray GDL-S (2.49±0.03 and 2.51, respectively; see Table III) are reasonably close to those obtained by Method C. In contrast, however, the τ/ε-ratios of the Freudenberg GDL-S evaluated by Method A and B (2.18±0.07 and 2.29, respectively) are significantly smaller than the values obtained by Method C and would thus be lower than the τ/ε-ratios of the Toray GDL-S. In the following, we will therefore compare the here obtained τ/ε-ratios with literature reports in order both to evaluate whether similar τ/ε-ratios for the two GDL-substrates can be expected and to provide a rationale as to why different τ/ε-ratios are obtained for the Freudenberg GDL-S when the analysis is done by Methods A and B versus by Method C.

As already mentioned earlier (see Introduction section), the Toray material has non-isotropic diffusive properties, namely a higher in-plane diffusivity (D^x) compared to its through-plane diffusivity (D^y), which in turn implies a higher through-plane tortuosity compared to its in-plane tortuosity. This was shown by Xu et al.[17] and Zhang et al.[43] using X-ray tomographic microscopy (XTM) derived GDL-S structures and a subsequent modelling of the tortuosity. In the study by Xu et al., the extracted τ/ε-ratio for a Toray GDL-S varied between 2.8-4.7 in through-plane direction, depending on whether the τ/ε-ratio was evaluated in the channel or in the land region of the flow field, while it varied between 2.5-2.8 in the in-plane direction. In the same study, the τ/ε-ratio for a similar Freudenberg GDL-S ranged between 2.8-3.3, thus falling in between the through-plane and the in-plane τ/ε-ratios of the Toray GDL-S.[17] Similarly, Zhang et al. reported a through-plane τ/ε-ratio of 3.3 and a lower in-plane τ/ε-ratio of 2.0 for the Toray GDL-S, while a similar Freudenberg GDL-S exhibited a τ/ε-ratio of 3 (all values approximately extracted at 0.15 strain).[43] These values may be compared with the here determined τ/ε-ratios derived from limiting current density measurements, where both in-plane and through-plane diffusion occurs simultaneously. For an anisotropic material like the Toray GDL-S, this will result in a τ/ε-ratio that is sort of averaged over the in-plane and the through-plane direction, so that it is not surprising that the thereby determined τ/ε-ratios of ~2.6 (via Method C) for the Toray and the Freudenberg GDL-S are rather similar. The reason why the τ/ε-ratio of the Freudenberg GDL-S determined via Method C using $D_{theo,PSD}$ is higher than that determined via Methods A or B lies in the fact that for the latter the pressure-independent contribution of the oxygen transport resistance is omitted by taking the first derivative with respect to pressure, so that the pressure-independent part of the transport resistance in the GDL-S is not taken into account in the analysis. We believe that Method C with the inclusion of Knudsen diffusion is the most accurate way to determine the τ/ε-ratio for GDL-S especially when measured at increased pressures and thus, the τ/ε-ratio determined at 300 kPa_{abs} of 2.53 for the Toray GDL-S and 2.45 for the Freudenberg GDL- S are chosen to be the most realistic. When using the porosity values of 74% and 67% for Toray and Freudenberg, respectively (see Table I), the tortuosities result in 1.87 for Toray and 1.64 for Freudenberg.

Carbon black distribution in the Freudenberg GDL-S and impact on oxygen diffusion.—Strictly speaking, the τ/ε-ratio determination using the PSD-based diffusion coefficient $D_{theo,PSD}$ would only be valid if no preferential pathway for oxygen transport exists: mass transport occurs statistically through the pores

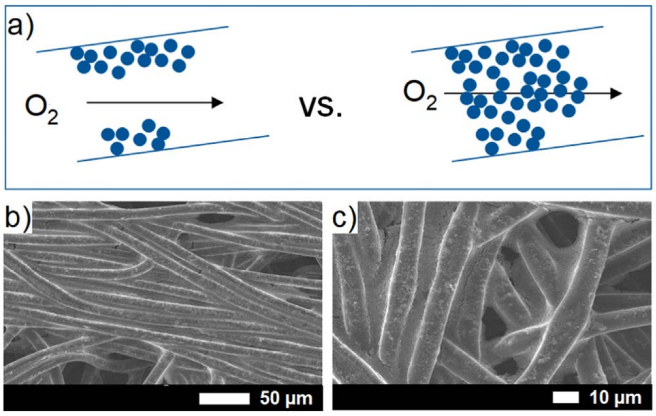

Figure 7. (a) Sketch of different oxygen transport pathways depending on the local distribution of the carbon black additive with respect to the carbon fibers. Left side: situation where the carbon black additive is located predominantly along the perimeter of the carbon fibers, allowing for quasi-unrestricted molecular oxygen diffusion through the large pores between the carbon fibers. Right side: situation where the carbon black additive is blocking an entire cross-section of the large pores between the carbon fibers, so that parts of the oxygen diffusion path are dominated by Knudsen diffusion through the small pores of the carbon black domains. (b) SEM top-view image of the Freudenberg H14 GDL-S at low magnification, showing that the carbon black additive fills the space between adjacent carbon fibers over distances on the order of ~150 µm. (c) Top-view SEM image at a larger magnification, showing more clearly the in part complete filling of the space between carbon fibers by carbon black domains.

according to the presence of that pore diameter within the structure. Figure 7a, where the carbon black additive is essentially coating the carbon fibers, leaving unblocked large pores in between the fibers, only reducing the average diameter of the large pores, shows a scenario, where a preferred pathway for mass transport exists: oxygen can travel through the large pores avoiding the additional transport resistance from the smaller pores of the carbon black. On the other hand, one can also imagine a scenario, where the carbon black domains are blocking an entire cross section of the oxygen pathways in the large pores, which is shown on the right side of Fig. 7a; in this case, oxygen diffusing through the large pores must intermittently diffuse through the carbon black domains, in which oxygen diffusion is slowed down by Knudsen diffusion. The effect of the Knudsen diffusion in the carbon black in the Freudenberg material would only be as significant, if the pores of the carbon black are used for oxygen transport. The contribution in the PSD-based diffusion coefficient is scaled with the volume fraction of the small pores in the carbon black domain with respect to the overall pore volume.

Thus, if our theory was valid, there must be a significant proportion of the carbon black situated as described on the right side of the sketch. Figures 7b and 7c show SEM top view images, where many adjacent fibers are covered with carbon black. Figure 7b, taken at a low magnification, shows that the carbon fibers are not only covered by the carbon black additive, but that significant parts of the space between adjacent carbon fibers are filled with a carbon black domain, over distances along the fibers that are on the order of 150 µm. At a higher magnification (see Fig. 7c), it can be confirmed that the carbon black domains indeed span across the entire distance between adjacent fibers. Albeit qualitatively, this indicates a morphology that is close to that shown on the right side of Fig. 7a, suggesting that a significant portion of oxygen needs to diffuse through carbon black domains, as they block parts of the direct diffusion pathways through the large pores of the GDL-S. This blockage of pores with carbon black, we believe, is the origin of the apparently higher Knudsen diffusion contribution than what is considered in the evaluation of $D_{\text{theo,PSD}}$, consistent also with the more constant τ/ε-ratio at higher pressures (see Table IV).

Application of Method C to determine the τ/ε-ratio of an MPL.—After having established the importance of including Knudsen diffusion contributions when determining the τ/ε-ratio from limiting current density measurements, we will next apply Method C to quantify the τ/ε-ratio of an MPL. For this, we applied MPL coatings based on vapor grown carbon fibers (VGCF) with different thicknesses on the Freudenberg H14 GDL-S, varying the MPL thickness between 30–140 µm and determining the τ/ε-ratio by Method C (see Table II).

Figure 8a shows the MIP-based pore size distribution of a free-standing VGCF MPL (brown line), showing a pore size distribution maximum at 880 nm, which is ~20% larger than the 720 nm reported by Simon et al.[24] for an analogously prepared VGCF-based MPL. This difference is ascribed to the different sample preparation for the MIP measurement, which affects the measured pore size: we recently discovered that the stacking of porous media in the MIP sample vial alters the measured pore size distribution, as additional volume is created between the layers. In terms of porosity, the value of 82% determined from the data in Fig. 8a is essentially identical with that measured by Simon et al. (83%).[24] Figure 8a also shows the theoretical contribution ratio of Knudsen and molecular diffusion versus pore diameter (green and orange lines; same as those depicted in Fig. 5a), indicating that molecular diffusion dominates at the peak pore diameter of 880 nm, with the molecular contribution ratio increasing from 84% at 115 kP_{abs} to 94% at 300 kPa_{abs}. However, a substantial amount of pore volume is present in pores that are smaller than the PSD maximum, and for these pores the molecular contribution ratio is substantially lower. For example, at a pore size of 500 nm, Knudsen diffusion contributes by 25% to the overall diffusion at a pressure of 115 kPa_{abs}. Therefore, since 20% of the pore volume is contained in pores of $\leqslant$ 500 nm, Knudsen diffusion needs to be included to describe the overall diffusion process in the VGCF-based MPL, using the approach described by Eq. 23.

To extract the effective oxygen diffusivity in the MPL, the dry-region oxygen transport resistance as a function of the MPL thickness was determined at different pressures, which is shown in Fig. 8b. As the MPL is not immediately in contact with the flow field, Baker et al. have simplified Eq. 16 and the resulting correlation is given in Eq. 24.[18]

$$\left(\frac{\tau}{\varepsilon}\right)_{\text{MPL}} = \frac{D_{\text{theo(MPL)}}}{D^{\text{y}}_{\text{eff(MPL)}}} = D_{\text{theo(MPL)}} \cdot \frac{\partial R_{\text{MPL}}}{\partial t_{\text{MPL}}} \qquad [24]$$

Here, $D_{\text{theo(MPL)}}$ and $D^{\text{y}}_{\text{eff(MPL)}}$ only refer to the oxygen diffusion coefficients in the MPL part of the GDL-S/MPL assembly with which the measurements were conducted. Since we assume that only R_{MPL} changes with MPL thickness, the derivative of R_{T} with respect to the MPL thickness t_{MPL} (see Fig. 8b) can be evaluated.

Figure 8b displays the dry-region oxygen transport resistance for different MPL thicknesses at the various pressures (115 kPa_{abs}, 150 kPa_{abs}, 200 kPa_{abs}, and 300 kPa_{abs}). For each pressure, the dry-region transport resistance increases linearly with MPL thickness and the slope of each line corresponds to the inverse of the effective diffusivity in the MPL, $D^{\text{y}}_{\text{eff(MPL)}}$ (see Eq. 24), whose values at the different pressures are depicted by the brown open triangles in Fig. 8c. According to Eq. 24, the value of the theoretical diffusion coefficient in the MPL phase ($D_{\text{theo(MPL)}}$) is required to determine the τ/ε-ratio of the MPL. Owing to the significant Knudsen diffusion contribution in the small pores of the MPL (see Fig. 8a), $D_{\text{theo(MPL)}}$ must be approximated with the theoretical mixed diffusion coefficient determined from the MPL pore size distribution in Fig. 8a and Eq. 23, $D_{\text{theo(MPL),PSD}}$, whose pressure-dependent values are depicted by the brown solid circles in Fig. 8c. These values can also be compared with the molecular diffusion coefficient $D_{\text{theo,ONW}}$ under the same conditions, which are depicted by the black solid squares (identical with the $D_{\text{theo,ONW}}$ values shown in Fig. 6). Owing to the significant Knudsen diffusion contributions in the small pores of the

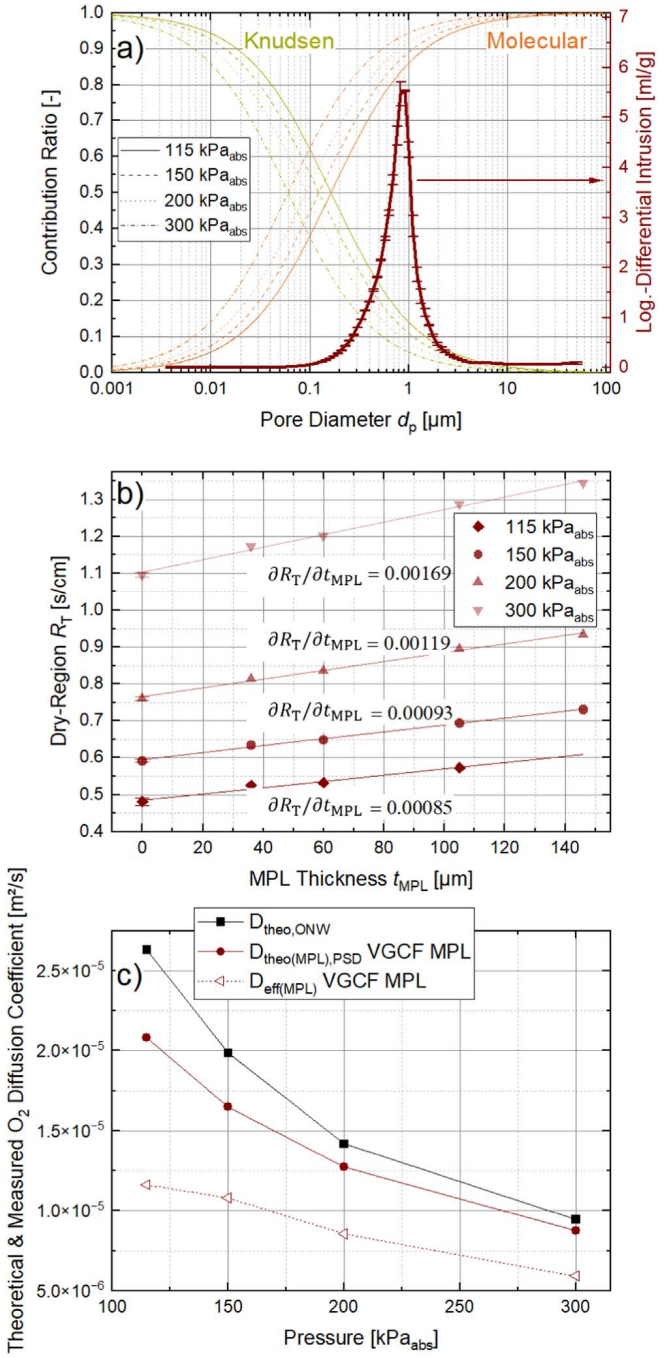

Figure 8. (a) Left *y*-axis: contribution ratio of Knudsen (green) and molecular diffusion (orange) as a function of the pore diameter at the conditions of the limiting current density measurements conducted at 80 °C/62% RH and 115 kPa$_{abs}$ (solid), 150 kPa$_{abs}$ (dashed), 200 kPa$_{abs}$ (dotted), or 300 kPa$_{abs}$ (dash-dotted); these are identical with the lines shown in Fig. 5. Right *y*-axis: MIP-based log.-differential pore size distribution of the VGCF MPL, measured with freestanding MPL layers. (b) Dry-region oxygen transport resistance over the MPL thickness for VGCF-based MPLs coated onto the Freudenberg H14 GDL-S at the above specified conditions. c) Pressure dependence of the various oxygen diffusion coefficients, determined under the above conditions: (i) the theoretical molecular diffusion coefficient $D_{theo,ONW}$ (black solid squares, acc. to Eqs. 7–8); (ii) the theoretical mixed diffusion coefficients $D_{theo(MPL),PSD}$ (acc. to Eq. 23) derived from the pore size distribution shown in panel a for the VGCF-based MPL (brown solid circles); iii) the effective diffusion coefficients $D^{y}_{eff(MPL)}$ of the VGCF-based MPL obtained from the slope of the regression lines in panel b (brown open triangles).

Table V. Comparison of the τ/ε-ratio calculated from the data shown in Fig. 8 via Method C (see last row in Table II) for the VGCF-based MPL coated onto the Freudenberg H14 GDL-S, with D_{theo} being either $D_{theo,ONW}$ (Eq. 8) or $D_{theo(MPL),PSD}$ (Eq. 23, based on the PSDs in Fig. 8a).

	τ/ε-ratio	
	VGCF-MPL	
Pressure	via $D_{theo,ONW}$	via $D_{theo(MPL),PSD}$
115 kPa$_{abs}$	2.26	1.79
150 kPa$_{abs}$	1.84	1.53
200 kPa$_{abs}$	1.72	1.49
300 kPa$_{abs}$	1.63	1.48

MPL, the $D_{theo(MPL),PSD}$ values are significantly smaller than the $D_{theo,ONW}$ values, particularly at the lower pressures; this is in stark contrast to the very minor differences between $D_{theo,ONW}$ and $D_{theo,PSD}$ in case of the large-pore GDL-substrates (see Fig. 6).

The τ/ε-ratios calculated from the measured $D^{y}_{eff(MPL)}$ values via Eq. 24, using either $D_{theo,ONW}$ or $D_{theo(MPL),PSD}$ as the theoretical diffusion coefficient ($D_{theo(MPL)}$) are summarized in Table V.

For the $D_{theo,ONW}$-derived τ/ε-ratios, the resulting values decrease from 2.26 at 115 kPa$_{abs}$ to 1.63 at 300 kPa$_{abs}$ (i.e., by ∼28%), even though τ/ε-ratios should be a pressure-independent materials property. This pressure-dependence is substantially reduced for the $D_{theo(MPL),PSD}$-derived τ/ε-ratios, which decrease from 1.79 at 115 kPa$_{abs}$ to 1.48 at 300 kPa$_{abs}$ (i.e., by ∼17%); in fact, only the τ/ε-ratio at the lowest pressure of 115 kPa$_{abs}$ deviates significantly from the values at the higher pressures (150 kPa$_{abs}$-300 kPa$_{abs}$). Averaging the $D_{theo(MPL),PSD}$-derived τ/ε-ratios over all four pressures yields $\tau/\varepsilon = 1.57\pm0.15$, while averaging over the highest three pressures yields $\tau/\varepsilon = 1.50\pm0.03$; for an MPL porosity of $\varepsilon = 0.82$, these τ/ε-ratios correspond to $\tau = 1.29\pm0.12$ (averaged over all four pressures) and $= 1.23\pm0.02$ (averaged over the highest three pressures). These values are slightly higher, yet considering measurement uncertainties in good agreement with the tortuosity of $\tau = 1.16$, than those reported for the VGCF-MPL by Bozzetti et al. using a structure determination.[42]

Discussion

The τ/ε-ratio has been measured in the literature by different techniques. Most of them use ex situ approaches, which do not have to consider the 2D diffusional transport that occurs in a PEM fuel cell due to the channel/land geometry of the flow field. The technique of this study on the other hand offers the in situ analysis of the diffusive transport in a fuel cell with actual flow field geometry using a correction factor for the 2D diffusional transport f as introduced by Baker et al.[18] In addition to the two methods proposed by Baker et al.[18] (here referred to as Method A and B), we have introduced a third approach (viz., Method C) to determine the τ/ε-ratio. While Methods A and B only include the pressure-dependent transport resistances, Method C allows an analysis of both, the pressure-dependent and the pressure-independent oxygen transport. In terms of diffusion mechanisms, Method C considers both molecular and Knudsen diffusion by utilizing the mixed oxygen diffusion coefficient determined from the pore size distribution of the porous medium ($D_{theo,PSD}$). Even though Knudsen diffusion is a pressure-independent phenomenon, the mean free path is highly pressure-dependent. Therefore, the pore size below of which Knudsen diffusion occurs as well as the contribution of Knudsen

diffusion to the overall diffusion for a given pore size changes with pressure (see Fig. 5).

While we believe that Method C can give the most accurate results for the τ/ε-ratio as molecular and Knudsen diffusion are considered, Methods A and B can be utilized for materials which only have large pores such as a Toray GDL-S. When small pores are present (for the pressure regime tested here: $<10\,\mu m$), Methods A and B underestimate the τ/ε-ratio, as they do not include the Knudsen diffusion effects in small pores, and thus Method C should be applied. The drawback of Method C is that prior knowledge of the pore size distribution is required. Most methods to determine the pore size distribution are limited to certain pore size regimes. For example, gas physisorption measurements can only resolve small pores (<100 nm), while X-ray tomographic imaging (even synchrotron based) is limited in resolution to $\sim$0.3–2.5 μm.[9,44,45] To assess a large range of pore diameters, only ex situ Mercury intrusion porosimetry is suitable. Here it should be noted, however, that standard MIP setups do not allow to measure the pore size distribution under compression, which can only be done with a special setup as suggested by Yoshimune et al.[46] However, we believe that MIP-based PSDs measured in the absence of compression still gives relevant information regarding the diffusion regimes in GDL-substrates and MPLs. This is supported, for example, by the report by Zenyuk et al., who showed that the pore size distribution of a Freudenberg GDL-S does not change significantly upon compression (in a range that is relevant for PEM fuel cells) and that it mostly results in a reduction in pore volume.

Even when the pore size distribution of a GDL-substrate is not known, it is possible to use Methods A, B, and C with the molecular diffusion coefficient ($D_{theo,ONW}$) when limiting current density measurements are conducted at high pressures. For example, comparing the τ/ε-ratios determined via Method C at 300 kPa_{abs} for the Toray and the Freudenberg GDL-S, the $D_{theo,ONW}$-derived values are only $\sim$1.5% (Toray) and $\sim$3.7% (Freudenberg) higher than the $D_{theo,PSD}$-derived values (see Table IV). For the VGCF-based MPL with its substantially smaller pores, this difference increases to $\sim$10% (see Table V), owing to the more significant Knudsen diffusion effects in smaller pores. Therefore, even higher differences would be expected for carbon black based MPLs, whose pore size distribution is shifted to substantially smaller pore sizes.[23]

When determining the τ/ε-ratio for the MPL, Method C contains three main sources of error. The first source is the compressibility of the MPL. Depending on the ratio of compressibility between the GDL-S and the MPL, the compression of the GDL-S and the MPL might differ depending on the MPL thickness. As the force between the flow field and the GDL-S was kept roughly constant for our limiting current measurements, according to pressure paper tests, the GDL-S and the MPL act as two springs in series. MPL and GDL-S might not compress in the same way as the thickness of the MPL changes. However, we believe that this impact is small. Atkinson et al. have analyzed the thickness ratio between the MPL and the GDL-S under different compression forces for a commercial H2315.[47] In their case, MPL and GDL-S compressed in a similar way and the thickness ratio stayed constant. Therefore, we expect that the differences between GDL and MPL compressibility are little.

The second source of error is the change of form factor with increasing overall GDL-S/MPL thickness, which varied from $\sim$180 μm including a 30 μm MPL to $\sim$300 μm including a 150 μm MPL), which equates to a decrease of the form factor from 1.52 to 1.35. This decrease means that the adjusted diffusion length becomes closer to the actual GDL-S/MPL thickness, as the thickness correction term accounting for the channel-land geometry is decreased. This difference in form factor changes mostly the dry diffusion length of the GDL-S, as it faces the flow field directly: its diffusion length is lowered by the form factor correction with a thicker MPL on top, which would cause a lowered dry-region transport resistance. In principle, this change in form factor can be corrected for mathematically. However, estimating the exact influence of the change in diffusion length of the GDL-S and the MPL in the bilayer is beyond the scope of this work.

The third source of error stems from neglecting the thermal conductivity of the GDL-S and the MPLs. While the impact of temperature gradients was discussed in the context of Fig. 3, where an increase of the temperature of the MEA with increasing current density can be deduced from the increase of the HFR, we have not considered the concomitant temperature distribution across the different anode and cathode GDLs, which is beyond the scope of this work.

Conclusions

In this study, we have determined the τ/ε-ratio of two GDL-substrates and of an MPL by a careful consideration of the relevant diffusion regimes. As a basis, we utilized the theory of diffusion in an operating fuel cell and the mass transport resistances of the different components as developed by Baker et al.[18] Applying their equations to different GDL-substrates with or without MPL types necessitates to consider both molecular and Knudsen diffusion. The original definition of the τ/ε-ratio as the ratio of the theoretical molecular diffusivity over the effective diffusivity does not correctly describe the physical phenomena in porous structures with a wide range of pores, where both diffusion mechanism occur simultaneously.

We have tested two different GDL-substrates with a similar structure, both containing a large fraction of the pore volume in pores $>10\,\mu m$. However, the Freudenberg H14 GDL-S contained additional small pores ($\sim$80 nm) originating from the carbon black additive that is added during its manufacturing. The results of our analysis of limiting current measurements at different pressures clearly showed that there is a significant contribution from Knudsen diffusion to the overall oxygen diffusion through the Freudenberg GDL-S. As the two methods used in the literature to determine the τ/ε-ratio from limiting current density measurements in a PEM fuel cell only use the molecular diffusion coefficient (here referred to as Methods A and B), we proposed a new method that allows to account for Knudsen diffusion contributions (here referred to as Method C). For this, the contribution ratio of Knudsen and molecular diffusion was weighed proportional to the pore size distribution, yielding a mixed diffusion coefficient based on the pore size distribution (PSD) in the porous medium ($D_{theo,PSD}$), which was determined by Mercury intrusion porosimetry (MIP). Using $D_{theo,PSD}$ for the determination of the τ/ε-ratio, we were able to reduce the non-physical pressure-dependence of the structure-dependent τ/ε-ratio. However, the thus determined τ/ε-ratios still decrease as the limiting current density measurement pressure increases, which shows that the contribution of Knudsen diffusion is larger than what we have estimated from the MIP-based pore size distribution. This underestimation of the Knudsen diffusion contribution could be understood when regarding the distribution of the carbon black domains in the Freudenberg GDL-S, where the carbon black domains block large areas between the carbon fibers, so that the oxygen transport is partially forced to proceed through the small pores of the carbon black domains. Including both Knudsen and molecular diffusion in Method C in the analysis for the Toray and the Freudenberg GDL-S resulted in approximately the same τ/ε-ratio of 2.5 translating in tortuosities τ of 1.87 and 1.64 for Toray and Freudenberg, respectively.

Method C developed for the GDL-substrates could be easily transferred to determine the τ/ε-ratio of an MPL, for which contribution of Knudsen diffusion cannot be neglected, owing to the small pore sizes. The evaluation of limiting current measurements again underlined the importance of including Knudsen diffusion. It was found that the τ/ε-ratio is smaller for the MPL structure ($\tau/\varepsilon = 1.5$) than for the GDL-S structure ($\tau/\varepsilon = 2.5$). Translated into tortuosities, the τ for the MPL structure resulted in 1.23 and for the GDL-S τ was between 1.64 (Freudenberg) and 1.87 (Toray).

This work also emphasizes the impact of the resistance in the flow field channels (R_{ch}) to the overall oxygen transport resistance.

As different GDL-substrates with different physical properties might penetrate to a different extent into the flow field channels, the channel resistance is subject to change. Thus, an experimental determination is preferred.

Finally, we developed a strategy, which method to quantify the τ/ε-ratio should be applied, depending on the material: when no small pores are present (such as for a Toray GDL-S) and thus the contribution of Knudsen diffusion is minor, Methods A, B, and C can be applied using the molecular diffusion coefficient. When materials are used which contain smaller pores (such as the Freudenberg GDL-S or an MPL) and thus Knudsen diffusion is important, Method C should be applied, ideally using the PSD-based diffusion coefficient. If the PSD is not known and therefore the determination of the PSD-based diffusion coefficient is not possible, the limiting current dataset at the higher pressure (in our case 300 kPa_{abs}) can give a reasonably accurate estimation of the τ/ε-ratio.

Acknowledgments

We gratefully acknowledge funding from the Swiss National Foundation under the funding scheme Sinergia (project grant number 180335). Furthermore, we are grateful for the materials provided free-of-charge by 3 M Dyneon, Germany (TF 5035GZ PTFE dispersion). The authors would like to express their gratitude for very valuable input from Daniel R. Baker. We additionally thank Davide Menga and Timon Lazaridis for conducting the Kr-physisorption measurements.

Appendix

This section displays a further analysis of the dataset presented in Fig. 4 justifying that a difference in channel resistance can be expected between the Freudenberg and Toray material due to the different penetration into the flow channels. Hoppe et al. have measured the penetration of a Freudenberg based GDL (H23C2) and a Toray GDL-S (TGP-H-060) into a 0.8 mm or a 1 mm wide channel.[39] While the Freudenberg GDL at 14% compression penetrated ~40 μm into a 1 mm wide channel, the Toray GDL-S at 15% compression intruded only ~15 μm into a 1 mm wide channel. A higher penetration into the channel reduces the depth of the channel s.

Figure 4c shows the dry transport resistance over the corrected thickness fh. When extrapolating the line to 0 thickness, the contribution of the GDL resistance is subtracted. When regarding Eq. 3 resulting $R_T - R_{GDL}$ equals the channel resistance R_{ch} and the other contributions to the transport resistance R_{other}. We assume that R_{other} mostly comprises the transport resistance of the electrode, which due to the small pore size, can be considered mostly pressure independent. Rearranging Eq. 3 leads to the following expression.

$$R_T - R_{GDL} = R_{ch} + R_{other} \quad [25]$$

In the following, we will examine Eq. 25 to understand which parameters contribute. According to Baker et al.,[18] the channel resistance can be written out as:

$$R_{ch} = A_{ch}\frac{e}{D_{theo,ONW}} + B_{ch}\frac{2NsL}{Q_{dry}}\frac{273}{T}\frac{p - p_W}{p_{ref}} \quad [26]$$

Baker et al. further elaborate that using the definition for the overall molecular diffusion coefficient $D_{theo,ONW}$ as a function of the binary diffusion coefficients $D_{theo,ON}$ and $D_{theo,OW}$ and the total pressure p and the water vapor pressure p_W (Eq. 27), the Eq. for R_{ch} can be rewritten (Eq. 28).

$$\frac{1}{D_{theo,ONW}} = \frac{1}{pD_{theo,ON}}\left[p + p_W\left(\frac{D_{theo,ON}}{D_{theo,OW}} - 1\right)\right] \quad [27]$$

$$R_{ch} = A_{ch}\cdot e\cdot\frac{1}{pD_{theo,ON}}\left[p + p_W\left(\frac{D_{theo,ON}}{D_{theo,OW}} - 1\right)\right] + B_{ch}\frac{2NsL}{Q_{dry}}\frac{273}{T}\frac{p - p_W}{p_{ref}} \quad [28]$$

We would like to simplify Eq. 28 substitute $p - p_W$ by x ($x = p - p_W$).

$$R_{ch} = A_{ch}\cdot e\left(\frac{1}{pD_{theo,ON}}\left[x + p_W\frac{D_{theo,ON}}{D_{theo,OW}}\right] + B_{ch}\frac{2NsL}{Q_{dry}}\frac{273}{T}\frac{x}{p_{ref}}\right) \quad [29]$$

By treating the terms $pD_{theo,ON}$ and $\frac{D_{theo,ON}}{D_{theo,OW}}$ as a unity, which is not a function of p, the derivative of Eq. 29 with respect to the pressure or in our case with respect to x results in:

$$\frac{\partial R_{ch}}{\partial p} = \frac{\partial R_{ch}}{\partial x} = A_{ch}\frac{e}{pD_{theo,ON}} + B_{ch}\frac{2NsL}{Q_{dry}}\frac{273}{p_{ref}}\frac{273}{T} \quad [30]$$

Combining Eqs. 25 and 30 results in:

$$R_T - R_{GDL} = A_{ch}\cdot e\left(\frac{1}{pD_{theo,ON}} \times \left[x + p_W\frac{D_{theo,ON}}{D_{theo,OW}}\right] + B_{ch}\frac{2NsL}{Q_{dry}}\frac{273}{T}\frac{x}{p_{ref}}\right) + R_{other} \quad [31]$$

Consequently, when plotting $R_T - R_{GDL}$ as extracted as the extrapolation to $fh = 0$ in Fig. 4c as a function of $x = p - p_W$, it results as a linear Eq. with a y-intercept and a slope as defined in Eqs. 32 and 33.

$$y_{intercept} = R_{other} + \frac{A_{ch}e}{pD_{theo,ON}}\quad p_W\frac{D_{theo,ON}}{D_{theo,OW}} \quad [32]$$

$$\text{slope} = \frac{\partial R_{ch}}{\partial p} = f(\text{channel intrusion depth}) \quad [33]$$

Thus, the term $R_T - R_{GDL}$ was plotted over $x = p - p_W$ in Fig. A1 for the Toray (blue) and the Freudenberg GDL-S (gray). It can be

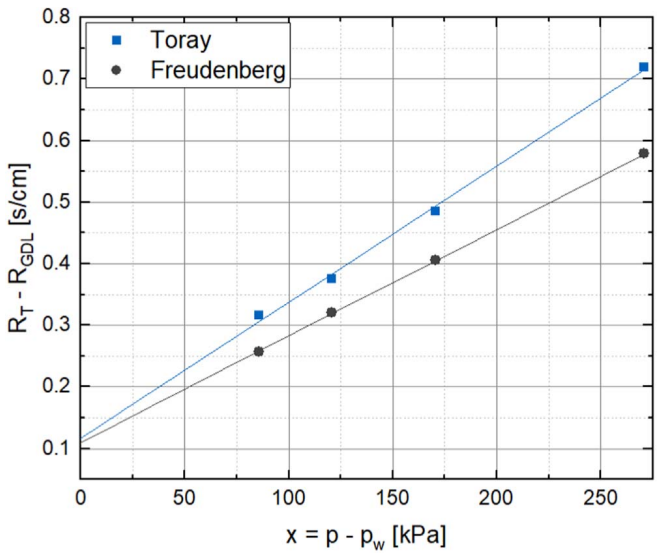

Figure A1. $R_T - R_{GDL}$ over $x = p - p_W$ for the Toray TP-060 (blue) and the Freudenberg H14 (gray) GDL-S: at $p - p_W = 0$ both linear approximations converge to the same constant value.

observed that a linear fit through the data points converges to the same value. According to Eq. $y_{intercept} = R_{other} + \frac{A_{ch}e}{pD_{theo,ON}} p_W \frac{D_{theo,ON}}{D_{theo,OW}}$ [32, the y-intercept consist partially of R_{other}, which comprises mostly the transport resistance of the electrode. The second term comes from the pressure independent influence of the water vapor pressure of the channel resistance as p_W does not change with pressure. The slope is influenced by many parameters. Parameters of the measurement or the setup (N, L, Q_{dry}, T, $D_{theo,AB}$) are constant for both materials. However, the channel depth s is a function of the channel intrusion depth. The higher the slope, the higher s, and thus the lower is the channel intrusion. As the slope for the Toray material is larger than for the Freudenberg material, the explanation with the intrusion depth of the material into the channel seems to fit the results from Hoppe.[39]

ORCID

Anne Berger https://orcid.org/0000-0003-3230-4730
Christoph Simon https://orcid.org/0000-0002-2381-7641
Hubert A. Gasteiger https://orcid.org/0000-0001-8199-8703

References

1. European Parliament Press Release, (14.2.2023), https://www.europarl.europa.eu/news/en/press-room/20230210IPR74715/fit-for-55-zero-co2-emissions-for-new-cars-and-vans-in-2035, accessed January 18, 2025.
2. P. Atanassov, V. D. Noto, and S. McPhail, *Electrochem. Soc. Interface*, **30**, 57 (2021).
3. Executive Department State of California, (23.9.2020)Exec. Ord. No. N-79-20, 3 C.F.R..
4. R. Borup, T. Krause, and J. Brouwer, *Electrochem. Soc. Interface*, **30**, 79 (2021).
5. T. Yoshizumi, H. Kubo, and M. Okumura, *SAE Technical Paper*, **2021- 01-0740** 6 (2021).
6. W. Yoshimune, S. Kato, M. Inagaki, and S. Yamaguchi, *Int. J. Heat Mass Transf.*, **191**, 122887 (2022).
7. D. Kramer, S. A. Freunberger, R. Flückiger, I. A. Schneider, A. Wokaun, F. N. Büchi, and G. G. Scherer, *J. Electroanal. Chem.*, **612**, 63 (2008).
8. R. Flückiger, S. A. Freunberger, D. Kramer, A. Wokaun, G. G. Scherer, and F. N. Büchi, *Electrochim. Acta*, **54**, 551 (2008).
9. I. V. Zenyuk, D. Y. Parkinson, L. G. Connolly, and A. Z. Weber, *J. Power Sources*, **328**, 364 (2016).
10. D. A. G. Bruggeman, *Ann. Phys.*, **416**, 636 (1935).
11. B. Tjaden, S. J. Cooper, D. J. L. Brett, D. Kramer, and P. R. Shearing, *Curr. Opin. Chem. Eng.*, **12**, 44 (2016).
12. M. M. Tomadakis and S. V. Sotirchos, *AlChE J.*, **39**, 397 (1993).
13. P. A. García-Salaberri, G. Hwang, M. Vera, A. Z. Weber, and J. T. Gostick, *Int. J. Heat Mass Transf.*, **86**, 319 (2015).
14. L. Chen, G. Wu, E. F. Holby, P. Zelenay, W-Q. Tao, and Q. Kang, *Electrochim. Acta*, **158**, 175 (2015).
15. A. Berson, H-W. Choi, and J. G. Pharoah, *Phys. Rev. E*, **83**, 026310 (2011).
16. G. Inoue, K. Yokoyama, J. Ooyama, T. Terao, T. Tokunaga, N. Kubo, and M. Kawase, *J. Power Sources*, **327**, 610 (2016).
17. H. Xu, M. Bührer, F. Marone, T. J. Schmidt, F. N. Büchi, and J. Eller, *J. Electrochem. Soc.*, **168**, 074505 (2021).
18. D. R. Baker, D. A. Caulk, K. C. Neyerlin, and M. W. Murphy, *J. Electrochem. Soc.*, **156**"B."991 (2009).
19. R. B. Bird, W. E. Stewart, and E. N. Lightfoot, *Transport Phenomena* (New York)(Wiley) (2006).
20. National Institute of Standards and Technology, *Phase change data in NIST Chemistry WebBook*, ed. P. J. Linstrom and W. G. Mallard (2024), https://webbook.nist.gov/chemistry/.
21. R. R. Rashapov, J. Unno, and J. T. Gostick, *J. Electrochem. Soc.*, **162**, F603 (2015).
22. F. Du et al., *J. Electrochem. Soc.*, **167**, 144513 (2020).
23. C. Simon, D. Kartouzian, D. Müller, F. Wilhelm, and H. A. Gasteiger, *J. Electrochem. Soc.*, **164**, F1697 (2017).
24. C. Simon, J. Endres, B. Nefzger-Loders, F. Wilhelm, and H. A. Gasteiger, *J. Electrochem. Soc.*, **166**"F."1022 (2019).
25. M. F. Mathias, J. Roth, J. Fleming, and W. Lehnert, *Handbook of Fuel Cells* Vol. 3, ed. W. Vielstich et al. (New York)(Wiley)517 (2010).
26. K-D. Wagner, A. Bock, K. Salama, and A. Weller, United StatesUS 2010/0219069 A1 (2010), Carl Freudenberg KG.
27. G.-G. Park, Y.-J. Sohn, T.-H. Yang, Y.-G. Yoon, W.-Y. Lee, and C.-S. Kim, *J. Power Sources*, **131**, 182 (2004).
28. J. Lobato, P. Cañizares, M. A. Rodrigo, C. Ruiz-López, and J. J. Linares, *J. Appl. Electrochem.*, **38**, 793 (2008).
29. N. Zamel, N. G. C. Astrath, X. Li, J. Shen, J. Zhou, F. B. G. Astrath, H. Wang, and Z-S. Liu, *Chem. Eng. Sci.*, **65**, 931 (2010).
30. L. Jabbour, C. Robin, F. Nandjou, R. Vincent, F. Micoud, J.-P. Poirot-Crouvezier, J. d'Arbigny, and M. Gerard, *J. Power Sources*, **299**, 380 (2015).
31. S. Oswald, *PhD thesis, Technical University of Munich* (2003), https://mediatum.ub.tum.de/doc/1692784/1692784.pdf accessed 6.6.2024.
32. R. K. F. Della Bella, B. M. Stühmeier, and H. A. Gasteiger, *J. Electrochem. Soc.*, **169**, 044528 (2022).
33. J. P. Owejan, J. E. Owejan, and W. Gu, *J. Electrochem. Soc.*, **160**, F824 (2013).
34. C. Simon, *PhD thesis, chapter 2.2, Technical University of Munich* (2020), https://mediatum.ub.tum.de/1534439 accessed 10.8.2024.
35. J. P. Owejan, J. E. Owejan, W. Gu, T. A. Trabold, T. W. Tighe, and M. F. Mathias, *J. Electrochem. Soc.*, **157**, B1456 (2010).
36. D. A. Caulk and D. R. Baker, *J. Electrochem. Soc.*, **157**, B1237 (2010).
37. K. C. Neyerlin, W. Gu, J. Jorne, A. Clark, and H. A. Gasteiger, *J. Electrochem. Soc.*, **154**, B279 (2007).
38. N. Nonoyama, S. Okazaki, A. Z. Weber, Y. Ikogi, and T. Yoshida, *J. Electrochem. Soc.*, **158**, B416 (2011).
39. E. Hoppe, *PhD thesis, RWTH Aachen* (2021), https://publications.rwth-aachen.de/record/820141, accessed 10.8.2024.
40. N. Wakao and J. M. Smith, *Chem. Eng. Sci.*, **17**, 825 (1962).
41. S. Reyes, E. Iglesia, and K. F. Jensen, *Solid State Ion.*, **32-33**, 833 (1989).
42. M. Bozzetti, A. Berger, R. Girod, Y.-C. Chen, F. N. Büchi, H. A. Gasteiger, and V. Tileli, *Chem. Commun.*, **58**, 8854 (2022).
43. H. Zhang, L. Zhu, H. B. Harandi, K. Duan, R. Zeis, P-C. Sui, and P. Y. A. Chuang, *Energy Convers. Manag.*, **241**, 114293 (2021).
44. Y-C. Chen, A. Berger, S. De Angelis, T. Schuler, M. Bozzetti, J. Eller, V. Tileli, T. J. Schmidt, and F. N. Büchi, *ACS Appl. Mater. Interfaces*, **13**, 16227 (2021).
45. Y. Nagai, J. Eller, T. Hatanaka, S. Yamaguchi, S. Kato, A. Kato, F. Marone, H. Xu, and F. N. Büchi, *J. Power Sources*, **435**, 226809 (2019).
46. W. Yoshimune, S. Kato, and S. Yamaguchi, *Int. J. Heat Mass Transf.*, **152**, 119537 (2020).
47. R. W. Atkinson III, Y. Garsany, B. D. Gould, K. E. Swider-Lyons, and I. V. Zenyuk, *ACS Appl. Energy Mater.*, **1**, 191 (2018).

4.2 Analysis of the Structural Parameters and the Water Filling Mechanism of the Porous Network of Microporous Layers

The article “Analysis of the Structural Parameters and the Water Filling Mechanism of the Porous Network of Microporous Layers“ was submitted in 10.10.2024 and accepted for publication in the Journal of the Electrochemical Society on 27.3.2025 distributed under the terms of the Creative Commons Attribution 4.0 License (CC BY). The permanent web link to the article is https://doi.org/10.1149/1945-7111/adc0c4.

After the development of the experimental method using limiting current measurements to determine the τ/ε-ratio for the MPL structure, this follow-up study examines two different MPL materials, which possess a similar porosity but differ in their characteristic pore size. A carbon black based MPL (pore size $\approx$ 80 nm) was compared with a vapor-grown carbon fiber MPL (pore size $\approx$ 800 nm). In addition, the τ/ε-ratio was determined computationally by using either a Laplace solver or the random walk method from the 3D-structure as determined using FIB-SEM.

The analysis of the experimental and theoretical approach agreed that the tortuosity τ of both MPLs is similarly between 1.2-1.3. The similar and low tortuosity can be reasoned by the high porosity of $\approx$ 80%. As in the last study, it was important to include Knudsen diffusion in the determination of the τ/ε-ratio. In the experimental approach, the incorporation of Knudsen diffusion was realized by comparing the experimentally determined diffusivity with the theoretical diffusion coefficient including Knudsen diffusion according to the information from the pore size distribution. In the computational τ/ε-ratio determination, the Knudsen diffusion was considered by using the PuMa solver, which includes Knudsen diffusion compared to the Laplace solver, which only includes molecular diffusion.

Additionally, the impact on the structure of different pore filling mechanisms depending on the hydrophobicity/ hydrophilicity is determined. It is expected that the hydrophobic MPL fills the largest pores first, while the hydrophilic MPL fills the smallest pores first. The differences in wettability of the two structures were shown using water sorption measurements. Additionally, ESEM images were recorded and the water bubble shape was analyzed. While the hydrophobic structure shows round bubbles, the hydrophilic MPL creates irregularly shaped bubbles. Singe-cell fuel cell measurements revealed that the hydrophobic structure possesses a better water removal ability, as demonstrated with a better performance and a lower oxygen transport resistance at the wettest tested conditions (50 °C, 200 kPa_{abs}, 120% RH). By filling the pores computationally either starting with the smallest or the largest pores, the τ/ε-ratio determination for the partially filled structures revealed a stronger increase of the τ/ε-ratio when the smallest pores are filled first compared to when the largest pores are filled first. The small pores are important to interconnect the network in the porous structure.

Author Contributions

A.B. and M.B. conducted the experimental and modeling work and analyzed the data (A.B.: preparation of MPLs, fuel cell testing; M.B. FIB-SEM and simulation). C.C. conducted and analyzed the water sorption measurements under the supervision of M.T. A.B., M.B., V.T. and H.G. discussed the data and their interpretation. A.B. and M.B. wrote and C.C., M.T., V.T. and H.G. revised the manuscript. All authors discussed the data, commented on the results, and reviewed the manuscript. V.T. and H.G. supervised and secured funding for the project.

Journal of The Electrochemical Society, 2025 **172** 036505

On Tortuosity and Water Management in Hydrophobic and Hydrophilic Microporous Layers with Different Carbon Structures

Michele Bozzetti,[1,=] Anne Berger,[2,=] Carlos Cuadrado Collados,[3] Matthias Thommes,[3] Hubert A. Gasteiger,[2,*,z] and Vasiliki Tileli[1,z]

[1]*Institute of Institute of Materials, École Polytechnique Fédérale de Lausanne, CH–1015 Lausanne, Switzerland*
[2]*Technical University of Munich, Germany, TUM School of Natural Sciences, Chemistry Department and Catalysis Research Center, Chair of Technical Electrochemistry, D-85748 Garching, Germany*
[3]*Department of Chemical and Bioengineering, Institute of Separation Science and Technology, Friedrich-Alexander-University Erlangen-Nürnberg, 91058 Erlangen, Germany*

To improve mass transport limitations in proton exchange membrane fuel cells (PEMFCs), a detailed analysis of the gas diffusion layer structure can aid to understand the transport processes of oxygen to the catalyst layer and the liquid water removal mechanism. Herein, the effect of tortuosity was studied using two different microporous layer (MPL) structures and their hydrophobic and hydrophilic clones. Focused ion beam—scanning electron microscopy tomography showed that all structures had similar porosity but different characteristic pore diameters. Volumetric analysis using the Laplace solver TauFactor and the PuMA random walk method yielded a tortuosity of 1.2–1.3 for both MPLs, and these values were confirmed by experiments based on limiting current measurements in a single-cell PEMFC. The inclusion of Knudsen diffusion in the MPL proved to be essential for both methods. Subsequent analysis using experimental operating conditions that induce liquid water formation suggested that different water filling mechanisms occur in MPLs with different surface wettability. A mechanistic understanding of the water filling processes was investigated by simulations, considering the effect of liquid water saturation in different pore size domains. It was found that the tortuosity increases more drastically when narrow pores are blocked by liquid water, consistent with the experiments.
 [DOI: 10.1149/1945-7111/adc0c4]

Manuscript submitted October 10, 2024; revised manuscript received March 11, 2025. Published March 27, 2025.

Proton exchange membrane fuel cells (PEMFCs) are subject to mass transport limitations mainly on the cathode side, where the by-product water from the cathodic reaction can saturate a portion of the available pore space in the gas diffusion layer (GDL), ultimately hampering the diffusion of molecular oxygen and PEMFC performance loss.[1] Understanding the mechanisms of liquid water saturation is a key step in optimizing the GDL design, and it requires a detailed knowledge of the microstructural parameters of the microporous layer (MPL), including the surface wettability.[2]

Diffusive gas transport in GDLs, which can be inferred from microstructural parameters, includes both bulk molecular diffusion and Knudsen diffusion. Molecular diffusion is the dominant diffusion mechanism in large pores and is strongly affected by pressure. The diffusion coefficient for a binary system of gases (A, B), $D_{\text{theo,AB}}$, can be described by Eq. 1, taken from Bird, Steward, and Lightfoot.[3] It is a function of pressure (p) and temperature (T) and includes two constants (a and b) as well as the critical pressure (p_{ci}) and temperature (T_{ci}) of each of the gases involved.

$$D_{\text{theo,AB}} = \frac{1}{p}\cdot a\left(\frac{T}{\sqrt{T_{\text{cA}}\cdot T_{\text{cB}}}}\right)^{b}\cdot(p_{\text{cA}}\cdot p_{\text{cB}})^{1/3}\cdot(T_{\text{cA}}\cdot T_{\text{cB}})^{5/12}\cdot(1/M_{\text{A}}+1/M_{\text{B}})^{1/2} \quad [1]$$

Knudsen diffusion is the dominant diffusion mechanism when the dimensions of the pore system are comparable to or smaller than the mean free path (λ), i.e. the distance the gas molecules can travel without collisions. Equation 2 defines the diffusion coefficient for Knudsen diffusion (D_{Knudsen}) that takes into account the pore diameter (d_{pore}), the gas constant (R), the temperature (T), and the molecular mass of the gas being transported (M). It should be noted that while the Knudsen diffusion coefficient is pressure independent, the mean free path is influenced by pressure, which can affect the contribution of Knudsen diffusion to the overall gas diffusion.

$$D_{\text{theo,Knudsen}} = \frac{4}{3}d_{\text{pore}}\sqrt{\frac{R\cdot T}{2\cdot\pi\cdot M}} \quad [2]$$

Knudsen diffusion occurs when λ is larger than the pore diameter. The mean free path is a function of the Boltzmann constant ($k_B = 1.38\cdot10^{-23} J\ K^{-1}$), the temperature T, the pressure p, and the collision cross section of the gas molecules σ (for O_2, $\sigma =$ 2.93 Å) as described by:

$$\lambda = \frac{k_B\cdot T}{\sqrt{2}\cdot\pi\cdot\sigma^2\cdot p} \quad [3]$$

To understand whether Knudsen or molecular diffusion dominates at a given pore size, the Knudsen number is used, which is defined as the ratio of the mean free path to the pore diameter, $Kn = \lambda/d_{pore}$. A common empirical approach is to use an mixed diffusion coefficient $D_{\text{theo,mixed}}$,[4] which is usually obtained by approximation using the Bosanquet additivity relation.[5]

The presence of liquid water in the pore network of GDLs results in a reduction of the available pore space for reactant transport. This effect is characterized by the substitution of the intrinsic structural parameters of the pore network by effective structural parameters that depend on the saturation level. This phenomenon can be described by the effective porosity ε_s, which is related to the initial porosity ε by the equation:

$$\varepsilon_s = \varepsilon\cdot(1-s) \quad [4]$$

where $s \in [0, 1]$ is the saturation, defined as the fraction of pore volume filled with liquid.

One of the most debated and studied structural parameters is the so-called tortuosity τ,[6] which is related to the effective diffusion coefficient ($D^{\text{y}}_{\text{eff}}$) in a porous medium by:

$$D^{\text{y}}_{\text{eff}} = D_{\text{theo}}\cdot\frac{\varepsilon}{\tau} \quad [5]$$

where D_{theo} is the diffusion coefficient of the conductive phase. A geometric interpretation of tortuosity can be derived from its original

[=]Equal Contribution.
*Electrochemical Society Fellow.
[z]E-mail: hubert.gasteiger@tum.de; vasiliki.tileli@epfl.ch

definition as the ratio of the diffusion path L_P to the external distance Δx.[7,8] The value of tortuosity is also affected by the water saturation of the pore network, as the length of the available diffusion paths increases with increasing saturation, as illustrated in Fig. 1. The concept of geometric tortuosity is insightful for understanding the structure of a GDL, but it is not easily related to transport properties via Eq. 5, due to the presence of complex geometries, constrictions within the pore network, and variations in the diffusion mechanism with respect to pore size.[9] Consequently, the direct influence of tortuosity on the effective diffusion coefficient raises the interest in characterizing the effective tortuosity τ_S as a function of water saturation.[10,11] The most popular method to characterize the tortuosity is flow-based simulations, which aim to extract the effective diffusion coefficient from a reconstructed 3D volume of the gas diffusion medium, although some path-finding methods are still used.[12] For the direct experimental determination of the tortuosity, X-ray computed tomography (X-ray CT) has been used to acquire 3D volumes of the macroporous GDL substrate (features and pores >5 μm),[13] while the implementation of focused ion beam—scanning electron microscopy (FIB-SEM) tomography has been shown to be able to resolve the pore size of the MPL (features and pores <1 μm).[14]

In addition, the effect of MPL wettability on the effective tortuosity values is another important aspect to explore as we expect different water filling mechanism depending on the surface properties. Hydrophobic MPLs are widely used as they create a capillary-pressure barrier. However, flooding is still frequently observed. Therefore, different alterations to the MPL composition have been proposed. One approach contains different layers of MPLs with different surface properties realizing a gradient in hydrophobicity/-philicity.[15–17] For achieving a better fuel cell performance at wet conditions, hydrophilic additives, such as TiO_2, carbon nanotubes (CNTs), or aluminosilicate, have been added to a PTFE containing MPL.[17–21] For these partially hydrophilic and partially hydrophobic MPLs, the implementation of preferential percolation pathways within hydrophobic domains has been studied as an attempt to confine liquid water to a limited volume that percolates through the diffusion layers, leaving the rest of the pore space available for gas diffusion.[22] For purely hydrophilic MPLs, it has been observed that hydrophilic MPLs are beneficial at dry conditions as they can retain the water closer to the CL.[23–25] On the other hand, a recent experimental study has shown that hydrophilic MPLs perform worse than hydrophobic materials of comparable structure under conditions of high relative humidity (RH),[26] and that hydrophilic coatings increase the oxygen transport resistance at high current density,[27] although a comprehensive explanation for their poorer liquid water management has not been proposed. For this study, the difference between a hydrophobic and hydrophilic MPL serves as a tool to experimentally assess the difference in performance and correlate it with a hypothetical filling mechanism, which is simulated on the 3D structure.

Herein, we analyze the pore network of two MPLs with different carbon structures and their hydrophobic (HPO) and hydrophilic (HPI) clones. We used a carbon-black based MPL (further on referred to as Li100) and a carbon fiber-based MPL (further on referred to as VGCF), coated on a commercial gas diffusion layer substrate (GDL-S). The MPL wettability was varied according to the binder used; PTFE for HPO and Nafion for HPI. The pore volumes were reconstructed by FIB-SEM tomography, and the tortuosity was calculated by theoretical calculations using a dedicated software and also verified by experimental tortuosity measurements in an operating single-cell PEMFC. The dissimilar carbon structure of the MPLs was found not to affect their average porosity and tortuosity, but their main difference was in their average characteristic pore size and pore size distribution. Further analysis included the effect of partial water saturation on the effective tortuosity τ_S for the HPO and HPI clones of the two MPL designs. Assuming that a different pore filling mechanism can be expected due to the different surface wettability of the MPL clones, the results reveal the contribution of narrower pore network connectivity, which is manifested as an increasing tortuosity value. It is concluded that the HPI MPLs, regardless of the carbon structure, attract water into the small pores by capillary forces, whereas the pores in the HPO clones hinder water filling, which preferably resides in larger pores, explaining well the superior performance of the HPO versions of the MPLs.

Experimental

Fabrication of MPL samples.—The preparation of hydrophobic and hydrophilic MPLs has been previously reported by Simon et al.[26,28] For hydrophobic MPLs, a PTFE dispersion (TF 5035GZ, 58 wt% PTFE from 3 M Dyneon) was used for binding and hydrophobization, targeting a final PTFE content of 20 wt% in the MPL. The slurry was prepared by mixing the carbon material (VGCF or Li100 carbon black) with deionized water (Milli-Q, 18 MΩ cm), Triton X-100 (Sigma Aldrich), and methyl cellulose (Sigma Aldrich) in an ARV-310 planetary mixer (Thinky, Japan), with the PTFE dispersion added in a subsequent mixing step. The slurry was immediately coated onto a Freudenberg H14 substrate (hydrophobically treated, Freudenberg, Germany), and the coated GDLs were immediately placed in an 80 °C oven for 30 min. The hydrophobic MPLs were heat treated according to the procedure described by Simon et al.,[28] which consists of several temperature steps with a final temperature hold at 380 °C.

The hydrophilic VGCF MPL was produced as described by Simon et al.[26] The recipe for the hydrophilic Li100 MPLs was modified in contrast to the VGCF procedure by reducing the carbon content and increasing the 1-propanol content from a value of 0.16 g_{carbon}/mL_{ink}, to a value of 0.08 g_{carbon}/mL_{ink}. In short, for both carbon types, the carbon material was mixed with the isopropanol at a high rotation rate of 2000 rpm for 2 min before the Nafion ionomer

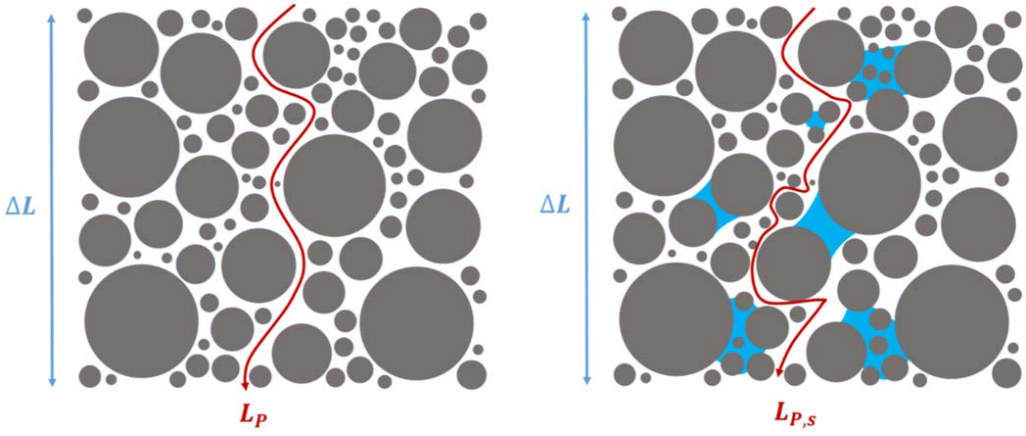

Figure 1. The tortuosity increase with water saturation can be understood from the geometrical interpretation of tortuosity by noticing that the partial filling of pores with water reduces the number of percolating gas paths through the pore network and thus increases their length $L_{P,s}$.

(D2021, Ion Power) was added targeting a Nafion content of 20 wt %. A second mixing step was performed at a lower rotation rate of 500 rpm for 10 min. The slurry was immediately used for coating, and the coated GDLs were placed in an oven at 80 °C for 30 min. No further heat treatment was carried out.

The same binder content of 20 wt% was chosen for PTFE and Nafion. Given that they have a similar density and the carbon material is the structure-giving element, the same porosity can be expected for the hydrophobic and the hydrophilic version of the MPL.

Sample preparation for microscopy.—Embedding of all samples was performed by atomic layer deposition (ALD) of zinc oxide using a BENEQ TFS200 instrument, as previously reported.[10] The chamber temperature was set at 200 °C and the precursors were not preheated. At this temperature, the PTFE structure remains intact, whereas the Nafion has been reported to have an upper limit of thermal stability between 230 and 280 °C.[11,22] To ensure that no relevant structural degradation occurred during the embedding process, the hydrophilic samples were left in an oven at 200 °C for 2 h (the time required for ALD infiltration) and then inspected by SEM where no evident structural degradation was seen. Another mitigating factor for the risk of structural degradation is the fact that the first zinc oxide layers should act as a structural reinforcement by surrounding the polymeric domains. As a consequence, the thermal stability of the sample is required for a much shorter time than 2 h, viz. in the range of 10–20 min. The penetration depth of the zinc oxide infiltration was between 15 and 20 μm in all samples. The deposition consisted of 1000 cycles with a pulse duration of 600 ms for both H_2O and diethylzinc, with a waiting time of 900 ms after each pulse and a purging time of 3 s. Surface polishing was performed with an argon ion beam (Ilion II, Gatan) operated at 4 keV in dual beam cross section polishing mode.

3D structure acquisition and reconstruction.—Three-dimensional nano-tomography data were acquired with a ZEISS CrossBeam 540 FIB-SEM equipped with Atlas 5 tomography software, which allows voxel expansion on the *y*-axis to compensate for the 54° tilt between the ion and electron beams and provide isotropic voxels. The milling conditions were 30 keV and 700 pA, while the scanning electron beam imaging was done at 1.5 keV and 500 pA. The voxel size was 7 nm for Li100 MPLs and 10 nm for VGCF MPLs. Prior to image acquisition, three alignment notches were milled at 20 pA on the top surface of the platinum protective layer and then covered with a carbon layer for contrast. These notches were also used to generate the transformation matrix to align each slice by correcting for electron beam drift. The alignment process was performed using the *MultiStackReg* plugin for ImageJ, a registration plugin based on minimizing the mean square intensity difference between a reference and a test data set.[29] To segment the zinc oxide embedded pore phase from the carbon based structure of the MPL, a deep learning voxel classifier called YaPiC based on a U-net architecture was used.[30] Details of the segmentation process are reported elsewhere.[14]

Analysis of 3D structure.—The characterization of the pore size distribution was performed using the *local thickness* algorithm included in the BoneJ library[31] by applying a distance transform to the stack and then assigning to each voxel the largest included sphere in the pore phase containing the voxel. The filling of the hydrophobic MPL with liquid water was simulated by removing larger pore domains from the network, while for the hydrophilic MPL this filling was simulated by removing the narrower sized pore network. The obtained water saturation was quantified by the porosity difference with the original pore network. The characterization of the tortuosity was initially performed using TauFactor,[32] a Laplace solver that extracts the tortuosity from the effective diffusion coefficient by comparing the diffusion in an equivalent volume completely filled with the conducting phase (i.e. in this case with pure gas phase). It was then evaluated by a random walk method based on the mean square displacement of the diffusing particle, included in the PuMA software.[33] PuMA requires the input of the diffusing species (oxygen), the thermal velocity and the mean free path. To obtain these parameters, the temperature T and pressure P we chosen based on the values used for the limiting current experiments, that is $T = 80$ °C, P = 170 kPa. The thermal velocity in these conditions was calculated to be $v_{th} = 680$ m s^{-1}. The mean free path (in voxel unit) was calculated by choosing oxygen as the diffusing gas molecule and computing the ideal gas mean free path $\bar{\lambda}$ from the molecule square kinetic diameter d_k^2, the gas temperature T and pressure P, using the classical relationship for the mean free path: $\bar{\lambda} = \frac{k_B T}{\sqrt{2}\pi d_k^2 P}$.

Mercury intrusion porosimetry.—Mercury intrusion porosimetry (MIP) measurements were performed using an Autopore Instrument (9600, Micromeritics Instrument Corporation, USA). The MIP measurements were carried out using a penetrometer. A mass of ∼70 mg and ∼100 mg of Li100 and VFCF, respectively, was added to the penetrometer (sample holder) with a 5 ml bulb volume and 0.392 ml stem volume. The sample amount resulted in a stem volume usage of ∼57% and ∼86%, respectively. To minimize the influence of the hydrostatic pressure of Mercury at lower pressures, the pressure range of 0.5–45 psi was measured in a horizontal position, while the pressure range of 45–61,000 psi was measured in a vertical position. The pressure steps were evenly distributed on the logarithmic scale, with 25 points per decade. The pressure was held constant at each step until the intrusion rate was less than 0.001 μl/(g·s). The pore diameter d_{pore} was determined using the Washburn equation, which takes into account the surface tension of Mercury γ_{Hg} (here: 0.480 N m^{-1}) and the contact angle θ (here: 140°). The pore diameter was calculated as a function of pressure p.

$$d_{\text{pore}} = -\frac{4 \cdot \gamma_{\text{Hg}} \cdot \cos\theta}{p} \qquad [6]$$

Scanning electron microscopy.—SEM images for visual representation were taken on a JSM-IT200 InTouchScope™ (JEOL, Japan) microscope, using an accelerating voltage of 10 kV. Sample preparation for cross-sections was performed using an IB-19520CCP cross-section polisher (JEOL, Japan). The samples were ion-milled without prior embedding at an accelerating voltage of 6 kV for 5.5 h at a temperature of −40 °C using an argon source.

Single-cell fuel cell testing.—Differential-flow single-cell fuel cell tests were conducted on a 5 cm^2 active area using a special cell design developed by Baker et al.[34] and modified according to the suggestions of Du et al.[35] A flow field originally designed to accommodate an active area of 50 cm^2 was used, with 14 channels distributed in three serpentines with a width and depth of 0.5 mm and 0.8 mm, respectively (land width = 0.5 mm). The active area of 5 cm^2 was situated at the cathode outlet and covered the straight channels of the last serpentine to avoid a pressure gradient along the active area. Due to the special cell configuration, three operational aspects have to be considered: (i) the temperature sensor to control the cell temperature has to be placed directly behind the active area of the cell, (ii) the pressure of the cell has to be regulated according to the cathode outlet pressure, (iii) the dew point of the humidifier (which is usually specified at the cell inlet pressure) has to be converted using the Antoine equation to obtain the correct RH at the cathode outlet pressure, accounting for the pressure drop along the serpentine flow field. The flow fields were positioned between two gold-plated copper current collectors, which were electrically insulated from the adjacent in-house made aluminum end plates.

A Primea Mesga catalyst coated membrane (CCM, W.L. Gore & Associates A510.1/M715.18/C580.4) was cut to an area of 8.25 cm^2 (5.5 cm × 1.5 cm). The platinum loading of the CCM is 0.4

mg_{Pt} cm^{-2} for the cathode electrode and 0.1 mg_{Pt} cm^{-2} for the anode electrode. The CCM was laminated with a PEN-foil subgasket (CMC 61325, CMC Klebetechnik, Germany), resulting in an active area of 5 cm × 1 cm. Gas diffusion layers (GDLs) were cut to the same dimensions as the CCM. The anode GDL was a commercial Freudenberg H14C10, while the cathode GDL was added as indicated. The cathode GDL substrate (GDL-S) was a Freudenberg H14 (hydrophobically treated).

The compression of the cell was individually selected to give a contact pressure of 1.4–1.6 MPa, which was verified by a pressure sensitive film (FUJIFILM Prescale film, super low pressure range, LLW) in separate experiments, whereby the pressure sensitive film was positioned between the cathode flow field and the cathode GDL. The pressure was maintained for 2 min, before the film was removed, scanned (Epson Perfection V33), and finally evaluated using the provided software (Fujifilm FPD-8010E). The Freudenberg H14 GDL substrate + MPL was compressed to a total compression of 15%–20%, depending on the thickness of the MPL.

Electrochemical characterization was performed using a fully automated fuel cell test station (G60, Greenlight Innovation, Canada). To precondition the catalyst-coated membrane (CCM), the fuel cell was subjected to ten cycles of the following voltage-hold sequence under H_2/air flows of 1390/3320 nccm at 80 °C, 100% relative humidity (RH), and 150 kPa_{abs}: 45 min at 0.6 V, 5 min at open circuit voltage (OCV), and 10 min at 0.85 V. After preconditioning, a recovery step was carried out by holding the voltage at 0.3 V at 40 °C, 100% RH, and 170 kPa_{abs} under H_2/air flows of 2000/5000 nccm.

Polarization curves were obtained in potentiostatic mode using a differential-flow of H_2/air at flow rates of 2000/5000 nccm. After pre-conditioning the cell at 0.75 V for 15 min, the cell voltage was lowered from 0.9 to 0.3 V in 0.05 V steps. The OCV point was recorded last, and a stabilization time of 5 min was allotted for each voltage step. The average data from the last 30 s of each step were computed. An EIS measurement was then conducted using a "hybrid mode" and a voltage perturbation of 10 mV in a frequency range from 100 kHz to 10 Hz. The high frequency resistance (HFR) was determined by locating the x-axis intercept in the Nyquist plot.

Limiting current measurements were conducted by diluting oxygen in nitrogen at the cathode side to achieve O_2 concentrations of 0.5%, 1%, 2%, 4%, 8%, 12%, 16%, 21%, 24%, and 28%, following the methods employed by Baker et al.[34] and Simon et al.,[28] with a total flow rate of 5000 nccm. Pure H_2 (2000 nccm) was supplied to the anode side. To scan the mass transport limited current regime, the voltage was set to 0.3 V, 0.15 V, 0.1 V, and 0.05 V, and held for 2 min at each voltage step. The last 15 s for each data point were averaged.

The resistance to oxygen transport under differential-flow condition, denoted as R_T, is defined in Eq. 7. It depends on various factors such as the molar fraction of dry oxygen (x_O^{dry}), the cell pressure (p), the water vapor pressure (p_w), the cell temperature (T), the observed limiting current density (i_{lim}), the Faraday constant (F), and the universal gas constant (R). This expression is derived by combining Fick's law with Faraday's law.

$$R_T = 4 \cdot F \cdot \frac{x_O^{dry}}{i_{lim}} \frac{p - p_w}{R \cdot T} \quad [7]$$

The cell temperature is controlled through thermocouples in the flow field of the cell on anode and cathode directly placed behind the active area. Due to the heat release during operation and due to the thermal resistance of the GDL and electrode material, a temperature gradient in through-plane direction can be expected. For this work, the cell temperature is taken as the set temperature as assessing the temperature gradient would require detailed computational modeling, which is beyond the scope of this work.

Environmental SEM imaging.—A Thermofischer Scientific Quattro ESEM with a Peltier cooling stage was used to observe water condensation on the MPL surfaces. Samples were grounded to the crucible with conductive copper tape. The operating pressure

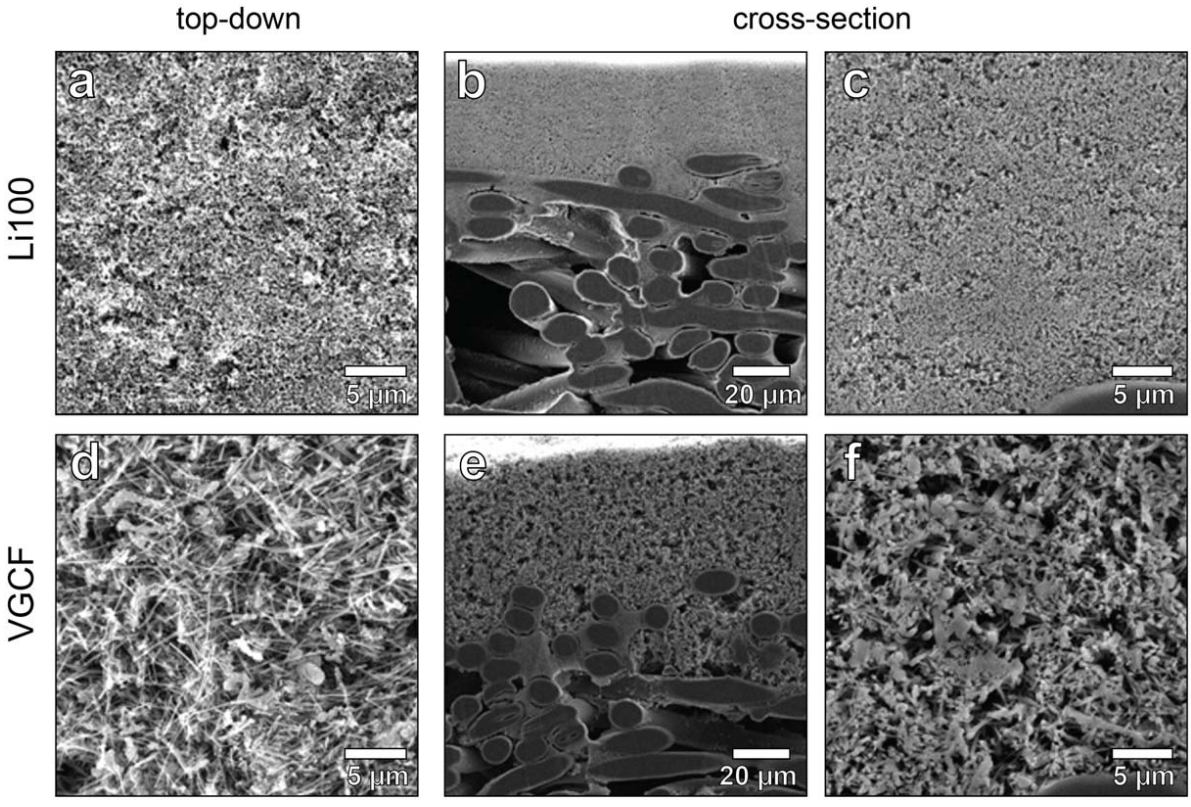

Figure 2. SEM images of hydrophobic Li100 (a)–(c) and VGCF (d)–(f) MPLs, depicting the difference in the carbon structures.

was 900 Pa and imaging was performed at 10 kV with a current of 0.4 nA and a frame time of 2 s.

Adsorption measurements.—High resolution gas adsorption measurements were performed on a commercial Autosorb iQ automatic volumetric adsorption analyzer from Quantachrome (Boynton Beach, FL, USA) equipped with 1, 10, and 1000 Torr transducers. Argon at 87 K was used as adsorptive (Ar 6.0 purchased from AirLiquide). Prior to the sorption measurements, carbon materials were outgassed at 200 °C for 12 h under high vacuum.

Water adsorption experiments were performed at 298 K with a dedicated volumetric (manometric) sorption analyzer (Vstar, QuantaTec-Anton Paar), where the manifold was held at temperatures >100 °C allowing to obtain highly accurate water adsorption measurements. Water adsorption experiments were performed on a fresh sample from the same homogeneous batch that was used for argon adsorption experiments.

Results and Discussion

Morphological comparison of hydrophobic Li100 and VGCF MPLs.—Figure 2 depicts the top-down and cross-sectional morphology of the two distinct MPLs as revealed by SEM. The top-down view SEM images reveal the morphological difference between the two MLPs, where Li100 is identified by a compact structure with some porosity (Fig. 2a) and VGCF is identified as a fibrous network (Fig. 2d), whose individual fibers are between 10–20 μm in length and 150 nm in diameter, according to the manufacturer. Both MPLs are coated on a fibrous GDL-S (seen in part in Figs. 2b and 2e), however, the carbon black of the GDL-S that the manufacturer (Freudenberg) is adding during processing[36] is not visible within the resolving power of the SEM. In the cross-sectional image shown in Fig. 2c, the Li100-based MPL shows the presence of different pore sizes that can be up to hundreds of nanometers, while the VGCF-based MPL (Fig. 2f) is shown to exhibit much larger pores on the μm size. Previously, Simon et al. reported for the same MPLs that the Li100-based MPL[28] has a broad pore size distribution ranging between 10–100 nm, and that the pore size in the VGCF-based MPL[26] lies between 100-5000 nm, as determined using MIP measurements. Overall, the structures differ mainly in the pore diameters due to the different carbon structures: while the Li100 MPL is made with a carbon black material, yielding a characteristic, MIP-based pore size distribution maximum at ∼70 nm in MIP,[28] the latter is about an order of magnitude higher (∼700 nm) for carbon fiber-based VGCF MPL.[26] Interestingly, it was previously reported that both structures have a similar porosity of approximately 80%.[26,28] To analyze the structures in terms of tortuosity, we first performed fuel cell measurements under dry operating conditions for Li100 and VGCF MPLs with different thicknesses.

Determination of τ/ε from single-cell limiting current measurements.—Limiting current measurements were performed at a low RH of 62% and the oxygen transport resistance, R_T, of cells containing the two different MPLs of different thicknesses each was extracted at low limiting current densities (<1.25 A cm^{-2}), which was realized by regulating the oxygen concentration in nitrogen (⩽ 4% O_2 in N_2). Figure 3 shows the R_T values for the Li100 (panel a) and the VGCF (panel b) MPLs as a function of the MPL thickness, acquired at cell pressures of 115 kPa_{abs}, 150 kPa_{abs}, 200 kPa_{abs}, and 300 kPa_{abs}. The R_T values for cells with the uncoated GDL substrate are plotted in black for each pressure level. While the linear regression fits of the VGCF MPL R_T values at each pressure accurately project to the R_T value of the GDL-S at an MPL thickness of 0 μm, the regression lines for the Li100 MPL project to a higher R_T value at 0 μm thickness than that of the uncoated GDL-S. This difference can be understood as an additional interfacial transport resistance between the GDL-S and the Li100 MPL.

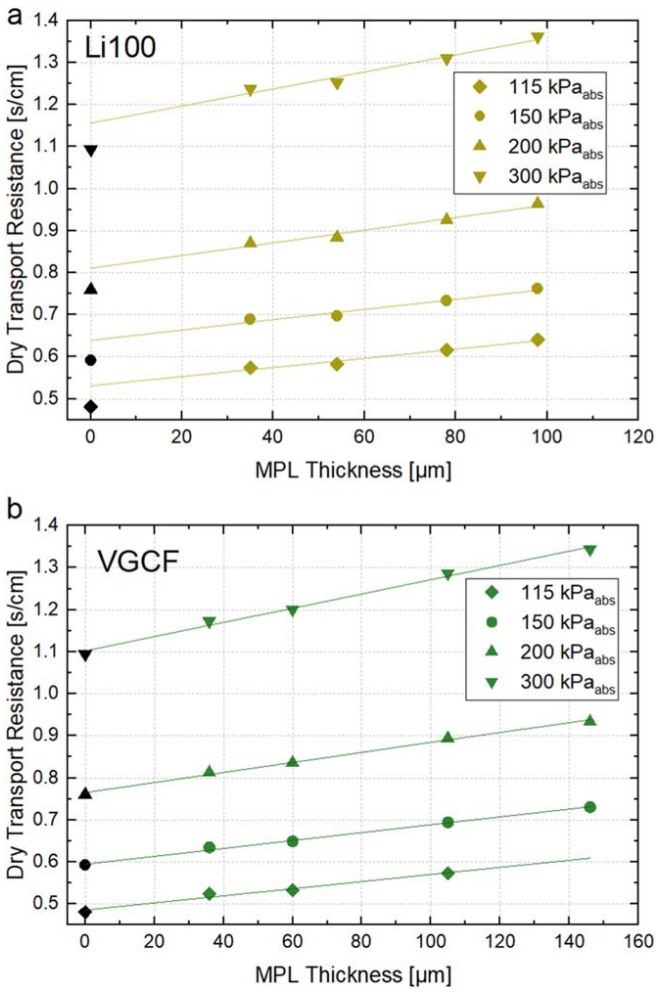

Figure 3. Dry oxygen transport resistance vs MPL thickness measured at 80 °C and 62% RH at cell pressures of 115 kPa_{abs} (square), 150 kPa_{abs} (circle), 200 kPa_{abs} (upward triangle), and 300 kPa_{abs} (downward triangle) for: (a) the Li100 MPL; (b) the VGCF MPL. Both MPLs were coated on a Freudenberg H14 GDL-S. The data for the VGCF MPL are discussed in more detail elsewhere.[37].

According to the literature, the transition regime between the molecular and Knudsen diffusion regimes spans across a wide range of Knudsen numbers. Tomadakis et al. claim that the transition regime spans between Knudsen numbers of 0.02–50.[5] When taking the peak diameter of 75 μm of the MIP-based pore size distributions, the Knudsen number of the Li100 is between 1.41 for 115 kPa_{abs} and 0.54 for 300 kPa_{abs} (T = 80 °C, diameter of oxygen molecule 3Å[38]). For the peak diameter of 830 μm of the pore size distribution of the VGCF MPL, the Knudsen number is smaller and ranges between 0.13 at 115 kPa_{abs} and 0.05 at 300 kPa_{abs} (T = 80 °C, k_B = $1.38 \cdot 10^{-23}$, diameter of oxygen molecule 3 Å[38]). Thus, when only considering the MIP-based peak diameters of both MPLs, a significant contribution of both diffusion processes would be expected for the Li100 while mostly molecular diffusion would be expected for the VGCF MPL.

While Knudsen diffusion coefficient is calculated according to Eq. 2, the molecular diffusion coefficient needs to account for a ternary gas mixture, where oxygen diffuses in a mixture of nitrogen and water vapor. The molecular diffusion coefficient is calculated as a function of the binary diffusion coefficient of oxygen in nitrogen ($D_{theo,ON}$), the binary diffusion coefficient of oxygen in water ($D_{theo,OW}$), and the water mole fraction x_W according to Eq. 8 (for further information see Baker et al.[34])

$$D_{\text{theo,ONW}} = \left(\frac{1 - x_W}{D_{\text{theo,ON}}} + \frac{x_W}{D_{\text{theo,OW}}} \right)^{-1} \quad [8]$$

To better determine the diffusion regime in each case, the data are replotted in Fig. 4a. On the left *y*-axis, the contribution ratio of Knudsen (blue) and molecular diffusion (gray) for O_2 is plotted over the range of pore diameter from 1 nm to 100 μm for the four investigated pressure levels. For this, the mixed diffusivity coefficient $D_{\text{theo,mixed}(d_{\text{pore}},p)}$ was evaluated using the Bosanquet equation:[5]

$$D_{\text{theo,mixed}} = \left(\frac{1}{D_{\text{theo,Knudsen}}(d_{\text{pore}})} + \frac{1}{D_{\text{theo,ONW}}(p)} \right)^{-1} \quad [9]$$

The ratio of the contribution of Knudsen diffusion to the overall diffusion of O_2, denoted as η_{Knudsen} and depicted by the blue lines in Fig. 4a, can then be determined by:

$$\eta_{\text{Knudsen}} = \frac{\frac{1}{D_{\text{theo,Knudsen}}}}{\frac{1}{D_{\text{theo,mixed}}}} \quad [10]$$

Similarly, the contribution of molecular diffusion to the overall diffusion of O_2 (corresponding to 1 - η_{Knudsen}) is depicted by the gray line in Fig. 4a. The yellow and blue lines in Fig. 4a show the MIP-based pore size distributions of the Li100 and the VGCF MPLs, respectively, plotted against the right *y*-axis. The pore size distributions measured here for both MPL are very similar to what has been reported previously,[16,18] yet they are shifted to slightly higher pore size diameters (PSD peak 75 nm instead of 67 nm for Li100 and 830 nm instead of 722 nm for VGCF). The small deviation arises from a different sample preparation method, as we have recently learned that stacking sheets of MPL differently will result in slightly changed pore size diameter. Looking at the pore size distributions of both MPLs, Fig. 4a demonstrates that the pore sizes of the Li100 MPL lie entirely in the mixed region between molecular and Knudsen diffusion of O_2 under the experimental conditions of Fig. 3. As the pore size distribution of the VGCF MPL extends to pore diameters as low as 100 nm, there also is a large portion of the VGCF MPL pores in the mixed region, so that Knudsen diffusion of O_2 should play a role also for the VGCF MPL.

Figure 4b shows the pressure-dependent effective diffusion coefficients of O_2 in air at 80 °C and 62% RH (D_{eff}) for the hydrophobic Li100 MPL (open yellow circles) and VGCF MPL (open green triangles), determined from the slope of the oxygen transport resistances vs MPL thickness at the various pressures shown in Fig. 3, with D_{eff} corresponding to the inverse of the slope of the regression lines. The black symbols in Fig. 4b represent the pressure-dependent theoretical ternary molecular diffusion coefficient of oxygen in nitrogen and water ($D_{\text{theo,ONW}}$) in air at 80 °C and 62% RH.[3,34]

For these two MPLs, also a theoretical mixed diffusion coefficient using their MIP-based pore size distribution (PSD) was obtained ($D_{\text{theo,PSD}}$) according to the theory from Wakao et al.[39] and Reyes et al.[40] It is calculated for a specific pore diameter d_{pore} using the·Bosanquet equation (Eq. 9) and weighed by the fraction of the pore volume of that pore size $f_{(d_{\text{pore}})}$. This calculation is performed for all pore diameters based on the MIP data (Fig. 4a) and integrated over all pore diameters d_{pore}.

$$D_{\text{theo,PSD}} = \int D_{\text{theo,mixed}}(d_{\text{pore}}) \cdot f(d_{\text{pore}}) \cdot \mathrm{d}d_{\text{pore}} \quad [11]$$

The resulting $D_{\text{theo,PSD}}$ values for O_2 in air at 80 °C and 62% RH are shown in Fig. 4b for the Li100 MPL (solid yellow circles) and for the VGCF MPL (solid green triangles).

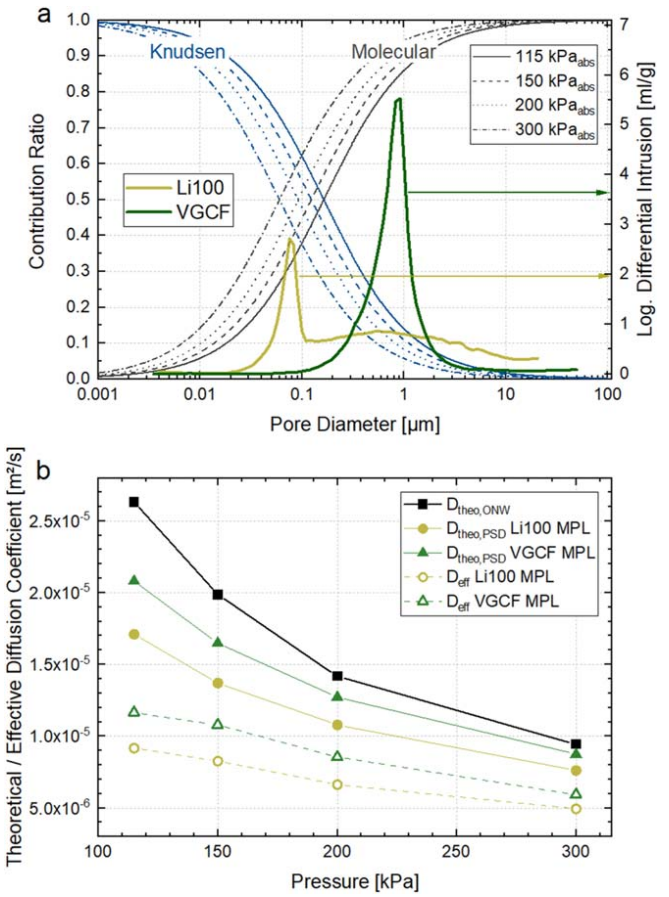

Figure 4. (a) Left axis: contribution ratio of molecular and Knudsen diffusion as a function of pressure and pore diameter (blue and gray lines); right axis: MIP-based pore size distribution of the hydrophobic Li100 MPL (yellow line) and the hydrophobic VGCF MPL (green line). (b) Pressure dependence of the theoretical (solid lines) and the effective (dashed lines) diffusion coefficients: theoretical ternary molecular diffusion coefficient for oxygen in nitrogen and water vapor under the experimental conditions of Fig. 3: 80 °C and 62%RH (black squares, solid line); theoretical diffusion coefficient as a function of pore size distribution for the Li100 MPL (yellow circles, solid line) and the VGCF MPL (green triangles, solid line); effective diffusion coefficients for the Li100 MPL (orange circles, dashed line) and the VGCF MPL (green triangles, dashed line), which were determined in situ via fuel cell limiting current measurements while varying the thickness of the hydrophobic MPLs on the GDL-S.

Compared to the molecular diffusion coefficients (black solid square in Fig. 4b), both PSD-based diffusion coefficients ($D_{\text{theo,PSD}}$, solid yellow and green symbols) are reduced due to Knudsen diffusion. Two trends can be observed: (i) the $D_{\text{theo,PSD}}$ values are lower for the Li100 MPL than for the VGCF MPL, because the smaller pores of the former are more strongly affected by Knudsen diffusion (as apparent from Fig. 4a), and (ii) the $D_{\text{theo,PSD}}$ values deviate more pronouncedly from the molecular diffusion coefficients (black symbols) at lower pressures, because the contribution of Knudsen diffusion is higher at lower pressures. However, at 300 kPa_{abs}, the $D_{\text{theo,PSD}}$ value of the VGCF MPL is almost identical with that for the theoretical molecular diffusion coefficient.

To calculate the tortuosity/porosity ratio from the limiting currents obtained from single-cell measurements, we relate the effective diffusion coefficient to the oxygen transport resistance of the MPL (R_{MPL}). According to the theory of Baker et al.,[34] R_{MPL} can be described as the MPL thickness (t_{MPL}), divided by the effective diffusion coefficients $D_{\text{eff(MPL)}}$:

Table I. Summary of the τ/ε ratios for the hydrophobic Li100 and VGCF MPLs, evaluated from the experimentally determined D_{eff} values (see open yellow and green symbols in Fig. 4b) at different pressures, using either the molecular diffusion coefficient $D_{theo,ONW}$ (black symbols in Fig. 4b) or using the theoretical mixed diffusion coefficient $D_{theo,PSD}$ (solid yellow and green symbols in Fig. 4b) in Eq. 11.

	τ/ε ratios			
	Li100 MPL		VGCF MPL	
Pressure (kPa_{abs})	Using $D_{theo,ONW}$	Using $D_{theo,PSD}$	Using $D_{theo,ONW}$	Using $D_{theo,PSD}$
115	2.87	1.87	2.26	1.79
150	2.40	1.66	1.84	1.53
200	2.22	1.63	1.72	1.49
300	1.96	1.54	1.63	1.48

$$R_{MPL} = \frac{t_{MPL}}{D_{eff(MPL)}} \quad [12]$$

Thus, τ/ε can be determined by using the partial derivative of R_{MPL} by the MPL thickness t_{MPL} as shown in Eq. 13. It needs to be noted that Fig. 3 shows the total transport resistance from the sum of the individual transport resistances from the MPL, GDL-S, the electrode and other resistances (e.g. flow channel resistance): $R_T = R_{MPL} + R_{GDL} + R_{electrode} + R_{other}$. However, as we assume all other terms to be constant with changing MPL thickness, the derivative of the total transport resistance R_T with respect to the MPL thickness t_{MPL} (slope in Fig. 3) equals the derivate of R_{MPL} with respect to t_{MPL}.

$$\left(\frac{\tau}{\varepsilon}\right)_{MPL} = \frac{D_{theo,x(MPL)}}{D^{y}_{eff(MPL)}} = D_{theo,x(MPL)} \cdot \frac{\partial R_{MPL}}{\partial t_{MPL}} \quad [13]$$

Here, as $D_{theo,x(MPL)}$ one would typically use the molecular diffusion coefficient ($D_{theo,molecular}$), but as will be shown in the following, the more proper value for the typical pore sizes of an MPL is the mixed diffusion coefficient ($D_{theo,PSD}$). A more detailed analysis on how to determine the effective diffusivity from oxygen transport resistance measurements for GDL-S and MPLs is described by Berger et al.[37]

The measured effective diffusion coefficients (D_{eff}, open symbols in Fig. 4b) extracted from the dataset shown in Fig. 3 are plotted in Fig. 4. The effective diffusion coefficients are substantially lower than the $D_{theo,PSD}$ values, but their overall trend is consistent: i) the D_{eff} values for the Li100 MPL are always lower than those for the VGCF MPL; ii) the D_{eff} values do not decrease as significantly as one would expect from the molecular diffusion coefficients ($D_{theo,ONW}$), confirming that there must be a significant contribution from Knudsen diffusion.

The results for the τ/ε ratios are given in Table I for the hydrophobic Li100 and VGCF MPLs, depending on whether molecular diffusion alone (i.e., $D_{theo,ONW}$ Fig. 4b or a combination of Knudsen and molecular diffusion (i.e., $D_{theo,PSD}$ in Fig. 4b) is considered in Eq. 11. The thus calculated τ/ε ratios vary significantly with pressure for a given MPL when the molecular diffusion coefficient ($D_{theo,ONW}$) is used in Eq. 11, which is contrary to the expectation of a constant τ/ε ratio, as this should represent purely geometric properties of the MPL. While the τ/ε ratio decreases with increasing pressure by ~32% (from 2.87 to 1.96, see Table I) for the Li100 MPL, a similar ~28% decrease can be observed for the VGCF MPL (from 2.26 to 1.63). On the other hand, when the τ/ε ratio is calculated using $D_{theo,PSD}$ in Eq. 11, the decrease of the τ/ε ratio with increasing pressure is substantially smaller, namely ~18% and ~17% for the Li100 and the VGCF MPL, respectively (see Table I); nevertheless, there still remains a clear pressure dependence of the calculated τ/ε ratio. This suggests that Knudsen diffusion is still underestimated in the PSD-based diffusion coefficient, implying that diffusion through small pores plays a larger role than statistically expected from the MIP-based pore size distribution. As Knudsen diffusion is less significant at higher pressures, the τ/ε ratio obtained at the highest pressure likely is the most accurate estimate.

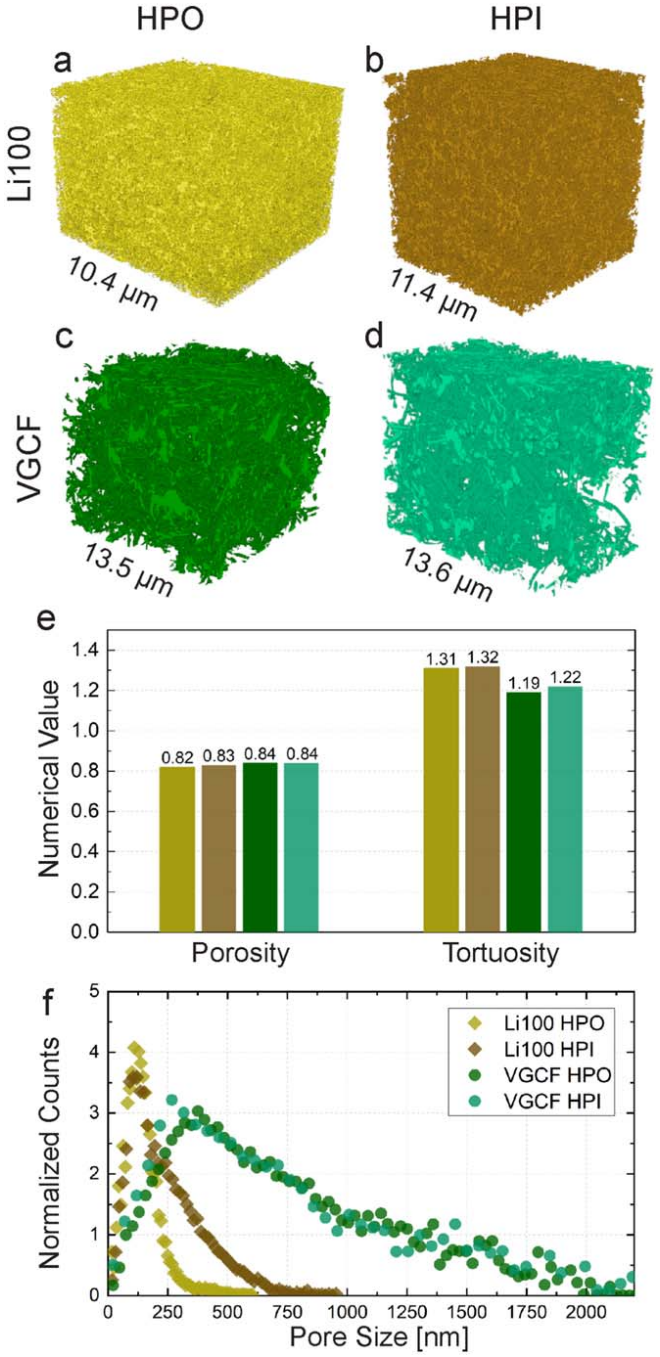

Figure 5. FIB-SEM reconstructed MPL volumes of (a) HPO Li100, (b) HPI Li100, (c) HPO VGCF, and (d) HPI VGCF. (e) Porosity and tortuosity values of the MPLs. Tortuosity values were calculated using the PuMA random walk method. (f) Pore size distribution of the four MPLs.

It is worth noting that when using the values at 300 kPa_{abs} for the PSD-based diffusion coefficient, the τ/ε ratio for the Li100 MPL is 1.54 and for the VGCF MPL is 1.48. As the porosity of both MPLs is approximately 80% (from MIP measurements shown in Fig. 4a and Refs. 16 and 18), the similar τ/ε ratios suggest that both MPLs

Table II. Tortuosity values for each of the four volumes analyzed with the Laplace solver TauFactor and the PuMA random walk method.

MPL	*TauFactor* τ_T	*PuMA* τ_P
Li100 HPO	1.22	1.31
Li100 HPI	1.24	1.32
VGCF HPO	1.16	1.19
VGCF HPI	1.17	1.22

also have a very similar tortuosity of $\tau \approx 1.2$. Such low tortuosity values are rather typical for high-porosity materials, as indicated by the majority of the commonly used τ/ε relations.[6,12,41–46]

Calculation of tortuosity via volumetric analysis of hydrophobic and hydrophilic clones of the MPLs.—Figures 5a–5d depict the 3D reconstructed volumes from the FIB-SEM measurements of the hydrophobic (HPO) and hydrophilic (HPI) versions of the Li100 and VGCF MPLs. A bar graph of the calculated porosity and tortuosity values of all pore networks is shown in Fig. 5e, which confirms the compatibility between the two clones of each design. The tortuosity values obtained with both the TauFactor[32] and PuMA[33] (porous microstructure analysis) software are listed in Table II. It should be noted that the calculation through PuMA includes the Knudsen contribution to the effective diffusivity and, considering the above discussion, it is expected to give more realistic results. The pore size distributions of the four MPLs are plotted in Fig. 5f and highlight the net difference in the characteristic size between the Li100 and VGCF designs, similar to what was observed by the MIP analysis of the hydrophobic MPLs (see Fig. 4a). This difference explains the different Knudsen contribution, since in the VGCF MPLs most of the pore network has a diameter $d_c \geqslant 500$ nm, leading to a net dominance of molecular diffusion over Knudsen diffusion. As seen in the pore size distribution, there is a perfect compatibility between the VGCF HPO and HPI structures (light and dark green), while the Li100 HPI MPL (yellow) has slightly larger pore sizes than its HPI clone (orange).

Water formation imaged by ESEM and determined by adsorption measurements.—In addition, to verify the surface wettability of the HPO and HPI clones of the Li100 and VGCF MPLs, we performed water condensation experiments in ESEM. Condensation was induced by using 100% water vapor atmosphere at 900 Pa in the SEM chamber while the samples were mounted on a Peltier stage and cooled to a temperature of 3 °C with a ramp rate of 0.2 °C min^{-1}. Images of the four samples are shown in Figs. 6a–6d, where differences in droplet shape and nucleation density can be used to assess the hydrophobicity or hydrophilicity of the samples. Dropwise growth occurred in all samples. However, the ESEM observations clearly show that both hydrophobic samples are characterized by surface nucleation of spherical droplets, while the hydrophilic samples exhibit both surface nucleation and liquid water breakthrough from the bulk. This is due to the different speed of water motion in hydrophilic media, where capillary pressure is not a limiting factor.

To help interpret the ESEM results, gas adsorption measurements were performed on the hydrophobic and hydrophilic Li100 MPLs. Figure 6e shows the argon 87 K adsorption isotherms which are essentially identical for the hydrophobic and the hydrophilic Li100 MPLs, indicating that the structures are the same in the low pore regime that can be measured by physisorption. On the contrary, the water adsorption isotherms in Fig. 6f show significant differences between the two samples indicating that the hydrophilic coating, associated with higher water adsorption, is present at all pore and external surfaces.

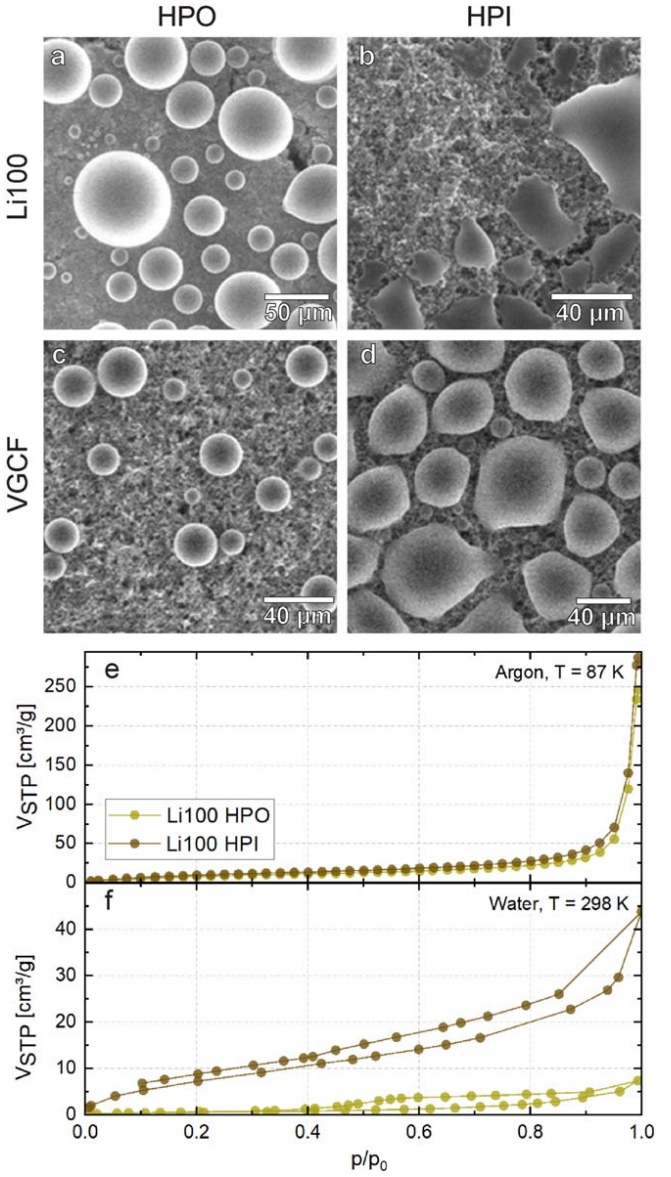

Figure 6. (a)–(d) SEM images showing the local surface hydrophobicity characteristics of the HPO and HPI clones of the Li100 and VGCF MPLs by liquid water droplet condensation in an ESEM. Hydrophobic samples have homogeneous spherical droplets while hydrophilic samples display mixed behavior. The essentially identical argon 87 K adsorption isotherms (e) and the different water adsorption isotherms (f) for HPO and HPI Li100 MPLs indicate that Li100 HPO and Li100 HPI differ only in surface chemistry, indicating a hydrophilic coating for the pore surfaces of Li100 HPO while Li100 HPI exhibits essentially a hydrophobic surface.

PEMFC single-cell performance with the hydrophobic and hydrophilic Li100 MPL.—Figure 7 shows the differential-flow H_2/air performance for the cells with the HPO (PTFE binder) and HPI (Nafion binder) clones of the Li100 MPL at three different operating conditions. Under the relatively dry conditions depicted in Fig. 7a, namely at 70% RH (80 °C, 170 kPa_{abs}), the HPO and HPI Li100 MPLs exhibit an essentially identical performance over the entire current density range (upper panel). The slightly higher performance of the hydrophobic MPL (yellow symbols/line at intermediate current densities (1–2.5 A cm^{-2}) can largely be ascribed to its ~5 mΩcm^2 lower HFR (middle panel), which is observed for all operating conditions, likely due to a slightly lower compression of the GDL, which would result in a slightly higher contact resistance and thus an accordingly higher HFR. The HFR

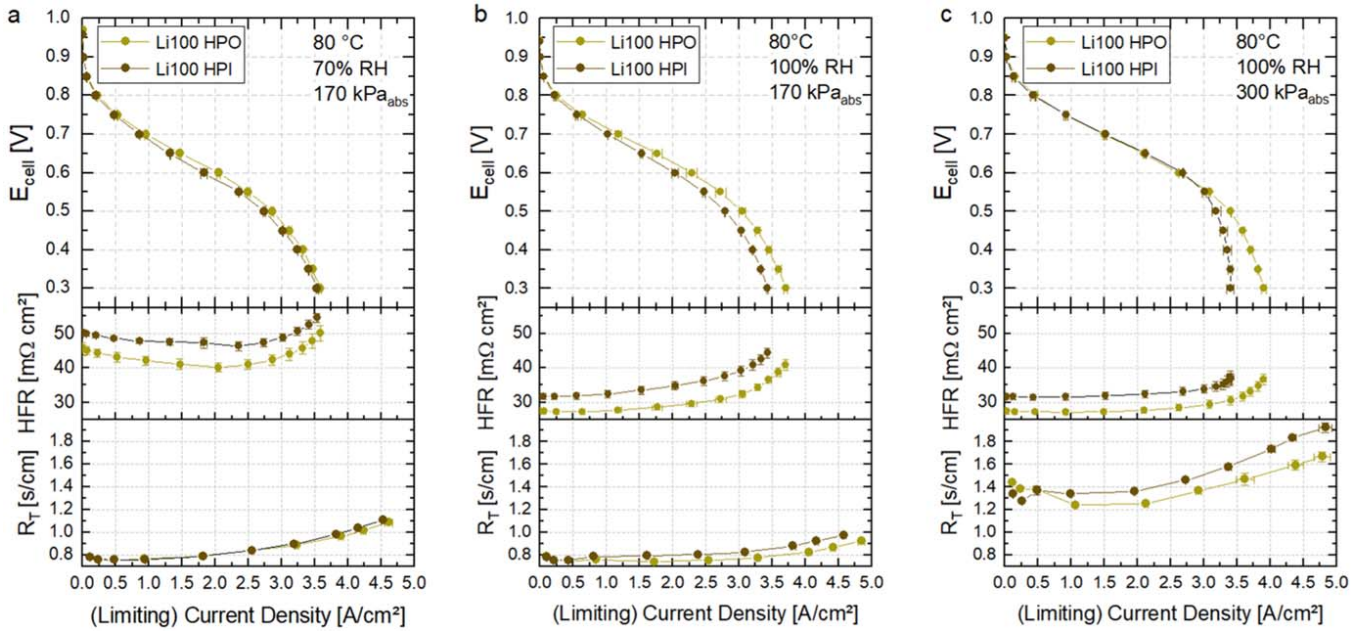

Figure 7. Differential-flow H_2/air performance curves with the hydrophilic (HPI) Li100 MPL (brown symbols/lines) and the hydrophobic (HPO) Li100 MPL (yellow symbols/lines), showing the cell voltage (E_{cell}, top panels) and the high-frequency resistance (HFR, middle panels) vs current density as well as the total oxygen transport resistance (R_T, bottom panels) vs the limiting current density. The H_2/air performance curves were recorded at different operating conditions: (a) dry conditions: 80 °C, 70% RH, and 170 kPa_{abs}; b) standard conditions: 80 °C, 100% RH, 170 kPa_{abs}; c) high pressure conditions: 80 °C, 100% RH, 300 kPa_{abs}. The error bars represent the standard deviation of two independently measured cells.

values (representing mainly the sum of the membrane resistance and the contact resistance between flow field and GDL) can in principle provide some information on the membrane hydration state, as the membrane resistance should decrease with increasing membrane hydration. For both MPLs, the HFR at the dry operating conditions first decreases with increasing current density up to ~2.5 A cm^{-2}, which can be explained by the increasing water production and thus a higher hydration state of the membrane. However, above ~2.5 A cm^{-2}, the heat production becomes dominant and although more water is being produced, the hydration state of the membrane decreases due to a growing temperature gradient between the MEA and the flow field. The oxygen transport resistance behavior under dry operating conditions (Fig. 7a, lower panel) is essentially identical for both MPLs over the entire limiting current density range. The fact that the dry transport resistance is similar suggests that the MPLs have the same oxygen diffusion resistance in the absence of liquid water, regardless of the binder used for fabricating the MPLs.

Figure 7b shows the single-cell H_2/air data for an increased RH of 100% compared to the above discussed 70% RH at the same temperature (80 °C) and pressure (170 kPa_{abs}). Under these conditions, the H_2/air performance with the hydrophobic MPL is clearly higher than that with the hydrophilic MPL, particularly as the current density increases (see upper panel of Fig. 7b), showing a ~250 mA cm^{-2} higher current density at 0.3 V. Besides the ~5 mΩcm^2 higher HFR of the hydrophilic MPL (as noted above, likely due to a slightly different GDL compression), the behavior of the HFR with current density is very similar for the two MPLs and can again be divided into two regions: up to ~2.5 A cm^{-2}, the HFR increases very slowly with current density, while above ~2.5 A cm^{-2} it increases more strongly, which can again be explained by an increase of the MEA temperature (i.e. the formation of a temperature gradient between flow field and MEA). The oxygen transport resistance is shown in the lower panel of Fig. 7b and has an essentially identical value at <0.5 A cm^{-2} as that observed for the 70%RH data in a, which thus also represents the dry transport resistance of the MPL structure in the absence of liquid water. At higher current densities, the oxygen transport resistances differ between the hydrophilic and the hydrophobic MPL, with the latter having a clearly lower transport resistance. Reflecting the behavior of the H_2/air performance curves, the differences in transport resistance appear at >0.8 A cm^{-2}. The difference in the oxygen transport resistances confirm the observations made for the H_2/air performances curves, where the cell with the hydrophobic MPL outperforms the cell with the hydrophilic MPL.

Figure 7c shows the H_2/air data at the conditions of Fig. 7b (80 °C, 100% RH), except that the pressure was increased to 300 kPa_{abs}. In contrast to the lower pressure condition, the H_2/air performance curves of both MPLs are essentially identical up to a current density of ~3 A cm^{-2} and only differ in the mass transport limited regime, where the hydrophobic MPL has a ~0.5 A cm^{-2} higher current density at 0.3 V, which is twice the difference observed at the lower pressure of 170 kPa_{abs} (Fig. 7b). The HFR remains constant for both MPLs up to ~3 A cm^{-2}, beyond of which an increase in HFR is observed. However, the increase in HFR is less than for the conditions presented at Figs. 7a and 7b, because the increase in MEA temperature and the associated decrease in RH at the MEA is compensated by the formation of liquid water at these high-pressure conditions, so that the hydration state of the membrane does not increase as much as for the other operating conditions. The oxygen transport resistance, shown in the lower panel of Fig. 7c, at a higher level compared to the other two operating conditions as it can be expected at higher pressures. The variations below 1 A cm^{-2} are artifacts stemming from the measurement protocol, where accumulated water at the end of the polarization curve needed to be removed. With increasing limiting current densities, the oxygen transport resistance of the hydrophilic MPL becomes increasingly larger compared to that of the hydrophobic MPL, with appreciable differences even at current densities where the H_2/air performance is still identical. This behavior suggests that there is indeed a difference in water management for the two MPLs as observed by the oxygen transport resistance even at low current densities, but this difference does not manifest itself in the H_2/air performance curves until much higher current densities are reached.

Figure 8 shows specifically selected operating conditions of 50 °C, 77% RH, and 400 kPa_{abs}, where the transition from the dry (no liquid water present in the catalyst layer) to the wet (presence of liquid water) regime is clearly visible in the oxygen transport

resistance. The oxygen transport resistance of the hydrophilic and hydrophobic Li100 MPL at low current densities has the same rather high value ~2.0 s cm^{-1} if compared to the values observed in Fig. 7. The transition from the dry to the wet regime occurs at the same current density of ~0.5 A cm^{-2} for both MPLs. However, the value of the wet oxygen transport resistance differs markedly between the two MPLs: for the hydrophobic MPL, it varies between 2.9–3.3 s cm^{-1}, while for the hydrophilic MPL ranges it gradually increases from ~3.5 to 3.8 s cm^{-1}. In view of the data presented in Figs. 7b and 7c, the hydrophilic MPL seems to hinder liquid water removal compared to the more hydrophobic MPL. Our results agree well with a previous study by Simon et al., who conducted similar experiments with an MPL containing a mixture of 80 wt% VGCF and 20 wt% of a slightly different carbon black (viz., Li400, with a lower specific surface area), using either PTFE or Nafion as a binder.[26] They also showed for the very same conditions that the cell with the hydrophobic MPL has a much lower oxygen transport resistance than the cell with the hydrophilic MPL in the wet regime, i.e. under conditions where liquid water is formed, while they showed identical oxygen transport resistances in the dry regime (i.e. at low current densities). Thus, we expect that the MPL discussed in this study, which contains 100% VGCF as the carbon material, will show the same trend of increased water removal behavior at wet conditions when using a hydrophobic binder.

Effect of water saturation on the tortuosity values of hydrophobic and hydrophilic MLPs calculated by volumetric analysis.— The relationship between water management and wettability of the MPLs can also be obtained by interrogating the pore size effect and effective tortuosity values as extracted from the volumetric analysis, but also considering wet conditions. The diffusion parameters previously calculated from FIB-SEM tomography refer to the whole pore network in dry conditions and therefore correspond to a water saturation level of $s = 0$. To describe the MPLs in wet conditions, we consider the partial saturation of the pore space. The expected behavior of the hydrophilic MPLs is to saturate narrower sized pore space, in contrast to the hydrophobic MPLs where the expected tendency is to fill larger pore domains first. Accordingly, we used the experimentally reconstructed pore networks of all four MPLs and simulated their pore saturation by filling either larger or narrower pore spaces, depending on the wettability of the MPLs.

Figures 9a–9d show the two- and three-dimensional morphology of water-filled pores for the HPO and HPI clones of VGCF MLPs with increasing saturation. The analysis was performed for the HPO and HPI versions of Li100 with similar results (volumes not shown). The tortuosity was evaluated for each reduced porosity volume of the four samples and the results are plotted in Fig. 9e. Comparing the two hydrophobic MPLs with different carbon structures, the results show that the diffusion coefficient of VGCF is less affected by partial saturation than that of Li100. This result is in good agreement with the performance studies under wet conditions of the two MPL designs.[26,28] With respect to the effective tortuosity as a function of saturation in the hydrophobic and hydrophilic Li100 MPLs, the Li100 HPI shows higher tortuosity than Li100 HPO at all saturation levels. This phenomenon can be understood by considering the constrictions that separate large pore domains.[14] Narrow pore space is highly interconnected, whereas large pore domains are separated by narrow constrictions, therefore, the abundance of percolating paths for gas diffusion is significantly reduced by narrower pore space filling. Similarly, the hydrophilic VGCF has higher tortuosity than the hydrophobic VGCF at all saturations, as in the Li100 structure, although with respect to Li100 MPLs the effective tortuosity difference is smaller at high saturations ($s > 0.5$) and larger at intermediate saturation values. We note that the increase in the error bars on the effective tortuosity values with increasing saturation in Fig. 9e is a result of the deep learning based algorithm used to segment the pore phase and the MPL structure, which generally leads to an increase in error with increasing saturation due

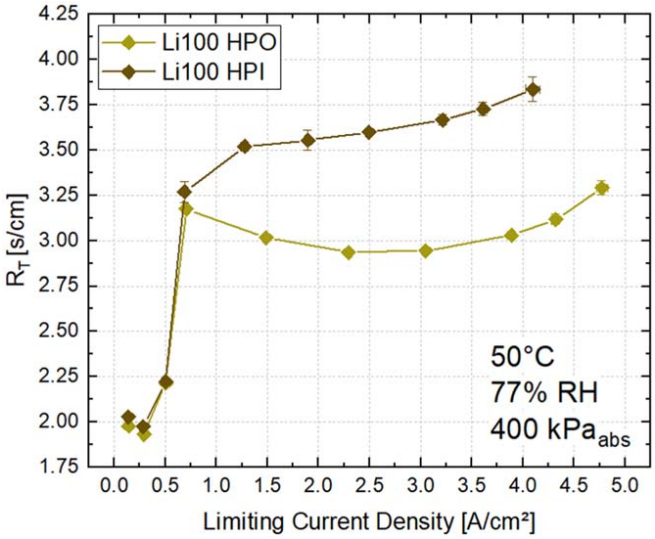

Figure 8. Oxygen transport resistance R_T as a function of limiting current density for the Li100 MPL with a hydrophobic (PTFE, brown) and a hydrophilic (Nafion, yellow) binder, acquired at 50 °C, 77% RH, and 400 kPa$_{abs}$. The error bars represent the standard deviation of two independently measured cells.

to its weight on the reduced available pore space. In practice, the results of the pore filling analysis suggest a superior performance of the hydrophobic clones of the MPLs in wet conditions, which is consistent with the cell performance tests shown in Fig. 7, and reveal that, although the MPLs have similar gas transport limitations in dry conditions, the hydrophobic performance is superior in high relative humidity conditions.

It is also possible to compare the oxygen transport resistance from Eq. 7 with the effective diffusion coefficient.[47,48] The proportionality $R_{T,O} \propto 1/D_{eff} \propto \tau_s/\varepsilon_s$ from Eqs. 12 and 13 relates the effective tortuosity to the oxygen transport resistance. Therefore, using the current limiting measurements to calculate the ratio between the oxygen transport resistance of hydrophobic and hydrophilic Li100, we can extract the saturation level of the MPL by finding the most compatible effective tortuosity ratio. Therefore, from Fig. 8 we find that $R_{T,O(\mathrm{HPI})}/R_{T,O(\mathrm{HPO})} = 1.20 \pm 0.08$ for Li100 MPL, which agrees well with the $\tau_{s(HPI)}/\tau_{s(HPO)} = 1.2$ at the saturation $s = 0.2$, as obtained from FIB-SEM tomography. This saturation value corresponds to the expected saturation interval[49] and this is a further confirmation of the compatibility of the two analysis methods. The assumption of the same saturation value for both MPLs under operating conditions allows the ε_S proportionality factor to be ignored, although this assumption requires further confirmation. The predicted effective tortuosity ratio for VGCF MPLs at the same saturation level is higher, $\tau_{s(\mathrm{HPI})}/\tau_{s(\mathrm{HPO})} = 1.4$.

Finally, we consider the effect of the Knudsen contribution. Figure 9f plots the Knudsen contribution at each saturation step, which was evaluated by subtracting the effective tortuosity values obtained with the different solvers, as described in the experimental methods. The volumetric analysis shows that Knudsen-based diffusion plays a major role at high saturation values in hydrophobic MPLs, as it dominates diffusion in the narrower channels that become dominant in hydrophobic-like saturations. This effect is negligible in the VGCF but not in the Li100 MPL. However, the expected saturation range under operating conditions is between $0.15 \leqslant s \leqslant 0.25$,[49] where the difference in Knudsen contribution between hydrophobic and hydrophilic Li100 is less than 0.1. A notable consequence of this is that the dependence on temperature and pressure is limited to the degree of pore saturation by liquid water. By further considering the effect of temperature and pressure on the mean free path of the gas molecules, it is revealed that it has

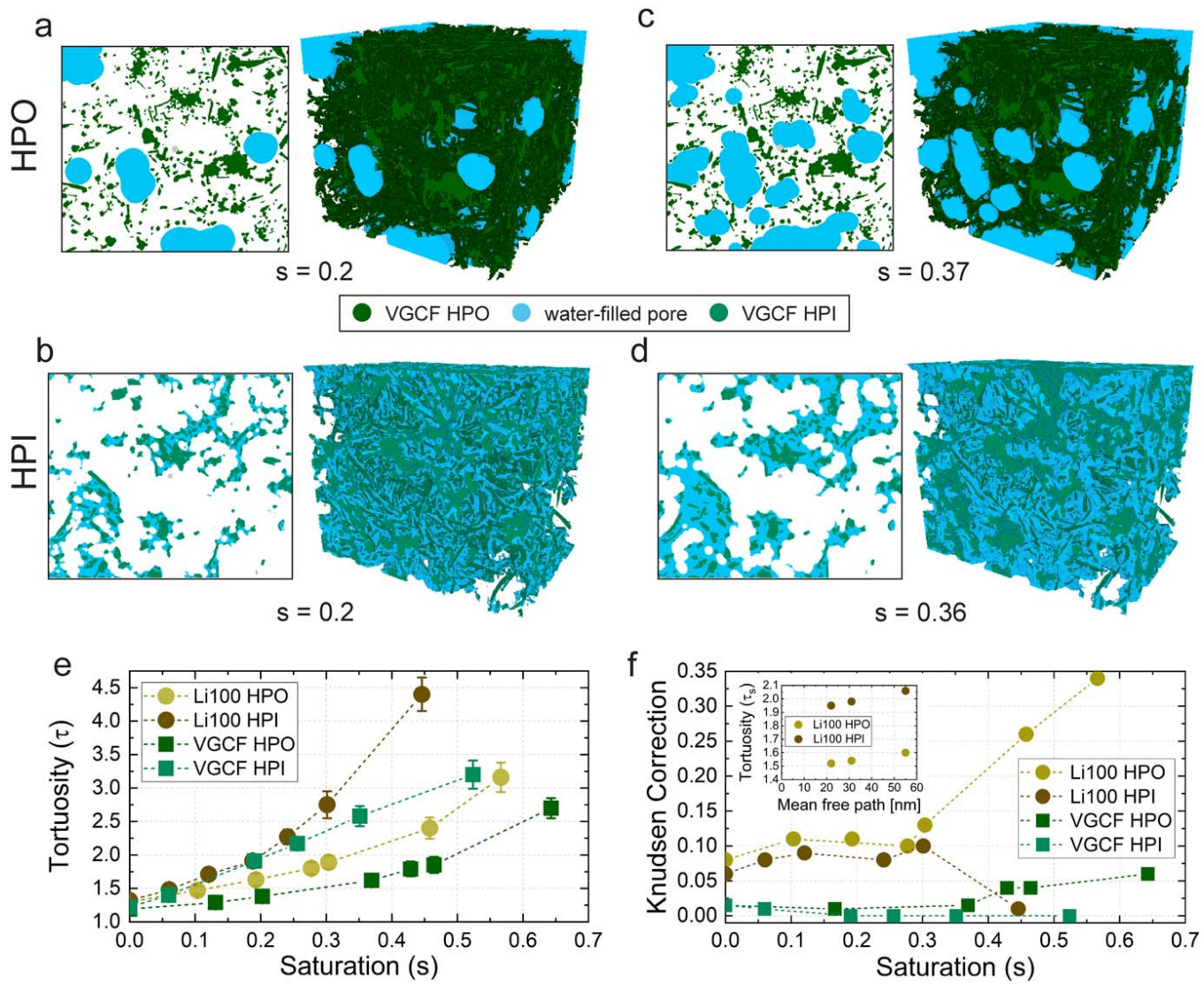

Figure 9. Two-dimensional and volumetric representation of water-filled pore structures (blue) in HPO (a), (c) and HPI (b), (d) VGCF at low and high saturation. (e) Tortuosity as a function of saturation (effective tortuosity) for the HPO and HPI clones of Li100 and VGCF. (f) Knudsen contribution on the effective tortuosity as a function of saturation and inset showing the tortuosity as a function of the mean free path at s = 0.2.

little influence on the effective tortuosity value, as shown in the inset of Fig. 9e, and therefore negligible influence on the $\tau_{s(HPI)}/\tau_{s(HPO)}$ ratio. The mean free path values correspond to the three different pressure and temperature conditions of the polarization curves in Fig. 7 and the plot in Fig. 8, resulting to a maximum $\tau_{s(HPI)}/\tau_{s(HPO)}$ variation of 0.01 that is negligible.

Conclusions

To conclude, we investigated the effective tortuosity τ_S as a function of pore network saturation using FIB-SEM volumetric analysis and limiting current measurements in an operating fuel cell. Two MPL designs were evaluated; a commercial carbon black one (Li100) and one consisting of carbon fibers (VGCF), and their hydrophobic and hydrophilic clones. The network parameters were extracted from the single cell limiting current experiments and compared to volume-based calculations using the Laplace solver TauFactor and the PuMA random walk method. A similar tortuosity value for the experimental and theoretical determination of 1.2–1.3 was found for both MPLs with the same porosity (~80%) and different characteristic pore size diameters (~100 nm vs ~800 nm).

From the FIB-SEM structures of the MPLs, a detailed study of the change in tortuosity with different pore filling was performed. Our findings show that the tortuosity for both MPL designs exhibits the larger increase with increasing saturation when narrower pores are saturated. This demonstrates the key role of narrower pore network for gas transport. The increase in tortuosity with saturation was found to be more pronounced for the MPLs, where the smallest pores were filled first (which we assume to resemble the hydrophilic MPL), as with the MPL, where the largest pores are filled first (which we assume to resemble the hydrophobic MPL). Comparing the tortuosity of the two different types of carbon materials, the MPL with the larger pores retains a higher tortuosity with increasing saturation compared to the MPL with smaller pores, which is consistent with experimental findings. This provides a tomography-based demonstration of the superiority of hydrophobic structures in wet conditions, which was demonstrated by single cell experiments.

The different Knudsen diffusion contribution between hydrophobic and hydrophilic Li100 increases with saturation but is not the main cause of the different τ_S values at operating conditions. Limiting current measurements were used to extract the oxygen transport resistance of hydrophobic and hydrophilic Li100 MPL. The ratio of volume-based calculated effective tortuosities was compared with the ratio from oxygen transport resistance measurements at the 0.2 saturation level for the hydrophobic and hydrophilic

Li100 MPLs, demonstrating the ability to use volumetric analysis to accurately infer water management properties of MPLs.

Acknowledgments

This work was supported by the Swiss National Science Foundation under award no. CRSII5_180335. Furthermore, we are grateful for the materials provided free-of-charge by Denka, Japan (Li100 acetylene black) and by 3 M Dyneon, Germany (TF 5035GZ PTFE dispersion).

ORCID

Anne Berger https://orcid.org/0000-0003-3230-4730
Hubert A. Gasteiger https://orcid.org/0000-0001-8199-8703
Vasiliki Tileli https://orcid.org/0000-0002-0520-6900

References

1. P. C. Okonkwo and C. Otor, "A review of gas diffusion layer properties and water management in proton exchange membrane fuel cell system." *Int. J. Energy Res.*, **45**, 3780 (2021).
2. G. Lin and T. V. Nguyen, "Effect of thickness and hydrophobic polymer content of the gas diffusion layer on electrode flooding level in a PEMFC." *J. Electrochem. Soc.*, **152**, A1942 (2005).
3. R. B. Bird, W. E. Stewart, and E. N. Lightfoot, *Transport Phenomena.*, ed. (Wiley, New York) (2006).
4. J. Haußmann et al., "GDL and MPL characterization and their relevance to fuel cell modelling." *ECS Trans.*, **69**, 1279 (2015).
5. M. M. Tomadakis and S. V. Sotirchos, "Effective diffusivities and conductivities of random dispersions of nonoverlapping and partially overlapping unidirectional fibers." *J. Chem. Phys.*, **99**, 9820 (1993).
6. B. Tjaden, D. J. L. Brett, and P. R. Shearing, "Tortuosity in electrochemical devices: a review of calculation approaches." *Int. Mater. Rev.*, **63**, 47 (2018).
7. J. Kozeny, *Ueber kapillare Leitung des Wassers im Boden. Sitzungsber Akad. Wiss., Wien* 136, pp 271–306 (1927), https://www.zobodat.at/pdf/SBAWW_136_2a_0271-0306.pdf.
8. N. Epstein, "On tortuosity and the tortuosity factor in flow and diffusion through porous media." *Chem. Eng. Sci.*, **44**, 777 (1989).
9. L. Holzer et al., "The influence of constrictivity on the effective transport properties of porous layers in electrolysis and fuel cells." *J. Mater. Sci.*, **48**, 2934 (2013).
10. Y. Wang and S. Wang, "Evaluation and modeling of PEM fuel cells with the Bruggeman correlation under various tortuosity factors." *Int. J. Heat Mass Transfer*, **105**, 18 (2017).
11. T. Rosén et al., "Saturation dependent effective transport properties of PEFC gas diffusion layers." *J. Electrochem. Soc.*, **159**, F536 (2012).
12. J. Fu, H. R. Thomas, and C. Li, "Tortuosity of porous media: image analysis and physical simulation." *Earth Sci. Rev.*, **212**, 103439 (2021).
13. Y.-C. Chen et al., "A method for spatial quantification of water in microporous layers of polymer electrolyte fuel cells by X-ray tomographic microscopy." *ACS Appl. Mater. Interfaces*, **13**, 16227 (2021).
14. M. Bozzetti et al., "On the role of pore constrictions in gas diffusion electrodes." *Chem. Commun.*, **58**, 8854 (2022).
15. F. Weng, C. Hsu, and M. Su, "Experimental study of micro-porous layers for PEMFC with gradient hydrophobicity under various humidity conditions." *Int. J. Hydrogen Energy*, **36**, 13708 (2011).
16. H. Ito et al., "Effect of through-plane distribution of polytetrafluoroethylene in carbon paper on in-plane gas permeability." *J. Power Sources*, **248**, 822 (2014).
17. T. Kitahara, H. Nakajima, M. Inamoto, and M. Morishita, "Novel hydrophilic and hydrophobic double microporous layer coated gas diffusion layer to enhance performance of polymer electrolyte fuel cells under both low and high humidity." *J. Power Sources*, **234**, 129 (2013).
18. D. Spernjak et al., "Enhanced water management of polymer electrolyte fuel cells with additive-containing microporous layers." *ACS Appl. Energy Mater.*, **1**, 6006 (2018).
19. T. Kitahara, H. Nakajima, and K. Ishikawa, "Microporous layer-coated gas diffusion layer for performance enhancement of polymer electrolyte fuel cells without humidification using anode gas recirculation." *J. Electrochem. Soc.*, **163**, F1366 (2016).
20. R. Schweiss, M. Steeb, and P. Wilde, "Mitigation of water management in PEM fuel cell cathodes by hydrophilic wicking microporous layers." *Fuel Cells*, **10**, 1176 (2010).
21. T. Kitahara, H. Nakajima, and K. Okamura, "Gas diffusion layers coated with a microporous layer containing hydrophilic carbon nanotubes for performance enhancement of polymer electrolyte fuel cells under both low and high humidity conditions." *J. Power Sources*, **283**, 115 (2015).
22. A. Forner-Cuenca et al., "Advanced water management in PEFCs: diffusion layers with patterned wettability: III. operando characterization with neutron imaging." *J. Electrochem. Soc.*, **163**, F1389 (2016).
23. T. Tanuma and S. Kinoshita, "Impact of cathode fabrication on fuel cell performance." *J. Electrochem. Soc.*, **161**, F94 (2014).
24. M. Islam et al., "Highly ordered nanoporous carbon scaffold with controllable wettability as the microporous layer for fuel cells." *ACS Appl. Mater. Interfaces*, **12**, 39215 (2020).
25. T. Kitahara, H. Nakajima, and K. Mori, "Hydrophilic and hydrophobic double microporous layer coated gas diffusion layer for enhancing performance of polymer electrolyte fuel cells under no-humidification at the cathode." *J. Power Sources*, **199**, 29 (2012).
26. C. Simon, J. Endres, B. Nefzger-Loders, F. Wilhelm, and H. A. Gasteiger, "Interaction of pore size and hydrophobicity/hydrophilicity for improved oxygen and water transport through microporous layers." *J. Electrochem. Soc.*, **166**, F1022 (2019).
27. P. Shrestha et al., "Hydrophilic microporous layer coatings for polymer electrolyte membrane fuel cells operating without anode humidification." *J. Power Sources*, **402**, 468 (2018).
28. C. Simon, D. Kartouzian, D. Müller, F. Wilhelm, and H. A. Gasteiger, "Impact of microporous layer pore properties on liquid water transport in PEM fuel cells: carbon black type and perforation." *J. Electrochem. Soc.*, **164**, F1697 (2017).
29. P. Thevenaz, U. E. Ruttimann, and M. Unser, "A pyramid approach to subpixel registration based on intensity." *IEEE Trans. Image Process.*, **7**, 27 (1998).
30. O. Ronneberger, P. Fischer, and T. Brox, "U-Net: Convolutional Networks for Biomedical Image Segmentation." *Medical Image Computing and Computer-Assisted Intervention – MICCAI 2015. MICCAI*, ed. N. Navab et al. (Springer, Cham) Lecture Notes in Computer Science, 9351 (2015).
31. M. Doube et al., "BoneJ: free and extensible bone image analysis in image." *J. Bone*, **47**, 1076 (2010).
32. S. J. Cooper, A. Bertei, P. R. Shearing, J. A. Kilner, and N. P. Brandon, "TauFactor: an open-source application for calculating tortuosity factors from tomographic data." *SoftwareX*, **5**, 203 (2016).
33. J. C. Ferguson, F. Panerai, A. Borner, and N. N. Mansour, "PuMA: the porous microstructure analysis software." *SoftwareX*, **7**, 81 (2018).
34. D. R. Baker, D. A. Caulk, K. C. Neyerlin, and M. W. Murphy, "Measurement of oxygen transport resistance in PEM fuel cells by limiting current methods." *J. Electrochem. Soc.*, **156**, B991 (2009).
35. F. Du et al., "Effects of PEMFC operational history under dry/wet conditions on additional voltage losses due to ionomer migration." *J. Electrochem. Soc.*, **167**, 144513 (2020).
36. M. F. Mathias, J. Roth, J. Fleming, and W. Lehnert, *Handbook of Fuel Cells.* (Wiley, New York) (2010).
37. A. Berger, M. Striednig, C. Simon, and H. A. Gasteiger, "Determination of the τ/ε-Ratio for gas diffusion substrates and microporous layers in a proton exchange membrane fuel cell." *J. Electrochem. Soc.*, **172**, 014508 (2025).
38. H. Haken, H. C. Wolf, H. Haken, and H. C. Wolf, *Molekülphysik und Quantenchemie: Einführung in die experimentellen und theoretischen Grundlagen* (Springer, Berlin, Heidelberg) 9 (1994).
39. N. Wakao and J. M. Smith, "Diffusion in catalyst pellets." *Chem. Eng. Sci.*, **17**, 825 (1962).
40. S. Reyes and E. Iglesia, "Application of percolation theory concepts to the analysis of gas-solid reactions." *Solid State Ionics*, **32**, 833 (1989).
41. I. V. Thorat et al., "Quantifying tortuosity in porous Li-ion battery materials." *J. Power Sources*, **188**, 592 (2009).
42. R. J. Millington, "Gas diffusion in porous media." *Science*, **130**, 100 (1959).
43. D.-S. Tsai and W. Strieder, "Application of heat balance integral in melting with initial subfreezing." *Int. Commun. Heat Mass Transfer*, **13**, 265 (1986).
44. M. T. Q. S. da Silva, M. do Rocio Cardoso, C. M. P. Veronese, and W. Mazer, "Tortuosity: a brief review." *Mater. Today Proc.*, **58**, 1344 (2022).
45. N. Zamel and X. Li, "Effective transport properties for polymer electrolyte membrane fuel cells - With a focus on the gas diffusion layer." *Prog. Energy Combust. Sci.*, **39**, 111 (2013).
46. A. Nabovati, J. Hinebaugh, A. Bazylak, and C. Amon, "Effect of porosity heterogeneity on the permeability and tortuosity of gas diffusion layers in polymer electrolyte membrane fuel cells." *J. Power Sources*, **248**, 83 (2014).
47. J. P. Owejan, T. A. Trabold, and M. M. Mench, "Oxygen transport resistance correlated to liquid water saturation in the gas diffusion layer of PEM fuel cells." *Heat Mass Transfer*, **71**, 585 (2014).
48. D. A. Caulk and D. R. Baker, "Heat and water transport in hydrophobic diffusion media of PEM fuel cells." *J. Electrochem. Soc.*, **157**, B1237 (2010).
49. J. Lee et al., "Investigating the effects of gas diffusion layer substrate thickness on polymer electrolyte membrane fuel cell performance via synchrotron X-ray radiography." *Electrochim. Acta*, **236**, 161 (2017).

4.3 Analysis of the MPL/GDL Interface: Impact of MPL Intrusion into the GDL Substrate

The article “Analysis of the MPL/GDL Interface: Impact of MPL Intrusion into the GDL Substrate“ was submitted in March 2023 and accepted for publication in the Journal of the Electrochemical Society in September 2023 distributed under the terms of the Creative Commons Attribution 4.0 License (CC BY). The paper was presented by Anne Berger at the 244th ECS meeting (October 2023) in Gothenborg, Sweden (abstract number: 1766). The permanent web link to the article is https://doi.org/10.1149/1945-7111/acfa26.

While the previous studies focused on gaining an understanding on, first, the structural parameters of the MPL, and second, the water saturation in different cell components depending on the MPL, this study designs a strategy to increase the water removal properties.

The MPL material was intruded into the H14 GDL-S material. The intrusion was achieved by mechanically pressing the wet MPL slurry immediately after the coating process into the GDL-S pores in a hydraulic press. This process leads to an inhomogeneous intrusion into the largest pores, which was confirmed by *ex-situ* techniques. The Li400 based MPL was chosen because of its larger pore size (peak pore size $\approx$ 220 nm) than the carbon black material (peak pore size $\approx$ 80 nm), which was added to the GDL-S during manufacturing. A clear distinction between both carbon types in SEM images was possible. Despite qualitatively revealing the inhomogeneous intrusion of the MPL material, the small section visible in the SEM cross-sectional images could not lead to a representative characterization of the intrusion. To get a representative measure of the intrusion, a simple approach of measuring the thickness difference between an unintruded GDL (here referenced as sheet-GDL) and an intruded-GDL at the same MPL carbon loading as well as a more sophisticated approach using MIP was developed. The requirement for the MIP analysis was that the MPL and the macropore GDL-S pore size range was clearly separated from one another, which was a second reason why the Li400 MPL was chosen in this study. Additionally, the MIP data needed to be analyzed by evaluating the pore volume at each pore size diameter normalized to the GDL area in cm² (in contrast to the conventionally used normalization by the sample mass). The MIP analysis revealed that the sheet-GDL only follows the surface contour of the GDL-S without any significant intrusion, while the intruded-GDL lacked significant pore space at pore diameters >5 µm compared to the pristine GDL-S.

After an *ex-situ* characterization, the GDL-S materials were tested in a single-cell fuel cell with a 5 cm² active area. The tests at different operating conditions revealed that there are two counter-acting effects. The pore filling of the large pores leads to an additional dry transport resistance, which caused a worse performance of the intruded-GDL at dry conditions compared to the sheet-GDL. When changing to con-

ditions where liquid water forms (higher pressure, lower temperature, higher RH), the performance of the intruded- and the sheet-GDL were similar, which led to the conclusion that an improved water removal ability of the intruded-GDL counter-balances the higher dry transport resistance. To tip this equilibrium, the measurements were repeated on a thicker GDL-S (H23 instead of H14), where the intruded MPL only filled 11-14% (depending on the determination method) of the GDL-S pores instead of 19-22% of the thinner GDL-S. Indeed, there was a better performance at wet conditions of the intruded-GDL.

To further analyze this improvement, *ex-situ* and *operando* XTM measurements were performed of the intruded- and sheet-GDL on the thick H23 substrate. The *ex-situ* analysis confirmed the inhomogeneous MPL intrusion into the largest pores of the GDL-S. The intrusion of the MPL material can be locally further than 80 µm into the substrate. *Operando* measurements revealed that the overall water saturation was lower for the intruded-GDL and, additionally, the maximum of the water saturation was shifted closer to the flow field side of the GDL.

Combining all these observations, the improvement of the performance of the intruded-GDL under wet conditions can be explained by a more directed water removal. The liquid water accumulates at designated locations, while the pores filled with MPL material remain free of liquid water and thus remain available for oxygen transport. While the intruded-GDL for the H23 substrate shows an improved behavior at wet conditions, it still suffers from the reduction of macropores that are now filled with MPL material. Large pores are crucial for water removal and for an enhanced oxygen diffusion to the CL. A better approach needs to be developed to create an intrusion a network of smaller pores.

Author Contributions

A.B. and Y.C. conducted the experimental work and analyzed the data (A.B.: preparation of MPLs, SEM images, MIP analysis, fuel cell testing; Y.C.: XTM measurements). J.G. and A.B. developed the process of intruding MPL material into the Freudenberg substrate. A.B. and Y.C. wrote and T.S., F.B., and H.G. revised the manuscript. All authors discussed the data, commented on the results, and reviewed the manuscript. F.B., H.G., and T.S. supervised and secured funding for the project.

Journal of The Electrochemical Society, 2023 **170** 094509

Analysis of the MPL/GDL Interface: Impact of MPL Intrusion into the GDL Substrate

Anne Berger,[1,=,z] Yen-Chun Chen,[2,=] Jacqueline Gatzemeier,[1] Thomas J. Schmidt,[2,3] Felix N. Büchi,[2] and Hubert A. Gasteiger[1]

[1]*Technical University of Munich, TUM School of Natural Sciences, Department of Chemistry and Catalysis Research Center, Chair of Technical Electrochemistry, D-85748 Garching, Germany*
[2]*Electrochemistry Laboratory, Paul Scherrer Institut, 5232 Villigen PSI, Switzerland*
[3]*Laboratory of Physical Chemistry, ETH Zürich, 8093 Zürich, Switzerland*

Interfaces are crucial for the water management in polymer electrolyte membrane fuel cells (PEMFCs). The introduction of a microporous layer (MPL) had a revolutionary effect on the water distribution by improving the interface between the catalyst layer and the gas diffusion layer substrate (GDL-S). Hence, it is vital to maximize the improvement by further characterizing and advancing the properties of the interfaces, in this case the MPL/GDL-S interface. This study aims at fabricating a GDL with an MPL that intrudes into the GDL-S, analyzing the impact on the GDL-S structure and on PEMFC performance. Mercury intrusion porosimetry (MIP) and ex situ X-ray tomography (XTM) show that the intrusion of the MPL into the hydrophobic GDL-S proceeds via the preferential filling of the GDL-S macropores, thereby reducing their size and volume fraction in the GDL-S. While an intruding MPL leads to a small performance increase under wet PEMFC operating conditions, this improvement could only be achieved by a careful management between the extent of MPL intrusion and the partial macropore blocking in the GDL-S. Furthermore, the impact of MPL intrusion on the liquid water saturation of the GDL was quantified by *operando* XTM. The results provide design guidelines for improved GDLs.

 [DOI: 10.1149/1945-7111/acfa26]

Manuscript submitted March 20, 2023; revised manuscript received August 29, 2023. Published September 29, 2023.

Light and heavy duty fuel cell electric vehicles (FCEVs) running on hydrogen will be essential for the electrification of the transportation sector. It is projected that the global passenger car FCEV fleet worldwide reaches a number of 15 million FCEVs in 2030.[1] Taking into account that the number as of 2021 was 35,000,[2] the sales of FCEVs need to grow exponentially. To pave the way, the development of FCEVs is financially supported by many major governments such as the US, China, Japan, and the European Union, while the use of commercial combustion engines (ICEs) is progressively banned.[1,3] To commercialize light-duty or passenger FCEVs, not only material improvements in terms of performance, durability, and robustness need to be accomplished, but also severe cost reductions are still necessary to be competitive.[4] Battery electric vehicles for this sector are already highly developed and are projected to replace ICEs in this category to a high percentage.[1,5] When regarding heavy-duty transportation for long driving ranges, where FCEV vehicles are expected to predominate over battery electric vehicles because of their weight advantage,[1,3] the characteristics in terms of efficiency and durability need to be boosted to meet the target of 2.7 kW/g_{PGM} (PGM=platinum group metal) at 0.7 V after a 25,000 h-equivalent accelerated stress test.[6]

To enhance the high current density performance of fuel cells based on a polymer electrolyte membrane (PEM), the activity of the catalyst itself and/or the mass transport to the catalyst need to be improved. This study focuses on the latter approach via an improvement of the mass transport through the gas diffusion layer (GDL), which typically consists of a macroporous GDL substrate (here referred to as GDL-S) coated with a microporous layer (MPL), whereby the MPL faces the catalyst layer (CL). At the cathode side, oxygen is transported through the GDL towards the CL, and product water is drained towards the flow-fields. As the reactant and product are diffusing through the same pores, water management is crucial for high current density performance. Many studies have focused on analyzing the liquid water formation and removal processes, and many aspects are already understood. However, there is still a need for better GDL materials to cover a wider range of operating conditions (dry vs wet conditions). This work focuses on the analysis of the GDL-S/MPL interface and demonstrates the importance of a directed transport path for water removal, which can serve as a guideline for designing GDLs with improved transport properties.

Interfaces play a special role in the localization of the accumulation of liquid water. The addition of an MPL to improve the CL/GDL interface had a revolutionary effect on PEM fuel cells. Weber et al. compared it to a valve, which can push water through from the electrode and towards the GDL.[7] Later on, Gostick et al. demonstrated that the MPL could lower the liquid water saturation in the GDL. They postulated that the percolation in the MPL can help to produce less dead-end water clusters and instead form more breakthrough water clusters that facilitate direct water transport through the GDL-S.[8] In subsequent work, they could verify through a computational study that the liquid water saturation at the CL/GDL interface was significantly lowered by an MPL.[9] The lower liquid water saturation at the CL/GDL interface is often explained by the saturation jump between the MPL and the GDL-S. Due to the different pore sizes in the MPL and the GDL-S, the capillary pressure is significantly different: the liquid water saturation can be expected to be lower in the smaller pores of the MPL and higher in the much larger pores of the GDL-S, with a sudden jump of the liquid water saturation at their interface.[10] The MPL saturation at wet/flooded PEM fuel cell operating conditions is usually reported to be below 10%,[11,12] while the GDL-S saturation at such conditions is on the order of 25%-50%.[11,13–15] Given the large impact of the insertion of an MPL in between the CL/GDL-S interface, a further improvement of the CL/MPL and MPL/GDL-S interface is imminent.

If the water formation at these interfaces is not controlled, interfacial effects can lead to a flooding with liquid water and hence increased mass transport resistances. Zenyuk et al. reported that an uneven boundary between MPL and catalyst layer leads to large interfacial gaps, which can serve as locations for liquid water formation.[16] When comparing a rougher to a smoother interface, they observed a higher liquid water saturation for the rougher interface, which would lead to enhanced mass transport losses.[16] However, water formation in the fuel cell is not necessarily detrimental. Localizing the flooding with liquid water to a specific location, where it does not negatively affect mass transport, can

=Equal Contribution
zE-mail: anne.berger@tum.de

mitigate the large transport losses from liquid water flooding. For the MPL, localized water formation is realized by introducing cracks[17,18] or larger pores (by means of a pore former) in the MPL.[19,20] The structure of the MPL cannot only change the liquid water saturation within the MPL but also significantly alter the saturation of the GDL-S. Nagai et al. have analyzed a Toray GDL-S with an MPL with and without pore former-induced pores (with a diameter of $\sim$10 μm) and found a lower liquid water saturation in the Toray substrate when coupled with the MPL with large pores.[13] Another example stressing the importance of localized liquid water formation was given by Csoklich et al.:[21] they have shown that through laser perforation of the GDL-S towards the flow field side, they could provide channels to redirect liquid water formation from under the rib of the flow-field towards the channel. They observed an improved performance even at the same overall liquid water saturation level when localizing the water clusters.

Consolidating all these individual studies, it is important to create an understanding of how liquid water formation can be impacted and steered to boost fuel cell performance. Adjusting the MPL/GDL-S interface is one approach to mitigate and localize flooding. Wong et al. have simulated the extent and localization of liquid water formation in a PEM fuel cell when using an MPL that intrudes into the GDL substrate (further on referred to as "intruded-GDL").[11] They have found that the thereby created introduction of small pores into the macroporous GDL substrate decreases the gas diffusivity at dry operating conditions, as the reduction of the GDL-S pore size and porosity creates an obstacle for oxygen diffusion. However, at wet operating conditions, the improved MPL/GDL-S interface formed by an MPL intruding into the GDL-S was predicted to lead to an increase in the oxygen diffusivity compared to a configuration where the MPL does not intrude into the GDL-S (further on referred to as "sheet-GDL"), showing a clear advantage. For the intruded-GDL, the overall liquid water saturation decreased and the location of the peak liquid water saturation was closer towards the flow-field side of the GDL.

In this study, we aim to get a better understanding of the impact of the MPL/GDL-S interface on the PEM fuel cell performance, especially at operating conditions where a liquid water flooding of the porous structures can be expected. We have prepared GDLs with an MPL that intrudes into the macroporous GDL-S (intruded-GDL), and are comparing them to the more typical configuration of an MPL that is located quasi perfectly on top of the GDL substrate (sheet-GDL). We characterize the intrusion of the MPL into the GDL-S by means of cross-sectional scanning electron microscopy (SEM) images, mercury intrusion porosimetry (MIP), and X-ray tomographic microscopy (XTM). The performance in a single-cell PEM fuel cell is analyzed in detail for different operating conditions, and the liquid water formation is tracked by *operando* XTM. Finally, we can draw a conclusion about the water drainage in a fuel cell and give a design guidance for GDLs with improved transport properties.

Experimental

MPL preparation.—Sheet-GDLs were prepared as shown previously.[19,22] The MPLs are based on the acetylene black Li400 (Denka; spec. surface area of 39 $m^2\,g^{-1}$ and average primary particle size of $\sim$48 nm). For binding and hydrophobization, a PTFE dispersion was used (TF 5135GZ, 58 wt% PTFE from 3M Dyneon), targeting a final PTFE content of 20 wt% in the MPL. The slurry was prepared by mixing the carbon black with deionized water (Milli-Q, 18 MΩ cm), Triton X-100 (Sigma Aldrich), and methyl cellulose (Sigma Aldrich) in an ARV-310 planetary mixer (Thinky), whereby the PTFE dispersion was added in a subsequent mixing step. For further details about the slurry preparation see Simon et al.[19]

The slurry was coated on either a Freudenberg H14 or an H23 substrate (both hydrophobically treated by the manufacturer), using a doctor blade and a stencil to yield a wet film thickness of 100 μm. The sheet-GDLs were dried immediately in an 80 °C oven for 30 min. To prepare intruded-GDLs, a GDL substrate coated with the MPL slurry was directly subjected to further treatment. The GDL-S with the wet MPL coating was first sandwiched between two Kapton® sheets, which were then sandwiched between two Gylon® sheets (Garlock, USA), and finally placed between two stainless steel metal plates. This assembly was subsequently placed in a hot-press device (Dr. Collin GmbH, Germany), where it was subjected to a pressure of 0.7 MPa at a temperature of 40 °C for 5 min. The thus prepared intruded-GDL was also dried at 80 °C for 30 min. In a final preparation step, the coated GDLs were subjected to a multi-step heat treatment procedure under air, with a maximum temperature of 380 °C, as described by Simon et al.[19] This treatment removes the slurry additives (methyl cellulose and Triton X-100) and sinters the PTFE.

Scanning electron microscopy.—Sample preparation for Scanning Electron Microscopy (SEM) was performed using an IB-19520CCP cross-section polisher (JEOL, Japan). The samples were ion-milled at an accelerating voltage of 6 kV for 5.5 h at a temperature of −40 °C using an argon source. SEM images were taken on a JSM-IT200 InTouchScope™ (JEOL, Japan) using an acceleration voltage of 10 kV.

Mercury intrusion porosimetry.—Mercury intrusion porosimetry (MIP) measurements were performed with an Autopore Instrument (9600, Micromeritics Instrument Corporation, USA) using a penetrometer (sample holder) with a 3 ml bulb and 0.096 ml stem volume. To reduce the influence of the hydrostatic pressure of Mercury in the low-pressure region, the pressure range of 5–40 psi was measured in a horizontal penetrometer position, while the pressure range from 40–61,000 psi was obtained in a vertical penetrometer position. The lower pressure limit of 5 psi was constrained by the filling procedure of the customized penetrometer. The pressure steps were chosen to achieve an even spacing on a logarithmic scale, with 25 points per decade in a given pressure range. The pressure at each pressure step was held constant until the intrusion rate was below 0.001 $\mu L g^{-1} s^{-1}$. To convert the pressure p to a pore diameter d_{pore}, the Washburn equation was applied:

$$d_{pore} = -\frac{4 \cdot \gamma_{Hg} \cdot \cos\theta}{p} \qquad [1]$$

with the surface tension of Mercury γ_{Hg} (0.480 N m^{-1}) and the contact angle θ (140°). The stem volume usage was always between 36%–80% for all measurements. Samples were added in a way that there was no stacking of the GDL layers.

Usually, the cumulative intrusion volume v_{pore} is given in units of ml g^{-1}. In this work, however, the data is given as an areal cumulative intrusion volume v^*_{pore} in units of $mlcm^{-2}_{GDL}$. The conversion of units was achieved by considering the sample mass m and the area of the GDL A_{GDL}:

$$v^*_{pore}\left[\frac{mL}{cm^2_{GDL}}\right] = v_{pore}\left[\frac{mL}{g}\right] \cdot \frac{m\,[g]}{A_{GDL}\,[cm^2_{GDL}]} \qquad [2]$$

The porosity ε of the sample can be calculated using the cumulative pore volume v_{pore} and the skeletal density $\rho_{skeletal}$:

$$\varepsilon = \frac{v_{pore}\,[mL/g]}{v_{tot}\,[mL/g]} = \frac{v_{pore}\,[mL/g]}{v_{pore}\,[mL/g] + \dfrac{1}{\rho_{skeletal}\,[g/mL]}} \qquad [3]$$

where v_{tot} represents the total sample volume per sample mass.

In addition to the total porosity ε, we would like to introduce the macropore-porosity $\varepsilon_{macropore}$, which is a function of the pore volume of the macropores $v_{macropore}$ (excluding the micropores from any carbon black additive):

$$\varepsilon_{\text{macropore}} = \frac{v_{\text{macropore}}[\text{mL/g}]}{v_{\text{tot}}[\text{mL/g}]} = \frac{v_{\text{macropore}}[\text{mL/g}]}{v_{\text{macropore}}[\text{mL/g}] + \frac{1}{\rho_{\text{skeletal}}[\text{g/mL}]}} \quad [4]$$

These two porosities (ε and $\varepsilon_{\text{macropore}}$) were only evaluated for the two GDL substrates (H14 and H23). The pore volume of the macropores $v_{\text{macropore}}$ was evaluated for pores larger than 5 μm; the reason for selecting this value is given in the mercury intrusion porosimetry section.

Ex situ X-ray tomographic microscopy (XTM) image acquisition.—All tomographic data were obtained by a computed tomography (CT) scanner (Phoenix nanotom m; General Electric, Germany) with a Phoenix|X-ray micro-focus tube. The X-ray tube acceleration voltage was 80 kV and the current 280 μA. Flat field correction was done prior to each tomographic scan. The distance between the sample and the X-ray focal point was 16.2 mm, and the distance between the detector and the X-ray focal point was 450 mm, giving a magnification of 27.8 and voxel edge length of 3.6 μm. During the scan, the sample holder and samples were completely in the field of view (FoV) of the detector at all sample rotation angles in order to avoid local tomography; this is an essential step to allow images across different scans to be comparable to one another. For tomographic image acquisition, every three projections (of the same rotation angle) were averaged to produce one radiographic image for later reconstruction, while the subsequent fourth projection was skipped to prevent movement artifacts during image recording. The X-ray exposure time for each projection was 1.5 s. A total of 2400 images were used for tomographic reconstruction. This experimental procedure resulted in an overall scan time of 4 h.

MPL segmentation in the XTM analysis.—The 32-bit tomographic image stacks of GDLs were first rotated in ImageJ using the "Transform" function (interpolation: bilinear) in order to align the surface of the MPL to the in-plane direction. The image stacks were then transformed to 8-bit and subsequently filtered with the edge-preserving "Bilateral Filter" provided in ImageJ with a spatial radius of 3 pixels and a range radius of 30 intensity values (in this case, grayscale values of the 8-bit images) to reduce image noise while separating the fiber, MPL, and void phases. For both GDLs, image segmentation by manual selection of sets of threshold values was performed. A set of threshold values consists of a lower boundary value and an upper boundary value. Upon thresholding, all pixels (or voxels) that have values within this range were assigned with the grayscale value 255, while all pixels (or voxels) with a value outside of this range were assigned the grayscale value 0. This procedure resulted in a binary image. One or two sets of threshold values were used to capture the MPL phase at different through-plane distances across the whole GDL thickness, because the grayscale values that represent the MPL phase change in the through-plane direction and one constant set of threshold values was not enough to capture the MPL phase throughout the GDL. The segmented images contained artifacts from GDL fibrous structure: they were cleared by performing the ImageJ "Erode" function once, followed by applying the ImageJ macro "MATLAB 3D Clearing" with a limit of 1000 voxels and with a connectivity of 6. Additionally, the two surfaces of the GDL are prone to edge enhancement artifacts, thus the MPL phase here was manually selected based on the bilateral filtered grayscale GDL image using ImageJ "Wand Tool" with tolerance levels of 4–7 and the mode setting "legacy."

Based on different threshold values for the MPL phase, the MPL segmentation results differ and three possible segmentation results are shown for the intruded-GDL in Fig. 1, labeled as "high threshold," "calibrated," and "low threshold." Details on the threshold values and the clearing processes are given in the appendix. The high threshold segmentation (red line) overestimates the MPL phase in the GDL substrate, which is confirmed by image inspection, showing that the void phase in the GDL (at a through-plane distance of ca. 110–220 μm) is often regarded as the MPL phase. However, it is challenging to judge the representativeness of lower threshold values only by inspection of the XTM images, as the GDL-S pores (void phase) do not have a constant gray scale value. Therefore, the averaged MPL intrusion depth of 27 μm obtained from the thickness measurement (TM) (see Table I) is used for calibration of the H23 substrate segmentation. The segmentation that gives the closest average intrusion depth estimation without significant overestimation of the MPL phase (the green curve in Fig. 1; the quality of segmentation is discussed below) is considered reasonable. All XTM analyses of the intruded-GDL are consequently based on this "calibrated" segmentation result.

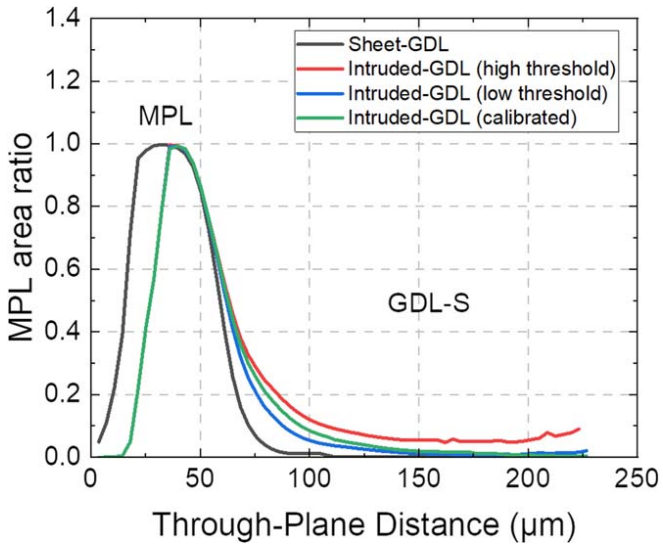

Figure 1. MPL area percentage profiles along the through-plane distance from the top of the MPL to the bottom of the GDL-S for the sheet-GDL and for the intruded-GDL based on the H23 GDL-S. For the intruded-GDL, the MPL area ratio is shown for three segmentation threshold values (high, calibrated, low). The calibrated curve uses thresholds to achieve the same average intrusion depth of the MPL into the GDL-S that was determined by a macroscopic approach based on thickness measurements (as will be explained below).

The quality of the MPL segmentation based on the "calibrated" approach is exemplified in Fig. 2. Comparing the in-plane GDL grayscale images of Figs. 2a–2c with the segmented MPL phase in green color of Figs. 2g–2i, respectively, it is judged that the MPL phase in Figs. 2a-2c is well captured by the MPL segmentation shown in Figs. 2g–2i. Hence, we believe that the segmentation quality is reasonable. However, the MPL phase is slightly underestimated, especially at the MPL/GDL-S interface, as seen in Fig. 2h. It is both the result of the erosion process (i.e., removing the boundary pixels of the segmented MPL phase, an essential process to remove image artifacts from noise) and the limited voxel resolution. These two reasons combined cause blurring at the boundaries of the GDL-S fibers and the MPL, leading to segmentation limitations. Such error cannot be further reduced by image erosion or dilation (i.e., adding an additional layer of pixels to the object boundary), because of the limited image resolution (voxel edge length = 3.6 μm).

MPL thickness heterogeneity.—The MPL phase determined by the "calibrated" segmentation is an 8-bit three-dimensional image stack (MPL image), where the grayscale value (GSV) of voxels of the MPL phase is 255, while the GSV of the other voxels are zero (binary image). Using imageJ process "Divide" (image division by a

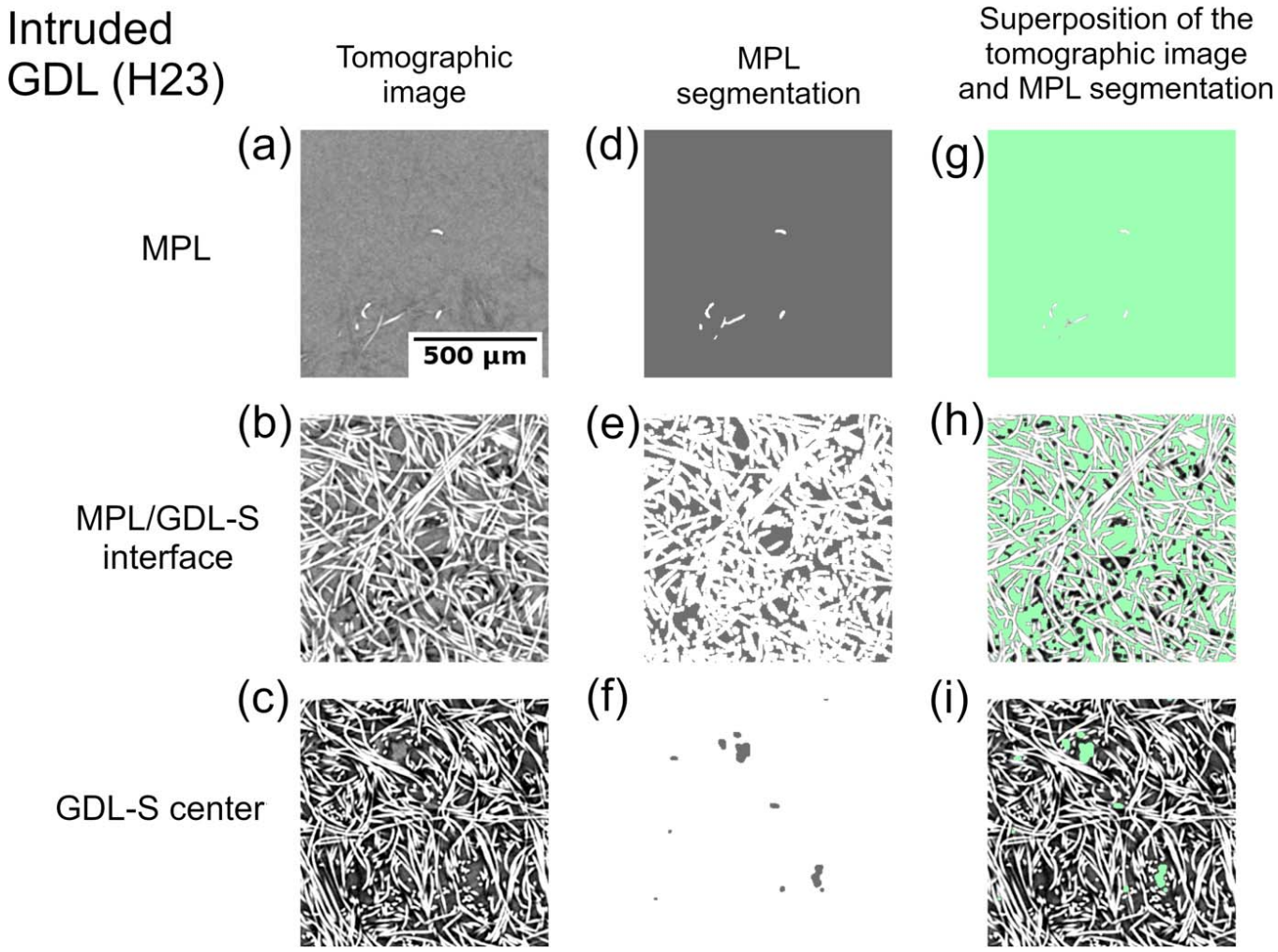

Figure 2. MPL segmentation based on the "calibrated" threshold values (see Fig. 1) for the H23-based intruded-GDL: (a)–(c) tomographic images of the MPL, MPL/GDL-S interface and of the GDL-S, respectively; (d)–(f) MPL segmentation (binary images) at each layer; (g)–(i) superposition of the tomographic image and MPL segmentation, whereby the MPL segmentation is colored green for better visualization. The segmentation quality can be inspected by comparing the tomographic images of (a)–(c) with (g)–(i).

constant scalar number) by a value of 255, the MPL phase is assigned the number 1. Subsequently, using ImageJ function "Z-Project" with projection type "Sum Slices" on the MPL image, the projection of MPL phase in the through-plane direction (z-direction) is obtained. Since the voxel edge length is 3.6 μm, the projection image is multiplied by a value of 3.6 using ImageJ process "Multiply" (image multiplication by a constant scalar). The obtained image is the "thickness map" of the MPL. Coloring of the thickness maps of the MPL is done by applying ImageJ LUT (Physics) onto the thickness map and set the display range (in ImageJ "Brightness and Contrast") to be between 0 and 80 μm. A calibration bar is added using ImageJ tool "Calibration Bar." The thickness heterogeneity is defined to be the standard deviation of the MPL thickness map (unit: μm). This parameter is thus subject to the voxel size of the CT scan and can only be compared across different MPL images when the voxel size is the same (i.e. 3.6 μm).

XTM based GDL substrate pore size distribution.—The influence of MPL intrusion on the GDL-S pore size distribution (PSD) is analyzed by a careful inspection of the intruded-GDL. The intruded-GDL is segmented by thresholding, which separates the MPL and fiber phases. After the segmentation, the MPL phase can be either removed from the reconstruction or can be regarded as a solid phase. The PSD of both configurations is obtained using the ImageJ function "Local Thickness."

XTM based GDL porosity profiles.—The through-plane porosity profiles of the GDLs are based on the volume ratio of the MPL phase and the void phase at each through-plane position in the GDLs. The porosity of the MPL phase is assumed to have a constant value of 68%, using the MIP-derived value reported by Simon et al. for analogously prepared Li400 carbon based free-standing MPLs.[19] Therefore, the GDL porosity is:

$$\varepsilon = \varepsilon_{\mathrm{XTM}} + (0.68 \cdot \phi_{\mathrm{MPL}}) \qquad [5]$$

using the void volume fraction $\varepsilon_{\mathrm{XTM}}$ and the MPL volume ratio ϕ_{MPL} as measured by XTM. The porosity profiles are necessary to derive the saturation profiles of liquid water for the *operando* XTM PEM fuel cell measurements.

5 cm^2 single-cell PEMFC measurement setup and analysis procedures.—Differential-flow single-cell PEMFC measurements were conducted using an in-house-designed hardware with aluminum endplates (adapted from the hardware design of Fuel Cell Technologies, USA) in combination with customized graphite flow fields (Poco Graphite, USA). The flow-field design is based on 7 channels (0.5 μm wide, 0.8 μm deep), which are arranged in one serpentine adding up to an active area of 5 cm^2 in a square configuration (land width = 0.5 μm). Details about the flow-field design are given in Ref. 23. All cells were assembled using a commercial catalyst coated membrane (CCM) from Gore (Primea

Mesga W. L. Gore & Associates A510.1/M715.18/C580.4 equipped with a sub-gasket) with cathode and anode loadings of 0.4 mg_{Pt}/cm^2 and 0.1 mg_{Pt}/cm^2, respectively. A commercial Freudenberg H14C10 GDL was used as the anode GDL. The cell compression was realized using a hard-stop sealing by applying a gasket of the appropriate thickness (Fiberflon GmbH & Co. KG). The cell compression, which varied between 13%–15%, was chosen to lead to a contact pressure of 1.4–1.6 MPa, which was confirmed using a pressure sensitive film (Prescale LLW, FUJIFILM).

The single-cells were operated using an automated fuel cell test station (G60, Greenlight Innovation, Canada) equipped with an additional potentiostat (Reference 3000, Gamry, USA) for electrochemical impedance spectroscopy (EIS) measurement. As a CCM break-in procedure, the cell was operated at H_2/air flows of 1390/3320 nccm at 80 °C, 100% relative humidity (RH), and 150 kPa_{abs}, while being subjected to 10 cycles of the following 3 voltage-hold steps: 45 min at 0.6 V, 5 min at open circuit voltage (OCV), and 10 min at 0.85 V. After the break-in procedure and after a set of two H_2/air polarization curves and two sets of limiting current measurements, a recovery step was implemented, consisting of a 2 h long voltage-hold at 0.3 V at 40 °C, 100% RH, and 170 kPa_{abs} under H_2/air flows of 2000/5000 nccm.

Differential-flow H_2/air (2000/5000 nccm) polarization curves were recorded in potentiostatic mode from 0.9 V to 0.05 V using 0.05 V steps, with the OCV point being recorded last. The voltage was held for 5 min to ensure stabilization, and the data from the last 30 sec of each voltage step was averaged. Afterwards, an EIS measurement was performed in "hybrid mode" with a voltage perturbation of 10 mV in a frequency range from 100 kHz to 10 Hz. The high frequency resistance (HFR) was determined from the x-axis intercept in the Nyquist plot.

Limiting current measurements were performed by diluting oxygen in nitrogen at the cathode side to achieve O_2 concentrations of 0.5%, 1%, 2%, 4%, 8%, 12%, 16%, 21%, 24%, and 28%, similarly to what was done by Baker et al.[24] and Simon et al.,[23] using a total flow rate of 5000 nccm. Pure H_2 (2000 nccm) was used at the anode side. To scan the mass transport limited current regime, the voltage was set to 0.3 V, 0.15 V, 0.1 V, and 0.05 V and held for 2 min at each voltage step before averaging the last 15 s for each data point. To convert the limiting current data into an oxygen transport resistance R_{T,O_2}, the following equation based on Fick's law and Faraday's law was used:

$$R_{T,O_2} = \frac{4 \cdot F \cdot x_{O_2,dry}}{i_{lim}} \cdot \frac{p_{abs} - p_{H_2O}}{R \cdot T_{cell}} \quad [6]$$

with the Faraday constant F, the dry oxygen mole fraction $x_{O_2,dry}$, the limiting current i_{lim}, the absolute pressure p_{abs}, the water partial pressure p_{H_2O}, the gas constant R, and the cell temperature T_{cell}.

Operando XTM fuel cell measurements.—The *operando* fuel cell imaging was carried out in the same laboratory CT scanner that was used for the dry GDL characterization (Phoenix nanotom m; General Electric, Germany). An in-house made humidifier[25] was placed within the CT scanner and connected to the H_2/air supply, with the gases being humidified by passing each reactant through Nafion® tubing immersed in water at a controlled temperature. The *operando* XTM fuel cell with an active area of 0.16 cm^2 was operated under differential-flow conditions (300 nccm H_2 and air); it is based on a two-channel flow-field design with a channel and land width of 0.8 mm (for details see Hong et al.[26]). The *operando* XTM fuel cell was operated at 49 °C, atmospheric pressure, and reactant inlet dew points of 47.5 °C (corresponding to 93% RH).

Prior to imaging at the specified conditions, the cells were conditioned at room temperature (ca. 26 °C) with H_2/air humidified at a dew point of 26–32 °C with the following sequence that was repeated for 10 times: constant 0.6 V for 45 min, 0.95 V for 10 min (no current), and 0.85 V for 5 min. To complete the conditioning procedure, multiple polarization curves were carried out until steady-state performance was achieved. For the *operando* X-ray tomographic imaging, the fuel cells were operated at 0.5 A cm^{-2} for at least 30 min prior to the start of X-ray tomographic imaging, assuring to have reached steady-state.

For the XTM measurements, the X-ray tube voltage was 80 kV and the current was 300 μa. Flat field correction was done prior to image acquisition and local tomography was avoided. The distance between sample and the X-ray focal point was 12 mm while the distance between the detector and the X-ray focal point was 400 mm, giving a magnification of 33.3 and a voxel edge length of 3.0 μm. At each rotation angle, one projection was taken and the subsequent projection was skipped to prevent motion artifacts. The exposure time for each projection was 0.5 s and a total of 2200 projections were scanned for later image reconstruction, resulting in a total acquisition time of ~37 min per scan.

The cell performance after all tomographic scans (cumulative X-ray exposure time of ~290 min) was assessed using the cell with the intruded-GDL, comparing the H_2/air polarization curves before and after the XTM measurements in order to judge possible radiation damage. As shown in the appendix, the performance degradation was judged to be minor with this radiation dose. Since the radiation damage is expected to primarily influence the CCM performance, the radiation damage for the sheet-GDL cell was assumed to also be minor, as the cells with the sheet-GDL and the intruded-GDL used the same CCMs and underwent the same dose and operation conditions. Hence, the XTM results are believed to be representative of the *operando* conditions during PEMFC operation.

Quantification of the liquid water volume fraction and saturation operando XTM.—Despite using a polychromatic X-ray source for tomographic image acquisition, the liquid volume fraction (LVF) of water in the MPL and GDL can still be quantitatively derived using an empirical calibration curve.[27] It was established that there is a linear relationship between the grayscale values and the linear attenuation coefficients of the phases constituting a GDL (viz., carbon, PTFE, and air in the voids) and water, using the acquisition parameters presented for the nanotom m CT scanner. Therefore, the LVF derivation is based on image subtraction. First, *operando* PEMFC images (wet images) and dry state PEMFC images (dry images) were obtained. The wet images were then aligned to the corresponding dry images using 3Dslicer3 with the "rigid" registration function, where no image deformation occurred during the alignment. However, to account for local membrane swelling during operation, which distorts local structures, an additional "affine" registration function step was applied. Dry images were then subtracted from the aligned wet images. The result is referred to as the difference image and gives the LVF distribution of water in the GDL (i.e., in the MPL and the GDL-S), since the only difference in the *operando* images and the dry images is the presence of liquid water. When the difference images are normalized by the average grayscale value (GSV) of the pure water phase, the resultant images provide the water volume fraction in each voxel. To reduce image noise and to visualize the LVF, a mean filter with a radius of 5 pixels and ImageJ "LUT" (Physics) were applied to the normalized difference images, rendering the "LVF maps." The LVF profiles are directly measured from the LVF maps.

With the porosity profile of the GDL obtained by using Eq. 5 at each through-plane distance for the phase segmented GDL, the saturation profile is obtained by dividing the liquid volume fraction (LVF) profile of water at each through-plane position by the GDL (both MPL and GDL-S) porosity at that position.

Results

In this work, sheet- and intruded-GDLs are prepared on two GDL substrates of ~140 μm (H14) and ~200 μm (H23) thickness (determined using a Mitutoyo thickness gauge). The first part of this section identifies the structure of the intruded-GDL based on the

H14 substrate using scanning electron microscopy (SEM) and mercury intrusion porosimetry (MIP) and evaluates the effect on the fuel cell performance. After having established the limitations and benefits of the intruded-GDL on the thin substrate, the intruded-GDL based on the thicker H23 substrate is analyzed using the above mentioned methods (SEM, MIP, fuel cell performance) with the addition of X-ray tomographic microscopy (XTM) in order to further investigate the spatial distribution of the intruding MPL within the GDL substrates. In a final step, the impact on water saturation is demonstrated using the H23 substrate. Based on these results, a possible water transport mechanism in the GDLs owing to MPL intrusion is proposed.

MPL intrusion for sheet- and intruded-GDLs (H14 GDL-S based) by SEM.—Since a water-based slurry is used for the preparation of the MPL, the hydrophobic treatment of the GDL substrate prevents a penetration of the MPL coating slurry into the GDL substrate structure. Therefore, the intrusion of the MPL slurry required for the preparation of an intruded-GDL is only possible by applying a mechanical force directly after the coating process (see Experimental section). This observation is consistent with experiments conducted with Toray GDL substrates with and without PTFE treatment, where the PTFE treatment significantly decrease the intrusion depth of a model fluid.[28] Bock et al. have achieved MPL intrusion by mechanical force via a different approach, where they used a stencil to press the slurry into the GDL-S.[29] However, their method pressed all MPL slurry into the substrate without leaving an MPL layer on top. Our here described method to prepare an intruded-GDL by one coating step creates a partially intruded MPL (characterized by an intrusion zone) and an additional remaining MPL layer on top of the GDL substrate. In this case, the partial intrusion of the MPL leads to a $\sim$14 μm lower thickness of the intruded-GDL (i.e., of the thickness of the MPL-coated GDL-S) when compared to a sheet-GDL (with the MPL sitting on top of the GDL-S) at identical MPL coating mass, demonstrating that a significant portion of the MPL had intruded into the GDL substrate.

The structure of the here prepared sheet- and intruded-GDL samples as well as the degree of MPL intrusion is first inspected by scanning electron microscopy (SEM). Figure 3 shows SEM images of the cross-sections of the sheet-GDL (Fig. 3a/c) and of the intruded-GDL (Fig. 3b/d). It can be observed that for the sheet-GDL the MPL is indeed located largely on top of the GDL-S (Fig. 3a), mostly apparent from the zoomed-in view in Fig. 3c that allows to distinguish between the Li400 based MPL and the carbon black material that was imbibed as part of the fabrication process of the GDL substrate:[30,31] while the Li400 based MPL shows pores that are beginning to be resolvable at this image magnification, the carbon black used by Freudenberg for the manufacturing of the GDL-S is represented as a smooth area in the picture, with pore sizes smaller than the image resolution. During the MIP analysis later in this study, the pore sizes of the different carbon black materials can be clearly distinguished. Based on this difference in pore size, the interface between the GDL-S and the Li400 based MPL is indicated by the red line in Fig. 3b (as well as in Fig. 3d for the intruded-GDL).

The intruded MPL has a thinner non-intruded MPL on top of the GDL-S, as MPL material penetrates into the GDL substrate (see Fig. 3b/d), so that the overall intruded-GDL is thinner than the sheet-MPL by a macroscopically measured thickness difference Δl (marked in Fig. 3f and determined with a Mitutoyo thickness gauge). It is also visible from Fig. 3b/d that the intrusion is not uniform but somewhat inhomogenous, mostly intruding into the larger pores of the GDL-S, which can be rationalized by the preferential intrusion of the aqueous MPL slurry into the larger pores of the hydrophobized GDL substrate. This hypothesis will be analyzed and validated by the following ex situ MIP and XTM analyses. Determining an average MPL intrusion thickness from SEM images is unfortunately not possible, as it is only possible to image a small and not sufficiently representative fraction of the MPL/GDL-S interfacial region.

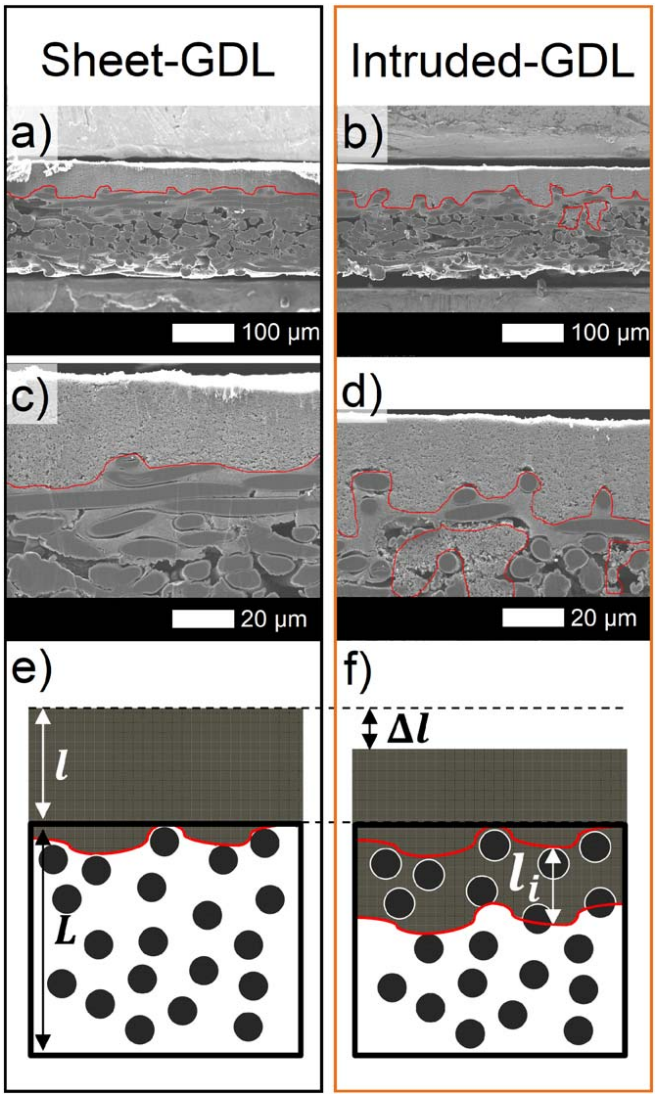

Figure 3. SEM cross-sectional images of the sheet-GDL (a), (c) and of the intruded-GDL (b),(d) based on the H14 GDL-S: while for the sheet-GDL the MPL is essentially sitting on top of the GDL-S, the intruded-GDL shows clear signs of an inhomogeneous intrusion of the MPL into the GDL-S. The red line indicates the interface between the MPL and the GDL-S. Panels e and f show a sketch of the sheet- and of the intruded-GDL, respectively, marking the following geometrical parameters: (i) the thickness L of the GDL substrate; ii) the thickness l of the MPL of the sheet-GDL; (iii) the absolute thickness difference Δl between the sheet-GDL and the intruded-GDL, caused by the partial intrusion of the MPL into the GDL-S in the latter case; and, iv) the intrusion depth l_i, which is defined as the thickness of the MPL intrusion zone in the GDL-S, referenced to the rough GDL-S surface and simplified as if it were a homogeneous intrusion. As described in the text, l_i can be determined via MIP (in this case denoted as $l_{i,MIP}$; see Eq. 8) or via a macroscopic thickness measurement (TM) approach, determining the thickness difference Δl between the sheet- and the intruded-GDL (denoted as $l_{i,TM}$; see Eq. 11).

Figures 3e and 3f show sketches to visualize the relevant dimensions that will be used in the following to quantify the average MPL intrusion depth. Figure 3e shows a sketch of a sheet-GDL, depicting a GDL-S with a thickness L and an MPL with a thickness l. The sketch in Fig. 3f shows an intruded-GDL, depicting an average intrusion depth l_i referenced to the rough surface of the GDL-S. The difference in overall thickness (GDL-S + MPL) between the sheet-GDL and the intruded-GDL is defined as Δl. As will be outlined below, the average intrusion depth l_i can be determined either from MIP measurements (in this case denoted as $l_{i,MIP}$) or by using a

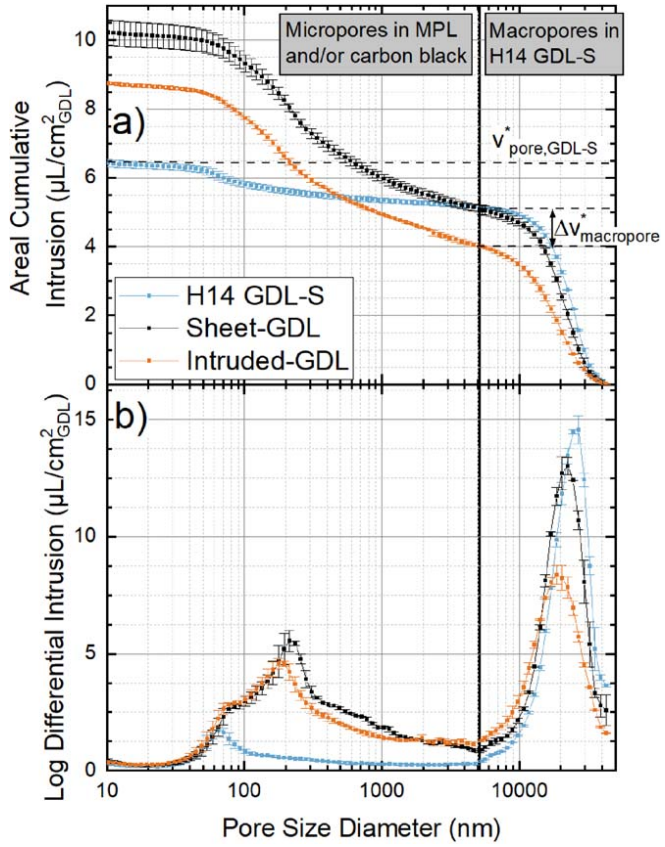

Figure 4. Mercury intrusion porosimetry results for the H14 GDL-S (blue) as well as for the H14-based sheet-GDL (black) and intruded-GDL (orange), whereby the intrusion of Mercury is given in units of $\mu l/cm^2_{GDL}$. (a) Cumulative intrusion volume referenced to the GDL area: the missing macropore volume $\Delta v^*_{macropore}$ in the intruded-GDL compared to the GDL-S represents the MPL intrusion depth of the intruded-MPL. (b) Log differential intrusion: the vertical black line at 5 μm pore size diameter marks the approximate distinction between the pore size region of the macropores in the GDL-S and the micropores in both the MPL and the original carbon black filler of the GDL-S. The error bars represent the standard deviation of two independent measurements.

macroscopic thickness measurement (TM) based approach, by which Δl is converted into an average intrusion depth (denoted as $l_{i,TM}$).

MPL intrusion for sheet- and intruded-GDLs (H14 GDL-S based) by MIP.—A reasonable method to estimate the average MPL intrusion depth is mercury intrusion porosimetry (MIP), which allows to quantify the fraction of the GDL-S pores which are filled by MPL material. Figure 4 shows the results of the MPL analysis for the H14 GDL-S as well as of the H14-based sheet- and intruded-GDLs. For this quantitative analysis to deliver meaningful results, two criteria need to be met: First, the pore sizes of the macropores belonging to the GDL-S need to be clearly separated from the pore sizes of the MPL structure (as discussed below, this is closely satisfied). Second, the area of the sampled GDL needs to be clearly defined to be able to extract the intrusion volume per GDL area. If the GDL area would not be defined for the MIP measurement, the mass ratio of MPL to GDL-S would need to be known as well as the areal weight of the GDL-S. Therefore, in contrast to the usual representation of the cumulative intrusion in units of $\mu l/g$, Fig. 4a displays the cumulative mercury intrusion in units of $\mu l/cm^2_{GDL}$. Correspondingly, Fig. 4b shows the representation of the log differential intrusion in $\mu l/cm^2_{GDL}$.

The cumulative Mercury intrusion curve of the H14 GDL-S (blue) shows a strong increase in the cumulative intrusion volume with increasing Mercury pressure between the largest measured pore of 43 μm and ~5 μm, followed by a smaller increase between ~200 and ~60 nm (Fig. 4a). These observations are reflected in the log differential intrusion plot (Fig. 4b), showing a large macropore volume with a peak at ~25 μm and a smaller micropore volume with a peak at ~80 nm (note that the area under the plot in Fig. 4b is directly proportional to the pore volume). Here, the macropores represent the pores of the fibrous network of the H14 GDL-S, while the micropores represent the pores formed by the carbon black filler in the Freudenberg GDL substrate, which is added during the impregnation in the manufacturing process.[30,31] These two regions are clearly separated, with a minimum in the pore size distribution at ~5 μm (see left end of macropore peak in Fig. 4b), which is marked by the vertical black line in Fig. 4. Based on this separation, we define that all pores above 5 μm are part of the macroporous network of the H14 GDL-S, making up the macropore volume $v^*_{macropore,\ GDL-S}$ in the H14 GDL-S. As commented above, this clear separation between the macropore and the micropore regions of the H14 GDL-S will later on allow to determine the MPL intrusion depth of the intruded-MPL.

The cumulative mercury intrusion curve of the sheet-GDL (black) in the macropore region of the H14 GDL-S (i.e., for pores $\geqslant$5 μm) is very similar to that of the H14 GDL-S without MPL. From SEM images (Fig. 3a/c), one can deduce that the MPL of the sheet-GDL intrudes into the surface roughness of the GDL-S. While surface roughness can, in principle, be detected at the respective pore diameter of the surface features, the MIP measurements shown in Fig. 4 could only be started at a mercury pressure corresponding to a pore diameter of 43 μm (acc. to Eq. 1), which does not capture the surface roughness features and thus only represents a bulk property. Clearly, however, the cumulative intrusion curve for the sheet-GDL is left-shifted to slightly smaller pores compared to the GDL-S without MPL, which can be attributed to the loss of some of the largest pores formed through the reduction of surface roughness at the MPL/GDL-S interface. At the same time, it can be seen that the difference in the overall macropore volume for pores of $\geqslant$5 μm (determined to be the macropore range for the H14 GDL-S) of the sheet-GDL and the H14 GDL-S is essentially identical (see intersection of the black and blue lines with the vertical black line in Fig. 4a, so that the MPL intrusion depth l_i of the sheet-GDL is negligible (as sketched in Fig. 3e).

On the contrary, the cumulative mercury intrusion curve of the intruded-GDL (orange) in the macropore region of the H14 GDL-S ($\geqslant$5 μm) differs significantly from that of the H14 GDL-S curve: the cumulative intrusion curve of the intruded-GDL is strongly left-shifted to smaller pores and the overall pore volume at $\geqslant$5 μm is reduced. The loss in pore volume in the GDL-S macropore regime and the substantial loss of larger pores becomes especially apparent in Fig. 4b, where the area under the curve is proportional to the pore volume. These MIP results confirm our initial hypothesis that the MPL material in the intruded-GDL predominantly fills into the larger pores, consistent with the inhomogeneous intrusion observed in the SEM images (Fig. 3b/d). The extent of macropore filling of the GDL-S by the intrusion of the MPL can be determined from the data in Fig. 4a from the difference of the macropore volume at $\geqslant$5 μm between the H14 GDL-S and the intruded-GDL, marked as $\Delta v^*_{macropore}$ in the figure.

A comparison of the microporous region in Fig. 4b, reflecting the pore size region of the MPL and the carbon black filler, the pore size distribution of the sheet- and the intruded-GDL overlay reasonably well. It only appears that a small fraction of the larger pores (~200 nm–1 μm) is missing for the intruded-GDL, which we ascribe to the plastic deformation upon compression of the MPL coating during the preparation of the intruded-GDL (at 0.7 MPa; see Experimental section). When estimating the reduction of MPL porosity upon compression, we can regard the differences in the area under the curve in the micropore region in Fig. 4b, which is proportional to the pore volume: the differences in the area under the curves between the sheet- and the intruded-GDL is less than 3%, so that the difference in MPL properties such as porosity and

interconnectivity of the pore network are believed to be equally minor.

In the following, the MIP result in Fig. 4 will be used to estimate the MPL intrusion depth l_i of the intruded-GDL. For this analysis, the porosity of the H14 GDL-S has to be evaluated first. The overall gravimetric intrusion for the H14 GDL-S is 0.87 ± 0.02 ml g^{-1} (determined from the MIP data underlying Fig. 4a). Using a skeletal density of 1.772 g cm^{-3} for a Freudenberg substrate with a similar PTFE content (H2315 T10A)[32] and Eq. 3, the overall porosity is determined to be 61%. When disregarding the smaller pores and only using the gravimetric intrusion of the macropores larger than 5 μm of 0.68 ± 0.01 ml g^{-1}, the macropore-porosity is only 55% (acc. to Eq. 4). The overall porosity of 61% is slightly below the range of 68%-80%, which is reported in the literature[32–35] for Freudenberg substrates (the exact type might differ). In the following, we would like to discuss why we might be underestimating the porosity in our MIP measurements compared to literature findings. The upper pore size limit that could be accessed in our MIP data was constrained by the filling protocol of our special penetrometer to 43 μm (at the same time, it was the only choice to obtain sufficiently accurate MIP data without stacking of GDLs, which we found to introduce artefacts). The right-hand-side data in the log differential intrusion plot (Fig. 4b), however, demonstrate that the starting point for pore filling would be at a pore diameter of slightly above 43 μm. When using a different penetrometer for the MIP measurement, which offers a broader pore size range of 10 nm–400 μm at the cost of a lower measurement accuracy, a porosity of 67% was obtained (data not shown). We believe that the difference can be mostly attributed to the GDL-S surface roughness, which is included in the larger pore size range. The porosity difference of 6% between the bulk property and the overall porosity that includes surface roughness is consistent with the data by Fishman et al., who analyzed the through-plane porosity profile of different GDL substrates and found that the surface roughness induced porosity changes the overall porosity by a difference of $\Delta\varepsilon = 7\%$ compared to the core porosity.[34]

We would also like to briefly mention a possible source of error that we noted during our experiments, which could lead to an overestimation of the porosity determined by MIP measurements. In the present study, the GDL samples were intentionally measured in a self-standing manner, i.e., without stacking them in the penetrometer. When stacking the GDL samples, we noted that the gaps between the samples create an additional pore space, which results in larger apparent pore diameters and a higher apparent porosity. In our experience, the stacking of two GDL-S sheets (= 1 interfacial area) leads to an error of + 3% in porosity. If there are more sheets stacked, the error is likely to increase.

In summary, we would like to state that our porosity values represent the core porosity of the GDL substrate and are therefore slightly lower than the values reported in the literature. Because our MIP measurements do not account for surface roughness, our reported average MPL intrusion depth value is referenced to the uneven interface of the GDL-S and the MPL, which is depicted by the red lines in Fig. 3e/f.

After having analyzed the H14 GDL-S porosity, the missing pores in the intruded-GDL can be evaluated by subtracting the areal cumulative intrusion of the intruded-GDL ($v^*_{\text{macropore,intr.-GDL}}$) from the areal cumulative intrusion of the GDL-S ($v^*_{\text{macropore,GDL-S}}$) at a pore size of 5 μm (vertical line in Fig. 4) that represents the macropore volume of the H14 GDL-S (see above):

$$\Delta v^*_{\text{macropore}}[\text{mL/cm}^2] = v^*_{\text{macropore,GDL-S}}[\text{mL/cm}^2] - v^*_{\text{macropore,intr.-GDL}}[\text{mL/cm}^2] \quad [7]$$

The macropore difference $\Delta v^*_{\text{macropore}}$ is marked in Fig. 4a and represents the areal pore volume that is filled with intruding MPL material. When evaluating the data shown in Fig. 4a, $\Delta v^*_{\text{macropore}}$ equals 1.15 μl cm^{-2}. Using the macropore volume fraction of the H14 GDL-S of $\varepsilon_{\text{macropore}} = 55\%$ (see above), $\Delta v^*_{\text{macropore}}$ can be converted to an MIP-based MPL intrusion depth ($l_{\text{i,MIP}}$) via:

$$l_{\text{i,MIP}} = \frac{\Delta v^*_{\text{macropore}}[\text{mL/cm}^2]}{\varepsilon_{\text{macropore}}} \quad [8]$$

Thus, the average MPL intrusion depth into the H14 GDL-S based on the here outlined MIP data analysis is $l_{\text{i,MIP}} =$ 21 μm. Furthermore, the effect of the MPL intrusion on the overall porosity of the H14 GDL-S, here referred to as ΔP_{all}, can be described by the ratio of $\Delta v^*_{\text{macropore}}$ to the overall pore volume v^*_{pore} of the H14 GDL-S (marked in Fig. 4a):

$$\Delta P_{\text{all,MIP}}[\%] = \frac{\Delta v^*_{\text{macropore}}[\text{mL/cm}^2]}{v^*_{\text{pore,GDL-S}}[\text{mL/cm}^2]} \cdot 100[\%] \quad [9]$$

$\Delta P_{\text{all,MIP}}$ represents the overall reduction of pore volume, which is an important descriptor regarding the impact of MPL intrusion on the oxygen transport resistance. To quantify the impact of MPL intrusion on the macropore volume fraction in the H14 GDL-S, $\Delta v^*_{\text{macropore}}$ can be compared to the macropore volume $v^*_{\text{macropore}}$ for pores ⩾5 μm of the H14 GDL-S:

$$\Delta P_{\text{macropore,MIP}}[\%] = \frac{\Delta v^*_{\text{macropore}}[\text{mL/cm}^2]}{v^*_{\text{macropore,GDL-S}}[\text{mL/cm}^2]} \cdot 100\% \quad [10]$$

Compared to the entire pore volume $v^*_{\text{pore GDL-S}}$ of 6.62 μl cm^{-12}, the effect of MPL intrusion leads to an overall loss of porosity of the GDL-S of $\Delta P_{\text{all,MIP}} \approx 17\%$. If only the GDL-S macropore volume $v^*_{\text{macro-pore,GDL-S}}$ of 5.16 μl cm^{-12} is considered, the loss of macropore porosity in the GDL-S would amount to $\Delta P_{\text{macropore,MIP}} \approx 22\%$.

MPL intrusion for sheet- and intruded-GDLs (H14 GDL-S Based) via thickness measurements.—To verify the conclusions from the MIP measurement, we additionally took a more macroscopic approach, where the overall intrusion degree can be estimated by examining the average thickness measurement (TM) of the sheet- and the intruded-GDL to determine the difference in their thickness Δl (see Fig. 3e/f for the definition of Δl). To make sure that the thickness difference only represents the difference in MPL intrusion and not the error from MPL fabrication, we cut out two pieces of each GDL of a defined area (2.4 by 2.4 cm), where the standard deviation of the weight was 0.1% of the average weight for all four pieces. When regarding these pieces, the two sheet-GDLs had an average thickness of 182 ± 1.4 μm, while the two intruded-GDLs had an average thickness of 168 ± 0.0 μm, leading to a difference of Δl= 14.0 ± 1.4 μm (note that the H14 based GDL-S had a thickness of roughly 140 μm). From these measurements, the TM-based intrusion depth $l_{\text{i,TM}}$ can be estimated as:

$$l_{\text{i,TM}} = \frac{\Delta l}{\varepsilon_{\text{macropore}}} \quad [11]$$

Converting the 14.0 μm MPL intrusion by the macropore-porosity $\varepsilon_{\text{macropore}}$ of the H14 GDL-S (55%, see above), one obtains an average MPL intrusion depth into the GDL-S of $l_{\text{i,TM}} = 26$ μm.

To estimate the thickness fraction of the GDL substrate over which the macropores are filled with the intruded MPL material, the obtained intrusion depth is divided by the overall GDL-S thickness L (see Fig. 3e) according to:

$$\Delta P_{\text{macropore,TM}} = \frac{l_{\text{i,TM}}}{L} \quad [12]$$

In this rough estimate, with $L = 140\,\mu$m for the H14 GDL-S, the intruded MPL material occupies 19% of the macropore volume of the GDL substrate.

To estimate the impact of the intrusion lon the total porosity, we can compare the thickness difference Δl with the MIP-derived overall porosity of $\varepsilon = 61\%$, yielding the overall GDL-S pore volume fraction filled by the MPL:

$$\Delta P_{\text{all,TM}} = \frac{\Delta l/\varepsilon}{L} \quad [13]$$

The total pore volume taken away by the MPL intrusion was 16% compared to the total pore volume.

The parameters describing the extent of MPL material intrusion into the H14 GDL substrate of the intruded-GDL that were obtained by either the MIP analysis or the average thickness measurements (TM) are summarized in Table II. In general, both methods agree reasonably well: i) the average MPL intrusion depth l_i is estimated to be 26 μm and 21 μm based on the TM approach and the MIP results, respectively; ii) the overall pore volume fraction of the GDL-S filled by the MPL (ΔP_{all}) is estimated to be 16% and 17% via TM and MIP, respectively; and, iii) the macropore volume fraction of the GDL-S filled by the MPL ($\Delta P_{\text{macropore}}$) is estimated to be 19% and 22% via TM and MIP, respectively.

5 cm^2 differential-flow single-cell PEMFC data with H14 GDL-S based GDLs.—The different GDLs applied at the cathode were characterized in a 5 cm^2 single-cell PEMFC, acquiring differential-flow H_2/air polarization curves and limiting current measurements. Figure 5 shows the polarization curves (upper panels), the HFR (middle panels), and the oxygen transport resistance (lower panel) for the sheet- and the intruded-GDL (both on H14 GDL-S) for three different operating conditions.

Figure 5a represents the data for 80 °C, 100% RH, and 170 kPa$_{\text{abs}}$. The H_2/air performance (upper panel) for the cell with the intruded-GDL (orange) is slightly but noticeably inferior to that of the cell with the sheet-MPL (black), especially at higher current densities. This observation agrees with the results from the oxygen transport resistance (lower panel), where the intruded-GDL shows a higher transport resistance of approximately 0.1 s cm^{-1} for all tested current densities between 0 and 5 A cm^{-2}. The higher transport resistance is consistent with the numerical simulation results from Wong et al.,[11] who projected a decreased oxygen diffusivity at dry conditions for an MPL intruding into the GDL substrate. Additional data were recorded at 70% RH at equal temperature and pressure of 80 °C and 170 kPa$_{\text{abs}}$ (not shown), and the intruded-MPL again showed a ~0.1 s cm higher oxygen transport resistance compared to that of the sheet-MPL. Thus, the intrusion of the MPL material into the GDL-S clearly poses an extra resistance to the diffusion of oxygen throughout the macroporous GDL-S, which appears to be independent of current density at dry conditions. The simultaneously recorded HFR (middle panel of Fig. 5a) of both types of cathode GDLs follows the same trend: it starts out at a value of 26–28 mΩ cm^2 at low current densities, then gradually increases with current density, followed by a more rapid increase above 3 A cm^{-2}. The latter behavior is caused by the increasing temperature difference between the MEA and the flow-field, where the cell temperature is controlled: the locally higher temperature from the heat generated in the MEA results in a lower local RH and thus a higher proton conduction resistance of the membrane.

When regarding the "wetter" operating conditions at which the removal of product water is hindered, such as at an increased pressure of 300 kPa$_{\text{abs}}$ (keeping the other conditions of 80 °C and 100% RH unchanged) due to the lower absolute water uptake capability of the gas phase, the H_2/air performance of the cells with either the sheet- or intruded-GDL at the cathode becomes essentially identical (upper panel in Fig. 5b). In addition, the oxygen transport resistance on average reaches a similar value for both GDL types (lower panel), even though it should be noted that the error bars for the intruded-GDL (based on two independent measurements) are significantly larger, which we ascribe to the larger sample-to-sample variation of the here prepared intruded-GDLs. The HFR (middle panel) rises substantially less at the higher current densities, which would be expected based on the higher local RH in the MEA at higher pressure when temperature and RH are kept constant. At even wetter operating conditions, where the formation of liquid water is expected, i.e., when operating a low temperature, high pressure, and with over-humidified reactants, the data in Fig. 5c (recorded at 50 °C, 120% RH, and 300 kPa$_{\text{abs}}$) show the same trend: an essentially identical H_2/air performance (upper panel) and oxygen transport resistance (lower panel) for both GDL types, except that the latter is substantially higher than for the other two conditions, reflecting the larger water saturation in the GDL.

To summarize, the data shown in Fig. 5 allow two conclusions: the MPL intrusion into the GDL-S leads to a ~0.1 s cm^{-1} higher oxygen transport resistance at dry conditions (Fig. 5a), which must derive from the morphological changes of the GDL substrate by the intruded MPL material, resulting in a slightly inferior H_2/air performance. When applying more humid conditions, where a higher liquid water saturation of the GDL can be expected, the intrusion of the MPL appears to have a positive effect that can compensate for the higher oxygen transport resistance of the intruded-GDL at dry conditions, so that the H_2/air performance of the sheet- and the intruded-GDL become essentially identical. However, this positive effect of MPL intrusion into the GDL-S under wet conditions is apparently not strong enough to lead to the superior H_2/air performance of the intruded- vs the sheet-GDL that was predicted in the simulations by Wong et al.[11]

The interplay of the dry diffusion resistance and the marginally improved mass transport at wet conditions is illustrated in Fig. 6. It shows the oxygen transport resistance for operating conditions where a transition can be observed between low GDL water saturation at low current densities and high GDL water saturation at high current densities, acquired at a cell temperature of 50 °C, at 77% RH, and at 400 kPa$_{\text{abs}}$. At very low current densities, the dry transport resistance shows again a ~0.1 s cm^{-1} higher value for the cell with the intruded-GDL compared to that with the sheet-GDL, while the oxygen transport resistance of the cell with the intruded-GDL is slightly lower or equal to that with the sheet-GDL.

In conclusion, the use of an intruded-GDL does not result in the significantly superior performance at wet conditions that was predicted in the simulation study by Wong et al.[11] The MIP results demonstrate that the intrusion of the MPL into the GLD-S has led to a significant reduction of 22% of large pores (see $\Delta P_{\text{macropore,MIP}}$ in Table II) in the GDL-S, caused by the preferential filling of the GDL-S macropores with the MPL material (see Fig. 4). As larger pores have a higher oxygen diffusivity due to their lowered Knudsen diffusion contribution, and as they offer a more efficient drainage of liquid water, the lowering of the macropore size and volume fraction by the intruded MPL material has a negative contribution on fuel cell performance. This drawback is counterbalanced by keeping pathways for oxygen diffusion during very wet operating conditions through the intruded MPL segments of the GDL-S, as the intruded MPL segments have a lower liquid water saturation. If this hypothesis were true, one would expect that the use of an intruded-GDL prepared with a thicker GDL-S, for which the MPL intrusion should result in less of an overall macropore size and volume fraction loss (assuming that the MPL intrusion length l_i remains similar), should more substantially improve fuel cell performance, as more macropores would be available for mass transport.

MPL intrusion for sheet- and intruded-GDLs (H23 GDL-S based).—The MIP data for the GDLs based on the Freudenberg H23 substrate (hydrophobically treated) are shown in Fig. 7 analogously to Fig. 4, with the areal cumulative intrusion (Fig. 7a) and the log

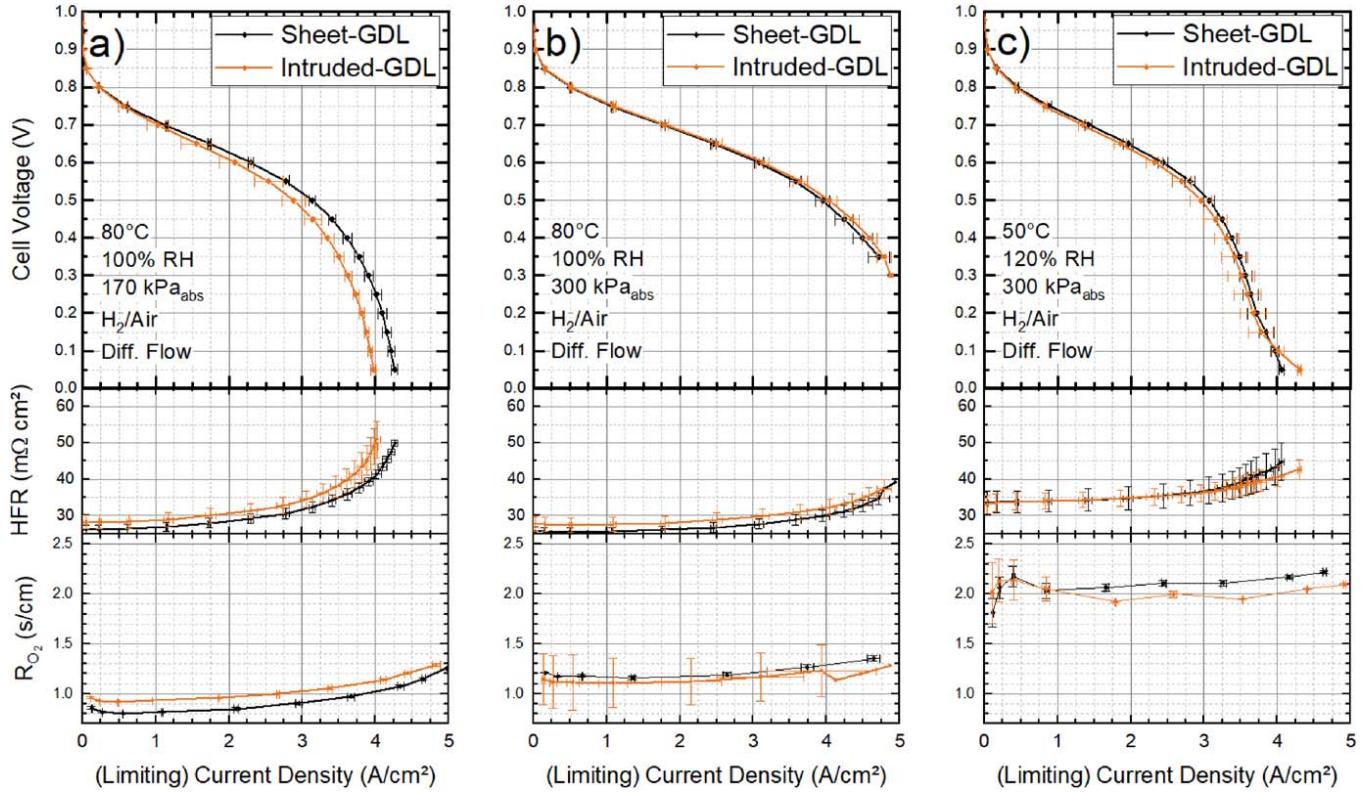

Figure 5. Differential-flow H_2/air performance curves (upper panels), the simultaneously recorded HFR values (middle panels), and the oxygen transport resistance values (lower panels) acquired with H14 GDL-S based sheet- (black) or intruded-GDLs (orange) at the cathode, evaluated at different operating conditions: (a) 80 °C, 100% RH, 170 kPa_{abs}; (b) 80 °C, 100% RH, 300 kPa_{abs}; and, (c) 50 °C, 120% RH, 300 kPa_{abs}. The cells had CCMs based on an 18 μm reinforced membrane with a Pt loadings of 0.1/0.4 $mg_{Pt}\,cm^{-2}$ (anode/cathode) and a Freudenberg H14C10 GDL was used at the anode. The error bars represent the standard deviation of two independent measurements.

differential intrusion (Fig. 7b) in terms of $\mu l/cm^2_{GDL}$. The blue curve represents the results for the GDL-S, with the macropore volume defined for pores $\geqslant$5 μm and a micropore region that is centered round at 80 nm. The overall porosity when evaluating the cumulative volume according to Eq. 3 is 61%, and the pore volume fraction of macropores ($\geqslant$5 μm; acc. to Eq. 4) is 54%, which, within the experimental error, are the same as those obtained for the H14 GDL-S.

The areal intrusion volume and the pore size distribution curve in the macropore region ($\geqslant$5 μm) obtained for the sheet-GDL (gray) on the H23 substrate are very similar to those of the H23 GDL-S, indicating that there is little intrusion of the sheet-MPL into the GDL-S. On the other hand, for the intruded-GDL, the intrusion of the MPL material into the H23 GDL-S is clearly indicated by the cumulative volume loss of 0.83 $\mu l\,cm^{-2}$ in the macropore region (marked as $\Delta v^*_{macropore}$ in Fig. 7a). This pore volume loss is reflected in the log differential intrusion plot, which indicates that the amount of larger pores (>20 μm) is reduced. The micropore region, representing the MPL and the carbon black filler of the GDL-S, almost perfectly overlaps for the sheet- and the intruded-GDL.

Following the same MPL intrusion depth analysis that was used above, the average MPL intrusion depth determined by MIP ($l_{i,MIP}$) for the H23 GDL-S based intruded-GDL of 15 μm is slightly lower than the 21 μm found for the H14 GDL-S based intruded-GDL. However, essentially identical MPL intrusion depths of 26 μm and 27 μm for the H14 and the H23 GDL-S based intruded-GDLs, respectively, were obtained by the thickness measurement (TM) based approach ($l_{i,TM}$), originating from the very similar Δl values (14.0 vs 14.5 μm, respectively). These values are summarized in Table I. It must be noted that both methods yield zero-order estimates of the MPL intrusion depth and are subject to experimental errors, whereby the largest potential source of error is that in the MIP based method, the GDL-S measurements need to be conducted on a GDL-S sample piece that has the same thickness as the piece used to prepare the intruded-GDL (a deviation of 5 μm translates directly to

Table I. Comparison the MPL intrusion characteristics of the intruded-GDL prepared either with the H14 GDL-S (~140 μm) or with the H23 GDL-S (~200 μm): average MPL intrusion depth l_i, loss of the overall GDL-S pore volume fraction by MPL material intrusion ΔP_{all}, and loss of the macropore volume fraction in the GDL-S by MPL material intrusion $\Delta P_{macropore}$. These were determined either by averaged thickness measurements (TM) in combination with the MIP based macropore porosity of $\varepsilon_{macropore}$ = 54% of the H23 GDL-S, or by Mercury intrusion porosimetry (MIP). The numbers in the curly brackets {} reference the number of the equation that was used for the calculation.

	MIP		TM	
Method and relevant equation	H14	H23	H14	H23
Thickness difference Δl (see Fig. 3e/f)	—	—	14.0 μm	14.5 μm
Averaged MPL intrusion depth l_i (see Fig. 3f)	21 μm {8}	15 μm {8}	26 μm {11}	27 μm {11}
MPL-filled GDL-S pore volume fraction ΔP_{all}	17% {9}	9% {9}	16% {13}	12% {13}
MPL-filled GDL-S macropore fraction $\Delta P_{macropore}$	22% {10}	11% {10}	19% {12}	14% {12}

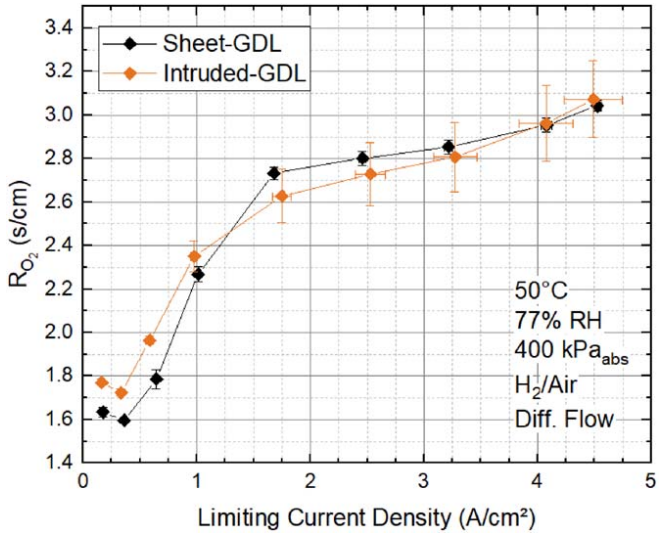

Figure 6. Limiting current measurements at operating conditions where the transition from low to high water saturation in the H14 GDL-S based cathode GDLs can be observed (50 °C, 77% RH, 400 kPa_{abs}) for the sheet-GDL (black) and for the intruded-GDL (orange). The cells had CCMs based on an 18 μm reinforced membrane with a Pt loadings of 0.1/0.4 mg_{Pt} cm^{-2} (anode/cathode) and a Freudenberg H14C10 GDL was used at the anode. The error bars represent the standard deviation of two independent measurements.

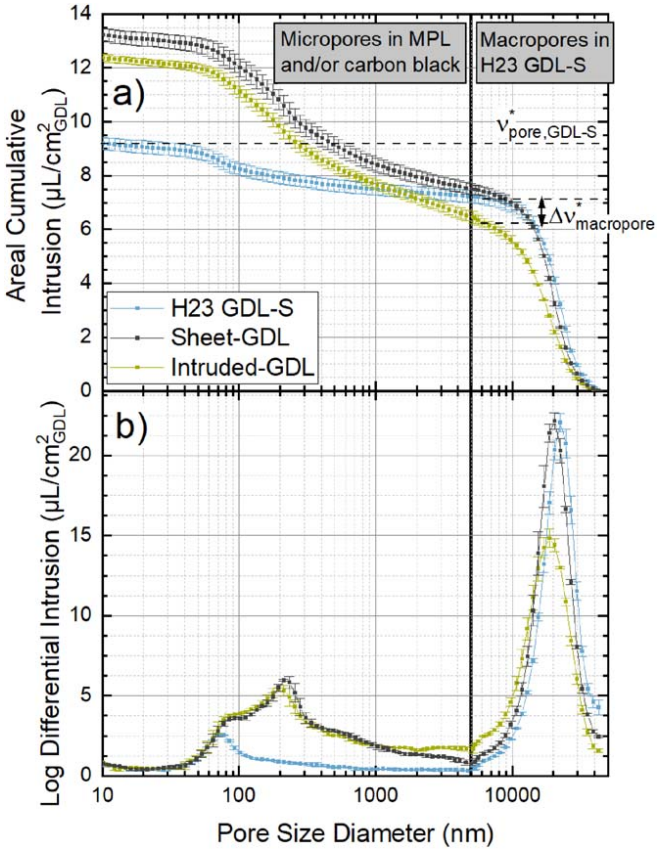

Figure 7. Mercury intrusion porosimetry results for the H23 GDL-S (blue) as well as for the H23-based sheet-GDL (gray) and intruded-GDL (green), whereby the intrusion of mercury is given in units of $\mu l/cm^2_{GDL}$. a) Cumulative intrusion volume referenced to the GDL area: the missing macropore volume $\Delta v^*_{macropore}$ in the intruded-GDL compared to the GDL-S represents the MPL intrusion depth of the intruded-GDL. b) Log differential intrusion. The vertical black line at 5 μm pore size diameter marks the approximate distinction between the pore size region of the macropores in the GDL-S and the micropores in both the MPL and the original carbon black filler of the GDL-S. The error bars represent the standard deviation of two independent measurements.

an error of 5 μm in $l_{i,MIP}$). Therefore, the unexpectedly low $l_{i,MIP}$ value for the H23 GDL-S based intruded-GDL likely represents an experimental outlier. With this in mind, we believe that the here presented MPL intrusion depth analysis reasonably well confirms our initial hypothesis that the MPL intrusion depth obtained for GDL substrates that have a similar macropore size and volume fraction is only a function of the applied compression and the time under compression during preparation: as macropore size and volume fraction were essentially identical and as the same preparation procedure was used, the here observed similar MPL intrusion depths (see Table I) are in line with this hypothesis.

Finally, a comparison of the macropore volume fraction of the GDL-S that is lost due to MPL material intrusion ($\Delta P_{macropore}$) between the intruded-GDLs based on either the H14 GDL-S or the H23 GDL-S reveals that $\Delta P_{macropore}$ is significantly lower when using the thicker H23 GDL-S: it reduces from 22% to 11% based on the MIP analysis and from 19% to 14% based on the TM based approach. While the two analysis approaches result in slightly different absolute $\Delta P_{macropore}$ values, the loss of macropore volume fraction of the GDL-S is substantially lower for the intruded-GDL based on the thicker H23 GDL-S, consistent with our expectations.

XTM based morphological characterization of H23 GDL-S based GDLs.—As MIP and macroscopic analysis do not give local information of the MPL intrusion into the GDL-S, further analysis was performed. X-ray tomographic microscopy provides quantitative data on thickness distribution and intrusion depth of the MPL over a larger area (28 mm^2). First, the intrusion of the sheet- and intruded-GDLs based on the H23 GDL substrate are compared in the form of thickness maps in Fig. 8. The MPL thickness maps are additive through-plane projections of the MPL phase thickness in the segmented images. The average thickness difference of the MPLs may be influenced by the minor segmentation error at the MPL/GDL-S interfacial region due to insufficient voxel resolution (voxel edge length = 3.6 μm), where the fiber edge mingles with the MPL phase in the images.

The sheet-GDL shows a significantly smoother MPL (thickness heterogeneity = 7 μm) compared to the intruded-GDL (thickness heterogeneity = 14 μm). The minor regional thickness variation of the MPL of the sheet-GDL may reflect the surface contour of the

Table II. Characteristics of the MPL intrusion into the H14 GDL substrate of the intruded-GDL, determined either by averaged thickness measurements (TM) in combination with the MIP based macropore porosity of $\varepsilon_{macropore}$ = 55% of the H14 GDL-S (~140 μm), or by Mercury intrusion porosimetry (MIP). The numbers in the curly brackets {} reference the number of the equation that was used for the calculation.

Method and relevant equation	TM	MIP
Thickness difference Δl (see Fig. 3e/f)	14.0 μm	—
Averaged MPL intrusion depth l_i (see Fig. 3f)	26 μm {11}	21 μm {8}
MPL-filled GDL-S pore volume fraction ΔP_{all}	16% {13}	17% {9}
MPL-filled GDL-S macropore fraction $\Delta P_{macropore}$	19% {12}	22% {10}

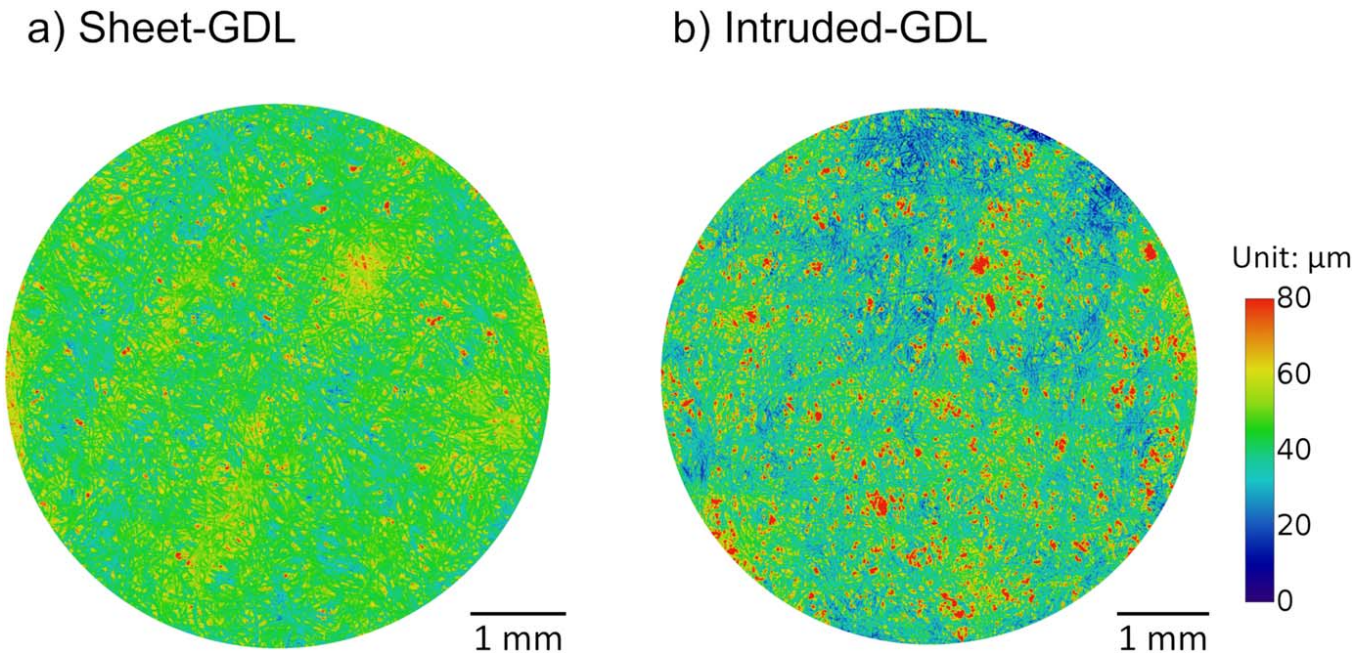

Figure 8. MPL thickness maps of a) the sheet-GDL and b) the intruded GDL, revealing the different MPL thickness heterogeneity and intrusion structure of the MPLs (both on H23 GDL substrates): the MPL of the sheet-GDL shows an average thickness of 46 μm and a thickness heterogeneity of 7 μm, while that of the intruded-GDL shows an average thickness of 43 μm and a thickness heterogeneity of 14 μm.

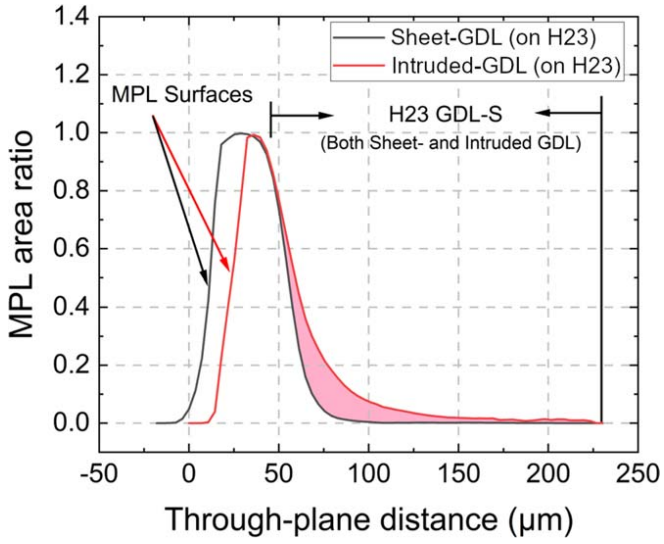

Figure 9. Ratio of the MPL area over the overall GDL cross-sectional area with respect to the through-plane distance based on the calibrated segmentation (see Fig. 1), starting from the MPL surface toward the GDL-S for the sheet- and intruded-GDL based on the H23 GDL substrate.

H23 GDL-S. In contrast, the intrusion of the MPL material into the GDL-S of the intruded-GDL is dominated by the frequent locations where the MPL thickness is $\geqslant$80 μm. The thickness heterogeneity is defined as the standard deviation of the MPL thickness map subject to the voxel resolution (voxel edge length = 3.6 μm). It is a measure of MPL thickness variation in the in-plane directions.[36]

The difference in distribution of the MPL across the thickness of the GDLs is quantitatively illustrated as MPL area ratio profiles in Fig. 9. Here, the MPL phase area ratio with respect to the GDL area at each through-plane position from the surface of the MPL is plotted.

The MPL distributions in Fig. 9 reveal that the intruding part of the MPL in the GDL-S is localized near the MPL side. In fact, 89% of all MPL intrusion is localized in the upper 50% of the GDL thickness (upper side = MPL side). With the intrusion of the MPL, the overall pore size distribution of the intruded-GDL changes.

Influence of intruded MPL material on the pore size distribution of the GDL-S.—When considering the MPL phase as solid, the alteration of the GDL macropore (=void) size distribution and the volume fraction filled by the intruded MPL material can be estimated. The results are shown in Fig. 10.

It is clear from Fig. 10a that the intrusion of the MPL material divides and/or fills the GDL-S macropores. When the pore size distribution (PSD) for the entire GDLs are analyzed as shown in Fig. 10b, a clear shift to smaller pore sizes is observed for the intruded-GDL (red), compared to when the MPL is absent (black). The number of pores of 40 μm is reduced by 80% and pores of 30 μm by 46%. Nevertheless, since the intrusion of the MPL is highly localized in the GDL-S part near the MPL, after which the intrusion drastically decreases (see Fig. 9), the PSD of the bottom half of the GDL substrate, which contains only 11% of the MPL material will remain largely unaffected by the intrusion.

It was already shown by the MIP analysis that the intrusion of the MPL material shifts the pore size distribution of the GDL-S to smaller pores, as the intrusion of the MPL is a result of capillary force due to pressing the aqueous MPL slurry into the hydrophobic GDL-S pores. The tomographic analysis now allows to quantify this effect. The GDL substrate fiber structure of the intruded H23 GDL is isolated and its pore size distribution (in the absence of MPL) is estimated, shown in Fig. 10b as the black curve.

Regarding the MPL phase only and calculating the diameter of the substrate pores that contain the MPL phase, the blue curve in Fig. 10b shows the PSD of the substrate pores containing the MPL phase. If the MPL intrusion were to proceed equally into all GDL-S pores, i.e., if the intrusion of the MPL material were not to have a preference for larger pore sizes, the two PSD curves (black and blue) would have similar peak location and shape, varying majorly in the normalized pore volume. The difference in peak positions of the GDL pores containing the MPL phase (located at larger pore diameters of 20–25 and 35 μm, indicated by the blue arrows) vs that of the H23 GDL substrate (at 20 μm, indicated by the black arrow) however underlines the preference of MPL intrusion into the

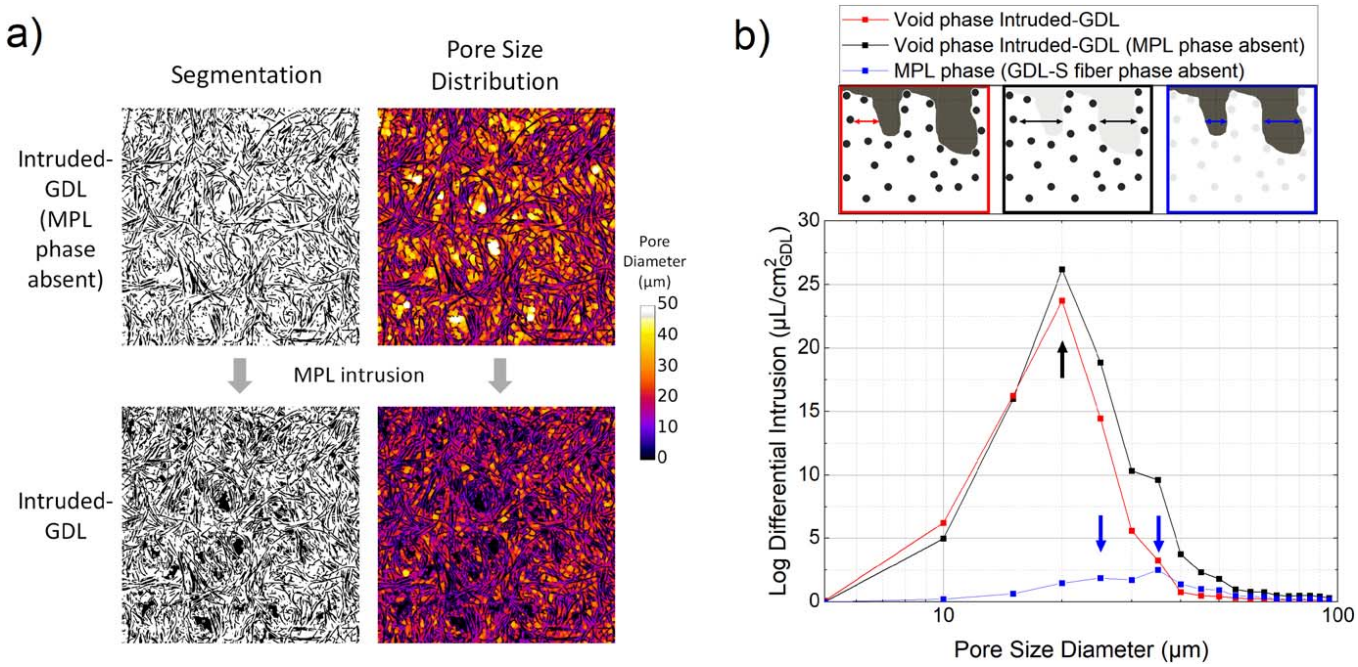

Figure 10. Influence of MPL intrusion on the GDL-S pore size distribution using the intruded-GDL (on H23) as an example: a) horizontal tomographic image slices at the MPL/GDL-S interfacial region (located at the 97 μm through-plane distance shown in Fig. 9), comparing the case where the MPL phase was computationally removed from the intruded-GDL, so that only the fiber structure of the GDL-S remains (upper images), and the case when the MPL (intrusion) is present, i.e., showing the fiber structure and the MPL phase of the intruded-GDL (lower images); both the segmented binary images (black and white) and the substrate void pore size distribution (colored images) are provided, whereby the MPL phase is regarded as solid in the binary images and when estimating substrate void pore size distribution. b) Comparison between the substrate void pore size distribution in the absence of MPL (black curve, GDL-S) and in the presence of MPL (red curve, intruded-GDL). The diameter of the intruded MPL phase only is shown in blue. The intruded H23 GDL substrate was used to make these analyses. The sketch on top of panel b) visualizes the three different configurations.

larger GDL-S pores. Quantification shows that more than 94% of the MPL material intruded into GDL-S pores larger than 10 μm.

5 cm^2 differential-flow single-cell PEMFC data with H23 GDL-S based GDLs.—The fuel cell performance results using sheet- and intruded-GDLs based on the H23 GDL-S on the cathode are shown in Figs. 11 and 12. Figure 11 shows the H_2/air polarization curves (upper panel), the associated HFR values (middle panel), and the oxygen transport resistance (lower panel) at three different operating conditions, analogous to the data shown in Fig. 5 for the H14 GDL-S based GDLs.

Figure 11a shows the data at the first set of operating conditions of 80 °C, 100% RH, and 170 kPa$_{abs}$, revealing a marginally inferior H_2/air performance (upper panel) and a $\sim$0.1 s cm^{-1} higher oxygen transport resistance (lower panel) for the intruded-GDL (green) compared to the sheet-MPL (gray). The HFR values recorded during the H_2/air performance curves are identical within the error of measurement (middle panel) for both cathode GDLs. These data with the H23 GDL-S based GDLs are very similar to those obtained with the H14 GDL-S based GDLs (see Fig. 5). As was the case for the latter, the same offset in oxygen transport resistance of $\sim$0.1 s cm^{-1} was also observed under drier operating conditions (80 °C, 70%RH, and 170 kPa$_{abs}$: data not shown) for the H23 GDL-S based GDLs, supporting the hypothesis that it is due to the negative effect of the MPL intrusion at conditions where the liquid water saturation in the GDL is low. The fact that the MPL intrusion depth is very similar for the intruded-GDLs based on the two different GDL substrates (see Table I) also explains their essentially identical additional oxygen transport resistance at these relatively dry operating conditions, where the water transport in liquid form does not play a major role.

Upon increasing the cell pressure to 300 kPa$_{abs}$ (maintaining 80 °C and 100%RH) to create wetter operating conditions (Fig. 11b), liquid water formation can be expected, and now the H_2/air performance of the cell with the intruded-GDL (green) outperforms the sheet-GDL (gray) at high current densities (i.e., at cell voltages below 0.60 V). For example, at a cell voltage of 0.5 V, the current density of the intruded-GDL is on average $\sim$250 mA cm^{-2} higher compared to the sheet-GDL. However, as already seen for the H_2/air polarization curves with the H14 GDL-S based intruded-GDL (Fig. 5a), the cell-to-cell variation, reflected by the error bars, increases. At the same time, the oxygen transport resistances (lower panel of Fig. 11b) show no real difference between the sheet- and the intruded-GDL. In combination with the large sample-to-sample variation, this indicates that these operating conditions mark the tipping point between the negative effect on the performance caused by the additional oxygen transport resistance from the intruded MPL material and the performance gain due to the better water management upon MPL intrusion. At the even wetter operating conditions achieved by lowering the cell temperature to 50 °C and using over-humidified reactant gases at 120% RH (keeping a pressure of 300 kPa$_{abs}$), the H_2/air performance of the intruded-GDL is clearly superior to that of the sheet-MPL (upper panel in Fig. 11c), and the oxygen transport resistance (lower panel) is now $\sim$10% lower (by $\sim$0.25 s/cm^{-1}) for the intruded-GDL compared to the sheet-GDL. At these conditions, the positive impact of the improved water management by the intruded-GDL outweighs its slightly higher dry oxygen transport resistance.

Finally, a comparison of the HFR values for the sheet- and the intruded-GDLs based either on the H14 GDL-S (Fig. 5 or on the H23 GDL-S (Fig. 11) reveals essentially identical HFR values and a very similar dependence of the HFR with current density (particularly noticeable by comparing Figs. 5a and 11a). This suggests that the thermal management is comparable between the different GDL substrates (H14 and H23) and the GDL design (sheet- or intruded-GDL).

Figure 12 further underlines the observations and conclusions from the discussion of Fig. 11 by evaluating the oxygen transport resistance at a condition that lead to transition from a low to a high liquid water saturation in the GDL for the H23 GDL-S based GDLs

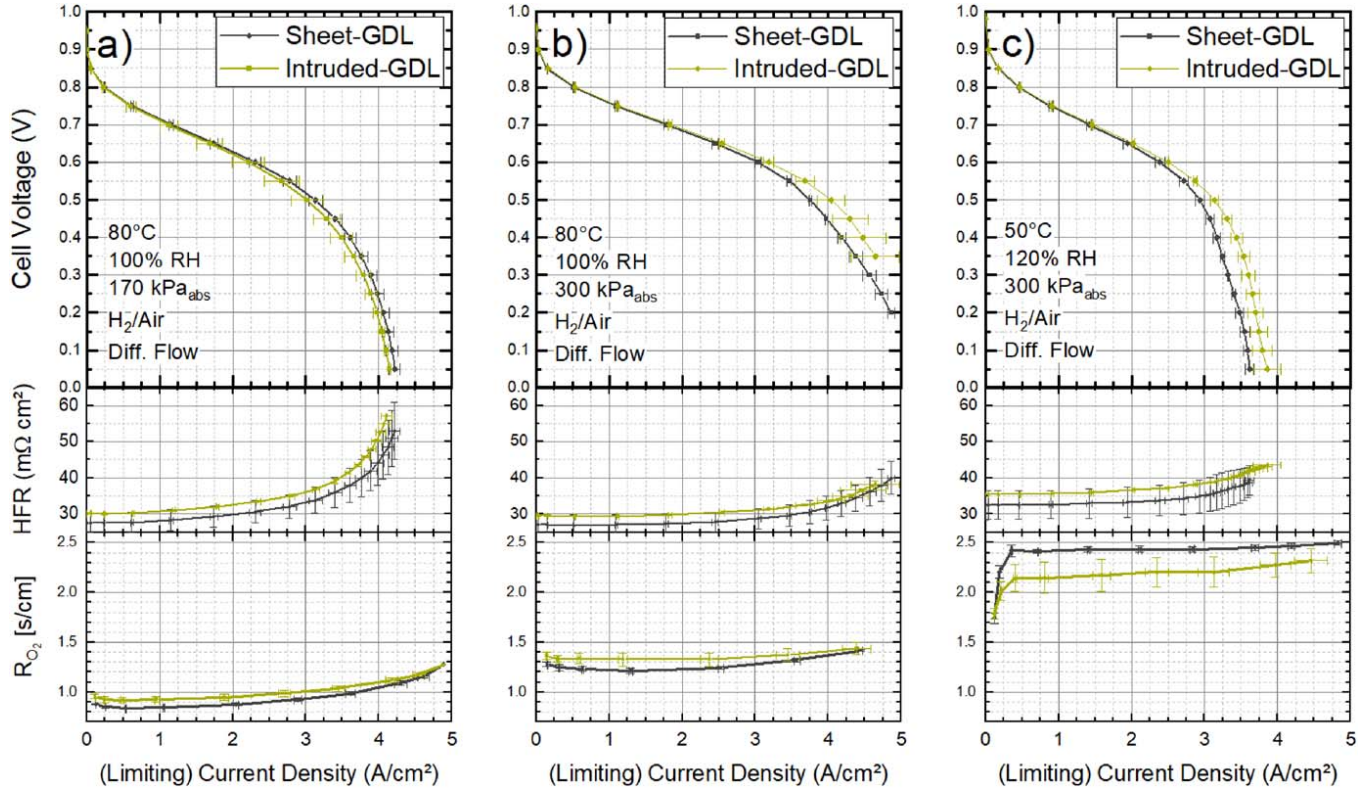

Figure 11. Differential-flow H_2/air performance curves (upper panels), the simultaneously recorded HFR values (middle panels), and the oxygen transport resistance values (lower panels) acquired with H23 GDL-S based sheet- (gray) or intruded-GDLs (green) at the cathode, evaluated at different operating conditions: (a) 80 °C, 100% RH, 170 kPa_{abs}; (b) 80 °C, 100% RH, 300 kPa_{abs}; and, (c) 50 °C, 120% RH, 300 kPa_{abs}. The cells had CCMs based on an 18 μm reinforced membrane with a Pt loadings of 0.1/0.4 mg_{Pt} cm^{-2} (anode/cathode) and a Freudenberg H14C10 GDL was used at the anode. The error bars represent the standard deviation of two independent measurements.

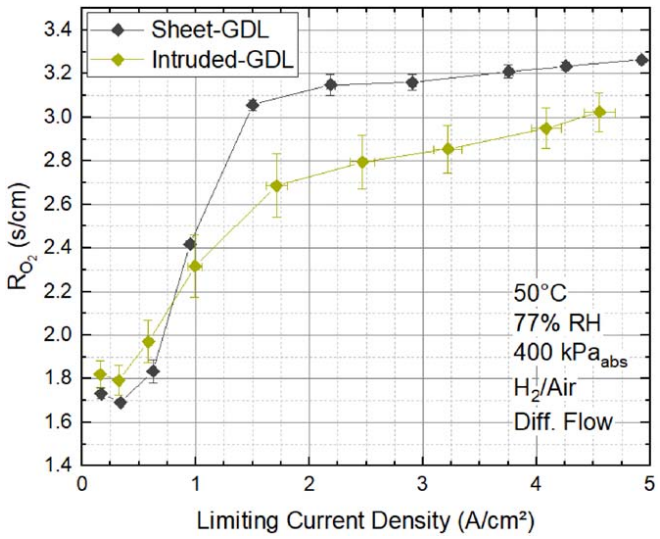

Figure 12. Limiting current measurements at operating conditions where the transition from low to high water saturation in the H23 GDL-S based cathode GDLs can be observed (50 °C, 77% RH, 400 kPa_{abs}) for the sheet-GDL (gray) and for the intruded-GDL (green). The cells had CCMs based on an 18 μm reinforced membrane with a Pt loadings of 0.1/0.4 mg_{Pt} cm^{-2} (anode/cathode) and a Freudenberg H14C10 GDL was used at the anode. The error bars represent the standard deviation of two independent measurements.

(analogous to Fig. 6 for the H14 GDL-S based GDLs). At low current densities, the oxygen transport resistance is ~0.1 s cm^{-1} higher for the intruded-GDL, representing the additional dry transport resistance from the intruded MPL material. The onset for the rapid increase of R_{O2}, marking the increase in liquid water saturation of the GDL, occurs at the same current density for both GDL types. However, at higher current densities, where the liquid water saturation level in the GDLs is high, the oxygen transport resistance is ~10% lower for the intruded-GDL compared to the sheet-GDL. Thus, the intrusion of the MPL into the GDL-S leads to a clear oxygen transport resistance advantage at operating conditions where the liquid water saturation in the GDL is high.

Operando XTM of the liquid water distribution in H23 GDL-S based intruded-GDL.—To further understand the performance difference between the H23 GDL-S based sheet- and intruded-GDLs at humid operating conditions, X-ray tomographic microscopy was used to obtain the steady-state liquid water distribution in the GDLs at humid operating conditions (49 °C, 93% RH). Here, due to the limitation of the gas pressure to atmospheric pressure, higher mass transport resistances occur at already <1.5 A cm^{-2}. Hence, the fuel cell performance is lower from the one illustrated in Fig. 11c. Therefore, the *operando* XTM cells were characterized at 0.5 A cm^{-2}. We believe that even though this condition does not exactly reproduce the condition at which the performance difference was observed in Fig. 11, the steady-state water distribution may still offer insight to the origin of the performance difference at high current densities.

The steady-state water saturation profiles at 49 °C, 93% RH, and atmospheric pressure at 0.5 A cm^{-2} are shown in Fig. 13. The water saturation profiles were obtained considering the actual porosity of the GDLs. The MPL-only region is excluded from these analyses due to its tendency to exhibit X-ray imaging artifacts, caused by the catalyst shining from the catalyst layer in its vicinity. The "Interface" region in Fig. 13 describes the region of the GDL-S in which the MPL material content is >10 vol% judged by XTM. The previous analysis of the structure of the sheet- and intruded-GDL has

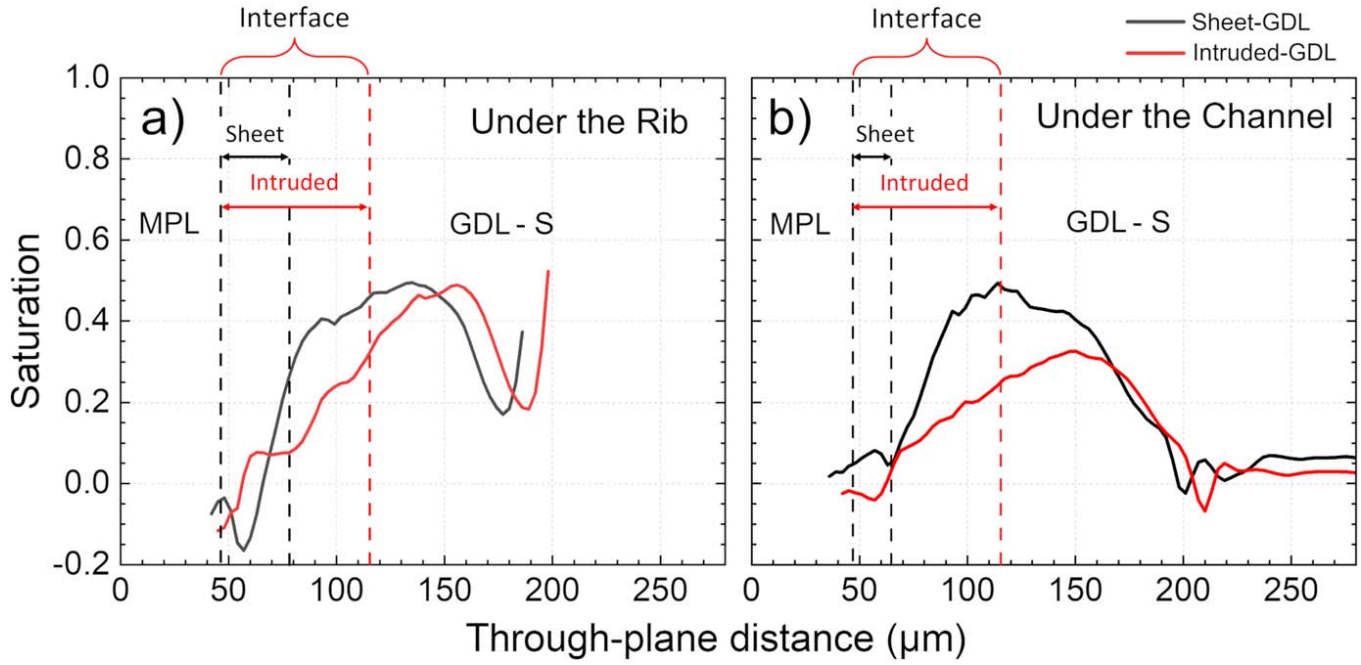

Figure 13. Water saturation profiles obtained from *operando* XTM fuel cell analyses at steady-state (H_2/air at 49°C, 93% RH, and ambient pressure) with the H23 GDL-S based sheet-GDL (black curves) and the intruded-GDL (red curves) operated at 0.5 A cm^{-2}: (a) under the rib region; (b) under the channel region. The interface is defined to be the MPL/GDL-S mixed region where the MPL phase is at least 10% in volume fraction. The interface thickness so defined is different for the sheet-GDL (ca. 20–30 μm) and intruded-GDL (ca. 70 μm), as shown in the figure.

indicated a very inhomogeneous, localized intrusion. Thus, the interfacial region that is marked in Fig. 13 is significantly wider than the averaged intrusion depth as defined for the MIP and TM analysis.

The water saturation in the sheet- and intruded-GDLs mainly differs in the MPL/GDL-S interface region of the intruded-GDL (Fig. 13a/b, at through-plane distances of ca. 50–120 μm), where the liquid water saturation differs up to 20% between the two GDL types. In the GDL substrates (at through-plane distances >150 μm), saturation between the two GDLs is similar, which is expected for the same operation condition and substrates. The saturation behavior is similar for both the rib (Fig. 13a) and the channel regions (Fig. 13b), suggesting that the MPL intrusion has the effect to lower the saturation in the MPL/GDL-S interface regions only. As a consequence of the saturation reduction, a more efficient oxygen transport is allowed, and is hypothesized to give rise to the performance improvement observed at wet and high current density conditions shown in Fig. 11c.

In the following, we would like to connect the saturation difference between the sheet- and the intruded-GDL to the difference in oxygen transport resistance, as depicted in Fig. 11 and Fig. 12 at flooded conditions. In Fig. 11c, the oxygen transport resistance at 50 °C, 120% RH, and 300 kPa_{abs} is presented with a difference of ~0.2–0.3 s cm^{-1} between the sheet- and the intruded-GDL. Compared to an absolute value of 2.4 s cm^{-1}, the difference amounts to ~8%–13%. In Fig. 12, the difference in oxygen transport resistance is ~0.2–0.4 s cm^{-1}, which corresponds to an improvement of ~6%–13% from the sheet- to the intruded GDL. These values are lower than the 20% saturation difference in the MPL/GDL-S zone, because this improvement concerns only a rather narrow part of the GDL, while the oxygen transport resistance is a global value of the entire GDL.

Liquid water saturation analysis in the intruded GDL region.— To gain insights with regards to the reason for the lower liquid water saturation at the MPL/GDL-S interface region in the intruded-GDL, the *operando* liquid water distribution in the MPL/GDL-S interfacial region of the intruded-GDL is further analyzed to find the location of the liquid water in the intruded-GDL. Thus, an in-plane cross-section slice is considered at the through-plane distance of 122 μm for the rib section, indicated by Fig. 13a. The dry GDL structure at this slice (Fig. 14a) shows that part of the large pores are (partially) occupied by MPL material (marked in green). The *operando* water distribution in terms of liquid volume fraction (LVF) at each voxel is given in Fig. 14b, with the calibration bar at the right-most side of the figure.

When the steady-state LVF map is masked by the MPL phase, showing only the LVF within the MPL phase (Fig. 14c), little water is observed and the LVF is estimated to be only ~3% of that of the total MPL volume. On the contrary, in the GDL macropores (Fig. 14d), 56% of the GDL macropore volume is filled with liquid water at steady-state.

The absence of liquid water in the MPL phase means that the MPL material in the GDL-S pores excludes liquid water from the volume occupied by the intruded MPL material. Therefore, the intrusion of MPL reduces the liquid water saturation in the MPL intrusion zone by making the intruded macropores unfavorable for liquid water accumulation, either by reduced PSD or by replacing the initial void volume with MPL material. As the MPL phase has a porosity of 68%, this pore volume within the intruded MPL material is still available for oxygen transport. The effective diffusivity is less than for empty pores, but much higher than for liquid water filled pores. This exclusion of water from the MPL/GDL-S interface region therefore gives the intruded-GDL an advantage for oxygen transport under very wet conditions.

Discussion

The here used method to prepare an intruded-GDL, namely applying a compressive force onto an aqueous MPL slurry to force its intrusion into a hydrophobized GDL substrate, results in an intrusion of the MPL material into the large pores of the GDL substrate, as these impose the lowest capillary pressure. This intrusion of the MPL material into the GDL-S macropores lowers the macropore size and volume fraction, leading to an increased oxygen transport resistance at dry conditions, i.e., at conditions where the liquid water saturation of the GDL is low. Hence, at operating conditions, where little liquid water formation can be

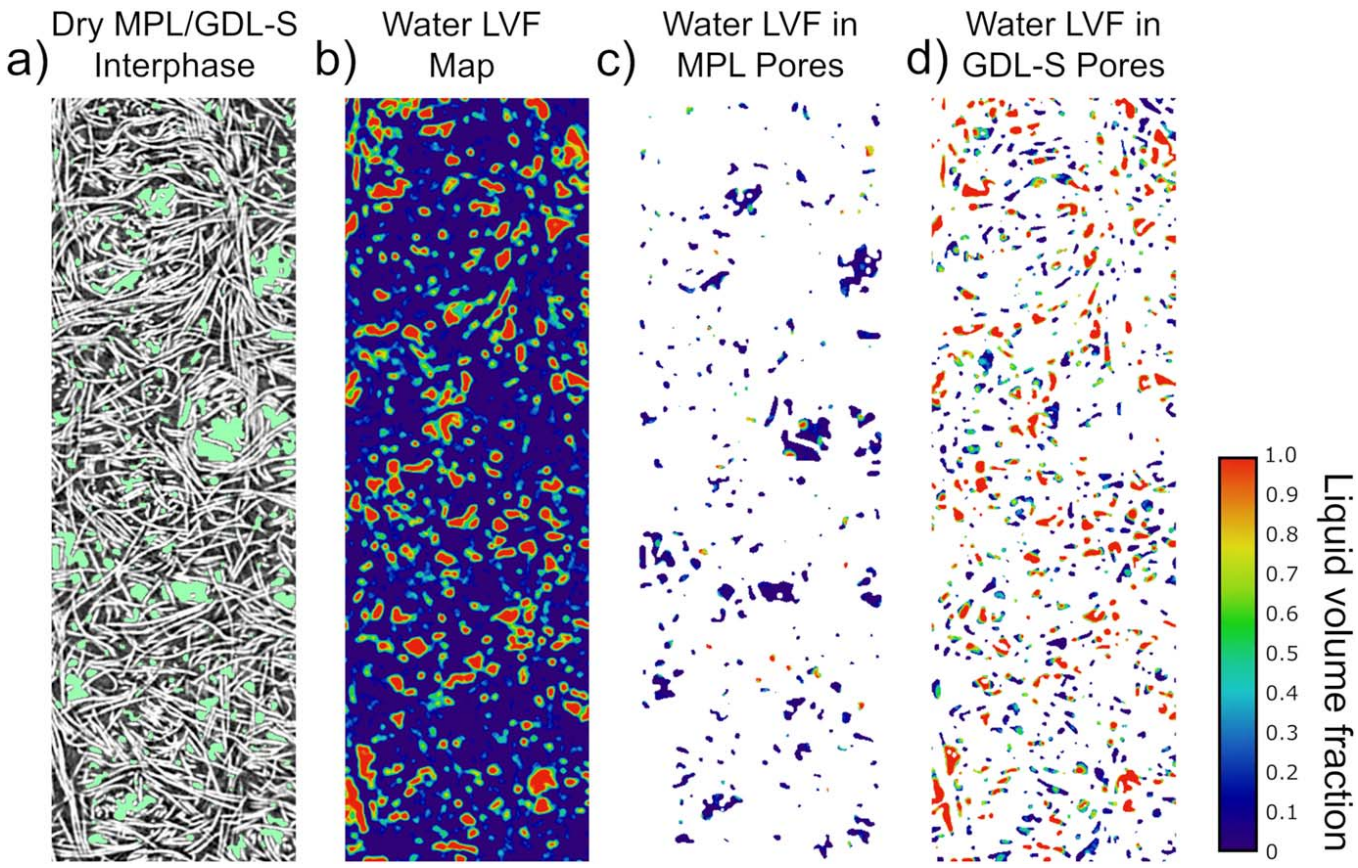

Figure 14. Steady state water distribution in the MPL/GDL-S interfacial region of the intruded H23 GDL cell under the rib; shown here is the cross-section at a through-plane distance of 122 μm, as indicated by Fig. 13a: (a) in-plane tomographic image of the MPL/GDL-S interface at the dry state, with the MPL phase colored in green; (b) steady-state LVF map showing roughly the liquid water volume fraction (LVF) at each voxel (with image noise present); (c) LVF map masked by the MPL phase, giving an estimation of the LVF in the MPL; (d) LVF map masked by the GDL void phase, showing water in the GDL pores (MPL phase is excluded). LVF data are obtained from steady-state H_2/air operation at 0.5 A cm^{-2}, 49 °C, 93% RH, and ambient pressure.

expected (these include operation at 80 °C, 100% RH, and low absolute pressures), the fuel cell performance using the intruded-GDL on the cathode is even slightly compromised when the intruded-GDL is based on a thin GDL substrate (here the H14 GDL-S with a thickness of ~140 μm). At conditions, where more liquid water formation can be expected, e.g., at lower temperatures, higher pressures, and/or a higher inlet gas RH, the performance of the intruded-GDL is similar to that of the sheet-GDL, demonstrating two concurrent and counteracting phenomena: i) an increase of the oxygen transport resistance due to the reduction of the GDL-S macropore size and volume fraction by the intruded MPL material; ii) an improved oxygen transport resistance under conditions where the liquid water saturation of the GDL is high, due to the ability to transport oxygen through the MPL phase intruded into the GDL-S. The results from this study demonstrate that for the thinner H14 GDL-S based GDLs, the intruded-GDL loses ~19%–22% of the macropores in the GDL-S (see $\Delta P_{\text{macropore}}$ in Table I), which results in a higher oxygen transport resistance at dry operating conditions and thus in an inferior fuel cell performance compared to a sheet-GDL. However, when using GDLs based on thicker substrates like the H23 GDL-S, the MPL intrusion depth remains roughly unchanged, so that the loss of macropore volume in the GDL-S is only ~11%–14% (see Table I). In this case, the above described trade-off between increasing the dry oxygen transport resistance while decreasing the wet oxygen transport resistance upon MPL material intrusion into the GDL-S is swayed sufficiently to obtain a clearly better performance at wet conditions for the intruded-GDL compared to the sheet-GDL.

It is known that water forms preferably in the larger pores due to the effect of the capillary forces. Hence, the saturation in the MPL material is (very) low, meaning that the transport of water through the small pores of the MPL is dominated by gas phase transport. Liquid water accumulates in the larger pores of the GDL-S, preferably under the rib as reported in the literature.[13,14] Nagai et al. have studied the water formation and drainage through X-ray tomography.[13] For a homogenous MPL without cracks or larger pores, they have postulated that liquid water is drained out of the GDL by repeated spontaneous interconnection and redispersion of water clusters. The water clusters that they have seen were mostly fully connected throughout the thickness of the GDL-S, meaning that the water clusters formed locally continuous pathways extending from the MPL through the GDL substrate towards the flow-field. When they altered the MPL by introducing larger pores with a pore-forming agent, they observed a better fuel cell performance and a lower overall liquid water saturation in the GDL-S. They concluded that the water pathways must have formed preferably according to the MPL structure, and that at the same water production rate (i.e., at the same current density) the water must be drained at an increased speed for a smaller GDL saturation.

A similar interpretation can be used for the intruded-GDL. The *operando* X-ray tomography data show that the saturation of the intruded-GDL was generally lower than the saturation of the sheet-GDL. At the same time, the intrusion of the MPL material into the GDL-S pores has reduced the macropore volume fraction in the GDL substrate (corresponding to $\Delta P_{\text{macropore}}$ in Table I), which has altered the pathways for liquid water removal. While the remainder of the large pores can act as a place for water drainage, the generally lower liquid water saturation level requires a higher speed of water removal in the remaining large-pore pathways through the GDL-S at the same water production rate (current density).

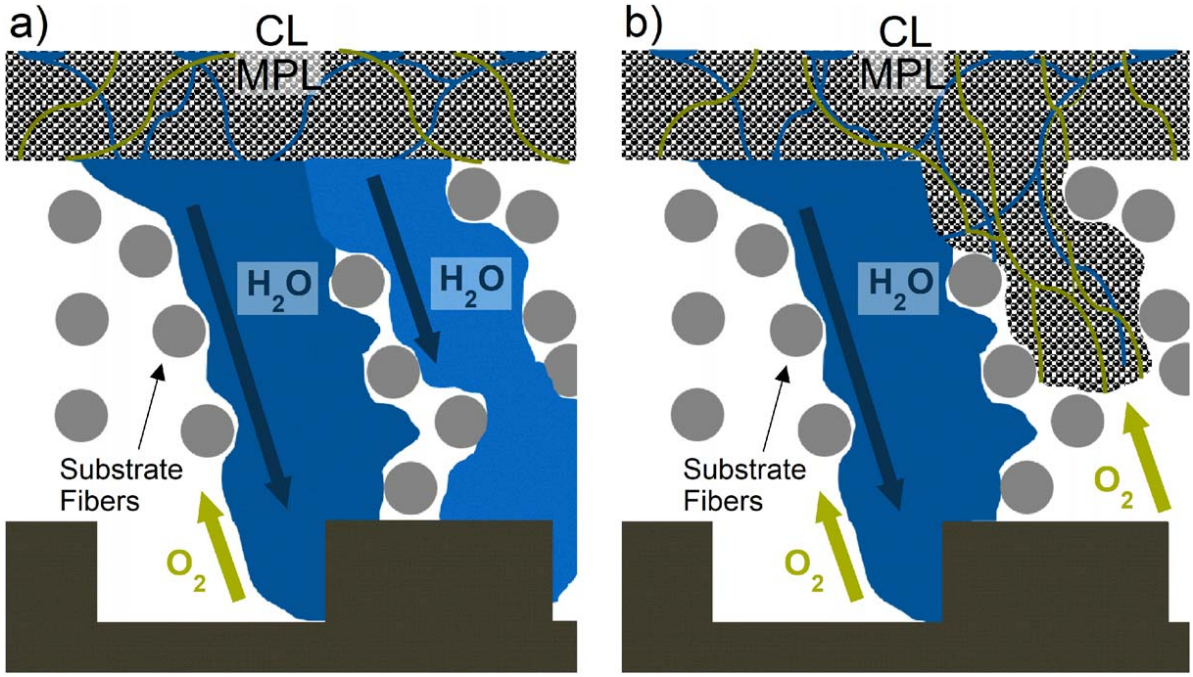

Figure 15. Sketch of the postulated water removal process for (a) the sheet-GDL and (b) the intruded-GDL. While for the sheet-GDL (a) water clusters block the pores randomly according to the capillary pressure and redistribute over time, the liquid water in the intruded-GDL (b) can create liquid water highways in the porous network that is left unintruded by MPL material, while the gas phase oxygen and water vapor transport takes place in the small pores of the intruded MPL material.

Figure 15 shows a sketch of the water removal process for a) the sheet- and b) the intruded-GDL. The sheet-GDL has no directed water transport in the GDL-S: liquid water preferably forms in the larger pores of the GDL-S, where it is transported along the path of least resistance, so that liquid water clusters can redistribute randomly throughout the porous network. On the other hand, for the intruded-GDL, there are clear liquid water pathways dictated by the MPL intrusion: MPL material has intruded into the largest pores, which are now available for gas phase diffusion of oxygen towards the CL or of water vapor from the electrodes to the flow-field. While there are less macropores that can be filled by liquid water, preferential liquid water pathways are created in which liquid water is transported across the GDL substrate via capillary fingering at an increased speed. However, there needs to be a careful balance. When too many of the GDL-S pores are filled with intruded MPL material, such as in case of the thin H14 based intruded-GDLs, the liquid water removal can become less efficient. Therefore, a minimum fraction of macropores need to be present to create a percolating network for fast water removal.

To achieve an optimum performance, an optimization procedure would have to take into account several network parameters, such as the GDL-S thickness, tortuosity, constriction size of the pore connection, and the pore connectivity. We assume that a filling of the smallest pores of the macroporous substrate ($\sim$5-20 μm) would lead to a preferential state, improving the performance under wet conditions. Furthermore, leaving larger pores open (i.e., free of intruded MPL material) would increase the oxygen diffusivity at drier conditions and would create a volume of preferred water formation at wet conditions. This configuration, however, would require a different preparation methodology for intruded-GDLs, as for the here used method based on aqueous MPL slurries, the MPL intrudes preferentially into the large pores of the hydrophobized GDL substrate.

Conclusions

As the structural properties of the MPL influence the PEM fuel cell performance, this work examines two types of MPLs prepared on a thin and a thick GDL substrate (GDL-S): a sheet-type MPL that does not intrude into the GDL-S, referred to as sheet-GDL, and an MPL that intrudes into the GDL-S, referred to as intruded-GDL. These GDLs are evaluated as cathode GDLs in single-cell, differential-flow PEM fuel cell measurements, covering a wide range of operating conditions from dry to wet conditions in order to unravel the general effect of MPL intrusion and the underlying possible water transport mechanisms. x-ray tomographic microscopy (XTM) is used as a complimentary method to gain insight into the spatial distribution of the intruded MPL material across the thickness of the GDL-S and on the steady-state water distribution in both the MPL and the GDL-S.

As shown by mercury intrusion porosimetry (MIP) measurements, the here prepared intruded-GDLs have an average MPL intrusion depth of $\sim$15–21 μm for both GDL-S types (Freudenberg H14 and H23 GDL substrates, with thicknesses of $\approx$140 and $\approx$200 μm, respectively), whereby XTM analysis shows that the intrusion is highly localized towards the MPL/GDL-S interface, with $\sim$89% of the total MPL intrusion residing in the upper half of the H23 GDL-S (with intrusion depths of $>$80 μm). Additionally, the intruded MPL material preferentially fills the macropores of the GDL substrates, driven by capillary pressure effects when coating an aqueous MPL slurry onto the hydrophobized GDL substrates. Based on MIP analyses, this results in a filling of $\sim$22% and $\sim$11% of the macropores in the H14 and the H23 GDL substrates, respectively.

When regarding fuel cell measurements at dry conditions, the intruded-GDLs exhibit a slightly higher oxygen transport resistance (by $\sim$0.1 s cm^{-1}) due to the higher oxygen diffusion resistance through the MPL pores. At conditions that result in a high liquid water saturation in the GDL-S (RH $\geqslant$ 100%, high pressure, and high current densities), the benefit of MPL intrusion into the GDL-S starts to manifest. As liquid water is known to be excluded from the MPL micropores during fuel cell operation, the intrusion of MPL material into the GDL-S efficiently prevents a large volume of GDL pores from being saturated with liquid water. At flooding conditions, the MPL filled GDL-S pores serve as additional oxygen transport pathways, which would otherwise have been filled by liquid water in the absence of MPL intrusion.

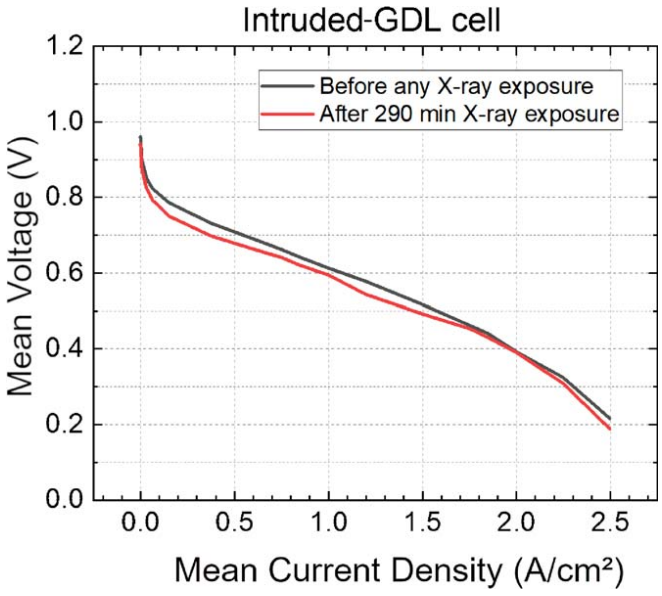

Figure 16. Radiation damage check for the intruded-GDL cell by polarization curves before and after 290 min of X-ray irradiation. All *operando* XTM images were characterized within this time.

The increased dry transport resistance, the loss of macropore volume in the GDL-S due to MPL material intrusion, and the improved liquid water management all affect the fuel cell performance. The chosen conditions and GDL-S thicknesses demonstrate that there is a clear tipping point at which the positive effects of the MPL intrusion dominate. A ∼22% loss of the macropore volume in the GDL-S for the H14 GDL-S based intruded-GDL is too high to increase the cell performance at wet conditions. Only for the thicker H23 GDL-S based intruded-GDL, where the loss of macropore volume in the GDL-S is lowered to ∼11%, the benefit of the MPL intrusion could be established at wet conditions. It is proposed that, while the sheet-GDL structure leads to randomly distributed liquid water percolation paths in the GDL-S, the intruded-GDL provides local confinement of liquid water clusters while providing oxygen and water vapor diffusion pathways through the intruded MPL material.

A similar water management strategy was suggested by Nagai et al. for an MPL that was fabricated using a pore-forming agent.[13] We suggest that intruding the MPL material into the GDL-S can create a similar positive effect to the water formation as an MPL with large pores and, analogously, an MPL with cracks. The intruded MPL material might be advantageous compared to an MPL with cracks in terms of membrane creep and damage under RH cycling conditions. The data from this work suggests that there are still certain drawbacks of an intruded-GDL prepared such that there is a preferential filling of the GDL-S macropores. If the MPL material intrusion can be guided and optimized, an intruded-GDL can enhance the water management of the cell even more significantly.

Acknowledgments

We gratefully acknowledge funding from the Swiss National Science Foundation under the Sinergia grant number 180335. Furthermore, we are grateful for the materials provided free-of-charge by Denka, Japan (Li400 acetylene black) and by 3M Dyneon, Germany (TF 5135GZ PTFE dispersion). We would like to thank Jens Eller (PSI) for providing optimized, state-of-the-art fuel cell imaging hardware and Christoph Csoklich (PSI) for the provision of the fuel cell humidifier and the instruction on *operando* experiments in the laboratory CT scanner. Furthermore, we are grateful for Thomas Gloor (PSI) for the technical support provided for the fuel cell experiments.

Appendix

Segmentation of intruding MPL material.—The three segmentation results shown in Fig. 1 are based on "bilateral filtered" (ImageJ function, see Experimental section) GDL images (8-bit). The different segmentations were obtained by using three different threshold values for the MPL phase, followed by image noise clearing processes, which were done globally once, and manually at selected domains of the GDLs. The details for threshold values and clearing processes for each of the three segmentations are given in Table III.

Note that the absolute threshold values here may not be reproduced exactly on other images if the original 32-bit tomographic images have a different maximal and minimal grayscale value (GSV) range than the images used here. It is because, in transforming the images from 32-bit to 8-bit, the images are rescaled and different maximal and minimal GSVs will result in different assignment of 8-bit GSVs.

Radiation damage check of the fuel cell after XTM measurements.—Catalyst coated membranes are known to be degraded by X-ray irradiation.[28,37] The performance of the cell using the intruded-GDL is checked before and after 290 min of X-ray exposure using the scanning parameters with an X-ray tube voltage of 80 kV and a current of 300 μA (see also Experimental section).

As seen in Figure 16, a slight voltage reduction after X-ray irradiation was observed (maximal voltage difference = 36 mV). Due to this relatively small voltage loss, the cell performance was regarded as largely maintained. Therefore, the X-ray imaging data are considered representative.

Table III. Details of the procedures and threshold values to obtain the segmentations of the MPL phase shown in Fig. 1.

Through-plane distance	High threshold	Calibrated	Low threshold
0–40 μm	Manual selection (magic wand tool)	Manual selection (magic wand tool)	Manual selection (magic wand tool)
40–108 μm	Threshold values 35–177 followed by 3D clearing	Threshold values 50–177 followed by 3D clearing	Threshold values 65–177 followed by 3D clearing
108–227 μm	Threshold values 35–177 followed by 3D clearing, plus additional 2D noise clearing on selected images (manually done)	Threshold values 56–177 followed by 3D clearing, plus additional 2D noise clearing on selected images (manually done)	Threshold values 65–177 followed by 3D clearing, plus additional 2D noise clearing on selected images (manually done)

ORCID

Anne Berger https://orcid.org/0000-0003-3230-4730
Yen-Chun Chen https://orcid.org/0000-0003-2161-9198
Thomas J. Schmidt https://orcid.org/0000-0002-1636-367X
Felix N. Büchi https://orcid.org/0000-0002-3541-4591
Hubert A. Gasteiger https://orcid.org/0000-0001-8199-8703

References

1. IEA, *Net Zero by*, **2050** (2021), (https://iea.org/reports/net-zero-by-2050, *Licence CC BY 4.0*).
2. IEA, *Global EV Outlook 2021* (2021), (https://iea.org/reports/global-ev-outlook-2021, License: CC BY 4.0).
3. D. A. Cullen, K. C. Neyerlin, R. K. Ahluwalia, R. Mukundan, K. L. More, R. L. Borup, A. Z. Weber, D. J. Myers, and A. Kusoglu, *Nat. Energy*, **6**, 462 (2021).
4. C. S. Gittleman, A. Kongkanand, D. Masten, and W. Gu, *Curr. Opin. Electrochem.*, **18**, 81 (2019).
5. O. Gröger, H. A. Gasteiger, and J.-P. Suchsland, *J. Electrochem. Soc.*, **162**, A2605 (2015).
6. R. L. Borup, A. Kusoglu, and A. Z. Weber, *FCHEA-Fuel Cell & Hydrogen Energy Association* (U.S. Department of Energy publisher, Los Alamos, New Mexico, United States) Vol. 2021, p. 12 (2021).
7. A. Z. Weber and J. Newman, *J. Electrochem. Soc.*, **152**, A677 (2005).
8. J. T. Gostick, M. A. Ioannidis, M. W. Fowler, and M. D. Pritzker, *Electrochem. Commun.*, **11**, 576 (2009).
9. J. T. Gostick, M. A. Ioannidis, M. D. Pritzker, and M. W. Fowler, *J. Electrochem. Soc.*, **157**, B563 (2010).
10. F. Ahmadi and R. Roshandel, *J. Fuel Cell Sci. Technol.*, **11**, 011004 (2013).
11. A. K. C. Wong, R. Banerjee, and A. Bazylak, *J. Electrochem. Soc.*, **166**, F3009 (2019).
12. K. T. Cho, A. Turhan, and M. Mench, *ECS Trans.*, **41**, 513 (2011).
13. Y. Nagai, J. Eller, T. Hatanaka, S. Yamaguchi, S. Kato, A. Kato, F. Marone, H. Xu, and F. N. Büchi, *J. Power Sources*, **435**, 226809 (2019).
14. H. Xu, M. Bührer, F. Marone, T. J. Schmidt, F. N. Büchi, and J. Eller, *J. Electrochem. Soc.*, **168**, 074505 (2021).
15. H. Xu, S. Nagashima, H. P. Nguyen, K. Kishita, F. Marone, F. N. Büchi, and J. Eller, *J. Power Sources*, **490**, 229492 (2021).
16. I. V. Zenyuk, E. C. Kumbur, and S. Litster, *J. Power Sources*, **241**, 379 (2013).
17. H. Markötter et al., *Electrochem. Commun.*, **34**, 22 (2013).
18. P. Deevanhxay, T. Sasabe, S. Tsushima, and S. Hirai, *J. Power Sources*, **230**, 38 (2013).
19. C. Simon, D. Kartouzian, D. Müller, F. Wilhelm, and H. A. Gasteiger, *J. Electrochem. Soc.*, **164**, F1697 (2017).
20. H. Tang, S. Wang, M. Pan, and R. Yuan, *J. Power Sources*, **166**, 41 (2007).
21. C. Csoklich, H. Xu, F. Marone, T. J. Schmidt, and F. N. Büchi, *ACS Appl. Energy Mater.*, **4**, 12808 (2021).
22. C. Simon, J. Endres, B. Nefzger-Loders, F. Wilhelm, and H. A. Gasteiger, *J. Electrochem. Soc.*, **166**, F1022 (2019).
23. C. Simon, F. Hasché, D. Müller, and H. A. Gasteiger, *ECS Trans.*, **69**, 1293 (2015).
24. D. R. Baker, D. A. Caulk, K. C. Neyerlin, and M. W. Murphy, *J. Electrochem. Soc.*, **156**, B991 (2009).
25. C. Csoklich, *From Stochastic to Deterministic Transport. Advanced Gas Diffusion Layers for Polymer Electrolyte Fuel Cells* (Doctoral Dissertation, ETH Zurich) (2022).
26. H. Xu, *Subsecond Operando X-ray Tomographic Microscopy of Liquid Water in Polymer Electrolyte Fuel Cells* (Doctoral Dissertation, ETH Zurich) (2021).
27. Y.-C. Chen, A. Berger, S. De Angelis, T. Schuler, M. Bozzetti, J. Eller, V. Tileli, T. J. Schmidt, and F. N. Büchi, *ACS Appl. Mater. Interfaces*, **13**, 16227 (2021).
28. X. Ding, J. P. Ebin, T. A. L. Harris, Z. Li, and T. F. Fuller, *AIChE J*, **60**, 4241 (2014).
29. R. Bock, A. D. Shum, X. Xiao, H. Karoliussen, F. Seland, I. V. Zenyuk, and O. S. Burheim, *J. Electrochem. Soc.*, **165**, F514 (2018).
30. K.-D. Wagner, A. Bock, K. Salama, and A. Weller, (United States)(Patent Application Publication publisher) (2010).
31. M. F. Mathias, J. Roth, J. Fleming, and W. Lehnert, *Handbook of Fuel Cells*, ed. W. Vielstich, H. A. Gasteiger, and A. Lamm (Wiley, New York) (2010).
32. R. R. Rashapov, J. Unno, and J. T. Gostick, *J. Electrochem. Soc.*, **162**, F603 (2015).
33. I. V. Zenyuk, D. Y. Parkinson, L. G. Connolly, and A. Z. Weber, *J. Power Sources*, **328**, 364 (2016).
34. Z. Fishman, J. Hinebaugh, and A. Bazylak, *J. Electrochem. Soc.*, **157**, B1643 (2010).
35. L. Jabbour, C. Robin, F. Nandjou, R. Vincent, F. Micoud, J.-P. Poirot-Crouvezier, J. D'Arbigny, and M. Gerard, *J. Power Sources*, **299**, 380 (2015).
36. Y.-C. Chen, C. Karageorgiou, J. Eller, T. J. Schmidt, and F. N. Büchi, *J. Power Sources*, **539**, 231612 (2022).
37. J. Eller and F. N. Büchi, *J. Synchrotron Radiat.*, **21**, 82 (2014).

5 Conclusion & Outlook

This thesis covers different topics regarding the mass transport of oxygen and water in GDLs. In the first part, the respective GDL-S and the MPL structures were characterized in regard to the oxygen diffusivity through the dry structure. A method was developed, which made it possible to characterize the τ/ε-ratio of the GDL-S or the MPL in the operating fuel cell using limiting current measurements. The analysis of the limiting current data revealed that small pores are more important for the diffusivity than statistically expected by their share to the overall pore volume. This observation could not only be drawn for MPLs, but also for the Freudenberg GDL-S, where carbon black was added to the GDL-S structure by the manufacturer. For the MPLs, the τ determination was supported by simulations of mass transport through the MPL structure, which was obtained by FIB-SEM. Two different MPL types were analyzed, which varied by their characteristic pore diameter, while possessing the same high porosity of $\approx$80%. Their tortuosities were determined by limiting current analysis and simulation to be the same value of 1.2-1.3. Following the analysis of the transport of oxygen reactant to the CL without the occurrence of liquid water inside the GDL-S or MPL pores, the examination extends to the formation of product water. From a structural side, simulations using a random walk approach revealed that a pore filling in an hydrophobic environment, where large pores are filled first, is important for maintaining a percolating MPL pore network under wet conditions.

To understand and finally improve liquid water removal, we have modified our MPL/GDL-S interface by an inhomogeneous intrusion into the GDL-S material, where MPL material was pushed locally into the largest pores of the GDL-S. The structure was characterized via MIP and XTM. Single-cell fuel cell tests under various conditions revealed that there are two influencing factors: the drawback of filling the open space of large pores with MPL material and the advantage of directed water removal. A better performance could be reached with the intrusion into thicker GDL-S materials, where after the intrusion more macropores where still available for water removal. The analysis of the water content of the GDL-S with XTM led to the conclusion that the inhomogeneous intrusion of the MPL material into the GDL-S has induced similar localized water clusters as in the case where an MPL was perforated with pore formers, while still maintaining a crack- and large-pore-free interface between the CL and the MPL for mechanical stability.

In summary, this thesis shows the development of new measurement approaches to quantify the tortuosity and porosity of GDL-substrates and MPLs, which can describe the diffusivity at dry conditions; it also shows approaches to analyze the pore connectivity, when the structure is being filled with water. Furthermore, it also revealed the importance of directed water removal within the GDL structure. Beyond this thesis, there have been decades of academic and industry research over which one has tried to characterize the GDL properties to find the right GDL compositions for fuel cells. It is difficult to suggest one final design, and the GDL still needs to be tailored to the working conditions in the fuel cell system. A GDL that can remove water well at wet conditions will not succeed to retain water during operation at dry conditions.

There are several problems that the composition of the GDL needs to account for. The major issue is that oxygen as the reactant and water as the product need to be transported through the same pores, while water in liquid form can block the pathways. If the GDL could create two networks, one for the reactant and one for the product, their transport could be channeled more efficiently. One way to localize water removal was achieved by adding pore formers to the MPL formulation. However, large pores or cracks are known to cause membrane failure upon RH cycles. As RH cycling procedures are difficult and require lengthy tests, it is not known if there is a compromise in feature shape and size (hole, crack), which can support a reinforced and chemically mitigated membrane state-of-health for the desired 30,000 hours lifetime for heavy-duty transport. This thesis suggests a different approach using local MPL material intrusion into the GDL-S to localize liquid water removal. However, our method had the unfortunate disadvantage of taking away the largest pores in the GDL-S, which rendered the approach unviable.

Despite the difficulties, I would like to try to summarize the findings of this thesis to suggest ideal GDL parameters, i.e. proposing design parameters for the “ideal“ GDL. Prerequisite is that the MPL creates a smooth support to the catalyst layer (no cracks, large pores) to ensure a sufficient life time of the membrane.

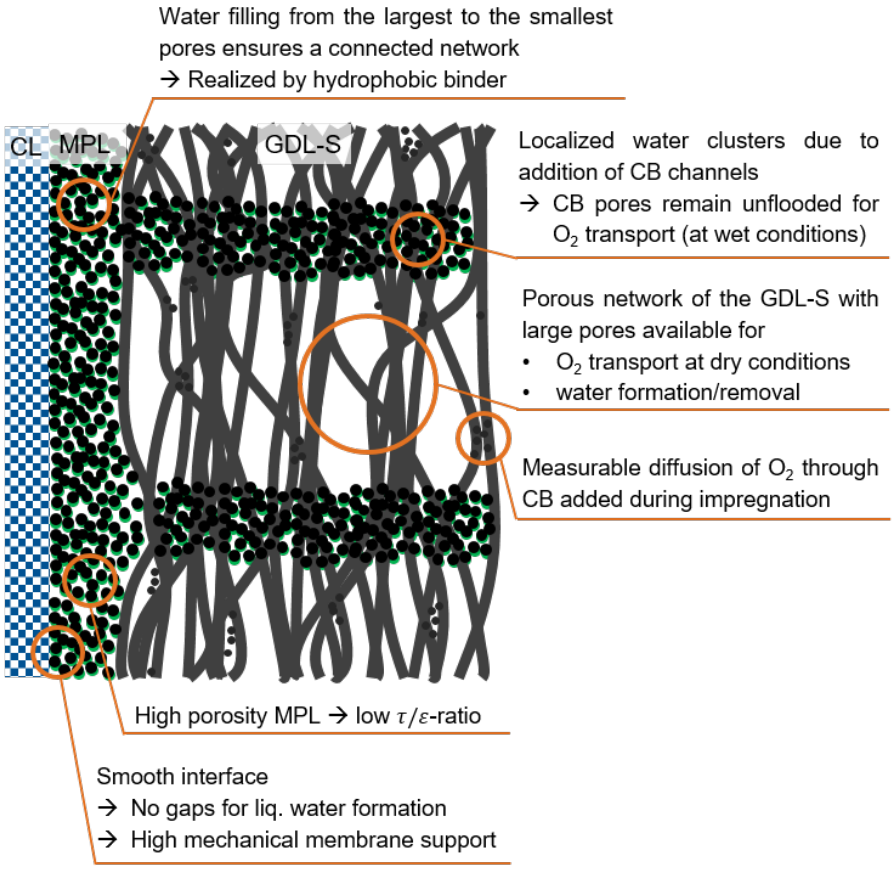

Figure 5.1 Proposal for an "ideal" GDL, incorporating the findings from this thesis, considering the requirement that the MPL needs to provide a smooth interface to the CL for lifetime requirement. Channels in the GDL made of MPL material need to guide water removal in the GDL-S; GDL-S and MPL need to be highly porous to ensure a low tortuosity; the binder material in the MPL must be highly hydrophobic to ensure a liquid water filling starting from the largest to the smallest pores, which guarantees a connectivity of the porous network at intermediate saturation.

The following list summarizes the important characteristics of the ideal GDL. The parameters are visualized in Fig. 5.1.

- A highly porous network of the MPL, which results in a low τ/ε-ratio.
- A hydrophobic binder within the MPL to ensure a water filling from largest to smallest pores so that a percolating pore network remains at the corresponding liquid water saturation.
- Carbon black in the GDL-S can add to overall oxygen diffusivity.
- Water formation is localized to specific locations, while other pathways are open to water transport, guided by intruding pillars of MPL material.
- Large pores need to be available in the GDL for oxygen transport at dry conditions and for water removal at wet conditions.

In conclusion, the "ideal" GDL, depicted in Fig. 5.1, combines a suite of complementary features that work synergistically to optimize performance under varying fuel cell conditions. The catalyst layer is situated

on the left side of Fig. 5.1 adjacent to the MPL. A smooth MPL surface facing the catalyst layer provides strong mechanical support, enhancing the membrane's resistance to stress. The MPL itself possesses a highly porous structure, which achieves a low τ/ε ratio, significantly enhancing reactant gas accessibility and minimizing transport losses. The use of a hydrophobic binder strategically ensures that liquid water, when formed under the operating conditions, invades the pore network in a controlled manner: from larger to smaller pores—preserving open pathways and preventing pore blockage, which is crucial for sustained operation and durability. Furthermore, incorporating local clusters of carbon black into the GDL substrate not only improves electrical conductivity but also boosts oxygen diffusivity. The deliberate localization of guiding pillars of carbon black material within the GDL-S ensures that water is efficiently directed away from the active area through the largest pores of the fibrous GDL substrate material, maintaining dry channels within the carbon black for uninterrupted oxygen gas flow. Importantly, in addition to enabling rapid water evacuation in humid environments, the free space of large pores in the fibrous GDL-S provides the benefit of facilitating oxygen delivery during dry conditions. Together, these engineered features provide a robust framework for maintaining optimal gas-liquid management, directly translating to enhanced fuel cell efficiency, resilience, and operational stability.

The proposed design can only be effective when the water transport through the MPL layer itself occurs in the gas phase. The extraction of water in its liquid state through the small hydrophobic pores of the MPL would pose considerable challenges. However, recapitulating the thermal conductivity aspect, a GDL with a low thermal conductivity could increase the thermal gradient between the CL and the flow field and therefore, a gas phase transport through the MPL is enhanced, while the proposed structure can tolerate a condensation of liquid water leading to capillary fingering in the GDL-S because of the inserted structures.

This thesis focuses on the cathode GDL. However, the anode GDL is also an important factor when considering the water management throughout the single-cell, as water back-diffusion from the cathode to the anode is affected. An important aspect that was beyond the scope of this thesis but is still a crucial design parameter, is the thermal conductivity of the GDL-S and the MPL structure (anode and cathode).

All in all, this thesis contributed to a better understanding of GDL properties, which has led to a proposal of an "ideal" GDL. To combat climate change, there is still a need to develop new technologies, as current solutions are not sufficient. PEMFCs are especially important in hard-to-abate industries among those heavy and long-distance transport. Water management remains a limiting factor for the operating regime of a fuel cell, because the GDL can only support certain conditions, where the membrane stays hydrated enough for proton conduction and where liquid water does not accumulate and, consequently, blocks the GDL structure. Continued research and a deeper comprehension of the subject can expand the operational range and enhance the reliability of PEMFCs.

Bibliography

[1] World Meteorological Organization (WMO). State of the global climate 2022. Report, WMO, 2023.

[2] Intergovernmental Panel on Climate Change. Climate change widespread, rapid, and intensifying – IPCC, 2021.

[3] UNFCCC. The paris agreement. *Paris Climate Change Conference*, 2015.

[4] Intergovernmental Panel on Climate Change. Ar6 synthesis report: Climate change 2023. *Summary for Law Makers*, 2023.

[5] International Energy Agency. Net zero by 2050, 2021.

[6] Thomas A. Deetjen, Liam Walsh, and Parth Vaishnav. Us residential heat pumps: the private economic potential and its emissions, health, and grid impacts. *Environmental Research Letters*, 16(8): 084024, 2021. ISSN 1748-9326. doi: 10.1088/1748-9326/ac10dc.

[7] International Energy Agency. Global EV Outlook, 2023.

[8] Gabriel Lopez, Javier Farfan, and Christian Breyer. Trends in the global steel industry: Evolutionary projections and defossilisation pathways through power-to-steel. *Journal of Cleaner Production*, 375:134182, 2022. ISSN 0959-6526. doi: 10.1016/j.jclepro.2022.134182.

[9] A. Peschel. Industrial perspective on hydrogen purification, compression, storage, and distribution. *Fuel Cells*, 20(4):385–393, 2020. ISSN 1615-6846. doi: 10.1002/fuce.201900235.

[10] Traton Group. Traton way forward, 2022. URL https://ir.traton.com/download/companies/traton/Companypresentation/TRATON_Company_Presentation_2022.pdf. Accessed: 10.8.2023.

[11] David A. Cullen, K. C. Neyerlin, Rajesh K. Ahluwalia, Rangachary Mukundan, Karren L. More, Rodney L. Borup, Adam Z. Weber, Deborah J. Myers, and Ahmet Kusoglu. New roads and challenges for fuel cells in heavy-duty transportation. *Nature Energy*, 6(5):462–474, 2021. ISSN 2058-7546. doi: 10.1038/s41560-021-00775-z.

[12] Hydrogen Europe. How hydrogen can help decarbonise the maritime sector. Report, Hydrogen Europe, 2021.

[13] Rainer Scholz, Nadija Gläser, Daniel Plauch, and Timo Schmidt. Towards zero emissions in rail transport. Report, Bundesministerium für Verkehr und digitale Struktur, 2020.

[14] David Kramer. Hydrogen-powered aircraft may be getting a lift. *Physics Today*, 73(12):27–29, 2020. ISSN 0031-9228. doi: 10.1063/pt.3.4632.

[15] Rinat R. Rashapov, Jonathan Unno, and Jeff T. Gostick. Characterization of PEMFC gas diffusion layer porosity. *Journal of The Electrochemical Society*, 162(6):F603, 2015. ISSN 1945-7111 0013-4651. doi: 10.1149/2.0921506jes.

[16] Iryna V. Zenyuk, Dilworth Y. Parkinson, Liam G. Connolly, and Adam Z. Weber. Gas-diffusion-layer structural properties under compression via x-ray tomography. *Journal of Power Sources*, 328:364–376, 2016. ISSN 0378-7753. doi: 10.1016/j.jpowsour.2016.08.020.

[17] Z. Fishman, J. Hinebaugh, and A. Bazylak. Microscale tomography investigations of heterogeneous porosity distributions of PEMFC gdls. *Journal of The Electrochemical Society*, 157(11):B1643, 2010. ISSN 1945-7111 0013-4651. doi: 10.1149/1.3481443.

[18] Christoph Simon, Dena Kartouzian, David Müller, Florian Wilhelm, and Hubert A. Gasteiger. Impact of microporous layer pore properties on liquid water transport in pem fuel cells: Carbon black type and perforation. *Journal of The Electrochemical Society*, 164(14):F1697, 2017. ISSN 1945-7111. doi: 10.1149/2.1321714jes.

[19] Wataru Yoshimune, Satoru Kato, Satoshi Yamaguchi, Yusuke Akimoto, Akihiko Koiwai, and Hiroshi Nakamura. Managing the pore morphologies of microporous layers for polymer electrolyte fuel cells with a solvent-free coating technique. *ACS Sustainable Chemistry & Engineering*, 9(23):7922–7929, 2021. doi: 10.1021/acssuschemeng.1c02105.

[20] Stefan Kreitmeier, Gabriel A. Schuler, Alexander Wokaun, and Felix N. Büchi. Investigation of membrane degradation in polymer electrolyte fuel cells using local gas permeation analysis. *Journal of Power Sources*, 212:139–147, 2012. ISSN 0378-7753. doi: 10.1016/j.jpowsour.2012.03.071.

[21] Jeff T. Gostick, Marios A. Ioannidis, Michael W. Fowler, and Mark D. Pritzker. On the role of the microporous layer in PEMFC operation. *Electrochemistry Communications*, 11(3):576–579, 2009. ISSN 1388-2481. doi: 10.1016/j.elecom.2008.12.053.

[22] Peter w. Atkins, Julio De Paula, and Jamers J. Keeler. *Physikalische Chemie*. Wiley-VCH, sixth edition edition, 2022. ISBN 978-3-527-34550-2.

[23] Frano Barbir. Chapter 2 - fuel cell basic chemistry and thermodynamics. In *PEM Fuel Cells*, pages 17–32. Academic Press, Burlington, 2005. ISBN 978-0-12-078142-3. doi: 10.1016/B978-012078142-3/50003-3.

[24] W. Gu, D. R. Baker, Y. Liu, and H. A. Gasteiger. Proton exchange membrane fuel cell (PEMFC) down-the-channel performance model. In W. Vielstich, H. A. Gasteiger, and A. Lamm, editors, *Handbook of Fuel Cells*, book section 43, pages 631–657. John Wiley & Sons, 2010. ISBN 9780470974001. doi: 10.1002/9780470974001.f500044. Major Reference Works.

[25] K. C. Neyerlin, Wenbin Gu, Jacob Jorne, and Hubert A. Gasteiger. Determination of catalyst unique parameters for the oxygen reduction reaction in a PEMFC. *Journal of The Electrochemical Society*, 153(10):A1955, 2006. ISSN 1945-7111 0013-4651. doi: 10.1149/1.2266294.

[26] J. Durst, A. Siebel, C. Simon, F. Hasché, J. Herranz, and H. A. Gasteiger. New insights into the electrochemical hydrogen oxidation and evolution reaction mechanism. *Energy & Environmental Science*, 7(7):2255–2260, 2014. ISSN 1754-5692. doi: 10.1039/C4EE00440J.

[27] Björn M. Stühmeier, Markus R. Pietsch, Jan N. Schwämmlein, and Hubert A. Gasteiger. Pressure and temperature dependence of the hydrogen oxidation and evolution reaction kinetics on Pt electrocatalysts via PEMFC-based hydrogen-pump measurements. *Journal of The Electrochemical Society*, 168(6):064516, 2021. ISSN 1945-7111 0013-4651. doi: 10.1149/1945-7111/ac099c.

[28] K. C. Neyerlin, Wenbin Gu, Jacob Jorne, and Hubert A. Gasteiger. Study of the exchange current density for the hydrogen oxidation and evolution reactions. *Journal of The Electrochemical Society*, 154(7):B631, 2007. ISSN 1945-7111 0013-4651. doi: 10.1149/1.2733987.

[29] Christophe Gerling, Matthias Hanauer, Ulrich Berner, and K. Andreas Friedrich. Full factorial in situ characterization of ionomer properties in differential PEM fuel cells. *Journal of The Electrochemical Society*, 168(8):084504, 2021. ISSN 1945-7111 0013-4651. doi: 10.1149/1945-7111/ac1812.

[30] C. H. Hamann and W. Vielstich. *Electrochemistry*, volume 86. John Wiley & Sons, Ltd, 1982. ISBN 0005-9021. doi: 10.1002/bbpc.19820860826.

[31] Patrick Zihrul, Ingmar Hartung, Sebastian Kirsch, Gerold Huebner, Frédéric Hasché, and Hubert A. Gasteiger. Voltage cycling induced losses in electrochemically active surface area and in H_2/air-performance of pem fuel cells. *Journal of The Electrochemical Society*, 163(6):F492, 2016. ISSN 1945-7111. doi: 10.1149/2.0561606jes.

[32] Christoph Simon. *Oxygen and Water Transport in the Microporous Layer of Polymer Electrolyte Membrane Fuel Cells*. Thesis, 2020.

[33] Timon Lazaridis and Hubert A. Gasteiger. Pt-catalyzed oxidation of PEMFC carbon supports: A path to highly accessible carbon morphologies and implications for start-up/shut-down degradation. *Journal of The Electrochemical Society*, 168(11):114517, 2021. ISSN 1945-7111 0013-4651. doi: 10.1149/1945-7111/ac35ff.

[34] Rodney L. Borup, Ahmet Kusoglu, Kenneth C. Neyerlin, Rangachary Mukundan, Rajesh K. Ahluwalia, David A. Cullen, Karren L. More, Adam Z. Weber, and Deborah J. Myers. Recent developments in catalyst-related PEM fuel cell durability. *Current Opinion in Electrochemistry*, 21:192–200, 2020. ISSN 2451-9103. doi: 10.1016/j.coelec.2020.02.007.

[35] Tomoo Yoshizumi, Hideki Kubo, and Masao Okumura. Development of high-performance fc stack for the new mirai, 2021.

[36] Venkata Yarlagadda, Michael K. Carpenter, Thomas E. Moylan, Ratandeep Singh Kukreja, Roland Koestner, Wenbin Gu, Levi Thompson, and Anusorn Kongkanand. Boosting fuel cell performance with accessible carbon mesopores. *ACS Energy Letters*, 3(3):618–621, 2018. doi: 10.1021/acsenergylett.8b00186.

[37] Craig S. Gittleman, Anusorn Kongkanand, David Masten, and Wenbin Gu. Materials research and development focus areas for low cost automotive proton-exchange membrane fuel cells. *Current Opinion in Electrochemistry*, 18:81–89, 2019. ISSN 2451-9103. doi: 10.1016/j.coelec.2019.10.009.

[38] Thomas Mittermeier, Alexandra Weiß, Frédéric Hasché, and Hubert A. Gasteiger. PEM fuel cell start-up/shut-down losses vs relative humidity: The impact of water in the electrode layer on carbon corrosion. *Journal of The Electrochemical Society*, 165(16):F1349, 2018. ISSN 1945-7111. doi: 10.1149/2.0931816jes.

[39] Robin Girod, Timon Lazaridis, Hubert A. Gasteiger, and Vasiliki Tileli. Three-dimensional nanoimaging of fuel cell catalyst layers. *Nature Catalysis*, 6(5):383–391, 2023. ISSN 2520-1158. doi: 10.1038/s41929-023-00947-y.

[40] S. Mizuno, T. Hayashi, H. Kubo, M. Okumura, T. Kurihara, and K. Mori. Development of the fuel cell stack for the second-generation mirai. *Toyota Technical Review*, 66(22), 2021.

[41] Elliot Padgett, Venkata Yarlagadda, Megan E. Holtz, Matthew Ko, Barnaby D. A. Levin, Ratandeep Singh Kukreja, Joseph M. Ziegelbauer, Ross N. Andrews, Jan Ilavsky, Anusorn Kongkanand, and David A. Muller. Mitigation of PEM fuel cell catalyst degradation with porous carbon supports. *Journal of The Electrochemical Society*, 166(4):F198, 2019. ISSN 1945-7111. doi: 10.1149/2.0371904jes.

[42] Kenji Miyatake. Membrane electrolytes, from perfluorosulfonic acid (pfsa) to hydrocarbon ionomers. In Robert A. Meyers, editor, *Encyclopedia of Sustainability Science and Technology*, pages 1–32. Springer New York, New York, NY, 2015. ISBN 978-1-4939-2493-6. doi: 10.1007/978-1-4939-2493-6_146-3.

[43] Ahmet Kusoglu and Adam Z. Weber. New insights into perfluorinated sulfonic-acid ionomers. *Chemical Reviews*, 117(3):987–1104, 2017. ISSN 0009-2665. doi: acs.chemrev.6b00159.

[44] C. K. Mittelsteadt and H. Liu. Conductivity, permeability, and ohmic shorting of ionomeric membranes. In W. Vielstich, H. A. Gasteiger, and A. Lamm, editors, *Handbook of Fuel Cells*. John Wiley & Sons, 2010. ISBN 9780470974001. doi: 10.1002/9780470974001.f500025.

[45] Satoru Hommura, Kengo Kawahara, Tetsuji Shimohira, and Yasutake Teraoka. Development of a method for clarifying the perfluorosulfonated membrane degradation mechanism in a fuel cell environment. *Journal of The Electrochemical Society*, 155(1):A29, 2008. ISSN 1945-7111 0013-4651. doi: 10.1149/1.2800171.

[46] Fuqiang Liu, Baolian Yi, Danmin Xing, Jingrong Yu, and Huamin Zhang. Nafion/PTFE composite membranes for fuel cell applications. *Journal of Membrane Science*, 212(1):213–223, 2003. ISSN 0376-7388. doi: 10.1016/S0376-7388(02)00503-3.

[47] Frank D. Coms, Han Liu, and Jeanette E. Owejan. Mitigation of perfluorosulfonic acid membrane chemical degradation using cerium and manganese ions. *ECS Transactions*, 16(2):1735, 2008. ISSN 1938-5862. doi: 10.1149/1.2982015.

[48] A. Frank de Bruijn and Gaby J. M. Janssen. Pem fuel cell materials: Costs, performance and durability. In Robert A. Meyers, editor, *Encyclopedia of Sustainability Science and Technology*, pages 7694–7730. Springer New York, New York, NY, 2012. ISBN 978-1-4419-0851-3. doi: 10.1007/978-1-4419-0851-3_152.

[49] G. O. Mepsted and J. M. Moore. Performance and durability of bipolar plate materials. In W. Vielstich, H. A. Gasteiger, and A. Lamm, editors, *Handbook of Fuel Cells*. John Wiley & Sons, 2010. ISBN 9780470974001. doi: 10.1002/9780470974001.f303027. Major Reference Works.

[50] Max Wei, Ahmad Mayyas, Timothy E. Lipman, Hanna Breunig, Roberto Scataglini, Shuk Han Chan, Joshua Chien, David Gosselin, and Nadir Saggiorato. Fuel cell systems: Total cost of ownership. In Timothy E. Lipman and Adam Z. Weber, editors, *Fuel Cells and Hydrogen Production: A Volume in the Encyclopedia of Sustainability Science and Technology, Second Edition*, pages 27–81. Springer New York, New York, NY, 2019. ISBN 978-1-4939-7789-5. doi: 10.1007/978-1-4939-7789-5_1020.

[51] Trung V. Nguyen. A gas distributor design for proton-exchange-membrane fuel cells. *Journal of The Electrochemical Society*, 143(5):L103, 1996. ISSN 1945-7111 0013-4651. doi: 10.1149/1.1836666.

[52] T. V. Nguyen and W. He. Interdigitated flow field design. In W. Vielstich, H. A. Gasteiger, and A. Lamm, editors, *Handbook of Fuel Cells*. John Wiley & Sons, 2010. ISBN 9780470974001. doi: 10.1002/9780470974001.f303031. Major Reference Works.

[53] M. F. Mathias, J. Roth, J. Fleming, and W. Lehnert. Diffusion media materials and characterisation. In W. Vielstich, H. A. Gasteiger, and A. Lamm, editors, *Handbook of Fuel Cells*. John Wiley & Sons, 2010. doi: 10.1002/9780470974001.f303046.

[54] Guangyi Lin, Shouyi Liu, Guangkai Qu, Yingjie Song, Tianya Li, Fumin Liu, and Yafei Hu. Effect of pore size distribution in the gas diffusion layer adjusted by composite carbon black on fuel cell performance. *International Journal of Energy Research*, 45(5):7689–7702, 2021. ISSN 0363-907X. doi: 10.1002/er.6350.

[55] Christoph Simon, Joseph Endres, Benjamin Nefzger-Loders, Florian Wilhelm, and Hubert A. Gasteiger. Interaction of pore size and hydrophobicity/hydrophilicity for improved oxygen and water transport through microporous layers. *Journal of The Electrochemical Society*, 166(13):F1022, 2019. ISSN 1945-7111. doi: 10.1149/2.1111913jes.

[56] Rüdiger Schweiss, Simon Hofmeister, Christian Meiser, Dana Dan, Alois Baumann, Tobias Kuster, Nico Haak, and Susanne Bache. Sigracet - our gas diffusion layer. *White Paper*, 2021.

[57] Jian Chen, Haifeng Xu, Huamin Zhang, and Baolian Yi. Facilitating mass transport in gas diffusion layer of PEMFC by fabricating micro-porous layer with dry layer preparation. *Journal of Power Sources*, 182(2):531–539, 2008. ISSN 0378-7753. doi: 10.1016/j.jpowsour.2008.04.031.

[58] Andrew Kai Cheung Wong, Rupak Banerjee, and Aimy Bazylak. Tuning MPL intrusion to increase oxygen transport in dry and partially saturated polymer electrolyte membrane fuel cell gas diffusion layers. *Journal of The Electrochemical Society*, 166(7):F3009, 2019. ISSN 1945-7111. doi: 10.1149/2.0021907jes.

[59] Adam Z. Weber and John Newman. Effects of microporous layers in polymer electrolyte fuel cells. *Journal of The Electrochemical Society*, 152(4):A677, 2005. ISSN 1945-7111 0013-4651. doi: 10.1149/1.1861194.

[60] Farzad Ahmadi and Ramin Roshandel. Effects of microhydrophobic porous layer on water distribution in polymer electrolyte membrane fuel cells. *Journal of Fuel Cell Science and Technology*, 11(1), 2013. ISSN 1550-624X. doi: 10.1115/1.4025522.

[61] Jin Hyun Nam and Massoud Kaviany. Effective diffusivity and water-saturation distribution in single- and two-layer PEMFC diffusion medium. *International Journal of Heat and Mass Transfer*, 46(24): 4595–4611, 2003. ISSN 0017-9310. doi: 10.1016/S0017-9310(03)00305-3.

[62] Jon P. Owejan, Jeanette E. Owejan, Wenbin Gu, Thomas A. Trabold, Thomas W. Tighe, and Mark F. Mathias. Water transport mechanisms in pemfc gas diffusion layers. *Journal of The Electrochemical Society*, 157(10):B1456, 2010. ISSN 1945-7111 0013-4651. doi: 10.1149/1.3468615.

[63] Yusuke Aoyama, Kengo Suzuki, Yutaka Tabe, and Takemi Chikahisa. Observation of water transport in the micro-porous layer of a polymer electrolyte fuel cell with a freezing method and cryo-scanning electron microscope. *Electrochemistry Communications*, 41:72–75, 2014. ISSN 1388-2481. doi: 10.1016/j.elecom.2013.12.029.

[64] J. Zhou, S. Shukla, A. Putz, and M. Secanell. Analysis of the role of the microporous layer in improving polymer electrolyte fuel cell performance. *Electrochimica Acta*, 268:366–382, 2018. ISSN 0013-4686. doi: 10.1016/j.electacta.2018.02.100.

[65] Mehdi Andisheh-Tadbir, Erik Kjeang, and Majid Bahrami. Thermal conductivity of microporous layers: Analytical modeling and experimental validation. *Journal of Power Sources*, 296:344–351, 2015. ISSN 0378-7753. doi: 10.1016/j.jpowsour.2015.07.054.

[66] Odne S. Burheim, Huaneng Su, Sivakumar Pasupathi, Jon G. Pharoah, and Bruno G. Pollet. Thermal conductivity and temperature profiles of the micro porous layers used for the polymer electrolyte membrane fuel cell. *International Journal of Hydrogen Energy*, 38(20):8437–8447, 2013. ISSN 0360-3199. doi: 10.1016/j.ijhydene.2013.04.140.

[67] Sehkyu Park, Jong-Won Lee, and Branko N. Popov. Effect of PTFE content in microporous layer on water management in PEM fuel cells. *Journal of Power Sources*, 177(2):457–463, 2008. ISSN 0378-7753. doi: 10.1016/j.jpowsour.2007.11.055.

[68] Xiaoli Wang, Huamin Zhang, Jianlu Zhang, Haifeng Xu, Xiaobing Zhu, Jian Chen, and Baolian Yi. A bi-functional micro-porous layer with composite carbon black for PEM fuel cells. *Journal of Power Sources*, 162(1):474–479, 2006. ISSN 0378-7753. doi: 10.1016/j.jpowsour.2006.06.064.

[69] Gu-Gon Park, Young-Jun Sohn, Sung-Dae Yim, Tae-Hyun Yang, Young-Gi Yoon, Won-Yong Lee, Koichi Eguchi, and Chang-Soo Kim. Adoption of nano-materials for the micro-layer in gas diffusion layers of pemfcs. *Journal of Power Sources*, 163(1):113–118, 2006. ISSN 0378-7753. doi: 10.1016/j.jpowsour.2005.11.103.

[70] Takashi Sasabe, Phengxay Deevanhxay, Shohji Tsushima, and Shuichiro Hirai. Soft x-ray visualization of the liquid water transport within the cracks of micro porous layer in PEMFC. *Electrochemistry Communications*, 13(6):638–641, 2011. ISSN 1388-2481. doi: 10.1016/j.elecom.2011.03.033.

[71] Chang Sun Kong, Do-Young Kim, Han-Kyu Lee, Yong-Gun Shul, and Tae-Hee Lee. Influence of pore-size distribution of diffusion layer on mass-transport problems of proton exchange membrane fuel cells. *Journal of Power Sources*, 108(1):185–191, 2002. ISSN 0378-7753. doi: 10.1016/S0378-7753(02)00028-9.

[72] Xin Shi, Daokuan Jiao, Zhiming Bao, Kui Jiao, Wenmiao Chen, and Zhi Liu. Liquid transport in gas diffusion layer of proton exchange membrane fuel cells: Effects of micro-porous layer cracks. *International Journal of Hydrogen Energy*, 47(9):6247–6258, 2022. ISSN 0360-3199. doi: 10.1016/j.ijhydene.2021.11.248.

[73] Jeong Hwan Chun, Dong Hyun Jo, Sang Gon Kim, Sun Hee Park, Chang Hoon Lee, and Sung Hyun Kim. Improvement of the mechanical durability of micro porous layer in a proton exchange membrane fuel cell by elimination of surface cracks. *Renewable Energy*, 48:35–41, 2012. ISSN 0960-1481. doi: 10.1016/j.renene.2012.04.011.

[74] Fumiya Akitomo, Takashi Sasabe, Toshihiko Yoshida, Hiroshi Naito, Katsuyuki Kawamura, and Shuichiro Hirai. Investigation of effects of high temperature and pressure on a polymer electrolyte fuel cell with polarization analysis and x-ray imaging of liquid water. *Journal of Power Sources*, 431:205–209, 2019. ISSN 0378-7753. doi: 10.1016/j.jpowsour.2019.04.115.

[75] Nobuaki Nonoyama, Shinobu Okazaki, Adam Z. Weber, Yoshihiro Ikogi, and Toshihiko Yoshida. Analysis of oxygen-transport diffusion resistance in proton-exchange-membrane fuel cells. *Journal of The Electrochemical Society*, 158(4):B416, 2011. ISSN 1945-7111 0013-4651. doi: 10.1149/1.3546038.

[76] Anne Berger, Michael Striednig, Christoph Simon, and Hubert A. Gasteiger. Determination of the τ/ε-ratio for gas diffusion substrates and microporous layers in a proton exchange membrane fuel cell. *Journal of The Electrochemical Society*, 172(1):014508, jan 2025. doi: 10.1149/1945-7111/ada63e.

[77] Michele Bozzetti, Anne Berger, Carlos Cuadrado Collados, Matthias Thommes, Hubert A. Gasteiger, and Vasiliki Tileli. On tortuosity and water management in hydrophobic and hydrophilic microporous layers with different carbon structures. *Journal of The Electrochemical Society*, 172(3):036505, mar 2025. doi: 10.1149/1945-7111/adc0c4.

[78] R.B. Bird, W.E. Stewart, and E.N. Lightfoot. *Transport Phenomena*. Wiley, 2006. ISBN 9780470115398.

[79] D. R. Baker, D. A. Caulk, K. C. Neyerlin, and M. W. Murphy. Measurement of oxygen transport resistance in PEM fuel cells by limiting current methods. *Journal of The Electrochemical Society*, 156(9):B991–B100, 2009. doi: 10.1149/1.3152226åĚt.

[80] Nagappan Ramaswamy, Swami Kumaraguru, Roland Koestner, Timothy Fuller, Wenbin Gu, Nancy Kariuki, Deborah Myers, Peter J. Dudenas, and Ahmet Kusoglu. Editors' choice—ionomer side chain length and equivalent weight impact on high current density transport resistances in PEMFC cathodes. *Journal of The Electrochemical Society*, 168(2):024518, 2021. ISSN 1945-7111 0013-4651. doi: 10.1149/1945-7111/abe5eb.

[81] Zijie Lu, James Waldecker, Mickey Tam, and Max Cimenti. Influence of MPL structure modification on fuel cell oxygen transport resistance. *ECS Transactions*, 69(17):1341, 2015. ISSN 1938-5862. doi: 10.1149/06917.1341ecst.

[82] Daniel Niblett, Adrian Mularczyk, Vahid Niasar, Jens Eller, and Stuart Holmes. Two-phase flow dynamics in a gas diffusion layer - gas channel - microporous layer system. *Journal of Power Sources*, 471:228427, 2020. ISSN 0378-7753. doi: 10.1016/j.jpowsour.2020.228427.

[83] Jung Ho Kang, Kyu-Jin Lee, Jin Hyun Nam, Charn-Jung Kim, Hee Sung Park, Sungho Lee, and Inchul Kwang. Visualization of invasion–percolation drainage process in porous media using density-matched immiscible fluids and refractive-index-matched solid structures. *Journal of Power Sources*, 195(9):2608–2612, 2010. ISSN 0378-7753. doi: 10.1016/j.jpowsour.2009.11.087.

[84] Yen-Chun Chen, Anne Berger, Salvatore De Angelis, Tobias Schuler, Michele Bozzetti, Jens Eller, Vasiliki Tileli, Thomas J. Schmidt, and Felix N. Büchi. A method for spatial quantification of water in microporous layers of polymer electrolyte fuel cells by x-ray tomographic microscopy. *ACS Applied Materials & Interfaces*, 13(14):16227–16237, 2021. ISSN 1944-8244. doi: 10.1021/acsami.0c22358.

[85] Yasutaka Nagai, Jens Eller, Tatsuya Hatanaka, Satoshi Yamaguchi, Satoru Kato, Akihiko Kato, Federica Marone, Hong Xu, and Felix N. Büchi. Improving water management in fuel cells through microporous layer modifications: Fast operando tomographic imaging of liquid water. *Journal of Power Sources*, 435:226809, 2019. ISSN 0378-7753. doi: 10.1016/j.jpowsour.2019.226809.

[86] J. P. James, H. W. Choi, and J. G. Pharoah. X-ray computed tomography reconstruction and analysis of polymer electrolyte membrane fuel cell porous transport layers. *International Journal of Hydrogen Energy*, 37(23):18216–18230, 2012. ISSN 0360-3199. doi: 10.1016/j.ijhydene.2012.08.077.

[87] C. Tötzke, G. Gaiselmann, M. Osenberg, J. Bohner, T. Arlt, H. Markötter, A. Hilger, F. Wieder, A. Kupsch, B. R. Müller, M. P. Hentschel, J. Banhart, V. Schmidt, W. Lehnert, and I. Manke. Three-dimensional study of compressed gas diffusion layers using synchrotron x-ray imaging. *Journal of Power Sources*, 253:123–131, 2014. ISSN 0378-7753. doi: 10.1016/j.jpowsour.2013.12.062.

[88] Nada Zamel, Xianguo Li, and Jun Shen. Correlation for the effective gas diffusion coefficient in carbon paper diffusion media. *Energy & Fuels*, 23(12):6070–6078, 2009. ISSN 0887-0624. doi: 10.1021/ef900653x.

[89] Denis Kramer, Stefan A. Freunberger, Reto Flückiger, Ingo A. Schneider, Alexander Wokaun, Felix N. Büchi, and Günther G. Scherer. Electrochemical diffusimetry of fuel cell gas diffusion layers. *Journal of Electroanalytical Chemistry*, 612(1):63–77, 2008. ISSN 1572-6657. doi: 10.1016/j.jelechem.2007.09.014.

[90] Yen-Chun Chen, Chrysoula Karageorgiou, Jens Eller, Thomas J. Schmidt, and Felix N. Büchi. Determination of the porosity and its heterogeneity of fuel cell microporous layers by x-ray tomographic microscopy. *Journal of Power Sources*, 539:231612, 2022. ISSN 0378-7753. doi: 10.1016/j.jpowsour.2022.231612.

[91] Michele Bozzetti, Anne Berger, Robin Girod, Yen-Chun Chen, Felix N. Büchi, Hubert A. Gasteiger, and Vasiliki Tileli. On the role of pore constrictions in gas diffusion electrodes. *Chemical Communications*, 58(63):8854–8857, 2022. ISSN 1359-7345. doi: 10.1039/D2CC02844A.

[92] Abhishek Nanjundappa, Alireza Sadeghi Alavijeh, Mohamed El Hannach, David Harvey, and Erik Kjeang. A customized framework for 3-d morphological characterization of microporous layers. *Electrochimica Acta*, 110:349–357, 2013. ISSN 0013-4686. doi: 10.1016/j.electacta.2013.04.103.

[93] A. Pournemat, H. Markötter, F. Wilhelm, S. Enz, H. Kropf, I. Manke, and J. Scholta. Nano-scale monte carlo study on liquid water distribution within the polymer electrolyte membrane fuel cell microporous layer, catalyst layer and their interfacial region. *Journal of Power Sources*, 397:271–279, 2018. ISSN 0378-7753. doi: 10.1016/j.jpowsour.2018.07.027.

[94] Jens Eller, Federica Marone, and Felix N. Büchi. Operando sub-second tomographic imaging of water in PEFC gas diffusion layers. *ECS Transactions*, 69(17):523, 2015. ISSN 1938-5862. doi: 10.1149/06917.0523ecst.

[95] Adrian Mularczyk, Qingyang Lin, Martin J. Blunt, Adrien Lamibrac, Federica Marone, Thomas J. Schmidt, Felix N. Büchi, and Jens Eller. Droplet and percolation network interactions in a fuel cell gas diffusion layer. *Journal of The Electrochemical Society*, 167(8):084506, 2020. ISSN 1945-7111 0013-4651. doi: 10.1149/1945-7111/ab8c85.

[96] Jens Eller, Jörg Roth, Federica Marone, Marco Stampanoni, and Felix N. Büchi. Operando properties of gas diffusion layers: Saturation and liquid permeability. *Journal of The Electrochemical Society*, 164(2):F115, 2017. ISSN 1945-7111. doi: 10.1149/2.0881702jes.

[97] Hong Xu, Minna Bührer, Federica Marone, Thomas J. Schmidt, Felix N. Büchi, and Jens Eller. Effects of gas diffusion layer substrates on PEFC water management: Part i. operando liquid water saturation and gas diffusion properties. *Journal of The Electrochemical Society*, 168(7):074505, 2021. ISSN 1945-7111 0013-4651. doi: 10.1149/1945-7111/ac1035.

[98] Suman Basu, Chao-Yang Wang, and Ken S. Chen. Phase change in a polymer electrolyte fuel cell. *Journal of The Electrochemical Society*, 156(6):B748, 2009. ISSN 1945-7111 0013-4651. doi: 10.1149/1.3115470.

[99] Yen-Chun Chen, Tim Dörenkamp, Christoph Csoklich, Anne Berger, Federica Marone, Jens Eller, Thomas J. Schmidt, and Felix N. Büchi. On the water transport mechanism through the microporous layers of operando polymer electrolyte fuel cells probed directly by x-ray tomographic microscopy. *Energy Advances*, 2(9):1447–1463, 2023. doi: 10.1039/D3YA00189J.

[100] Satoru Kato, Satoshi Yamaguchi, Wataru Yoshimune, Yoriko Matsuoka, Akihiko Kato, Yasutaka Nagai, and Takahisa Suzuki. Ex-situ visualization of the wet domain in the microporous layer in a polymer electrolyte fuel cell by x-ray computed tomography under water vapor supply. *Electrochemistry Communications*, 111:106644, 2020. ISSN 1388-2481. doi: 10.1016/j.elecom.2019.106644.

[101] Jin Hyun Nam, Kyu-Jin Lee, Gi-Suk Hwang, Charn-Jung Kim, and Massoud Kaviany. Microporous layer for water morphology control in PEMFC. *International Journal of Heat and Mass Transfer*, 52 (11):2779–2791, 2009. ISSN 0017-9310. doi: 10.1016/j.ijheatmasstransfer.2009.01.002.

[102] P. Boillat, E. H. Lehmann, P. Trtik, and M. Cochet. Neutron imaging of fuel cells – recent trends and future prospects. *Current Opinion in Electrochemistry*, 5(1):3–10, 2017. ISSN 2451-9103. doi: 10.1016/j.coelec.2017.07.012.

[103] A. Bazylak. Liquid water visualization in PEM fuel cells: A review. *International Journal of Hydrogen Energy*, 34(9):3845–3857, 2009. ISSN 0360-3199. doi: 10.1016/j.ijhydene.2009.02.084.

[104] A. Mohseninia, D. Kartouzian, M. Eppler, P. Langner, H. Markötter, F. Wilhelm, J. Scholta, and I. Manke. Influence of structural modification of micro-porous layer and catalyst layer on performance and water management of pem fuel cells: Hydrophobicity and porosity. *Fuel Cells*, 20(4):469–476, 2020. ISSN 1615-6846. doi: 10.1002/fuce.201900203.

[105] A. Mohseninia, M. Eppler, D. Kartouzian, H. Markötter, N. Kardjilov, F. Wilhelm, J. Scholta, and I. Manke. PTFE content in catalyst layers and microporous layers: Effect on performance and water distribution in polymer electrolyte membrane fuel cells. *Journal of The Electrochemical Society*, 168 (3):034509, 2021. ISSN 1945-7111 0013-4651. doi: 10.1149/1945-7111/abec53.

[106] Alfredo Iranzo and Pierre Boillat. Liquid water distribution patterns featuring back-diffusion transport in a PEM fuel cell with neutron imaging. *International Journal of Hydrogen Energy*, 39(30):17240–17245, 2014. ISSN 0360-3199. doi: 10.1016/j.ijhydene.2014.08.042.

[107] Kinanti Aliyah, Christian Prehal, Justus S. Diercks, Nataša Diklić, Linfeng Xu, Seçil Ünsal, Christian Appel, Brian R. Pauw, Glen J. Smales, Manuel Guizar-Sicairos, Juan Herranz, Lorenz Gubler, Felix N. Büchi, and Jens Eller. Quantification of PEFC catalyst layer saturation via in silico, ex situ, and in situ small-angle x-ray scattering. *ACS Applied Materials & Interfaces*, 15(22):26538–26553, 2023. ISSN 1944-8244. doi: 10.1021/acsami.3c00420.

[108] Pierre Toudret, Julie Wolanin, Gérard Gebel, and Arnaud Morin. Investigation of ionomer hydration and local relative humidity in platinum and non-noble based catalyst layers in proton exchange membrane fuel cells using SAXS. *Journal of Power Sources*, 586:233671, 2023. ISSN 0378-7753. doi: 10.1016/j.jpowsour.2023.233671.

[109] Jongmin Lee, Sylvie Escribano, Fabrice Micoud, Gérard Gebel, Sandrine Lyonnard, Lionel Porcar, Nicolas Martinez, and Arnaud Morin. In situ measurement of ionomer water content and liquid water saturation in fuel cell catalyst layers by high-resolution small-angle neutron scattering. *ACS Applied Energy Materials*, 3(9):8393–8401, 2020. doi: 10.1021/acsaem.0c00853.

[110] Christoph Simon, Frédéric Hasché, David Müller, and Hubert A. Gasteiger. Influence of the gas diffusion layer compression on the oxygen mass transport in PEM fuel cells. *ECS Transactions*, 69 (17):1293, 2015. ISSN 1938-5862. doi: 10.1149/06917.1293ecst.

[111] Fengmin Du, Tuan Anh Dao, Pia Valentina Josephine Peitl, Andreas Bauer, Kathrin Preuss, Alex Martinez Bonastre, Jonathan Sharman, Geoffrey Spikes, Markus Perchthaler, Thomas J. Schmidt, and Alin Orfanidi. Effects of pemfc operational history under dry/wet conditions on additional voltage losses due to ionomer migration. *Journal of The Electrochemical Society*, 167(14), 2020. ISSN 0013-4651 1945-7111. doi: 10.1149/1945-7111/abc83f.

[112] Ruediger Schweiss, Magnus Herb, Raj Earla, and Christian Meiser. On the importance of MPL structural characteristics for PEM fuel cell performance. *ECS Transactions*, 112(4):135, 2023. ISSN 1938-5862. doi: 10.1149/11204.0135ecst.

[113] David A. Caulk and Daniel R. Baker. Heat and water transport in hydrophobic diffusion media of pem fuel cells. *Journal of The Electrochemical Society*, 157(8):B1237, 2010. ISSN 1945-7111 0013-4651. doi: 10.1149/1.3454721.

[114] Kinanti Hantiyana Aliyah, Christian Appel, Christian Prehal, Manuel Guizar Sicairos, Lorenz Gubler, and Jens Eller. Operando liquid water saturation in PEFC catalyst layers determined via small angle x-ray scattering. *ECS Meeting Abstracts*, MA2022-02(39):1412, 2022. ISSN 2151-2043. doi: 10.1149/MA2022-02391412mtgabs.

[115] Hong Xu. *Subsecond Operando X-ray Tomographic Microscopy of Liquid Water in Polymer Electrolyte Fuel Cells*. Thesis, 2021.

[116] Christoph Simon, Frédéric Hasché, and Hubert A. Gasteiger. Influence of the gas diffusion layer compression on the oxygen transport in PEM fuel cells at high water saturation levels. *Journal of The Electrochemical Society*, 164(6):F591, 2017. ISSN 1945-7111. doi: 10.1149/2.0691706jes.

[117] Woo-kum Lee, Chien-Hsien Ho, J. W. Van Zee, and Mahesh Murthy. The effects of compression and gas diffusion layers on the performance of a PEM fuel cell. *Journal of Power Sources*, 84(1): 45–51, 1999. ISSN 0378-7753. doi: 10.1016/S0378-7753(99)00298-0.

[118] Jiabin Ge, Andrew Higier, and Hongtan Liu. Effect of gas diffusion layer compression on PEM fuel cell performance. *Journal of Power Sources*, 159(2):922–927, 2006. ISSN 0378-7753. doi: 10.1016/j.jpowsour.2005.11.069.

[119] Prodip K. Das, Xianguo Li, and Zhong-Sheng Liu. Effective transport coefficients in PEM fuel cell catalyst and gas diffusion layers: Beyond bruggeman approximation. *Applied Energy*, 87(9):2785–2796, 2010. ISSN 0306-2619. doi: 10.1016/j.apenergy.2009.05.006.

[120] V. Mishra, F. Yang, and R. Pitchumani. Measurement and prediction of electrical contact resistance between gas diffusion layers and bipolar plate for applications to PEM fuel cells. *Journal of Fuel Cell Science and Technology*, 1(1):2–9, 2004. ISSN 1550-624X. doi: 10.1115/1.1782917.

[121] Iwao Nitta, Olli Himanen, and Mikko Mikkola. Contact resistance between gas diffusion layer and catalyst layer of pem fuel cell. *Electrochemistry Communications*, 10(1):47–51, 2008. ISSN 1388-2481. doi: 10.1016/j.elecom.2007.10.029.

[122] K. C. Neyerlin, Wenbin Gu, Jacob Jorne, Alfred Clark, and Hubert A. Gasteiger. Cathode catalyst utilization for the ORR in a PEMFC: Analytical model and experimental validation. *Journal of The Electrochemical Society*, 154(2):B279, 2007. ISSN 1945-7111 0013-4651. doi: 10.1149/1.2400626.

[123] Anne Berger, Benjamin Strehle, Tanja Zünd, David Schreiner, and H.A. Gasteiger. Method porosimetry: Using mercury intrusion porosimetry in battery research. Technical report, Micromeritics, 2025.

List of Figures

Acknowledgements

This thesis would not have been possible without the support of many people.

I owe a great deal to my supervisor, Prof. Hubert Gasteiger. His consistent high-quality feedback and extensive knowledge in the field have played an important role in shaping my research skills. Working under his guidance has not only enhanced my understanding of what matters most but has also improved my ability to focus on key aspects. His attention to detail and constant support, especially during challenging times, have been instrumental. I appreciate that he trusts us with important issues, showing he believes in our abilities.

I am grateful to my colleagues for their dedication in keeping the lab running smoothly. The positive working atmosphere and helpful discussions have made my time here enjoyable and productive. The collective effort of the team has been crucial in maintaining the functionality of our test station, and I want to express a special acknowledgment to Yan-Sheng Li for this shared dedication and tireless work on the shared test bench. I also want to thank Timon Lazaridis, Ana Marija Damjanovic, Björn Stühmeier, Matthias Ernst, and Yan-Sheng Li for their insightful discussions. The exchange of ideas has created a supportive and intellectually stimulating environment.

I extend my sincere appreciation to our project partners, whose collaboration has significantly enriched my research projects. I want to thank Yen-Chun Chen, Michele Bozzetti, and Kinanti Aliyah Hantiyana for their dedicated work on shared publications. Engaging in discussions with professors and group leaders within the Synergia project has been particularly valuable. I express my gratitude to Thomas J. Schmidt, Felix N. Büchi, Vasiliki Tileli, Jens Eller, and Juan Herranz for their valuable insights and contributions.

I would like to extend my gratitude to my students Jacqueline Gatzemeier, Philip Mayer, and Theresa Hauth for their dedicated work and contributions to this research. Their efforts have not only supported the progress of the project and but also working alongside such motivated and capable individuals has been a rewarding experience.

I want to thank my parents, Angela and Uwe, my sister Juliane, and my friends for their constant support. Their encouragement and belief in me made this achievement possible. A special acknowledgment goes to Max, who has been a constant presence and pillar of support along this academic path.

I also appreciate everyone else who has contributed to my academic and personal growth, directly or indirectly. Your influence has played a crucial role in shaping this thesis. I am thankful to all these individuals and institutions for their support and collaboration. This work would not have been possible without them.